Segregation and Homogenization of Alloying Elements in X70 Steels

by

Rishav Raj

A thesis submitted in partial fulfillment of the requirements for the degree of

Master of Science

in

Materials Engineering

Department of Chemical and Materials Engineering

University of Alberta

Abstract

Solidification during continuous casting of X70 microalloyed steel results in two types of elemental segregation; microsegregation (interdendritic) and macrosegregation (at the centerline). Both micro and macrosegregation lead to deterioration of steel properties and, hence, a lower degree of segregation is highly sought after. The extent of segregation that occurs is dependent upon the continuous casting parameters and the composition of the steel. To reduce microsegregation, and to a lesser extent macrosegregation, homogenization of the cast material is undertaken. Homogenization is the process by which the cast steel is heated to a specific temperature and held for a period of time. During homogenization, diffusion of elements from regions of high concentration to low concentration occur. The ability to reduce segregation depends on the extent of segregation that occurs during solidification and on the homogenizing conditions.

A quantitative study of element segregation was undertaken in order to understand the solidification behavior of alloying elements during continuous casting of microalloyed steels. Two X70 steels, S1 and S2, were studied to quantify the as-cast segregation and the effect of homogenization on segregation. The steels were chosen based on their different nominal compositions of Mn, Cr and Nb. A third steel, S3, was used to study the unidirectional solidification of microalloyed steel at two different cooling rates. The study presented in this work is comprised of two components; measurement and prediction of segregation during solidification, followed by the modeling and laboratory testing of the homogenization process.

Electron microprobe analysis (EMPA) was used to map the concentration distribution of Mn, Cr, Nb and P, and to quantify their extent of segregation in industrial as-cast slabs. Segregation ratio (S.R.), defined as the ratio of measured concentration to the nominal composition, was used

as a measure to quantify the extent of segregation. Bridgman directional solidification was used to study the effects of cooling rate on the partition coefficients for Mn, Cr, Nb and P. Two samples were solidified at a cooling rate of 0.4ºC/s and 0.2ºC/s. Laboratory homogenization heat treatments were performed at 1000, 1100 and 1200ºC for 3, 6 and 12 h to study the effects of homogenization on segregation. ThermoCalc software was used to simulate solidification and diffusion of alloying elements. The Scheil module was used to model segregation during solidification and the DICTRA (Diffusion Controlled Transformation) module was used to model the diffusion of alloying elements during homogenization.

Among the studied elements, Mn displayed the highest degree of microsegregation ratio (1.09-1.10), followed by Cr (1.04-1.08) and P (<1.00). The degree of macrosegregation ratio was highest for P (>3.00) followed by Mn (1.20-1.50) and Cr (1.10-1.13). The precipitation of Nb in the form of carbonitrides during casting complicated the EMPA segregation measurements for Nb.

The measured microsegregation concentration profiles of Mn, Cr and Nb in as-cast slabs compared equally well with both Gulliver-Scheil (GS) and modified GS calculations, while microsegregation profiles for P were better predicted using the modified GS calculations. The inclusion of back diffusion for P during modified GS calculations resulted in a closer match with the experimentally obtained values.

A decrease in partition coefficient was observed for Mn, Cr and P with a decrease in cooling rate from 0.4ºC/s to 0.2ºC/s. The magnitude of the decrease in the partition coefficients was low for Mn and Cr (<0.05), as compared with P (>0.05). Formation of precipitates of Nb again inhibited the partition coefficient calculation for Nb. Being a more robust method as compared to S.R., the partition coefficient calculation method was also applied to as-cast and homogenized samples data for Mn to further explore its usage.

The decrease in S.R. after homogenization was negligible for Mn and Cr in the interdendritic samples. The P microsegregation ratio decreased from 0.66 to 0.48 after 6 h at 1200°C. In centerline samples, the macrosegregation ratios for Mn and P decreased to 1.21 from 1.45 and 2.06 from 3.90, respectively. The change in macrosegregation ratio for Cr was relatively low (<0.10). The extent of diffusion for P was considerably higher as compared with Mn, Cr and Nb in both EMPA and ThermoCalc results. The degree of diffusion of elements was lower in the DICTRA predictions as compared with the EMPA results from the homogenized samples.

مكتوب

It’s written...

Acknowledgements

I am grateful to Dr. Hani Henein for providing me with the opportunity to work as a researcher in the field of steel casting. His invaluable guidance has molded me into a better researcher and a better human. I am extremely thankful to Dr. Barry Wiskel for his detailed insights and instructions throughout the course of my research work. This thesis would have never taken shape without his continued support.

I express my sincere thanks to Dr. Laurie Collins for shaping this project and for sharing his knowledge and understanding over numerous discussions. His input has had a great impact on the project. I would also like to thank Dr. Douglas Ivey and Dr. Muhammad Arafin for their feedback and support. I am thankful to Andrew for ensuring the completion of my experiments. I appreciate his eagerness to help and patience to work with me.

A special thanks to Jonas, Aziz, Rangasayee and Neil for always being available to help me out. Their assistance with both academic and non academic aspects has been vital. I am grateful to my group members, Mehdi, Steffen, Lu, Vanda, Tailin and Mingzhang for participating in my project through discussions. I appreciate all your input.

I am blessed to have a skilled brother. Thanks babu (Rohit) for helping me with all the codes and being there whenever and wherever I needed anything. A sincere thanks to all my friends and a big thanks to Anna for keeping me on track and motivating me throughout. I deeply appreciate it.

I would also like to thank EVRAZ NA, TC Energy and NSERC for funding the project. Most of all, I am fully indebted to my parents for being selfless and allowing me to fly. Thank you mummy and papa!

Contents

List of Figures

List of Tables

1. Introduction

Microalloyed steel is one of the most widely used structural materials in the construction, transportation, automobile and pipeline industries. The addition of small amounts of alloying elements like Mn, Nb, Ti, etc. to conventional low C steel results in microalloyed steels [1-4], which exhibit enhanced mechanical properties at a lower cost [5-7]. The production of microalloyed steel begins with continuous casting, followed by thermomechanical controlled processing (TMCP) which can include homogenization heat treatment, rough rolling, final rolling and lamellar cooling depending on the final product.

During continuous casting (a solidification process), enrichment of solutes (alloying elements) in liquid steel occurs as the steel solidifies because of the lower solubility of alloying elements in solid iron. The enrichment of solutes leads to an inhomogeneous spatial distribution of alloying elements in the solidified steel, also known as segregation. Segregation is broadly divided into two types, microsegregation (interdendritic segregation) and macrosegregation (centerline segregation).

Segregation can negatively affect the properties of steel [8-11] and cannot be avoided; hence, the solidified steel slabs go through a homogenization (heat treatment) process [12] in order to reduce the severity of segregation. During homogenization, solute redistribution (diffusion from regions of high concentration to low concentration) takes place as the steel slabs are reheated and held at higher temperatures. The homogenization heat treatment is an energy intensive process; therefore, its understanding is essential. The research aims of this work are:

1. Quantify the magnitude of micro and macrosegregation of Mn, Cr, Nb and P in continuously cast microalloyed steel slabs using EMPA.
2. Study the effect of cooling rate on partition coefficients of Mn, Cr, Nb and P using Bridgman unidirectional solidification.
3. Study the effect of homogenization time and temperature on segregation.
4. Predict the amount of segregation during solidification and the extent of diffusion during homogenization using the Scheil and DICTRA modules of ThermoCalc.
5. Compare ThermoCalc segregation predictions with measured as-cast data.
6. Compare the reduction in segregation of laboratory homogenized samples with the reduction predicted by DICTRA.

A literature review of segregation during continuous casting of microalloyed steels and the use of Bridgman solidification to study the solidification structure of alloys is presented in Chapter 2. The segregation and directional solidification parts are followed by a background study of steel homogenization and the application of EMPA to quantify element concentration. Following EMPA, a description of ThermoCalc based theoretical models and previous work in the field of modeling segregation and diffusion of alloying elements in microalloyed steels are reviewed.

Following the literature review is the materials and experimental methods chapter (Chapter 3). This includes a description of the steels studied, their composition and origin. Experimental techniques used for composition analysis, directional solidification and homogenization heat treatment are also described in this chapter. Finally, the theoretical models for predicting the amount of segregation during solidification and the magnitude of diffusion during homogenization are presented.

The segregation measurement and calculation results are shown and discussed in Chapter 4 of this thesis. The chapter starts with the Mn EMPA results for as-cast samples. The trends and values observed in the Mn EMPA maps are compared with previous Mn segregation measurement studies. Following the Mn EMPA results, Cr, Nb and P segregation results are presented and discussed. The predictions of segregation through the simple GS and modified GS calculations are also presented and compared with the EMPA segregation measurements.

Chapter 5 contains the EMPA results from directionally solidified Bridgman samples. The effect of changing cooling rate on segregation trend of Mn, Cr, Nb and P is evaluated in terms of partition coefficient (k) of the elements. The measured k values are compared with the predicted k values from GS calculations and with the available literature.

The homogenization heat treatment results are presented in Chapter 6 of this thesis. The measured changes in segregation ratio values for Mn, Cr, Nb and P are also compared with DICTRA based homogenization simulations and with previous work on steel homogenization.

Finally, the findings are summarised and conclusions are drawn based on these findings in Chapter 7. The areas that need more work both experimentally and theoretically are identified. In the end, possible future work to build up-on the work done in the thesis and to further enhance the models is outlined.

2. Literature review

This chapter contains a review of microalloyed steels and the effects of the addition of alloying elements on the properties of the steels. Furthermore, an overview of the continuous casting process and how it results in micro and macrosegregation in cast slabs along with the consequences of segregation is discussed. Additionally, the chapter includes a description of directional solidification using a Bridgman furnace and previous studies on the effects of soft reduction and homogenization heat treatment on segregation. The use of the electron microprobe for composition analysis and the application of ThermoCalc to predict segregation and diffusion trends of alloying elements in microalloyed steels are also reviewed in this chapter.

2.1 Microalloyed steel and the role of alloying elements

Microalloyed steels are formed by the addition of small amounts of alloying elements to conventional low C steels [1-4]. They are known for their low cost and superior mechanical properties like yield strength and toughness [13-16]. They possess yield strengths in the range of 500-700 MPa and some research also suggests that the yield strength for microalloyed steels could reach up to 1000 MPa [17]. The typical composition for microalloyed steels comprises 0.04 to 0.12 wt% C, as high as 2 wt% Mn and Cr, and less than 0.5 wt% Nb [18-20]. The alloying elements assist in grain refinement, solute strengthening and precipitate strengthening.

The most commonly added alloying element in steel is Mn. The addition of Mn delays austenite decomposition and promotes an acicular microstructure which results in better strength and toughness for the steel [21-24]. It also increases the strength of alloyed steel by solid solution strengthening because of its interaction with the iron matrix and increases ferrite microhardness [25-27]. Another important alloying addition in microalloyed steels is Nb. It helps in retarding austenite recrystallization through solute drag and strain induced precipitation [28-35], which eventually lead to better toughness. Chromium in steel facilitates bainite transformation [36-38] and assists in increasing the solubility of Nb [39-42], however, it is not as effective in retarding recrystallization [43-44]. Segregation of elements occur during solidification of steels and has been extensively studied because of its impact on strength, toughness and corrosion resistance of the steel [45-58]. Another important element from a segregation point of view is P, which is an interstitial solute in steel, and is present in steel as an impurity in small amounts [58-60]. It assists in solid solution strengthening but has a negative impact on mechanical properties due to its segregation

[61-63]. Segregation cannot be eliminated and results in performance degradation of the steel. Segregation during continuous casting of microalloyed steels is reviewed in the following section.

2.2 Segregation during continuous casting of microalloyed steel

This section contains a review of the continuous casting process, followed by the types of segregation observed during continuous casting of steels. Subsequent sub-sections also present information on the ways to study and quantify segregation.

2.2.1 Continuous casting

Continuous casting is the most widely used solidification process in steel production. During continuous casting, liquid metal is poured from a ladle into a tundish before being poured into molds. The tundish allows a continuous flow rate of liquid metal into the molds while the ladles refill. When the liquid metal enters the mold it starts to solidify. Once a shell of solid is formed, the steel is transferred on to support rolls where it is further cooled with the help of water sprays. The mold walls are cooled using flowing water to ensure heat extraction throughout the length of the mold. After solidification is complete, also called the metallurgical length for casting, a torch is used to cut the solidified slabs to the desired length. Figure 2.1 shows a schematic of continuous casting of steel slabs.

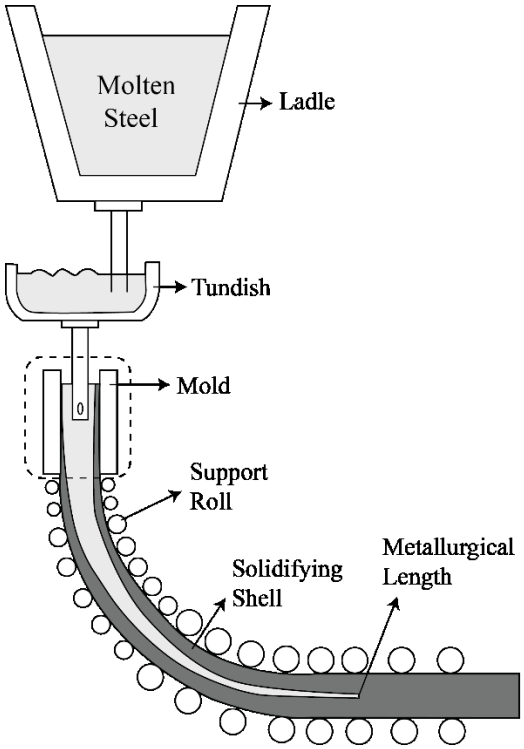

Fig. 2.1: Schematic representation of continuous casting of slab.

The evolution of microalloyed steels in the past few decades has greatly influenced the pipeline and transportation industries. Many interrelated phenomena like segregation, fluid flow, heat transfer, mass transfer, phase transformations and shrinkage take place during the continuous casting of microalloyed steels. Continuous casting has a direct influence on the quality of the final product and, hence, a comprehensive understanding of the overall process is essential.

When liquid steel comes in contact with the mold walls it experiences undercooling. Solidification begins from the mold walls when the driving force from undercooling exceeds the required amount of energy for transformation. Microalloyed steels, as with many other alloys are anisotropic materials and favor growth of the solid in some directions as compared to others because of the difference in surface energies of different growing planar fronts. Anisotropy combined with constitutional supercooling during solidification leads to dendritic growth, which is the most typically observed solidification morphology in as-cast structures. Figure 2.2-a shows dendritic growth in an as-cast steel billet. Dendrites are tree-like structures with a primary arm growing opposite to the direction of heat extraction. As primary dendrites grow larger, several secondary and tertiary arms start to grow in directions perpendicular to the primary dendrite arms. The dendrite arm spacing is a common solidification parameter which is related to cooling rate, microstructure and also segregation. Figure 2.2-b shows a schematic of dendrites and illustrates the measurement of dendrite arm spacing. λ_1 and λ_2 are primary and secondary dendrite spacings, respectively.

a) 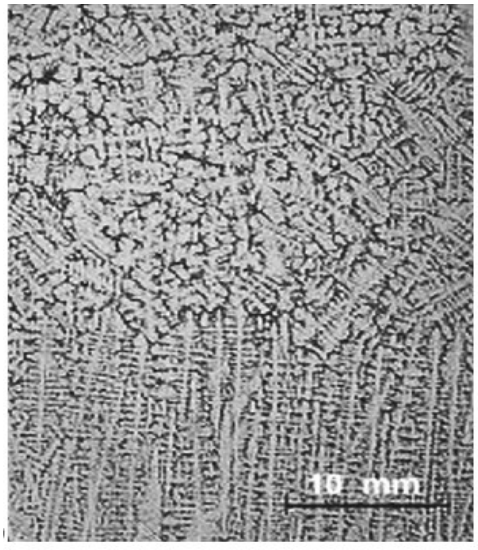

b) 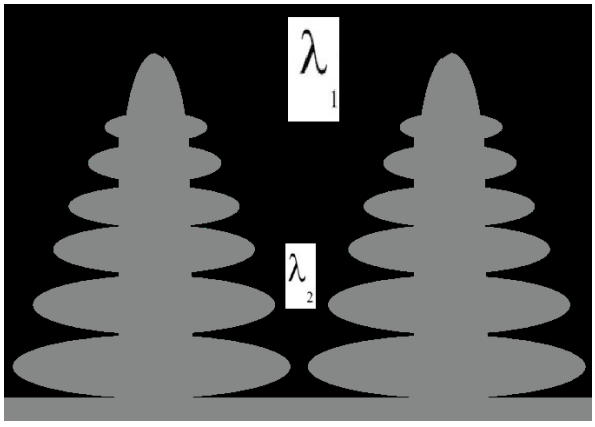

Fig. 2.2: a) Dendritic growth in as-cast steel billet [65] and b) representation of dendrites.

Interdendritic regions are richer in solute elements as compared to dendritic centers. The segregation of solutes in these interdendritic regions is known as microsegregation. As solidification proceeds, the temperature gradient decreases and an equiaxed grain structure is observed near the center of continuously cast slabs as shown in Figure 2.3. This region contains the metallurgical centerline (the last liquid to solidify) and is enriched with alloying elements over a larger scale (few centimeters).

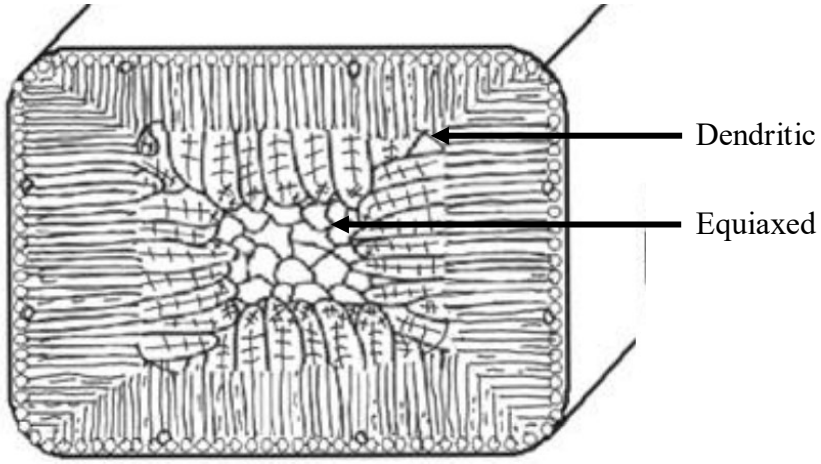

Fig. 2.3: Schematic representation of solidification structure in continuous cast steel slab [67].

2.2.2 Microsegregation

Microsegregation, also referred to as interdendritic segregation, occurs due to entrapment of solute rich liquid in interdendritic regions during solidification of alloys [68]. At the initial stage of solidification, liquid transforms into solid and the remaining liquid gets enriched in solute elements because of the lower solubility of solutes in the forming solid. Therefore, the next solid that forms has a higher solute content. This leads to a concentration gradient within the formed solid and is known as microsegregation. The extent of microsegregation for an element depends on its partition coefficient in the alloy [69]. The partition coefficient (k) at a particular temperature is defined as the ratio of solute concentration in the forming solid to that in the remaining liquid.

$$Partition\ coefficient\ for\ x\ (k_x) = \frac{C_s}{C_L} \qquad 2.1$$

where C_s and C_L are the concentration of solute in the solid and liquid phases, respectively.

During solidification, the extent of partitioning of solute elements between the solid and liquid phases depends on their partition coefficient. Partition coefficients for solute elements are calculated based on binary phase diagrams and are assumed to be independent of temperature for

most cases [70-72]. If the partition coefficient for an element is less than 1, which is commonly the case for solutes in microalloyed steels [73-74], the liquid becomes enriched in solutes as solidification proceeds. A value of partition coefficient close to 1 results in a smaller degree of segregation [75]. A list of partition coefficients obtained for different elements in steel is given in Table 2.1. Among substitutional solutes, Mn and Cr have a relatively high partition coefficient and are less likely to segregate, whereas, Nb and interstitial elements like C, P and S have relatively low partition coefficients and are likely to segregate more. As Nb is also a ferrite stabiliser, hence, has a lower k value in austenite than in ferrite. This means that the interdendritic segregation of Nb would be greater at the austenite/liquid interface than at the δ-ferrite/liquid interface. However, this is not typically applicable to low C microalloyed steels because of the lower likelihood of austenite formation.

Table 2.1: Equilibrium partition coefficients between liquid/δ-ferrite and liquid/austenite [76, 77].

Element	*k (δ/L)*	*k (γ/L)*
C	0.19	0.34
P	0.23	0.13
S	0.05	0.04
Mn	0.76	0.78
Nb	0.40	0.22
Cr	0.95	0.86

Figure 2.4 shows a comparison of the variation in segregation ratios for Mn and P, with Mn^o and P^o being the nominal content of Mn and P in the respective steels. Segregation ratio is defined as the ratio of measured and nominal concentration for individual elements. The theoretical line in the figure is calculated based on GS calculations with C_L and C_o as the predicted and nominal concentration of the respective elements. Since the partition coefficient of P is lower, P segregates considerably more than Mn. The individual data points in the figure were obtained through experiments. The black circles and diamonds correspond to the measured microsegregation ratios and the white circles and diamonds correspond to the measured semi-macro/centerline segregation ratio. Good agreement was observed between the measured data

points and the theoretical line. This supports the use of partition coefficients of solutes as a fundamental property to quantify segregation. It also confirms the hypothesis that a higher expected segregation ratio corresponds to a lower value of partition coefficient and vice-versa.

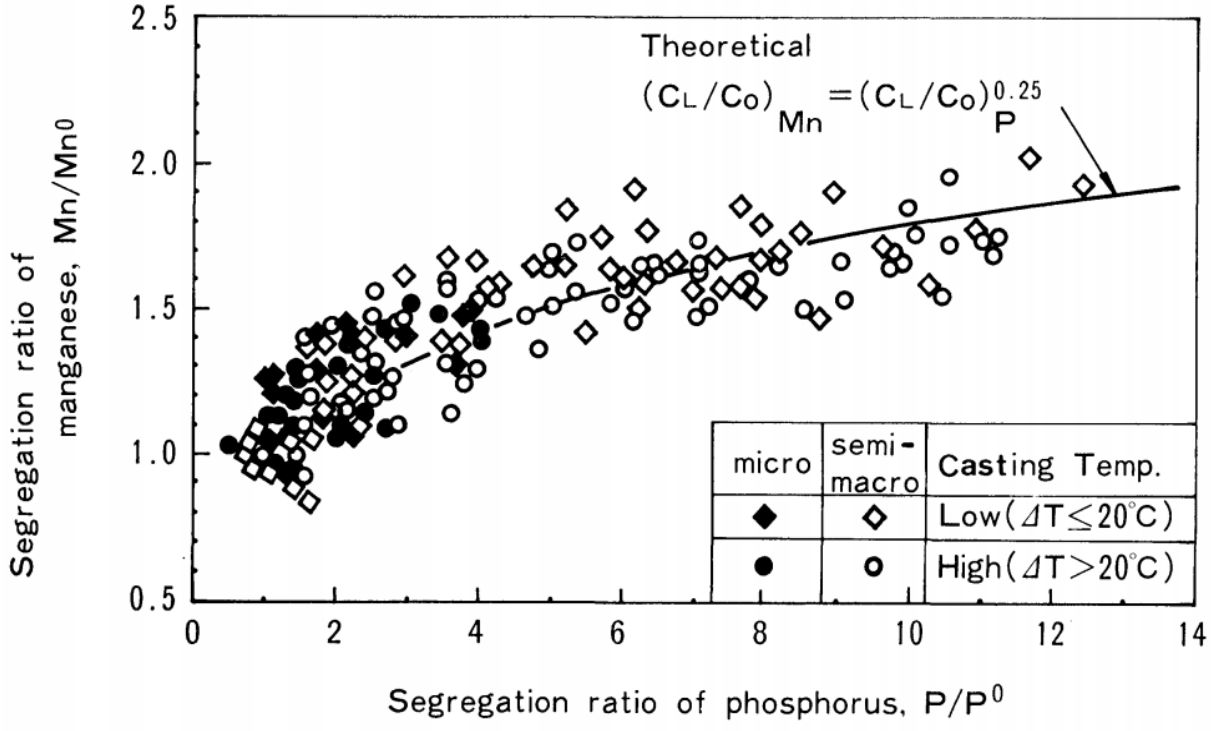

Fig. 2.4: Segregation ratio of Mn versus segregation ratio of P [78].

2.2.3 Macro/Centerline segregation

Another form of segregation that occurs during continuous casting of steels is centerline segregation or macrosegregation. Macrosegregation occurs due to the flow of solute rich liquid towards the center of as-cast slabs and encompasses a larger scale, ranging from hundreds of microns to even a few centimeters along the thickness of a slab [79-85]. An example of centerline segregation is shown in Figure 2.5. The severity of centerline segregation is an important factor in the resulting mechanical and corrosion properties [87-96], and, hence, a number of studies have focused on the quantification and modeling of centerline segregation in steels and the ways to reduce it [97-101]. It has been shown that severe macrosegregation leads to an increased susceptibility to sulfide stress and hydrogen induced cracking [102, 103]. A higher centerline concentration of Mn during casting also leads to more MnS formation, which results in a decreased corrosion resistance

and decreased low temperature toughness of pipes formed using these cast slabs [95, 96, 107]. The next section describes the method used to quantify segregation.

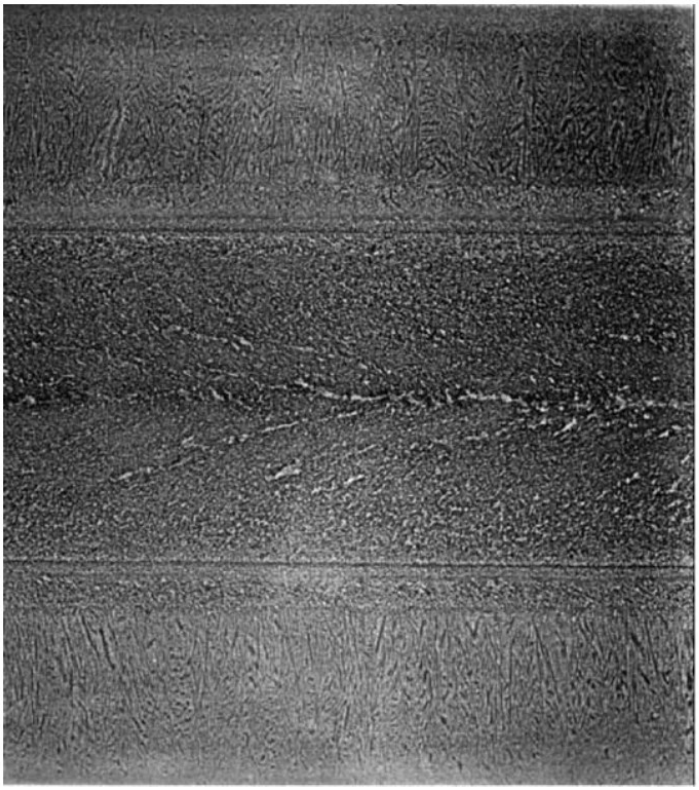

Fig. 2.5: Segregation variation across the thickness of a steel slab [105].

2.2.4 Quantification of segregation

Segregation of elements is quantified using the segregation ratio or segregation coefficient. The segregation ratio (S.R.) is defined as the ratio of measured concentration to the nominal composition for individual elements in the alloy.

$$S.R.\,for\,Mn = \frac{\text{Measured [Mn]}}{\text{Nominal [Mn]}} \qquad 2.2$$

Two of the most commonly used experimental techniques for segregation measurements are electron microprobe analysis (EMPA) and scanning electron microscopy (SEM). An EMPA map and line scan from a previous study on segregation in continuous cast steel with 0.26 wt% C is shown in Figure 2.6. The brighter regions of the map contain a higher concentration of Mn, Cr, Mo and Si. This is also evident from the measured element content where there is an increased concentration in the brighter segregation spot region. The maximum measured segregation ratios for Mn and Cr in the studied steel were 1.50 and 1.51 respectively.

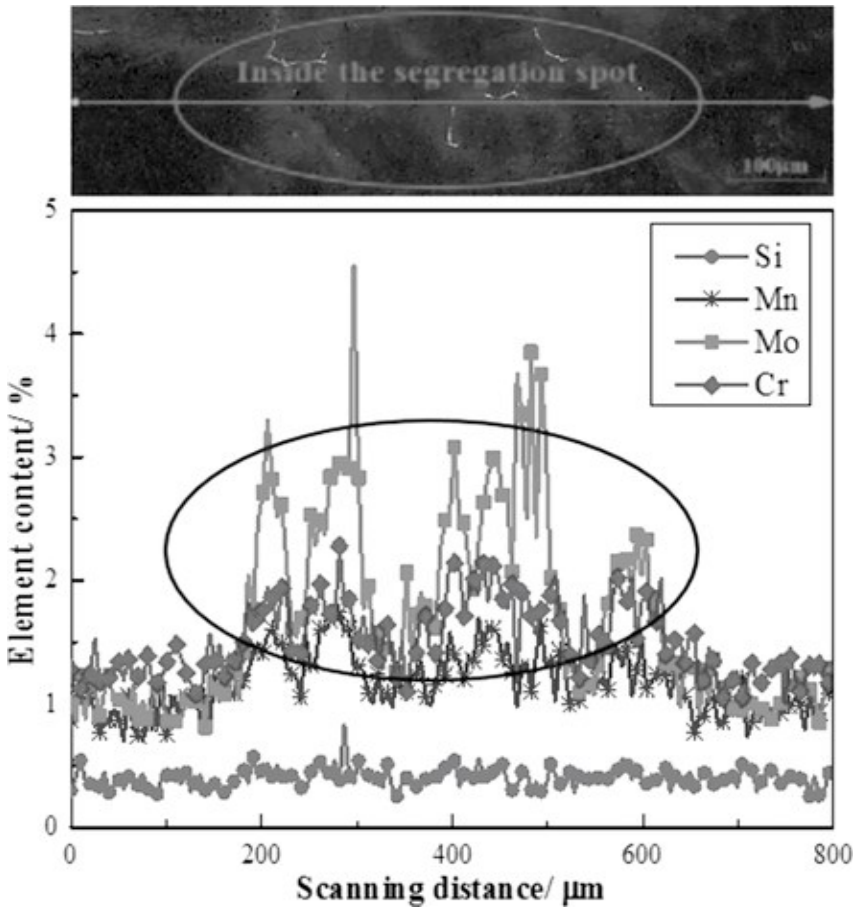

Fig. 2.6: Segregation and variation of Si, Mn, Mo and Cr across the thickness of a steel slab [106].

Figure 2.7 shows an SEM image along with the Mn concentration distribution from the interdendritic region for a different steel [107] with a nominal composition of 13.00 wt% Mn.

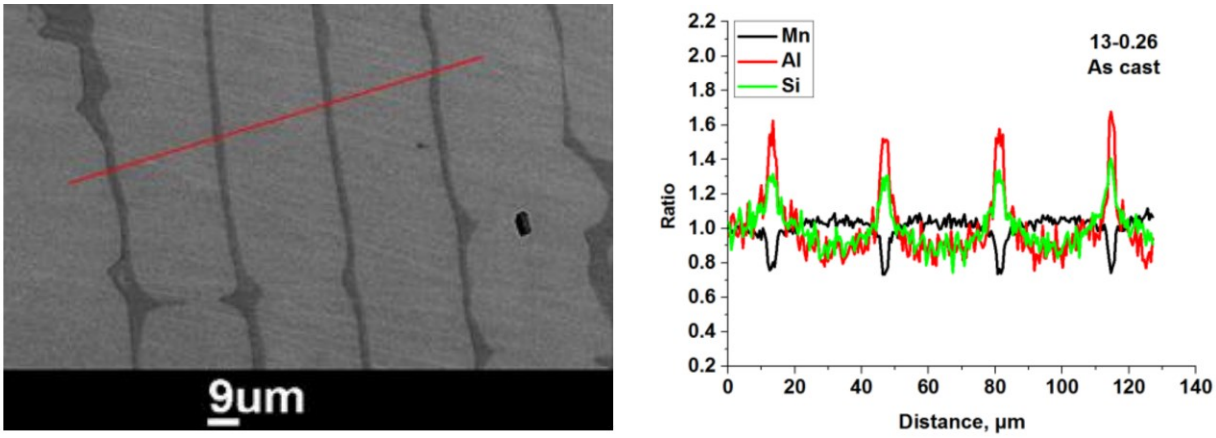

Fig. 2.7: SEM image from dendritic segregation and the variation of Mn across the red line scan [107].

Interstitial elements like C, S and P are known to segregate more at the centerline of slabs. Figure 2.8 and 2.9 show the segregation profiles across the centerline of two different continuous cast steel slabs. The degree of segregation for C, P and S is above 1.5, whereas for Mn the degree of macrosegregation is below 1.5, in both cases.

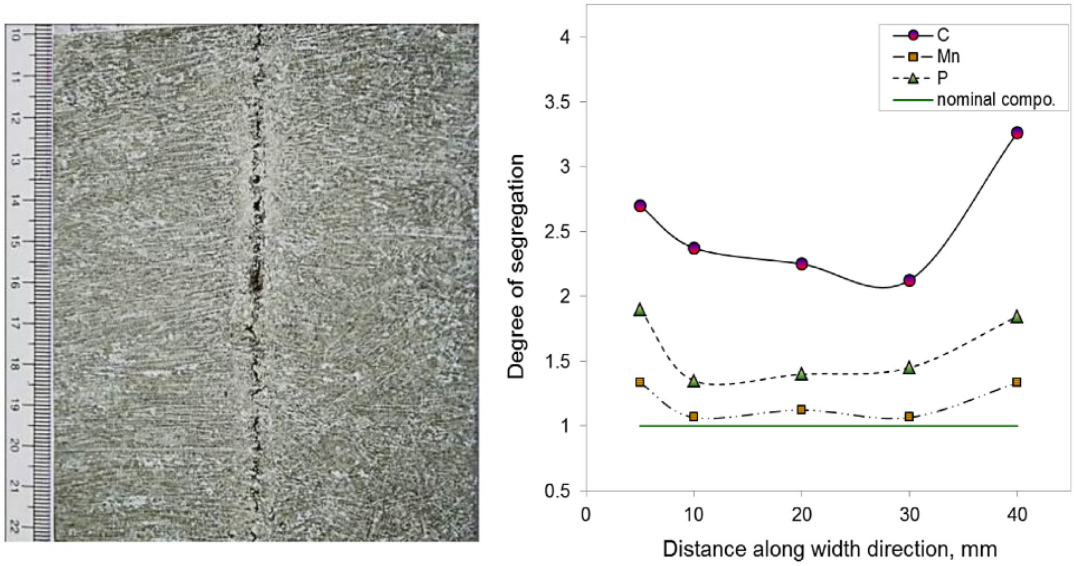

Fig. 2.8: Variation in the degree of segregation for C, Mn and P across the centerline region of a steel slab [80].

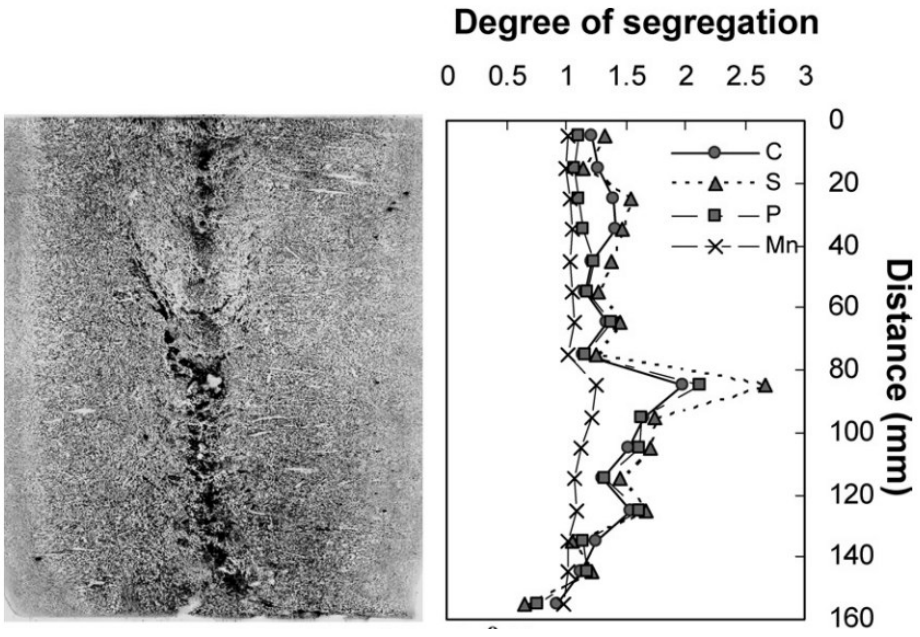

Fig. 2.9: Variation in C, S, P and Mn across the centerline region of a steel slab [108].

Both micro and macrosegregation of common alloying elements like Mn, Cr, Nb and P result in a negative impact on steel properties. Segregation of Mn leads to decrease in toughness and strength of the steel [96, 109]. It also increases crack susceptibility in steels by assisting hydrogen induced cracking [110]. Segregation of Nb leads to unwanted precipitate formation and bimodal grain distribution resulting in reduced toughness [111, 112]. Segregation of P results in decreased strength and steel embrittlement [113]. Therefore, a better understanding of segregation and the ways to reduce it is important. In the following sections, the use of directional solidification study using Bridgman solidification and the application of soft reduction and homogenization heat treatment to reduce segregation are reviewed.

2.3 Bridgman Directional Solidification

Bridgman directional solidification is a well established technique to study the effect of cooling rate on solidification structure of alloys [114-120]. A Bridgman furnace is a vertical cylindrical furnace which usually consists of 2 to 3 different zones. A cylindrical sample is lowered into the furnace with the help of a cord. The top part of the furnace, called the hot zone, contains heating coils which melt the sample. The bottom part of the sample, which is in the cold zone stays solid and acts as a nucleation point. Dendrites start to grow as the sample is further lowered. Once a steady state is reached, the cord is cut and the sample is dropped in a water bath. A schematic of a Bridgman furnace is shown in Figure 2.10.

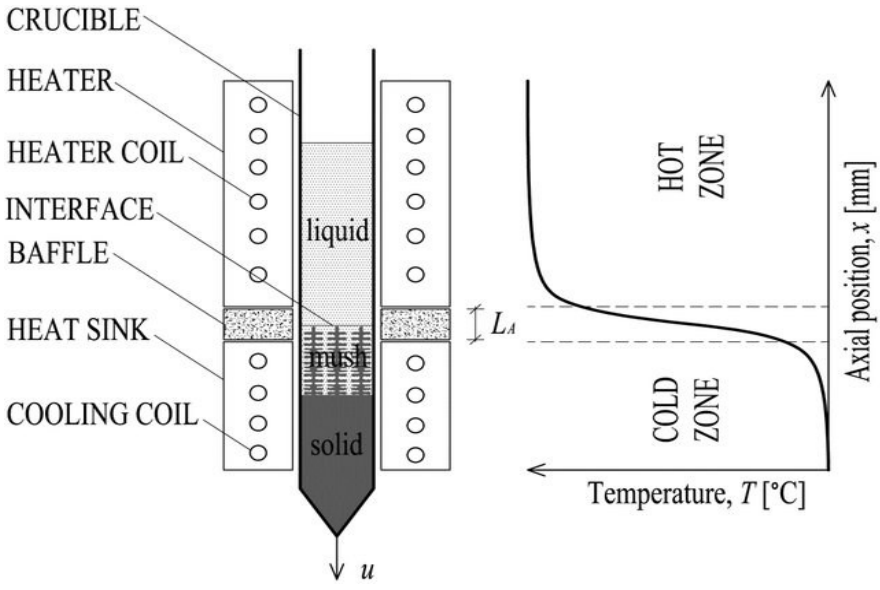

Fig. 2.10: Schematic of a Bridgman furnace [121].

The cooling rate for the samples is varied by changing the temperature gradient and pull velocity, which can be controlled independently. The resulting cooling rate is simply the product of the temperature gradient and pull velocity. A faster cooling rate and a larger dendrite arm spacing lead to increased microsegregation; however, cooling rate and dendrite arm spacing are inversely related [122-125]. Faster cooling does not allow enough diffusion time, which increases segregation; faster cooling also results in smaller dendrite arm spacing, which reduces segregation. As such it is difficult to correlate microsegregation and cooling rate.

There has been limited work in the field of directional solidification of steels [126-134]. Figure 2.11 shows the morphology of dendrites in directionally solidified Fe-C-Mn-Al alloys with varying C content at constant growth velocity and temperature gradient. It was found that the C content affects the dendritic morphology. The primary dendrite arm spacing decreased with increasing growth velocity. The primary dendrite arm spacing also decreased with increasing C content.

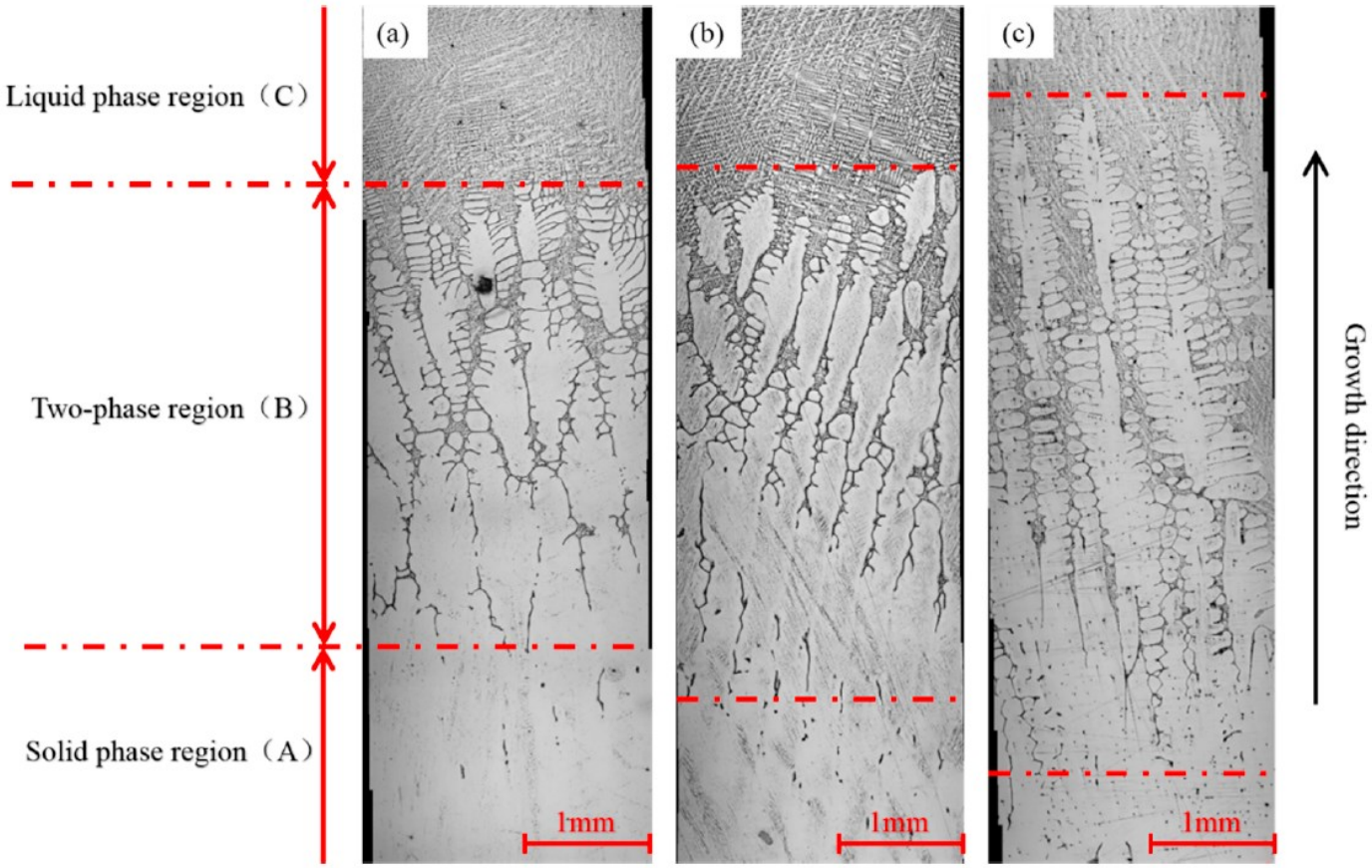

Fig. 2.11: Directionally solidified Fe-C-Mn-Al alloys with a) 0.06 C wt%; b) 0.24 C wt% and c) 0.68 C wt% [135].

2.3.1 Partition coefficient determination

The effect of cooling rate on microsegregation is also quantified through partition coefficient calculations [136-141]. The random sampling approach by Flemings et al. [142] is the most widely used method of available techniques [143] for quantifying partition coefficient calculation. It is also known as the area scan approach or point matrix method [144, 145]. In this method, the mass percentage of certain element is measured at several data points (>100) using either EMPA or SEM. These points are either part of several line scans or a grid encompassing the dendrites near the solid-liquid interface [146-150]. This method is also employed in casting [151] and is preferred since it is not just based on few points [152, 153]. The method avoids selecting only the minimum and maximum solute concentrations. A negative aspect of the method is the inclusion of random errors and that the beam size should be large enough to cover multiphase regions in the case of a multiphase system [153].

Figure 2.12-a depicts the random sampling approach using a measurement grid. Once the composition data is obtained, the data is sorted in ascending order. After sorting, integers starting from 0 to N-1 are allotted to the sorted data, with N being the total number of data points. After ranking, the ranks are converted to fraction solid by dividing the ranks by N. This ensures that fraction solid always lies between 0 and 1. The resulting distribution is plotted as shown in Figure 2.12-b, and is then used to back calculate partition coefficient using curve fitting.

a)

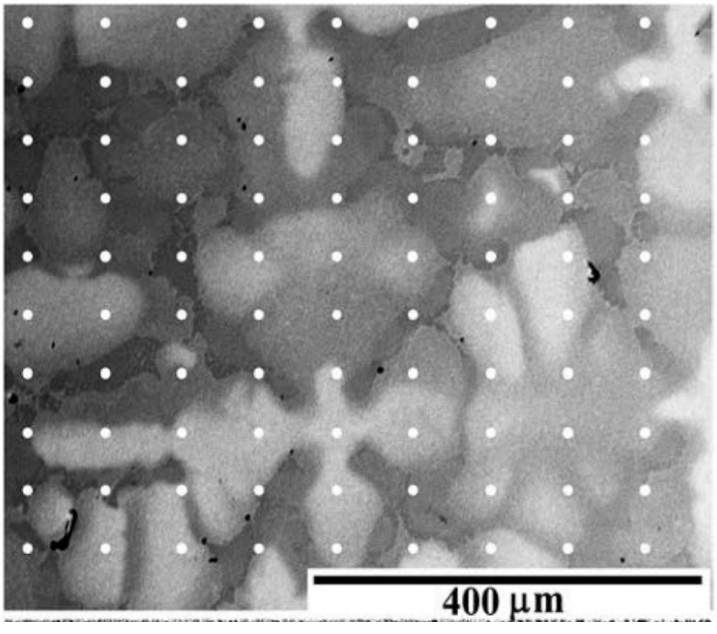

Fig. 2.12: a) Example of point measurements using the grid method [154].

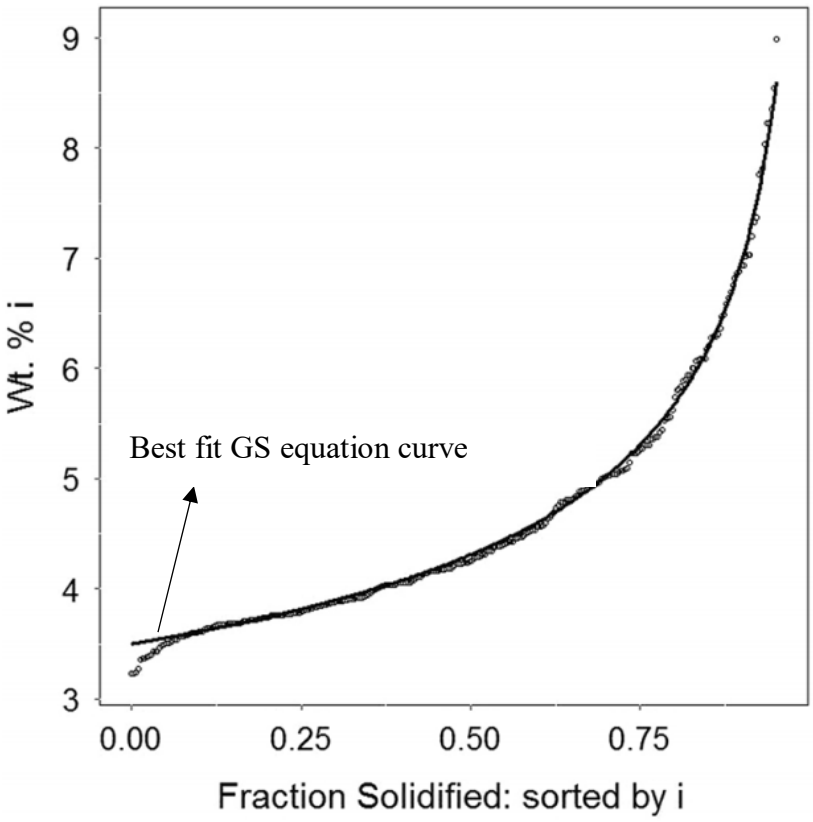

b)

Fig. 2.12: b) Example of sorted point measurements as a function of the fraction solid along with the representative GS curve [155].

2.4 Soft reduction

As discussed in Section 2.2.3, centerline segregation significantly influences the properties of the final cast product and a lower degree of macrosegregation is preferred. There are many available techniques to minimise centerline segregation, such as mechanical soft reduction [156-163], thermal soft reduction [164-167] and electromagnetic stirring, [166-169], with mechanical soft reduction being the most flexible and frequently employed during continuous casting of steels. Mechanical soft reduction results in a reduction of centerline segregation due to the redistribution of the remaining liquid during the last stage of solidification. Redistribution of liquid occurs due to the applied mechanical force with the help of rolls, as shown in Figure 2.13.

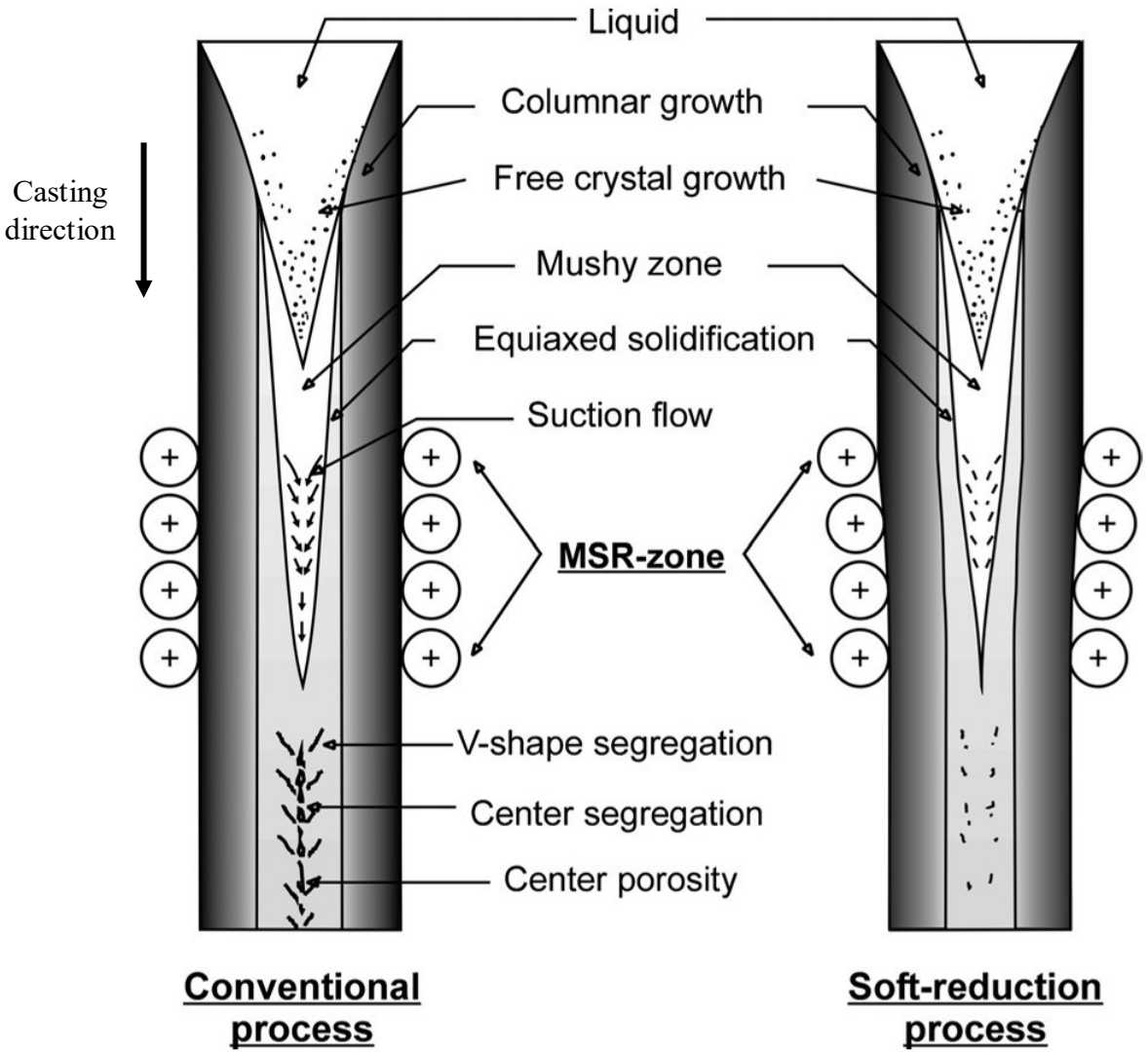

Fig. 2.13: Schematic of mechanical soft reduction during continuous casting [159].

Better understanding of segregation behavior of alloying elements during continuous casting could help increase the efficiency of the soft reduction process. Numerous efforts have been put towards modeling soft reduction [170-174]; however, theoretical modeling of soft reduction is extremely complex because of concurrent phenomena such as fluid flow, solute redistribution and shrinkage [175-179]. Soft reduction parameters are generally based on industrial trials and experience [170, 174]. Figure 2.14-a is taken from a study which compares the effect of soft reduction on C segregation, where soft reduction resulted in a decrease in C segregation ratio from 1.39 to 1.09. Figure 2.14-b is from another study that shows a comparison of a high C steel billet cast with and without the implementation of mechanical soft reduction. It is clear from the macrographs that soft reduction results in a decrease in macrosegregation.

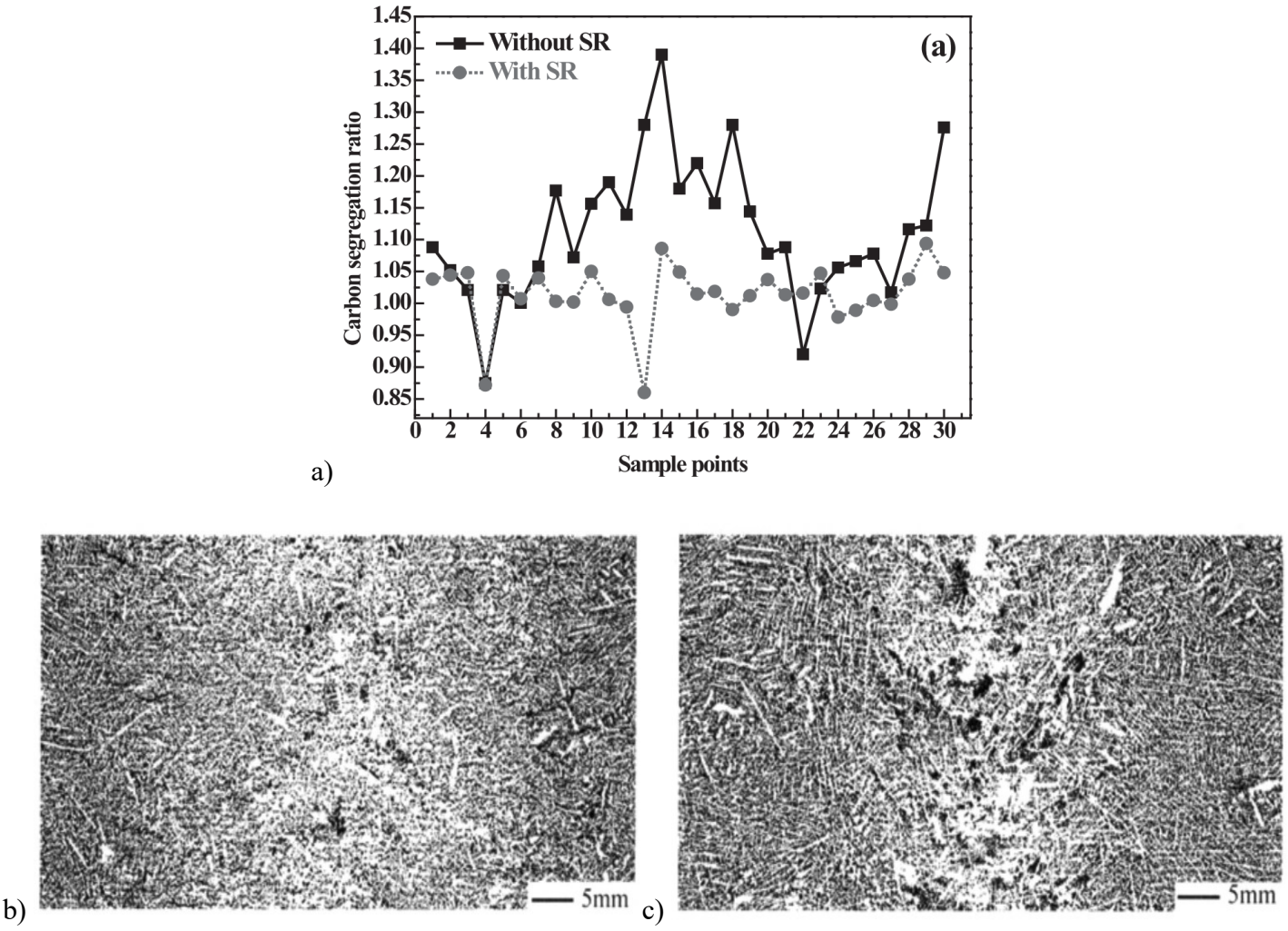

Fig. 2.14: a) C segregation ratio comparison with and without soft reduction; longitudinal macrostructure comparison [174] b) with soft reduction [157] and c) without soft reduction [157].

2.5 Homogenization

Homogenization is a heat treatment process which is employed to as-cast microalloyed steel slabs for various reasons including but not limited to:

i. Homogenization of local composition at the micron scale because of diffusion of elements [180-186]. This leads to a decrease in the severity of segregation.
ii. Grain refinement due to recrystallization [187, 188].
iii. Softening of as-cast slabs for subsequent rolling processes [189].
iv. Dissolution of precipitates and unwanted second phase particles that are formed during solidification [190-196].

The objective of homogenization is to achieve a homogeneous distribution of elements/ phases throughout the slabs. The heating rate and the soak temperature are key factors in determining the effectiveness of the overall process. Rapid heating may lead to thermal distortion or warpage, whereas slower heating could result in thermal shock and undesirable results [197-203]. The soak temperature is decided based on a number of competing factors including grain growth, precipitate dissolution and segregation reduction. Microalloyed steel slabs are typically soaked at around 1200ºC [205, 206]. A higher soak temperature leads to a reduction in the time needed to achieve the required degree of homogenization. As a consequence of heating, grain growth takes place [207-211] which negatively affects the final mechanical properties [212-218] and, hence, it is essential to optimize the homogenization process.

Redistribution of alloying elements during homogenization occurs by a diffusion process. The diffusion of different elements during homogenization depends on their respective diffusion coefficients in steel. Table 2.2 contains the calculated diffusion coefficients of common alloying elements in austenite based on experimental investigations. Interstitial elements in steel, like C, S and P, have a higher diffusivity as compared to substitutional elements like Mn and Cr. As such, the magnitude of reduction in segregation is likely to be more for interstitial elements like P, C and S as compared to substitutional elements like Mn and Cr. Since it is difficult to reduce Mn segregation, the change in Mn segregation ratio is often considered to be the measure to evaluate the effectiveness of the homogenization process.

Table 2.2: Diffusion coefficients of elements in austenite at 1200ºC [76].

Element	D *(γ)* (m^2/s)
Mn	7.89×10^{-15}
Cr	2.06×10^{-15}
Nb	2.94×10^{-14}
P	3.28×10^{-13}
C	1.30×10^{-10}

Figure 2.15 shows the degree of homogenization (defined by Equation 2.3) for Mn, Nb, P and S at 1250ºC taken from a previous study on a low C (0.066 wt%) steel containing 1.26 wt% Mn, 0.028 wt% Nb and 0.011 wt% P. The S.R. was 1.23 for Mn and as high as 3 for Nb and P in the as-cast slab. Homogenization was carried out at 1250ºC for up to 30 h. It is evident from the curve that S and P have a higher degree of homogenization as compared with Mn and Nb.

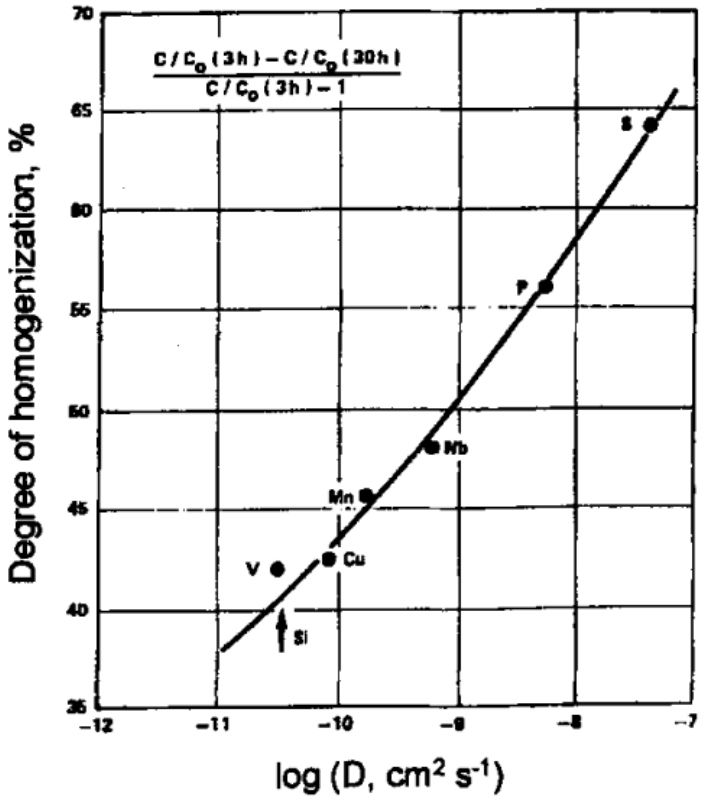

Fig. 2.15: Homogenization by diffusion annealing at 1250ºC [219].

$$Degree\ of\ homogenization = \frac{\frac{C}{C_o}(3\text{h}) - \frac{C}{C_o}(30\text{h})}{\frac{C}{C_o}(3\text{h}) - 1} \qquad 2.3$$

where C and C_o are the measured and nominal concentrations of the elements.

Figure 2.16 shows the variation in S.R. of Cr for a high C (0.42 wt%), high Cr (5.32 wt%) steel homogenized at 1200°C. The S.R. for Cr decreased from 2.07 to 1.09 in 30 h. The amount of decrease in S.R. for Cr became lower and insignificant after a homogenization time of 15 h. In another homogenization study [220] of a higher C (1.07 wt%), higher Cr (8.06 wt%) steel, the S.R. of Cr decreased from 4.59 to 1.35 after 5 h at 1180°C.

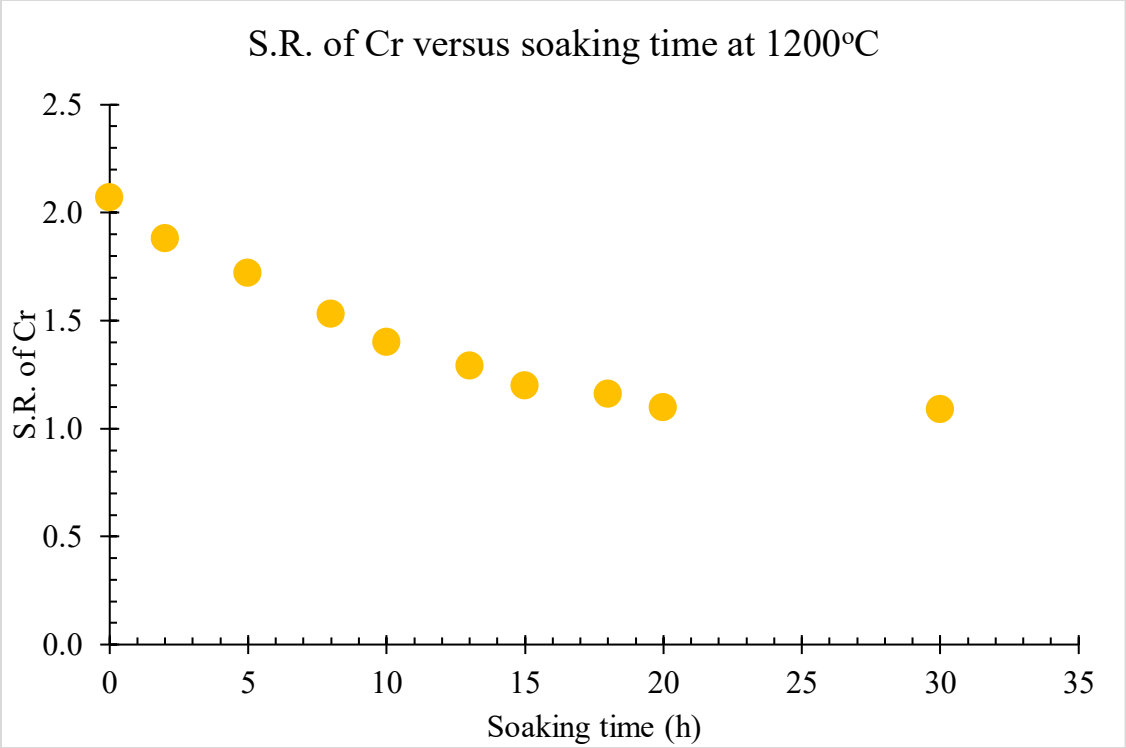

Fig. 2.16: S.R. of Cr versus soaking time at 1200°C [230].

2.6 Electron Microprobe Analysis

Elemental concentration can be quantified using electron microprobe analysis (EMPA). EMPA provides both qualitative and quantitative measure using wavelength dispersive spectroscopy (WDS) and energy dispersive spectroscopy (EDS). WDS has a better detection ability compared with EDS. EMPA is a commonly used technique for segregation measurements [222-232] since it provides superior control over beam parameters and covers a larger area in a shorter time compared to SEM [233-239]. EMPA can be used for a wide range of elements [239] and for a variety of alloys including microalloyed steels [240-249]. The setup details and previous research on the use of EMPA are reviewed in the following sub sections.

2.6.1 EMPA working

An electron beam is generated using an electron source as shown in Figure 2.17. X-rays of characteristic wavelengths are emitted when the beam interacts with the atoms on sample surface. The emitted X-rays are detected using EDS or WDS. WDS has a lower detection limit compared

with EDS because of peak overlap and poor peak energy resolution for EDS. The concentration of a given element is determined based on the ratio of counts of characteristics X-rays emitted from the sample to those from known standards.

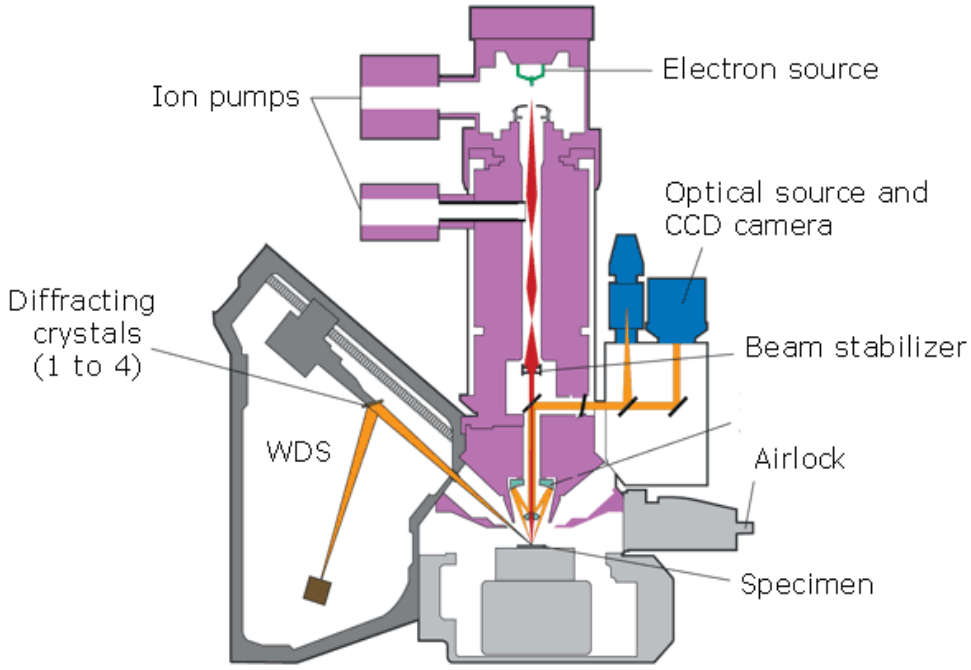

Fig. 2.17: Schematic of an EMPA system [250].

The major control parameters for EMPA are current, voltage and dwell time. The voltage is the most important factor that determines the interaction volume from which X-rays are produced. The interaction volume can be estimated in terms of the "X-ray range (R)" according to Equation 2.4 [326]. Further details of interaction volume are included in Appendix A-1.

$$\mathrm{R(nm)} = \frac{27.6\, A\, E_o^{1.67}}{Z^{0.89}\rho} \qquad 2.4$$

where E_o is the acceleration voltage in keV, A is the atomic weight, Z is the atomic number and ρ is the density of the sample in g/cm^3.

2.6.2 Concentration mapping and detection limits

For most cases, elemental mapping using EMPA is done at smaller dwell times (< 1 s) as the results are qualitative and do not require better detection limit. For quantitative analysis, however, the dwell time is high (up to 120 s) with the detection limits being 10 times better than for qualitative maps. The detection limit determines the accuracy of EMPA quantification and

depends on beam current as well as the dwell time. The detection limit for individual elements are calculated using Equation 2.5:

$$\text{Detection limit} = \sqrt{2} * \frac{3 * \sqrt{N_b} * C_{std}}{N_{np}} \qquad 2.5$$

where N_b and N_{np} are the net background counts and net peak counts, and C_{std} is standard concentration in wt%. Increased current and longer peak count times lead to an improvement in detection limit.

Figure 2.18 shows EMPA maps for Mn at varying dwell times and a constant pixel size of 6 µm x 6 µm. The maps were obtained at dwell times of 30 ms/point, 50 ms/point, 100 ms/point and 500 ms/point for a binary Fe-0.85 wt% Mn alloy. Each map has a size of 2.4 mm x 1.8 mm with 400 pixels in 'x' direction and 300 pixels in 'y' direction. Manganese distribution shows a dendritic segregation pattern. The segregation becomes sharper as the dwell time increases. The average counts per pixel increased from 138 to 2344 as the dwell time was increased from 30 ms/point to 500 ms/point. Table 2.3 contains the numerical comparison of dwell time, x-ray counts, measured Mn concentration, relative standard deviation and relative error for the respective maps. As dwell time was increased from 30 ms to 500 ms, the relative error (RE) as well as the relative standard deviation (RSD) for measured mass percent Mn also decreased.

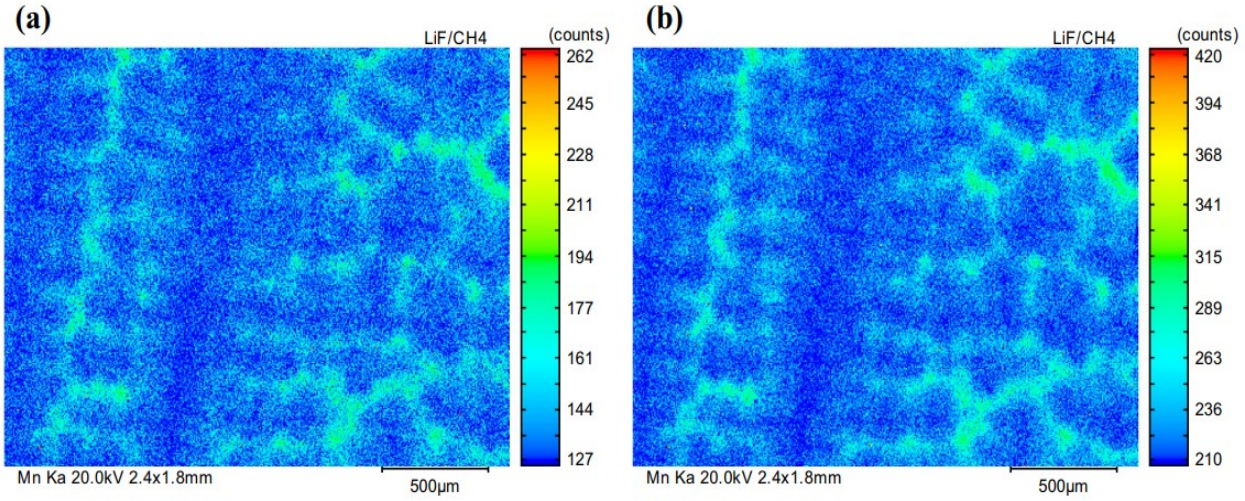

Fig. 2.18: EMPA Mn maps at dwell times of a) 30ms and b) 50ms [246].

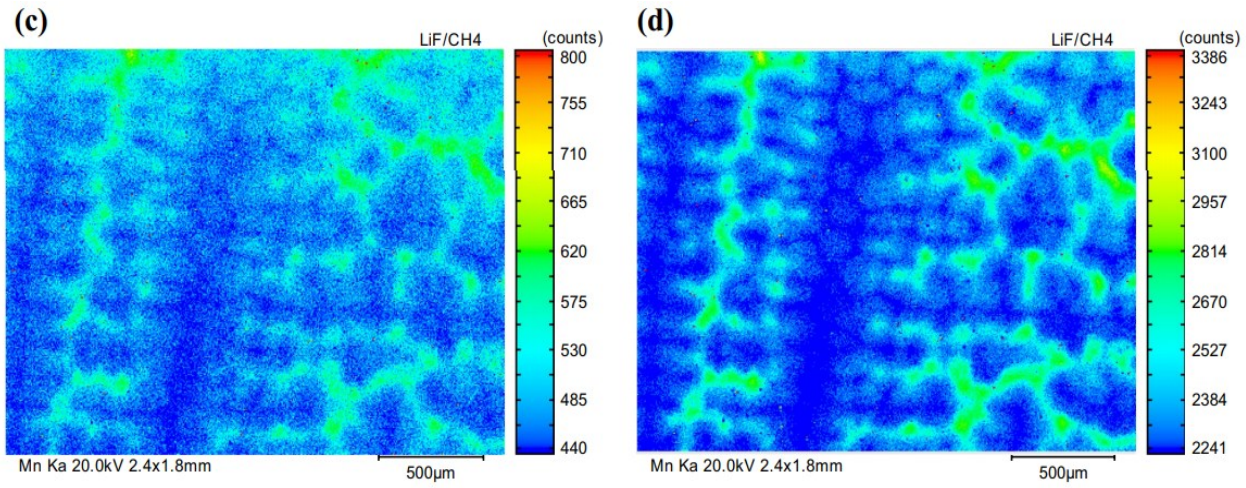

Fig. 2.18: EMPA Mn maps at dwell times of c) 100ms and d) 500ms [246].

Table 2.3: Dwell time versus counts, RE and RSD for Mn EMPA maps [246].

Dwell time (ms)	Counts	Mn (mass %)	RSD (%)	RE (%)
30	120	0.80	9.13	-5.9
50	200	0.80	7.07	-5.9
100	410	0.81	4.94	-4.7
500	2078	0.83	2.19	-2.4

EMPA has been shown to be very useful in mapping and quantifying heavier elements in steels. For example, the detection limit for Mn in microalloyed steel with a beam current of 200 nA and count time of 80 s was calculated as 0.005 wt % [247]. However, EMPA has limitations when quantifying lighter elements like C, which is present in low amounts in steel. The applied C coating on samples before EMPA analysis is another important factor that restricts C mapping and quantification. Because of these reasons this thesis work will not focus on C segregation measurements. Figure 2.19 shows microprobe maps for Mn, P, Cr and Ti at the centreline segregation region obtained from a study [248] for a steel slab with 1.50 wt% Mn (nominal) and approximately 0.10 wt% C. The maximum reported segregation ratio for Mn at the centerline was 2.43 and the maximum measured concentration for P at the centerline was 0.25 wt% for a nominal amount of P less than 0.025 wt%.

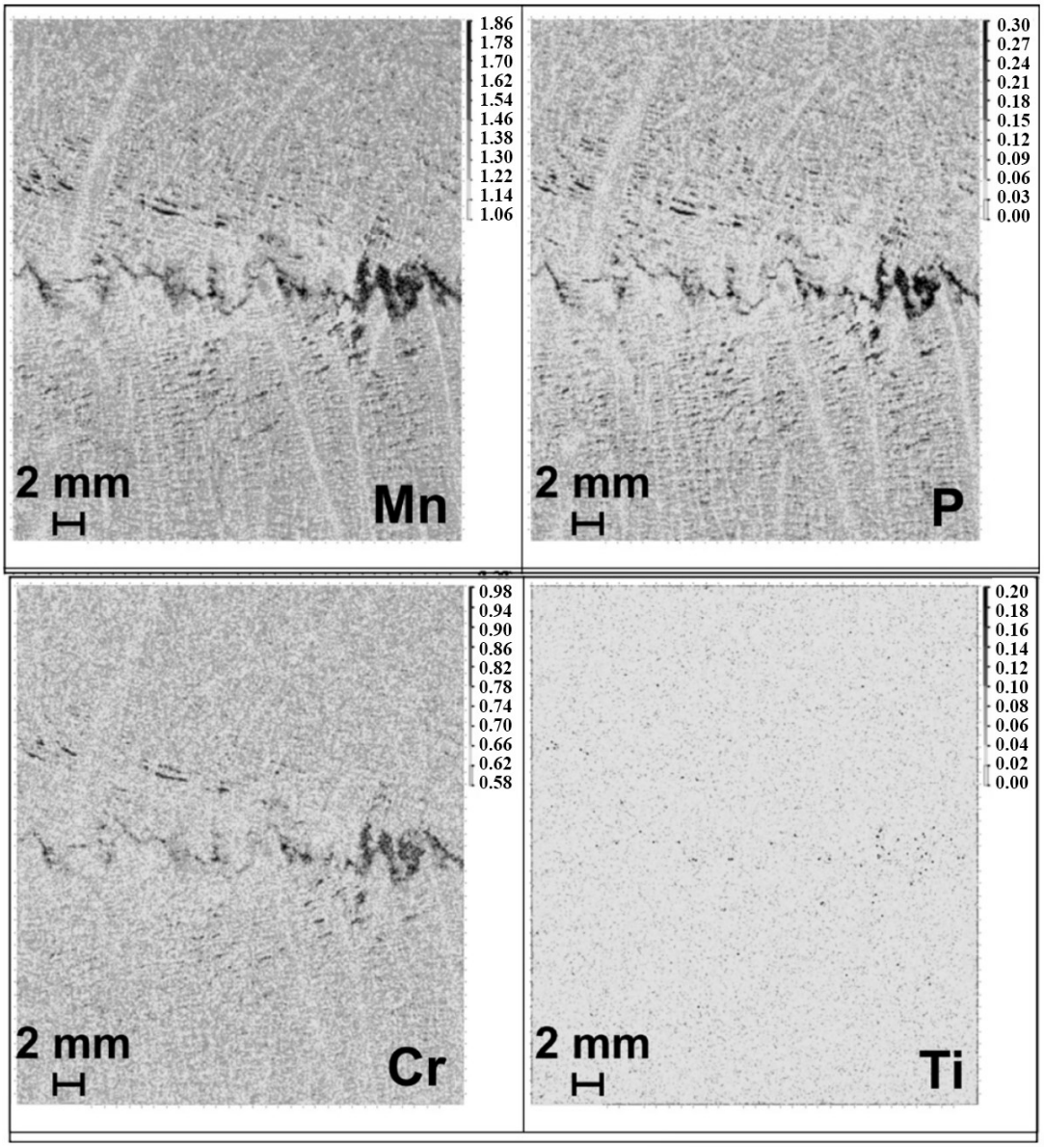

Fig. 2.19: Distribution for Mn, P, Cr and Ti from the centerline region of a steel slab [248].

2.7 Segregation and diffusion modeling

A number of approaches have been applied for solute redistribution and diffusion simulation in steels. This section focuses on the background of ThermoCalc software [251] based simulations. The ThermoCalc software package provides modules for equilibrium computational thermodynamics for multicomponent systems along with the option of including diffusion based kinetics. This section reviews the available options and previous attempts at modeling segregation and diffusion of solute elements in steels using ThermoCalc.

2.7.1 Segregation modeling

The basic idea behind segregation modeling is to obtain the concentration profile of solutes in the solid phase during solidification. Over the years, many segregation models have been proposed based on various assumptions. The equilibrium solidification model [70] and the GS solidification model [252] are two of the simplest and most widely used segregation models. These two models are also considered to be the two extreme cases of solidification [253-255] as the lever rule considers infinite diffusion of solute elements in the solid phase and the classical GS model considers no diffusion of solute elements in solid phase. The diffusion of solute elements in liquid phase is considered to be infinite in both lever rule and GS calculations, which is reasonable since there is convection of liquid and mobility of atoms is high in the liquid phase. For equilibrium solidification, as the temperature decreases, the phase fraction and composition is calculated using the lever rule, as shown with the help of schematic phase diagrams in Figure 2.20. At temperature T_1, the first solid forms with the solute concentration kC_o. As the temperature decreases, the concentration of solute in the solid and liquid phases follows the solidus and liquidus curves, respectively. At T_2, solidification completes with solute composition C_o in solid.

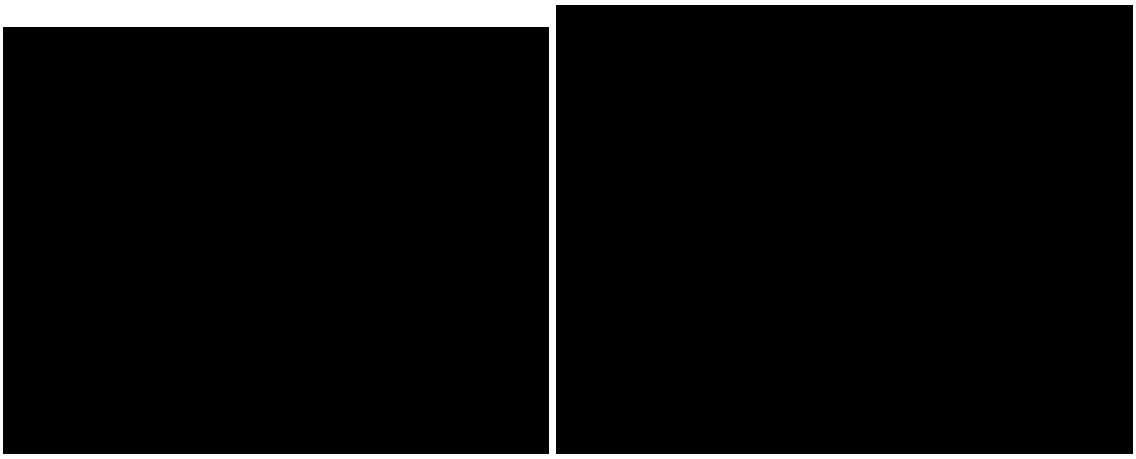

Fig. 2.20: Schematic of phase diagram illustrating partition of solute.

The application of the lever rule is limited [257-259] as practical solidification processes are fast and the diffusion of elements in the solid phase is slow. The opposite extreme of the lever rule is the classical GS solidification model, which considers no diffusion of elements in the solid phase. In this case, the first solid forms with the solute concentration of kC_o and remains at this concentration. As a result, the liquid becomes enriched in solute content so that the next solid that forms has a higher solute concentration. Figure 2.21 represents solute distribution following GS

solidification. The shaded region in the figure (df_s) represents a small amount of solid being formed leading to a small increase in solute concentration in the remaining liquid.

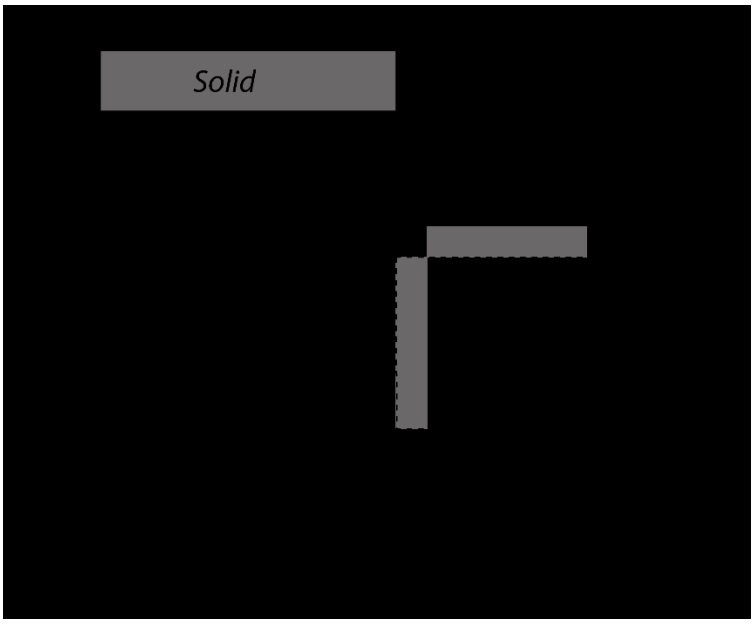

Fig. 2.21: Schematic of partition of solute during GS solidification.

Using conservation of mass for solute partitioned between the solid and liquid at the instance shown in Figure 2.21, the following equality is obtained:

$$(C_L - C_s^*)df_s = (1 - f_s)dC_L \quad 2.6$$

After substituting partition coefficient as C_s/C_L, using the boundary condition of $C_s^* = kC_o$ at $f_s = 0$, and performing integration on the differential Equation 2.6, one ends up with Equation 2.7, which is also commonly known as GS or Scheil's equation.

$$C_s = kC_o(1 - f_s)^{(k-1)} \quad 2.7$$

where C_s is the solute concentration in the solid phase, k is the partition coefficient of the solute in the alloy, C_o is the nominal solute composition and f_s and f_L are the fraction solid and fraction liquid, respectively.

Simple GS predictions are limited to rapid solidification processes and tend to differ considerably for slower cooling processes [150, 261-263]. In order to account for diffusion of elements and increase the accuracy of predictions, finite diffusion of solute in the solid phase is considered, which also forms the basis for modified GS calculations [264-270]. Partition coefficient is a significant factor in these modified models and the accuracy of k is a key factor in determining the accuracy of these models [69, 271]. For many cases, the partition coefficients of solutes are

considered to be constant [70, 286-287] to reduce computational complexity; however, partition coefficients for solutes are a function of temperature and phase composition [274-277]. Therefore, it is necessary to account for changing k during solidification particularly for microalloyed steels with multiple elements and phases. Recent studies on solidification prediction take varying k and diffusion of solutes [146, 278-285] into account with help of softwares like ThermoCalc [286] and MatCalc [287].

ThermoCalc software is a favoured option in recent studies on theoretical predictions for steel solidification [288-291]. ThermoCalc provides the option of performing modified GS calculations and to account for varying partition coefficients of alloying elements by incorporating thermodynamic and kinetic databases. Figure 2.22 shows the solidification prediction using the Scheil module of ThermoCalc. The figure presents a comparison of predicted solidification paths for a steel with 1 wt% C predicted using equilibrium, simple GS and modified GS calculations.

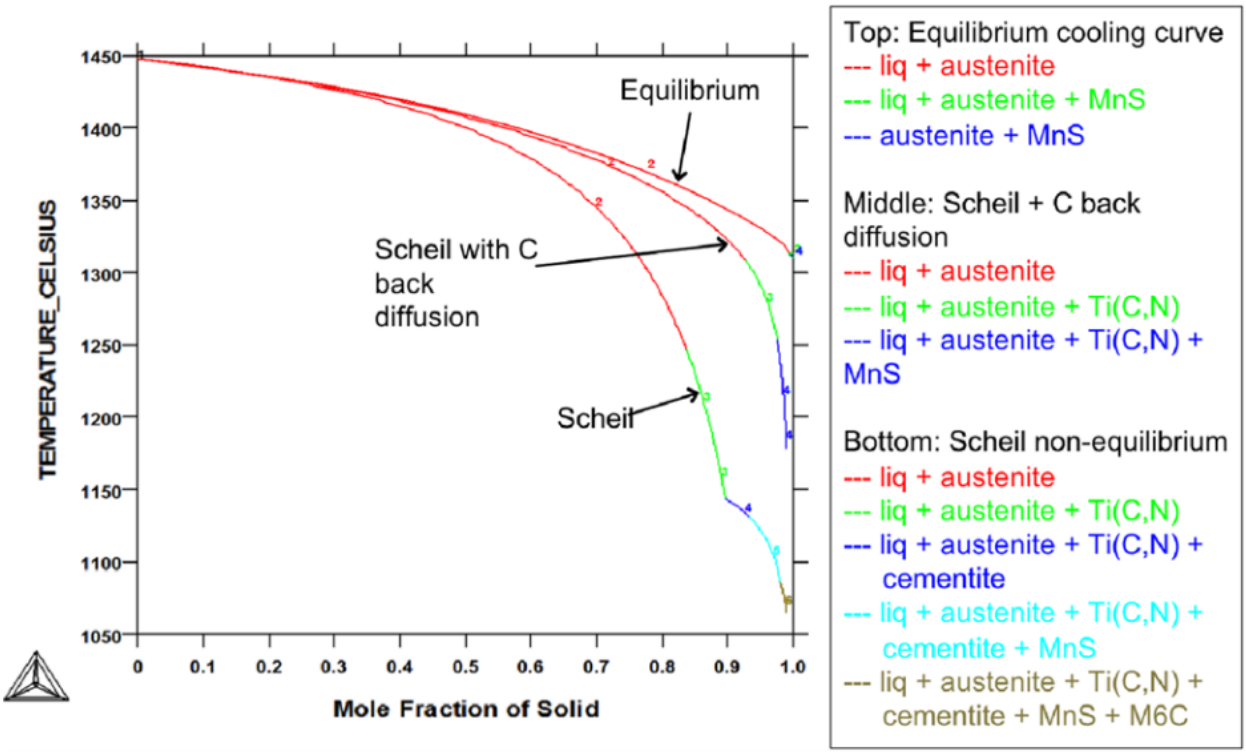

Fig. 2.22: Solidification paths for 1% C steel predicted using equilibrium, simple GS and modified GS calculations [293].

Figure 2.23-a and b show the predicted concentration profiles for Cr and Mn in the 1 wt% C steel. A difference was observed for concentration profiles between GS and modified GS predictions. The

difference was more pronounced in case of Cr with modified GS values closer to the measurements. A significant decrease in Cr was observed at 0.9 mole fraction of solid in the simple GS simulation due to the formation of chromium carbide.

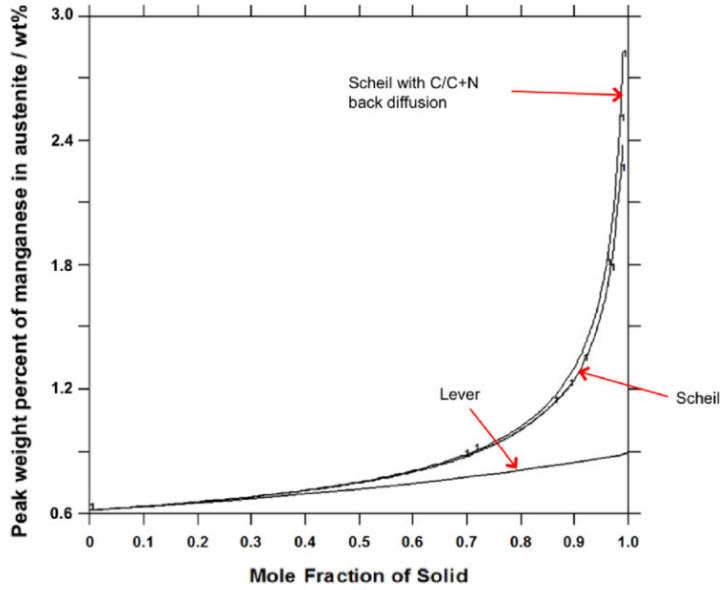

a)

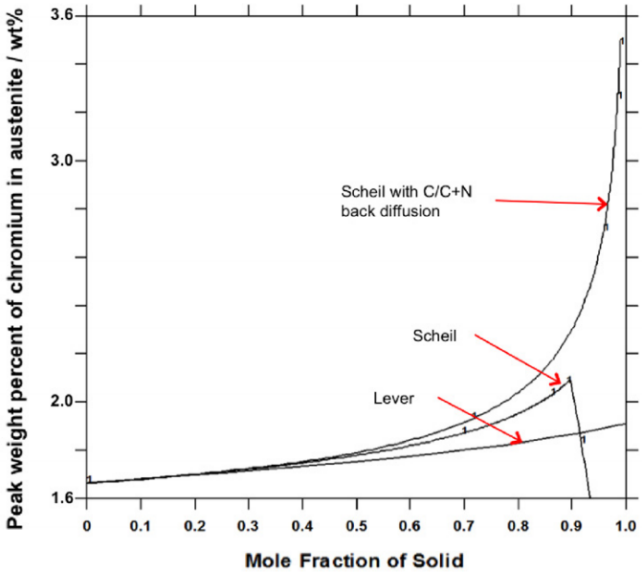

b)

Fig. 2.23: Concentration profiles for a) Mn and b) Cr for 1% C steel predicted using equilibrium, simple GS and modified GS calculations [293].

Figure 2.24 shows a comparison between the measured and predicted concentration profiles of Mn in a low C (0.20 wt%) steel with 1.47 wt% Mn. A better agreement was obtained

between the measurement and the modified GS prediction as compared with the simple GS prediction.

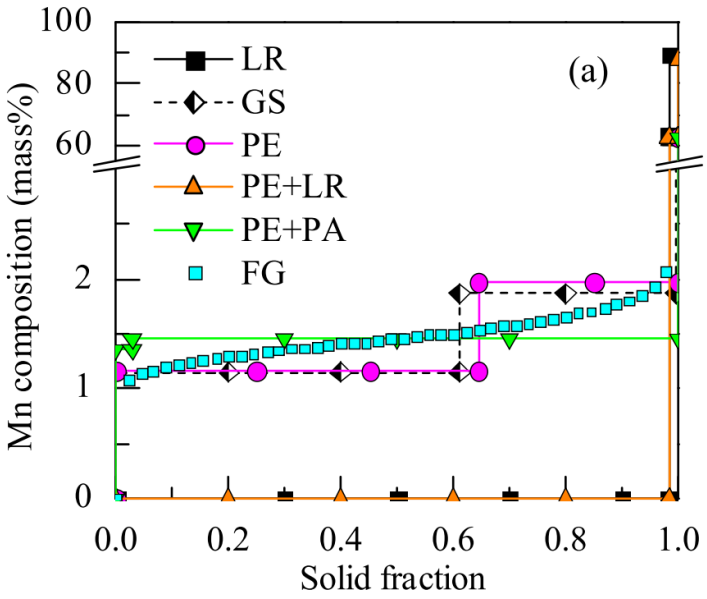

Fig. 2.24: Average Mn composition as a function of fraction solidified with FG sorting method and lever rule (LR), GS, partial equilibrium (PE) and para equilibrium (PA) microsegregation models [282].

In this thesis work, the results of ThermoCalc software based GS calculations for two different microalloyed steels are presented. Furthermore, the predicted concentration profiles for Mn, Cr, Nb and P are compared with EMPA measurements.

2.7.2 Diffusion modeling

The DICTRA (Diffusion Controlled Transformation) module of ThermoCalc is a modeling tool often used for diffusion simulations in multicomponent systems [294-297]. It can be used to simulate various time dependent physical processes including isothermal homogenization of alloys [298-301]. As discussed in Section 2.5, diffusion of elements occurs from regions of high concentration to regions of low concentration at high temperatures. The diffusion of elements is calculated based on Fick's 2nd law given by Equation 2.8:

$$\frac{\partial C_k}{\partial t} = \frac{\partial}{\partial z}\left(D_k \frac{\partial C_k}{\partial z}\right) \qquad 2.8$$

where C_k is the concentration of species k, t is time, z is the diffusion direction and D_k is the diffusivity of k. In reality, the diffusivity of an element depends on its local concentration and

temperature [302-304]. For multicomponent systems, the diffusivity of an element is affected by the concentration gradient of other elements [305]. In such cases, Equation 2.8 is modified to include the effects of other alloying elements through the introduction of a chemical potential term first proposed by Onsager [306]. The modified flux equation is given by Equation 2.9, which has been explained earlier in detail by Annika Borgenstam [307].

$$J_k = -\sum_{j=1}^{n-1} D_{kj}^{n} \frac{\partial C_j}{\partial z} \qquad 2.9$$

where J_k is the mass flux of species k in an n component system and D_k is the interdiffusion coefficient of k. The systems of partial differential equations (Equation 2.8 and 2.9) are solved in DICTRA using numerical methods with given appropriate boundary conditions and initial conditions defined by the user. Figure 2.25 shows the variation of diffusivity of Al at different temperatures across a varying concentration gradient of Al in binary Ni-Al system. The solid line in Figure 2.25 shows the predictions obtained through DICTRA simulations. Close agreement with the experimental measurements (symbols) was observed.

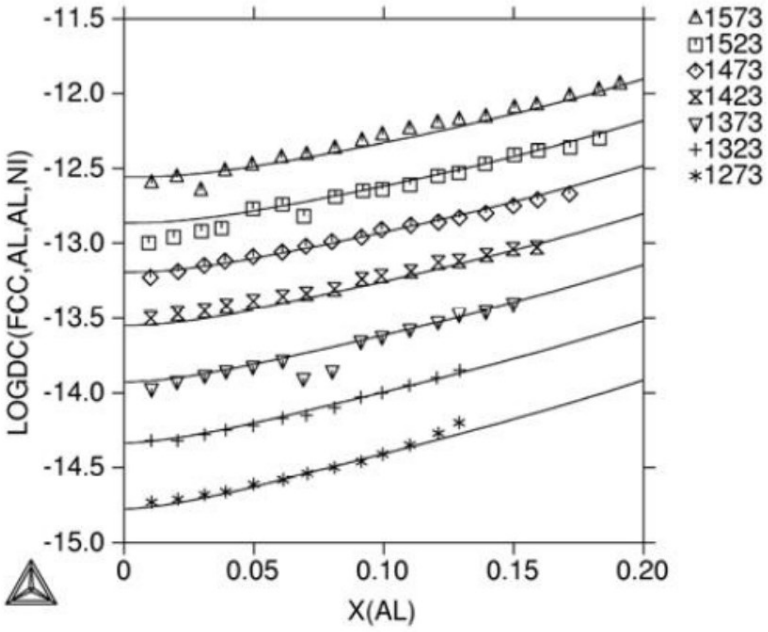

Fig. 2.25: Variation of diffusivity versus concentration of Al in the FCC phase of a binary Ni-Al system at different temperatures (K) [304].

Figure 2.26 shows the variation in C across the interface of two Fe-C-Si steels. Both steels had similar C content but different Si content. Uphill diffusion of C was observed. In this case, the

concentration gradient of Si resulted in movement of C. Good agreement was again observed between the measurements (symbols) and prediction (solid line) made using DICTRA.

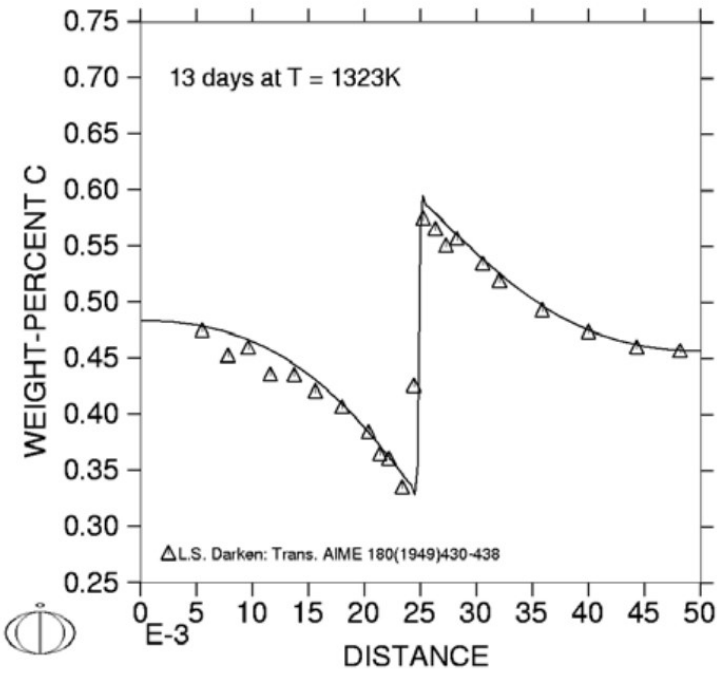

Fig. 2.26: Concentration variation of C across two joined Fe-Si-C steels with similar C contents and different Si contents [305].

DICTRA is fast and accurate; however, it is limited by simple system geometry and the accuracy of the kinetics database [286, 300, 308]. DICTRA is widely used for diffusion based simulations in steels [294-297]. In this work, the results of DICTRA based homogenization simulations with varying degrees of initial segregation for Mn, Cr, Nb and P are presented. The predictions are then compared with EMPA measurements of homogenized samples at 1000, 1100 and 1200°C for 3, 6 and 12 h.

2.8 Summary

This section has summarized the findings of this literature review. The first sub-section contains a summary of segregation trends of alloying elements in continuous cast steel slabs. It has been followed by the use of directional solidification to study the effect of cooling rate on segregation and the ways to reduce segregation. Finally, the applicability of EMPA to quantify segregation and the use of ThermoCalc to model segregation and diffusion in microalloyed steels have been summarised.

2.8.1 Segregation during continuous casting of microalloyed steel

Segregation of alloying elements occur due to enrichment of solutes during solidification of steels. It is categorised as two types; microsegregation and macrosegregation. Microsegregation occurs in the interdendritic regions (~ 100μm) while macrosegregation occurs near the geometric center of cast slabs (~ 10 mm). The degree of segregation of a particular element is dependent on its k value in steel. Elements like Mn and Cr have a higher k and, hence, they have a lower degree of segregation. Elements like Nb, P and C have a lower k and, hence, they have a higher degree of segregation. Elements with lower k are also likely to have a significantly higher degree of macrosegregation. S.R. is the most widely used measure to quantify segregation and is also used for reporting the extent of segregation in this thesis work. Both micro and macrosegregation cannot be avoided and are known to negatively affect the properties of steels; as such, considerable effort have been put into studying the segregation trends during microalloyed steel solidification.

2.8.2 Bridgman solidification

Bridgman directional solidification is a well established technique to study the solidification structure of alloys. The Bridgman furnace setup can be used to perform controlled solidification experiments. It is widely used to study solidification of alloys at varying cooling rates; however, limited work has been undertaken for directional solidification of microalloyed steels. Directional solidification studies often use the random sampling method to calculate k values for different solutes. To the knowledge of the author, little or no comprehensive work is available for segregation during directional solidification of microalloyed steel.

2.8.3 Segregation reduction

Measures such as soft reduction and homogenization are undertaken in order to reduce the extent of segregation. Soft reduction is the application of an external mechanical force during intermediate stage of casting. It results in redistribution of solute rich liquid and reduced centerline segregation. Soft reduction is a complex process and numerous efforts have been made to understand and model its effects. A reduction in C segregation ratio of up to 20% has been achieved in the past just by implementing soft reduction during casting.

Homogenization heat treatment is a post casting step employed by steel manufacturers to convert cast slabs into the final product. A major aim during homogenization is to reduce microsegregation. Diffusion of elements occurs from regions of high concentration (interdendritic)

to regions of low concentration (dendritic center) when the cast slabs are held at high temperatures (~1200ºC). The diffusion of different elements occur at varying rates depending on their diffusivities. Substitutional elements like Mn, Cr and Nb have a lower diffusivity in steel as compared to interstitial elements like C and P. The extent of reduction in microsegregation is dependent on both diffusivity as well as the initial concentration gradient of elements.

2.8.4 Segregation measurement

EMPA is a commonly used technique for quantification of the concentration of elements with a spatial resolution of a few microns. The electron microprobe is favored over SEM as it allows superior control over beam parameters and covers a larger area in a shorter time. EMPA is a well established technique for mapping and quantifying heavier elements in steels. However, it has certain limitations when quantifying lighter elements like C. EMPA is well suited for this thesis work, which is to study the concentration distribution of Mn, Cr, Nb and P in microalloyed steels.

2.8.5 Modeling using ThermoCalc

The ThermoCalc software package is a widely used tool to simulate thermophysical processes for multicomponent systems. It contains separate modules, like the Scheil solidification module, which can be used to model segregation of alloying elements in steel and the DICTRA module, which can be used to model diffusion of alloying elements in steel.

The Scheil solidification module further provides the option of performing modified GS calculations. Modified GS calculations allow some elements to be defined as fast diffusers. This is particularly important for steels as the diffusivity of C is significantly higher than other elements like Mn or Cr. It has been shown in previous studies that the modified GS calculations provide better predictions as compared to simple GS calculations.

The DICTRA module in ThermoCalc is used to model diffusion controlled processes in multicomponent systems. It is based on the numerical solution of diffusion equations using thermodynamic data from the thermodynamic database and mobility data from the kinetic database. It also takes into account the variation in diffusivity of an element with varying concentration gradient, which is important for homogenization simulations.

2.8.6 Research contribution

In this work, a thorough analysis for segregation of Mn, Cr, Nb and P in as-cast microalloyed steel slabs is presented. The effect of cooling rate on Mn, Cr, Nb and P segregation is then studied using directional solidification and is quantified through partition coefficient calculations. The effects of isothermal heating on Mn, Cr, Nb and P segregation are evaluated. Furthermore, the results are analyzed using ThermoCalc based segregation and diffusion simulations.

In the next chapter, details related to materials, experimental methods and modeling methods used in this thesis work are presented.

3. Materials and Experimental Methodology

This chapter contains a description of the microalloyed steels analyzed and the experimental procedures applied for electron microprobe analysis (EMPA). The first section presents the steels studied, sample locations and sectioning of the samples followed by a description of Bridgman directional solidification and homogenization experiments. The EMPA data acquisition and analysis are explained in the Section 3.4. Finally, the details of the theoretical models for predicting segregation and the effects of homogenization using ThermoCalc are presented.

3.1 Studied steels and sample location

Microalloyed steel samples from 3 different industrial heats were studied for this work. The compositions for all steels are shown in Table 3.1. Steel slab 2 (S2) had a lower Mn and a slightly higher Nb content as compared to steel 1 (S1) and steel 3 (S3). The C and P amounts were similar for S1 and S2. The individual compositions of Cr, Mo, Si, Cu and Ni have not been disclosed for proprietary reasons. For the Bridgman directional solidification study, two cylindrical rod samples were machined from the quarter thickness location of slab S3.

Table 3.1: Compositions of steels studied.

Steel	C (wt%)	Mn (wt%)	P (wt%)	Nb (wt%)	Cr+Mo+Ni+Si+Cu (wt%)
S1	0.039	1.59	0.01	0.075	1.08
S2	0.039	1.29	0.01	0.089	1.11
S3	0.048	1.57	0.01	0.074	1.13

Steels S1 and S2 were analysed to quantify the as-cast segregation behavior of alloying elements. Isothermal heat treatment was carried out on samples only from slab S1 to study the effects of homogenization on segregation of the alloying elements. The two cylindrical rods from S3 were resolidified at varying cooling rates using a Bridgman furnace to quantify the effects of cooling rate on partition coefficients of the alloying elements. The concentration distribution of elements was studied using EMPA.

Figure 3.1-a shows a schematic of as-cast microalloyed steel slab S1. The shaded region in Figure 3.1-a depicts the location in the ingot used to machine slab S1. Slab S2 also came from a similar relative location as S1 but from a different ingot. Both slabs were further machined into smaller blocks of 12 mm x 12 mm as shown in Figure 3.1-b. These smaller laboratory scale samples were numbered from 1-16 (top to bottom) and then used for subsequent homogenization experiments and EMPA analyses.

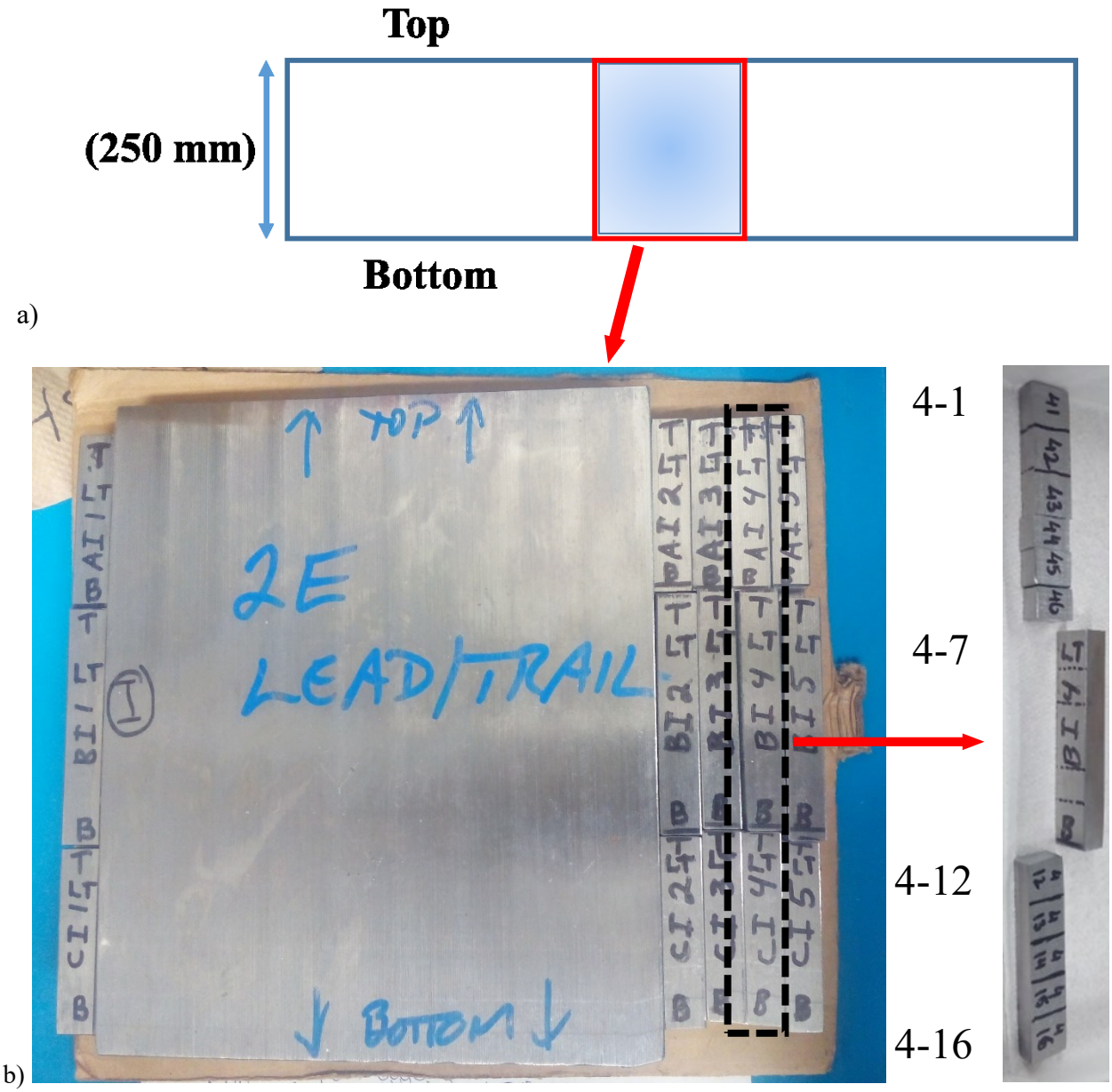

Fig. 3.1: a) Schematic representation of location within an ingot cross section used to machine S1 and b) image of cut sections of slab S1 along with enlarged view of section 4.

3.2 Bridgman solidification

Two cylindrical rods were machined from the quarter thickness location of as-cast slab S3, as shown in Figure 3.2. The dimensions of the rods were chosen based on the Bridgman furnace requirement.

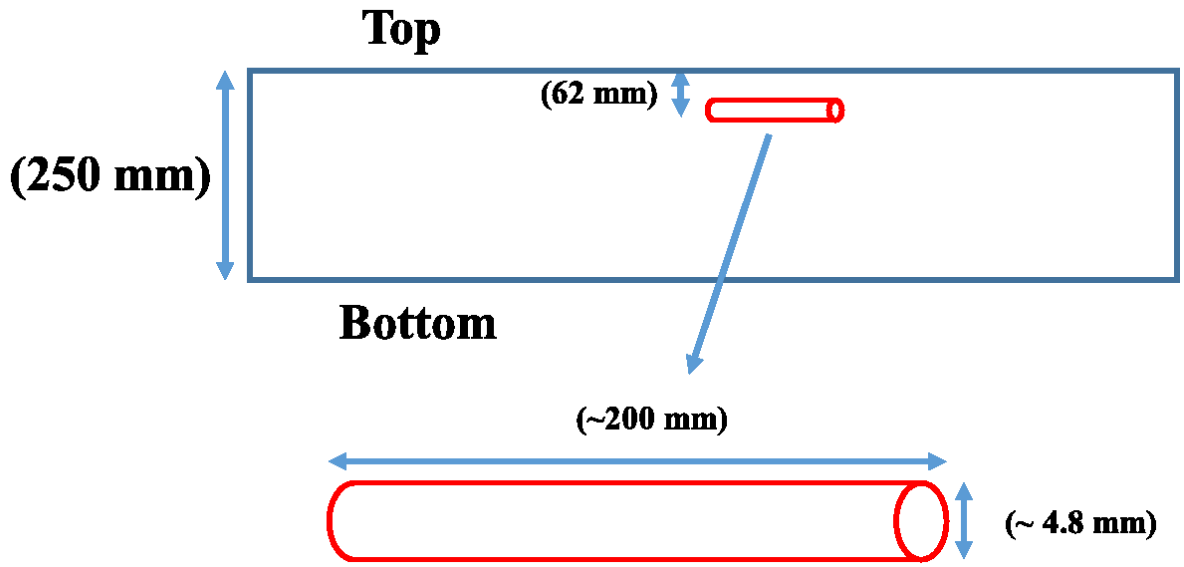

Fig. 3.2: Schematic of Bridgman rod samples obtained from quarter thickness location of slab S3.

The machined rods were then melted and partially solidified at two different cooling rates. Once an equilibrium was reached at the solid-liquid interface, the rods were quenched in a water bath. Rod 1 was solidified at a cooling rate of 0.4°C/s and rod 2 was solidified at 0.2°C/s. The cooling rate was changed through a change in pull velocity while a constant temperature gradient of 4000°C/m was maintained for both cases. The Bridgman test conditions are given in Table 3.2.

Table 3.2: Bridgman test conditions

Sample #	Temperature gradient (°C/m)	Pull velocity (mm/s)	Cooling rate (°C/s)
1	4000	0.1	0.4
2	4000	0.05	0.2

After solidification, the Bridgman samples were machined into semi-cylindrical halves and were further divided into 8 sections, as shown in Figure 3.3. These sections were then mounted and polished for EMPA analyses.

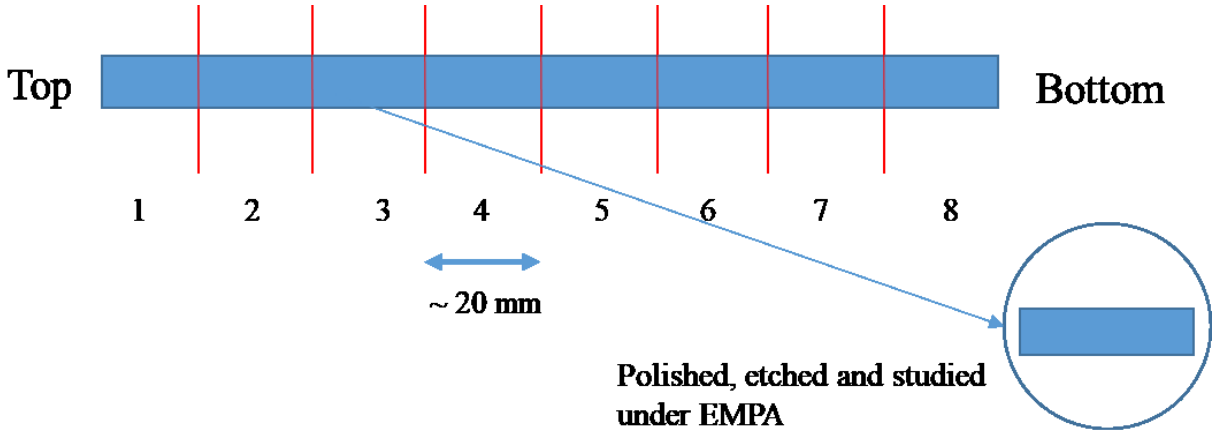

Fig. 3.3: Bridgman sample sectioning.

3.3 Homogenization

A homogenization heat treatment was performed using a Thermo Scientific Thermolyne bench top muffle furnace on the following two sets of samples taken only from slab S1:

a) Centerline (CL) samples: 90 mm from top (4-7, contains the metallurgical centerline)
b) Quarter thickness (QT) samples: 62 mm from bottom surface of slab (4-12)

The sample location and the homogenization time and temperature for each sample are listed in Table 3.3. For example, S1-7-1000-3 corresponds to a centerline sample from slab S1 homogenized at 1000°C for 3 h. Once homogenized for required time, the samples were air cooled. After cooling, the samples were mounted, polished and analyzed using EMPA.

Table 3.3: Homogenization schedule for S1 slab samples.

Sample name	Sample location	Temperature (°C)	Hold time (h)
S1 – 7 – 1000 – 3	CL	1000	3
S1 – 7 – 1100 – 3	CL	1100	3
S1 – 7 – 1200 – 3	CL	1200	3
S1 – 7 – 1000 – 6	CL	1000	6
S1 – 7 – 1100 – 6	CL	1100	6
S1 – 7 – 1200 – 6	CL	1200	6
S1 – 12 – 1000 – 3	QT	1000	3
S1 – 12 – 1100 – 3	QT	1100	3
S1 – 12 – 1200 – 3	QT	1200	3
S1 – 12 – 1000 – 6	QT	1000	6
S1 – 12 – 1100 – 6	QT	1100	6
S1 – 12 – 1200 – 6	QT	1200	6
S1 – 12 – 1000 – 12	QT	1000	12
S1 – 12 – 1100 – 12	QT	1100	12
S1 – 12 – 1200 – 12	QT	1200	12

3.4 Electron microprobe analysis

Electron microprobe analysis (EMPA) was used to map and quantify the concentration distribution of elements using a CAMECA SX100 setup. In the following sub-sections, sample preparation and EMPA operating parameters for mapping and point scans are described.

3.4.1 Sample preparation

The initially divided block samples were mounted in epoxy using 2.5 mm diameter molds. The orientation and the location of all the samples were tracked during all steps. The samples were

then polished up to a 1 μm surface finish using a Buehler Ecomet and Automet 250 autopolisher. A carbon coating was then applied to the samples before examination in the EMPA.

3.4.2 Mapping parameters and detection limit

A fully focused beam with a current of 200 nA generated from a 20 kV source was used for qualitative concentration mapping. A suitable map size was selected for different samples depending on the individual sample area. For most samples, a 10 mm x 10 mm area was mapped. All maps had a pixel size of 10 μm x 10 μm which translates to a 1000 x 1000 pixel grid for a 10 mm x 10 mm map. After mapping, point scans were performed in regions of interest on these maps to quantify the concentration of individual elements.

A peaking procedure was performed to calibrate the electron microprobe using standard element blocks before running point scans on unknown samples. A 5 μm diameter beam at 200 nA was used for the quantitative point scans. The X-ray range was calculated to be 1.57 μm, which resulted in an effective beam diameter of 8.14 μm, which falls within the map pixel size of 10 μm x 10 μm. The interaction volume was calculated as 144.35 μm^3. The dwell time for mapping was 10 ms while for point scans it was 30 s. Further details of quantitative point scans, the standards used and an example interaction volume calculation are given in Appendix A.

3.4.3 EMPA maps and point scans

The following 4 types of qualitative maps were obtained for each element in each sample:

i) Original grayscale map
ii) Enhanced grayscale map
iii) Color map
iv) Enhanced color map

It should be noted that only the original grayscale map is the true representation of the concentration distribution for an element. The grayscale values of the resulting image directly correspond to the intensity of the characteristic wavelength for a particular element. In other words, a higher grayscale value or a brighter spot on the map corresponds to a higher concentration of the element being mapped and vice versa. The enhanced grayscale, color and color enhanced maps, were obtained after processing the original grayscale map to improve the readability of the original grayscale map. Another attempt was made at enhancing the visibility of the maps by altering the pixel intensities of the original grayscale map. The original grayscale map was inverted (i.e., high

Mn concentrations become dark pixels and vice versa). In addition, a pixel threshold was defined based on grayscale distribution for the inverted image. The pixels were redefined as all black on one side of the threshold and as all white on the other side of the threshold. The resulting enhanced inverted map is shown in Figure 3.4-c.

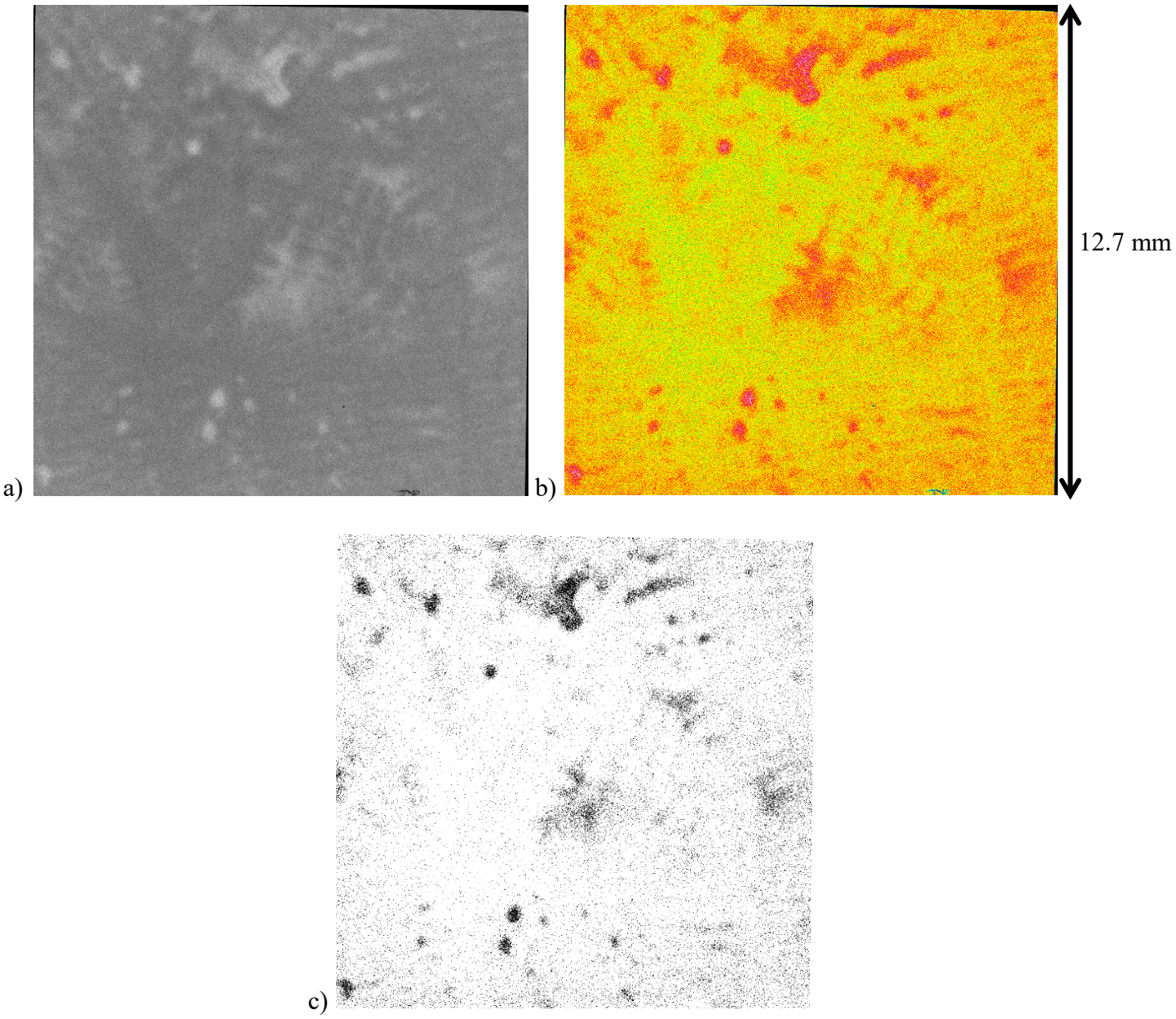

Fig. 3.4: Example EMPA maps for Mn: a) Original grayscale; b) enhanced color and c) enhanced inverted image from the centerline location.

Following mapping, point scans were performed at regular intervals within regions of interest on the qualitative EMPA maps to quantify the local concentration of elements within each sample. Each point scan location provided the composition of 5 different elements in the corresponding interaction volume. Figure 3.5 shows an example of an EMPA grayscale Mn map, point scan locations and variation of Mn for a centerline sample. Samples from centerline locations were used to quantify macrosegregation of elements.

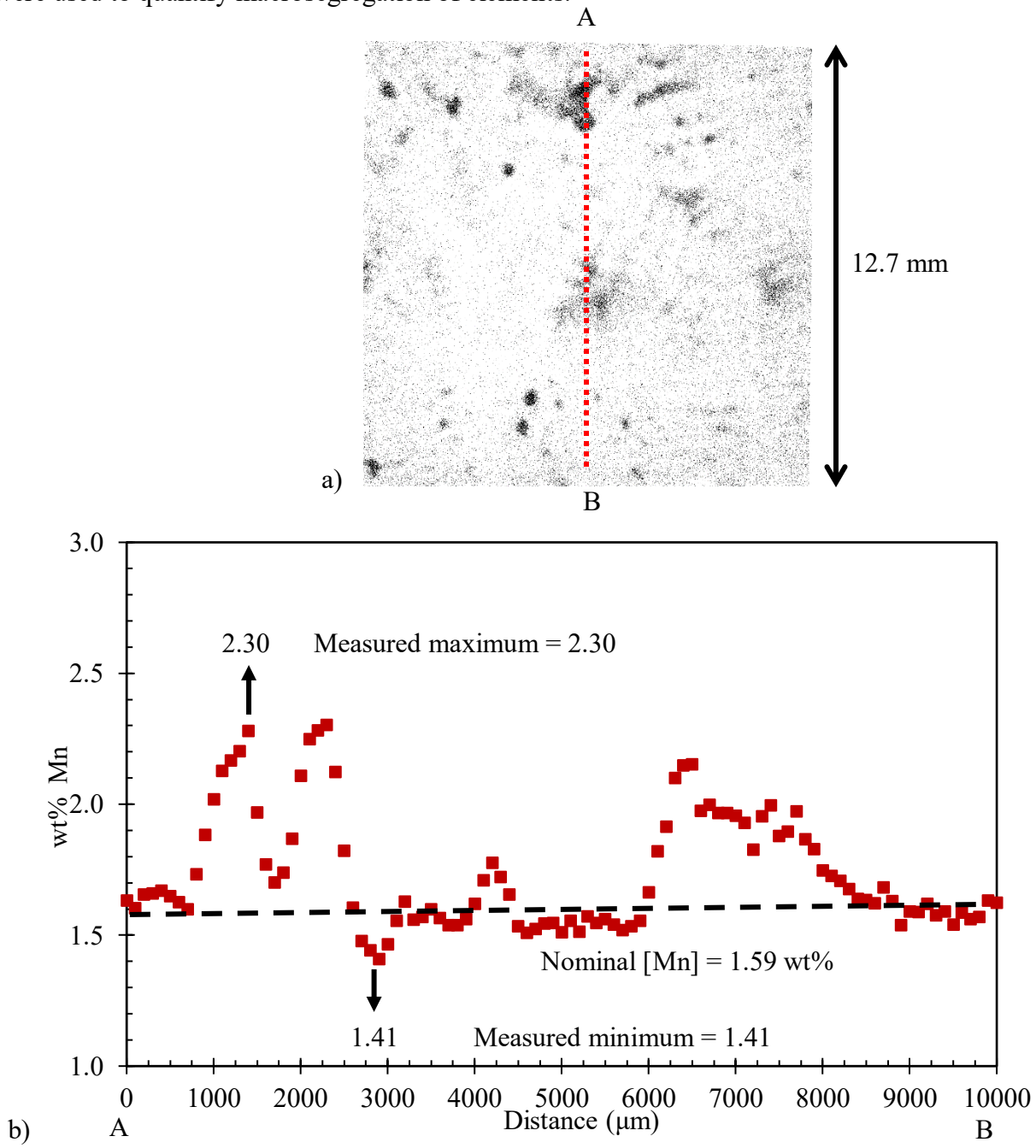

Fig. 3.5: a) Mn EMPA enhanced inverted map and b) wt% distribution across line AB.

After data acquisition, concentration as a function of position was plotted for each element. For each line scan, the maximum and minimum measured wt% values for elements were noted. The segregation ratios for each element were then calculated using Equation 2.2:

$$S.R.\,for\ Mn = \frac{\text{Measured Maximum [Mn]}}{\text{Nominal [Mn]}} = \frac{2.30}{1.59} = 1.45 \qquad 3.1$$

where [Mn] is the concentration of Mn.

3.4.4 EMPA data analysis of directionally solidified samples

Similar to slab samples, the Bridgman directionally solidified samples were mapped using EMPA. An example of Bridgman EMPA Mn map along with the wt% Mn vs distance line scan plot corresponding to line AB is shown in Figure 3.6.

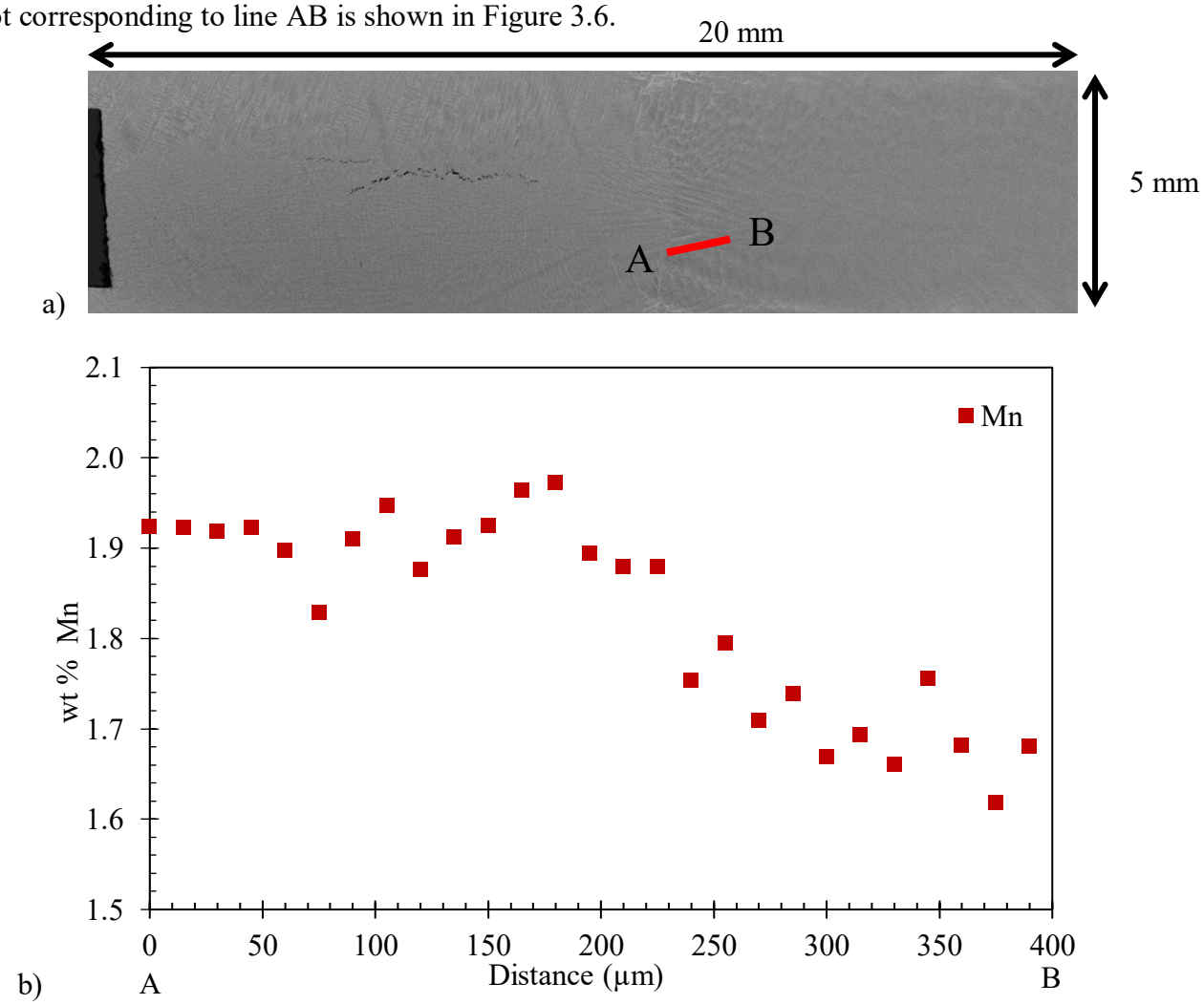

Fig. 3.6: a) EMPA Mn map for a section from Bridgman sample 1; b) Mn line scan plot corresponding to the line scan AB.

The point scan spacing for the Bridgman samples was kept smaller than that for the slab samples because of finer features for the Bridgman samples. For the example shown in Figure 3.6, the scan spacing between two points was 15 μm and the total number of scanned points was 26, thus covering a distance of approximately 400 μm. Once the EMPA data was obtained, the partition coefficient was calculated using the random sampling approach by Flemings et al. [142]. Partition coefficient determination in directionally solidified samples requires a large number (~500) of quantitative data points. However, the number of quantitative points analyzed using EMPA in the studied samples was statistically small (<50) because of time constraint and did not ensure the coverage of a large area. Hence, a method to convert the grayscale EMPA maps to concentration distribution was developed.

3.4.5 Conversion of grayscale EMPA map to concentration distribution

Each Bridgman EMPA original grayscale map had about 2000 x 500 pixels. Each pixel had a fixed location. Of the 2000 x 500 pixels, several pixels (26 for the example shown in Figure 3.7) were analyzed to find out the wt% Mn corresponding to those point scan locations. As mentioned in Section 3.4.3, grayscale value of each pixel on the original grayscale maps correspond to the concentration of that element in that location, therefore, the original grayscale EMPA maps were first converted into grayscale values (0-256) and the grayscale values corresponding to the point scan locations were noted. A relation between grayscale value and wt% Mn was established using the known measured wt% Mn at those point scan locations. Once the relationship between grayscale value and wt% Mn was established, the whole map was converted into a wt% Mn map using linear regression. This method is essentially based on curve fitting and uses a more advanced linear regression. An example conversion is shown in Appendix B. An example of the original grayscale map and the corresponding converted contour is shown in Figure 3.7 and 3.8, respectively.

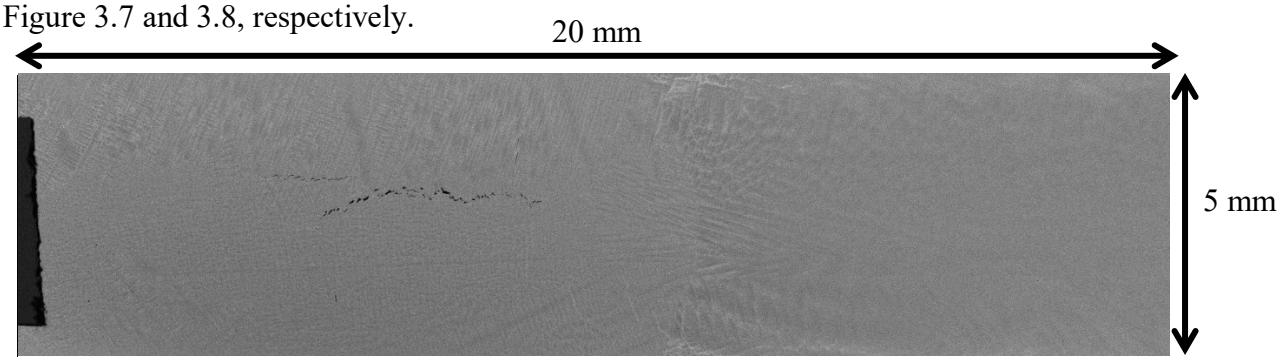

Fig. 3.7: EMPA Mn original grayscale map for section 4 from Bridgman sample 1.

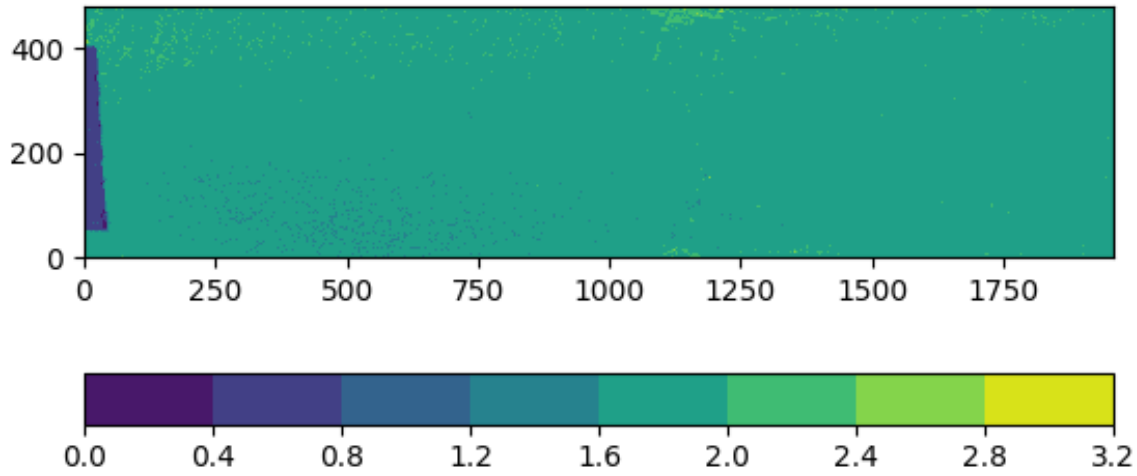

Fig. 3.8: EMPA Mn predicted concentration contour for section 4 from Bridgman sample 1.

As a result of conversion of the qualitative map into a quantitative contour, wt% Mn for 2000 x 500 points was known. After conversion, the wt% Mn from the area covering the solid-liquid interface (1000 µm x 500 µm) was used as the input for partition coefficient calculations. The input data was first sorted into ascending order and ordered integers were assigned to the sorted data points. The assigned ordered integers were then converted into fractions by dividing each of the integers by total number of data points. The normalized values were taken as the fraction solid and a composition versus fraction solid plot was obtained. A curve of the form of the GS equation (Equation 2.7) was then fitted to the obtained plot. The best fit curve was then used to back calculate the value of partition coefficient. An example for partition coefficient determination is shown below. The red dotted rectangle in Figure 3.9 illustrates the location used to select the input data for Bridgman sample 1.

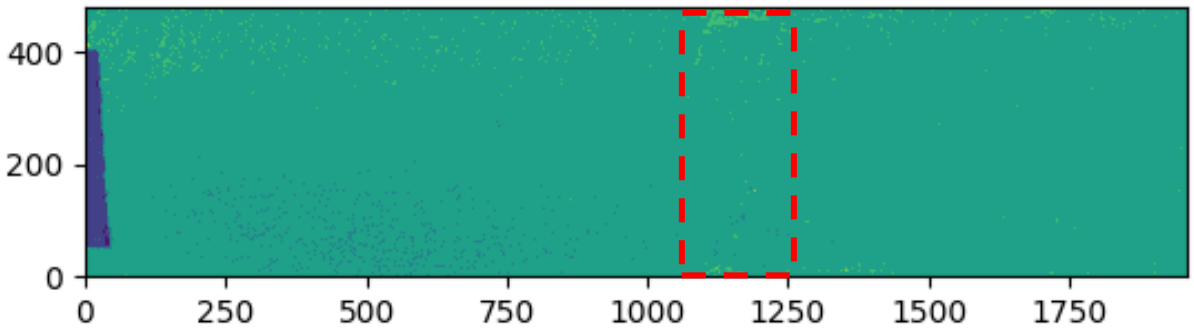

Fig. 3.9: Schematic illustrating input data from EMPA Mn predicted concentration contour for Bridgman sample 1 for partition coefficient calculations.

All the required data processing, such as sorting, counting and normalizing for the calculation of partition coefficients of the elements, was done using standard Python script functions. A detailed example is shown in Appendix C. The final composition versus fraction solid plot for the input data from Figure 3.8 and the corresponding best fit GS equation are shown in Figure 3.10.

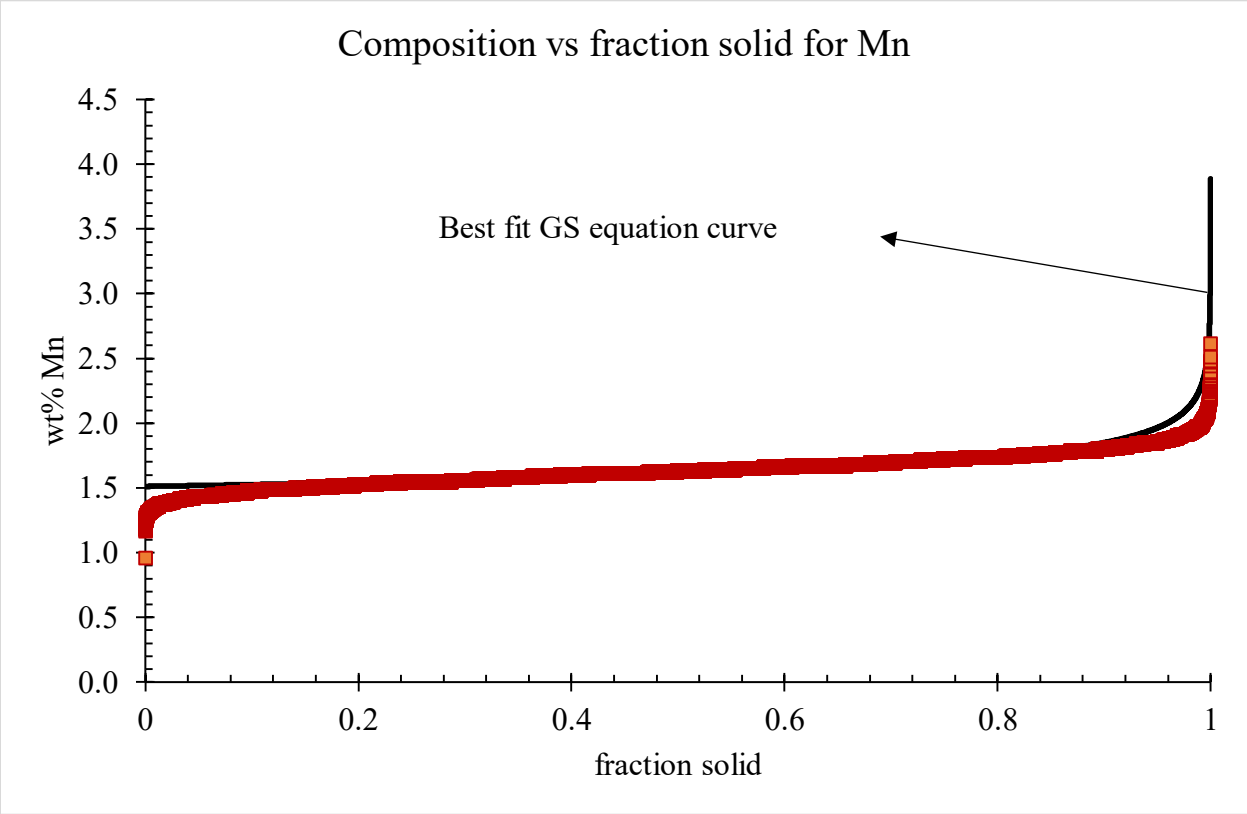

Fig. 3.10: Composition versus fraction solid for Mn in Bridgman sample 1 and the corresponding best fit GS equation.

The same method was applied for Cr, Nb and P for all Bridgman samples. The obtained partition coefficient values are discussed in Chapter 5.

3.5 Theoretical modeling of segregation and diffusion of alloying elements

ThermoCalc® 2020-a software package was used to model segregation and diffusion of alloying elements using the GS solidification and DICTRA modules respectively. TCFE8 and MOBFE3 databases were used for all calculations. The methods followed to obtain the predictions are explained in the following sections.

3.5.1 Segregation during solidification

The Scheil solidification simulation module of the ThermoCalc® software package was used for segregation modeling of steels S1 and S2. The Scheil solidification module in ThermoCalc was used to obtain the following results:

i) Fraction solid vs temperature with phase transformation

ii) The segregation profile of solutes in solid and liquid phases

The following 2 different approaches were used:

a) Simple GS

b) Modified GS

a) Simple GS solidification

For a simple GS calculation, the liquidus temperature of the alloy is calculated based on the Gibbs free energy of solid and liquid phases as a function of temperature. Starting at the melting point, the system temperature is decreased in steps. For each step, the composition and phase fraction of solid is calculated using the lever rule. Simple GS calculations consider no diffusion of solutes in the forming solid phase and, hence, the solid formed is stored and the next equilibrium is calculated based on the increased liquid concentration and so on. A reduced chemistry was used for the simple GS calculations in order to avoid other phase formation during the end stages of the solidification simulation. All elements with nominal composition less than 0.02wt% were not included in the simulations. The exceptions to this were P and S, which were included even though their nominal compositions were less than 0.02 wt%. Test calculations were performed with the inclusion of all elements to ensure that the removal of low wt% elements did not significantly alter the peritectic transformation temperature or concentration distribution of the solutes of interest (Mn, Cr, Nb and P). An Excel sheet containing the fraction solid (f_s) formed and the composition of each phase as a function of temperature was obtained for each run. Once the values from GS calculations were obtained, the microsegregation ratios for different elements were calculated using Equation 3.2 at fraction solid = 0.85 as suggested by a previous study [69] of microsegregation in Fe based multinary alloys:

$$Microsegregation\ ratio\ for\ Mn = \frac{\text{Concentration of Mn in solid phase at 85\% } f_s}{\text{Nominal [Mn]}} \quad 3.2$$

b) Modified GS solidification

In modified GS models, the diffusivity of selected solute(s) in solid phase is considered to be non zero. ThermoCalc steps through the same way for modified GS calculations as for simple GS calculations. The only exception is the addition of an extra step for equalizing the chemical potential of fast diffusers throughout the system before stepping to the next temperature. The Scheil module in ThermoCalc provides a direct option of considering some elements to be fast diffusers. This is particularly useful for interstitial solutes like C, P and S, which have considerably higher diffusivity in steels as compared to substitutional solutes like Mn and Cr. For modified GS calculations in this work, C, P and S were considered as fast diffusers. Similar to simple GS calculations, a reduced chemistry was used for modified GS calculations. Equation 3.2 was again used for microsegregation ratio calculation for the elements of interest.

3.5.2 Diffusion during homogenization

The effect of the homogenization heat treatment on segregation was simulated using the DICTRA module of ThermoCalc. The following two sets of diffusion simulations were performed:

a) Binary Fe-X models
b) Steel S1 with reduced chemistry

a) Binary Fe-X models

Simple binary Fe-X models were used to better understand the individual nature of diffusion of various alloying elements in steel with reduced computational complexity. A step profile for the alloying element was defined at t = 0 in a 300 μm wide 1-D austenite domain. Figure 3.11 shows an example of DICTRA based diffusion simulation for a binary Fe-Mn system. The initial profile of Mn in a 300 μm wide austenite phase is defined as a step function that goes from 1.60 wt% Mn to 2.32 wt% Mn at 250 μm. The initial profile is denoted by the blue line in Figure 3.10. The simulation time and temperature were set and the simulation was run. After simulation was complete, the decrease in peak segregation was noted at different times. The final concentration profile of Mn after 12 h (43,200 s) is denoted by the red line in Figure 3.11. The initial peak segregation values were based on the as-cast profiles for individual elements. The diffusion model used in this work is similar to that of a surface layer diffusion model. A detailed solution for the surface layer diffusion model is shown in Appendix D. The chemical diffusion coefficients as a function of temperature were also obtained for Mn, Cr, Nb and P directly

through the equilibrium calculator module of ThermoCalc using the TCFE8 and MOBFE3 databases.

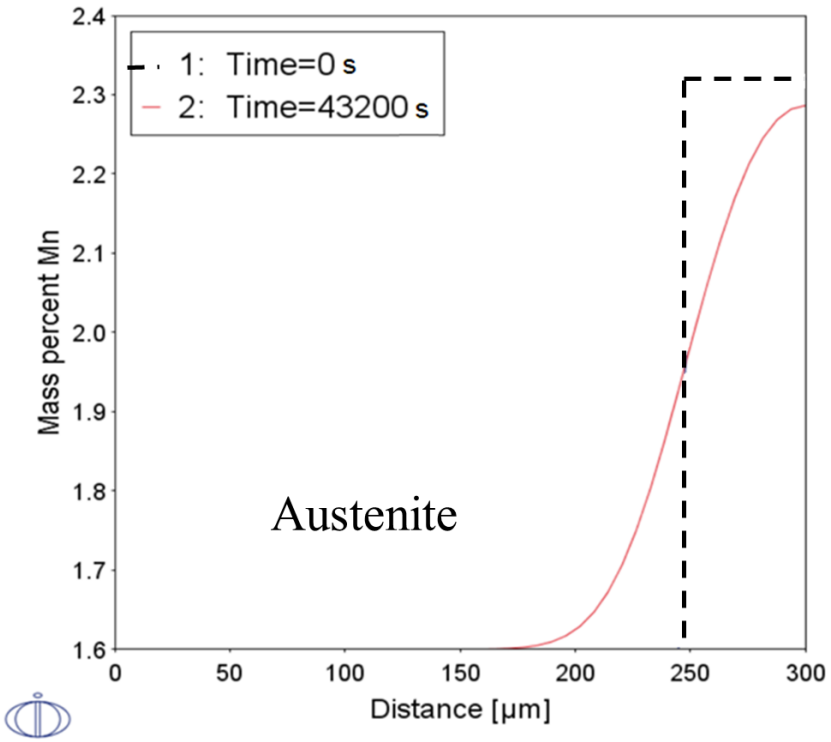

Fig. 3.11: Fe-Mn DICTRA diffusion simulation at 1200ºC for 12 h.

b) Steel S1 with reduced chemistry

Simulations with reduced chemistry (the same as defined during GS calculations) were also performed to confirm whether or not the binary models were sufficient to provide reasonable predictions. In this case, the initial profiles for all the elements were simultaneously defined at t = 0. The subsequent steps for simulations with reduced chemistry were the same as that in the case of the binary simulations. The obtained predictions from DICTRA simulations are discussed and compared with the EMPA results of homogenized samples in Chapter 6 of this thesis.

3.6 Summary

The experimental techniques used for machining, processing and analysis of microalloyed steel samples were described in this chapter. The models used for theoretical simulations were also presented. The results obtained using the discussed techniques for the studied steels are presented in the next chapter.

4. Segregation during continuous casting of microalloyed steels

The EMPA results of segregation from as-cast slabs S1 and S2 are presented and discussed in this chapter. The measured values are compared with the segregation calculation results from GS simulations. Trends and values observed in the EMPA data are also compared with the information available in the literature for continuous cast steel slabs.

4.1 Distribution of Mn in as-cast microalloyed steel slabs

This section presents the as-cast Mn EMPA maps and point scans data obtained from different locations throughout the thickness of as-cast microalloyed steel slabs.

4.1.1 As-cast EMPA data for Mn from slab S1

The as-cast Mn EMPA maps and point scans were obtained from different locations throughout the thickness of slab S1. Based on the initial through thickness mapping of S1 (included in Appendix E), four locations were chosen. The four chosen locations are schematically shown in Figure 4.1, and were the top (6 mm below the top surface), metallurgical centerline (90 mm below the top surface), quarter thickness (62 mm above the bottom surface) and bottom (6 mm above the bottom surface) of the slab.

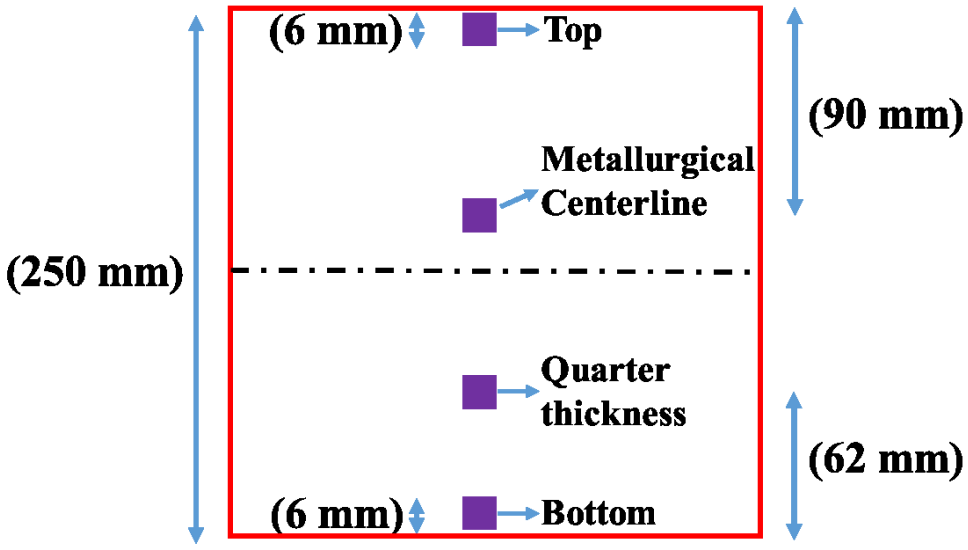

Fig. 4.1: Schematic showing EMPA sample locations for slab S1.

The Mn EMPA grayscale, enhanced grayscale and enhanced inverted maps from the top sample of S1 are shown in Figure 4.2. The enhanced grayscale EMPA map is a slightly modified

version (both brightness and contrast of the original grayscale map pixels were altered) of the original grayscale map. To further enhance the difference (visually) between regions of high and low Mn concentration, the original grayscale map was inverted (i.e., high Mn concentrations become dark pixels and vice versa). In addition, a pixel threshold was defined based on grayscale distribution for the inverted image - the pixels were redefined as all black on one side of the threshold, and as all white on the other side of the threshold. The resulting enhanced inverted map from the top sample is shown in Figure 4.2-c.

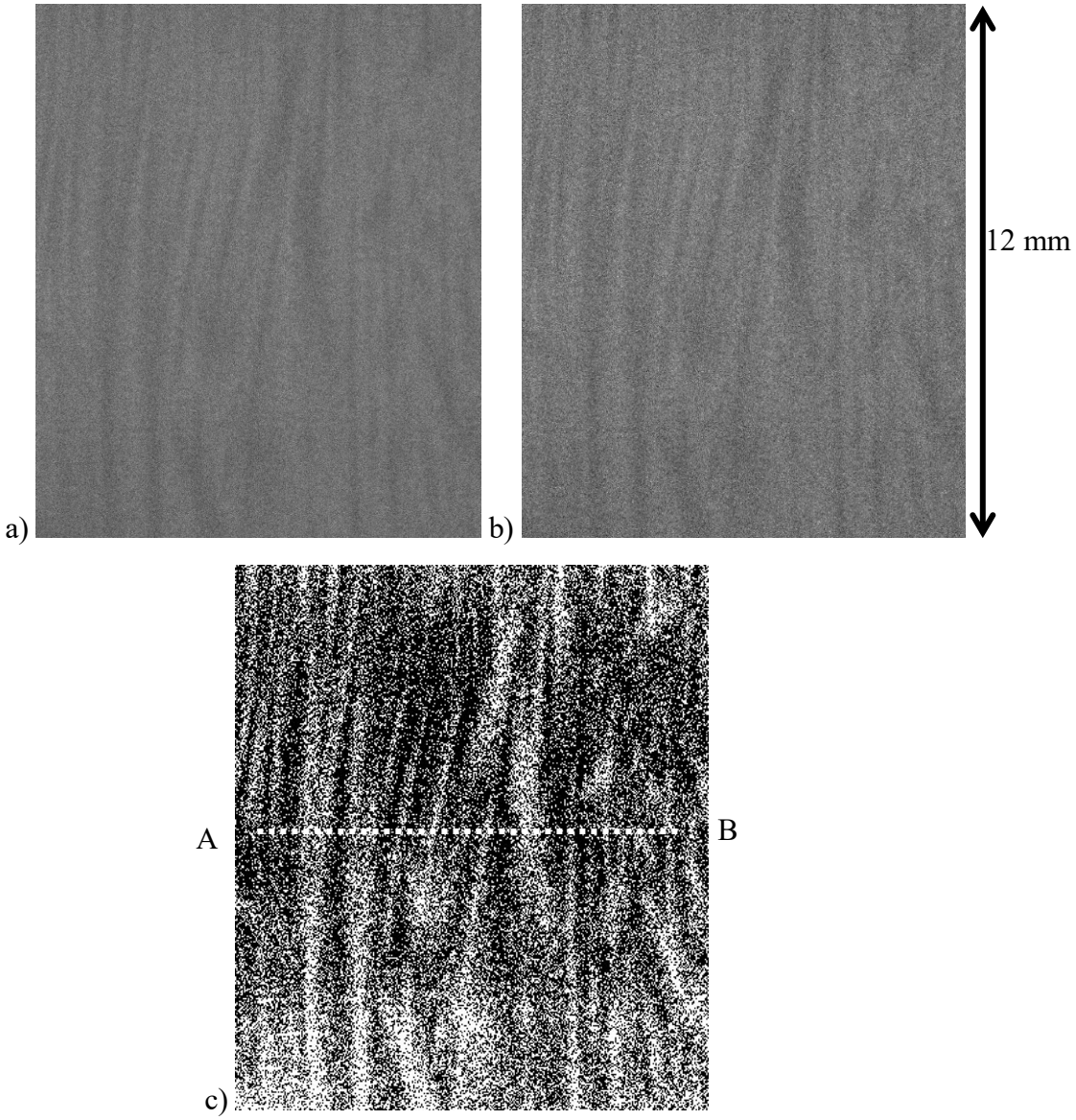

Fig. 4.2: As-cast a) grayscale, b) enhanced grayscale and c) enhanced inverted Mn map and line scan location (corresponding to dashed line AB) from the top sample of S1.

Primary solidification dendrites (darker areas indicating a high wt% Mn) separated by interdendritic regions of lower Mn content (lighter regions) are visible in Figure 4.2-c. The dotted line (i.e., AB in Figure 4.2-c) on the inverted map represents the selected location for the quantitative point scans. The entire wt% Mn vs. distance values obtained from the line scan AB are shown in Figure 4.3. The maximum and minimum measured wt% Mn for this line scan are 1.74 and 1.53, respectively. Note that these values do not necessarily represent the maximum and minimum wt% Mn values on the map. The wt% Mn values shown in Figure 4.3 exhibit an oscillatory behaviour of Mn concentration with scan distance. These oscillations represent the changing local composition of Mn in and between the primary dendrites.

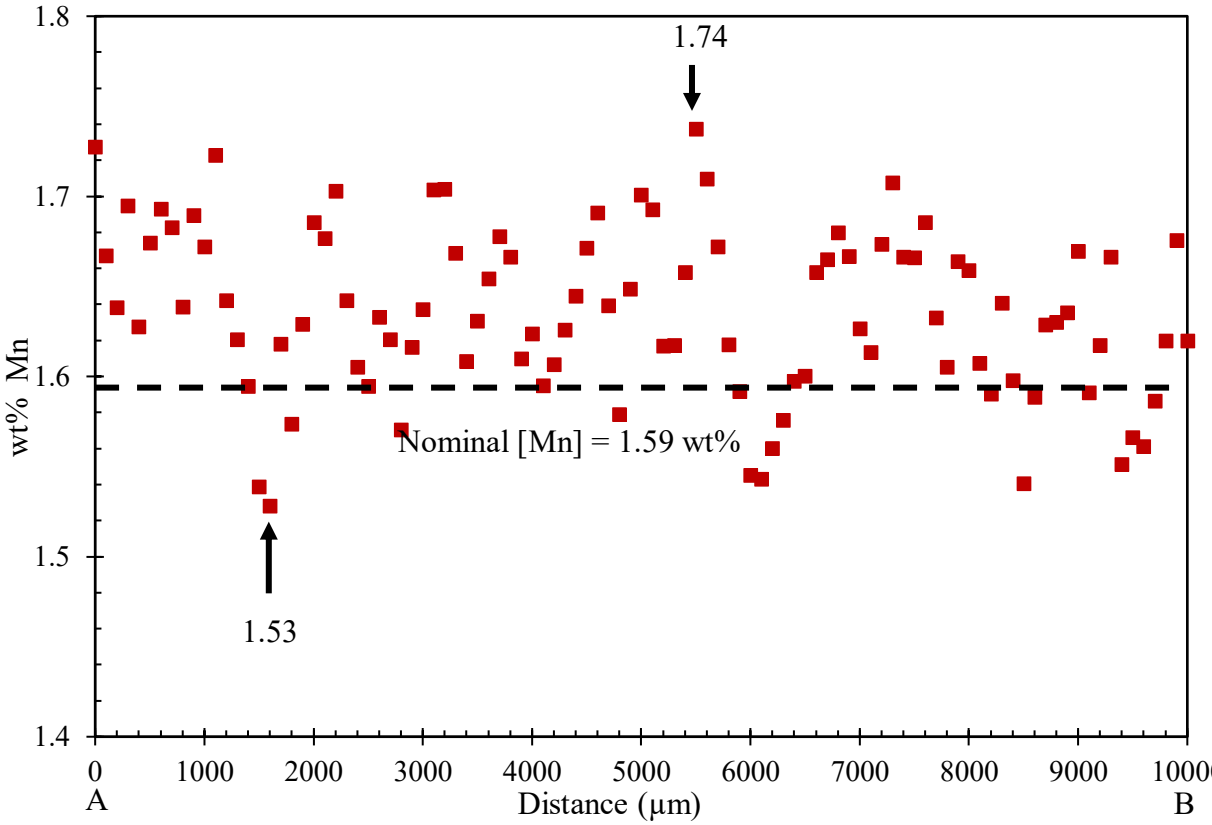

Fig. 4.3: Mn line scan corresponding to dashed line AB in Figure 4.2-c.

Figure 4.4 shows a magnified view of the line scan AB (in the range 3000-6000 µm). The peaks and troughs associated with either a higher wt% Mn in the interdendritic regions or a lower wt% Mn value at the centre of the primary dendrite are readily observed. Vertical dotted lines at each peak are added and the distance between the peak locations are labeled. For the top sample, values of primary dendrite arm spacing (PDAS) of 600, 800, 400 and 500 µm are observed as

shown in Figure 4.4. The average primary dendrite arm spacing value is calculated to be 567 µm with a standard deviation (SD) of 137 µm.

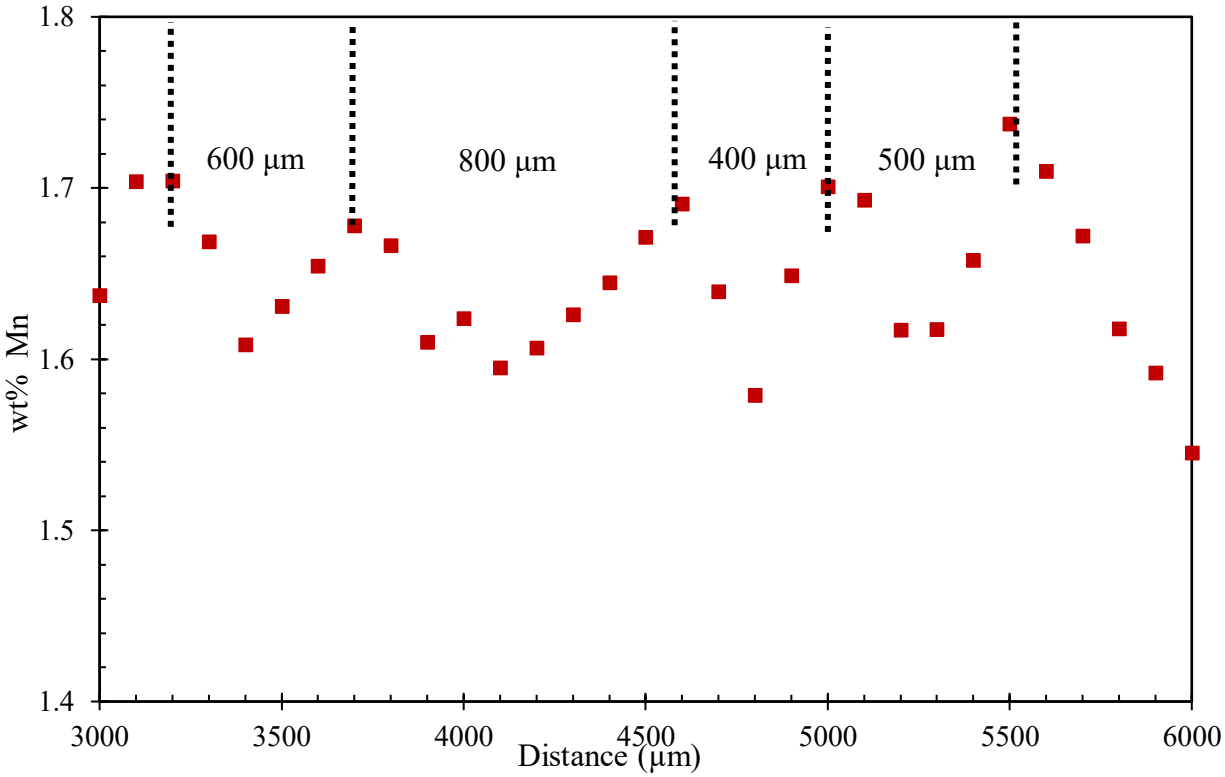

Fig. 4.4: Mn line scan corresponding to dashed line AB in Figure 4.2-c magnified in the 3000-6000 µm range.

The enhanced inverted map from the CL location of S1 is shown in Figure 4.5. Unlike Figure 4.2, well defined primary dendrites are not observed. The solidification structures (as defined by regions of high and low Mn content) are randomly oriented and discontinuous. This equiaxed type of structure corresponds to typical solidification structure near metallurgical centerline of continuously cast steel slabs.

Figure 4.5-b shows the wt% Mn values taken along line scan AB shown in Figure 4.5-a. The line scan passes through a dark region near the top of Figure 4.5-a. The dark region represents the large wt% Mn peak values observed between 800 and 2000 µm on the line scan. The maximum measured value of 2.30 wt% Mn is significantly higher than the maximum measured segregation value for the top sample in Figure 4.3. A minimum wt% Mn value of 1.41 is observed in the white region (corresponding to low Mn content in the inverted map).

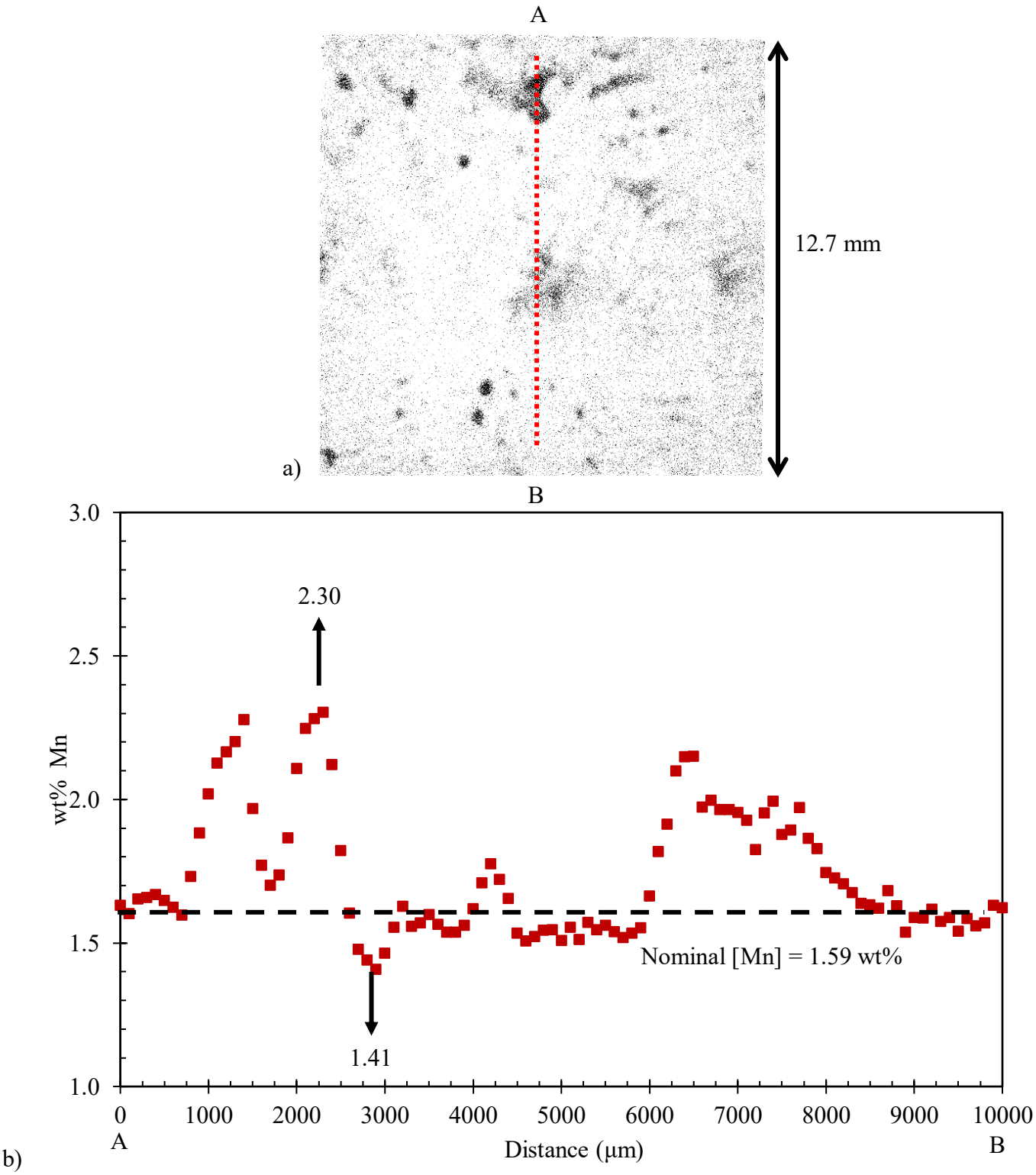

Fig. 4.5: a) As-cast EMPA enhanced inverted map and b) line scan plot for Mn from CL of S1.

The Mn map from QT sample of S1 is shown in Figure 4.6-a. A dendritic distribution of Mn similar to that of top sample is observed. The wt% Mn vs distance plot along the dotted line

AB is shown in Figure 4.6-b. The maximum and minimum measured wt% Mn are 1.75 and 1.59, respectively. All the measured wt% Mn values from point scans for the QT sample are above the nominal Mn content.

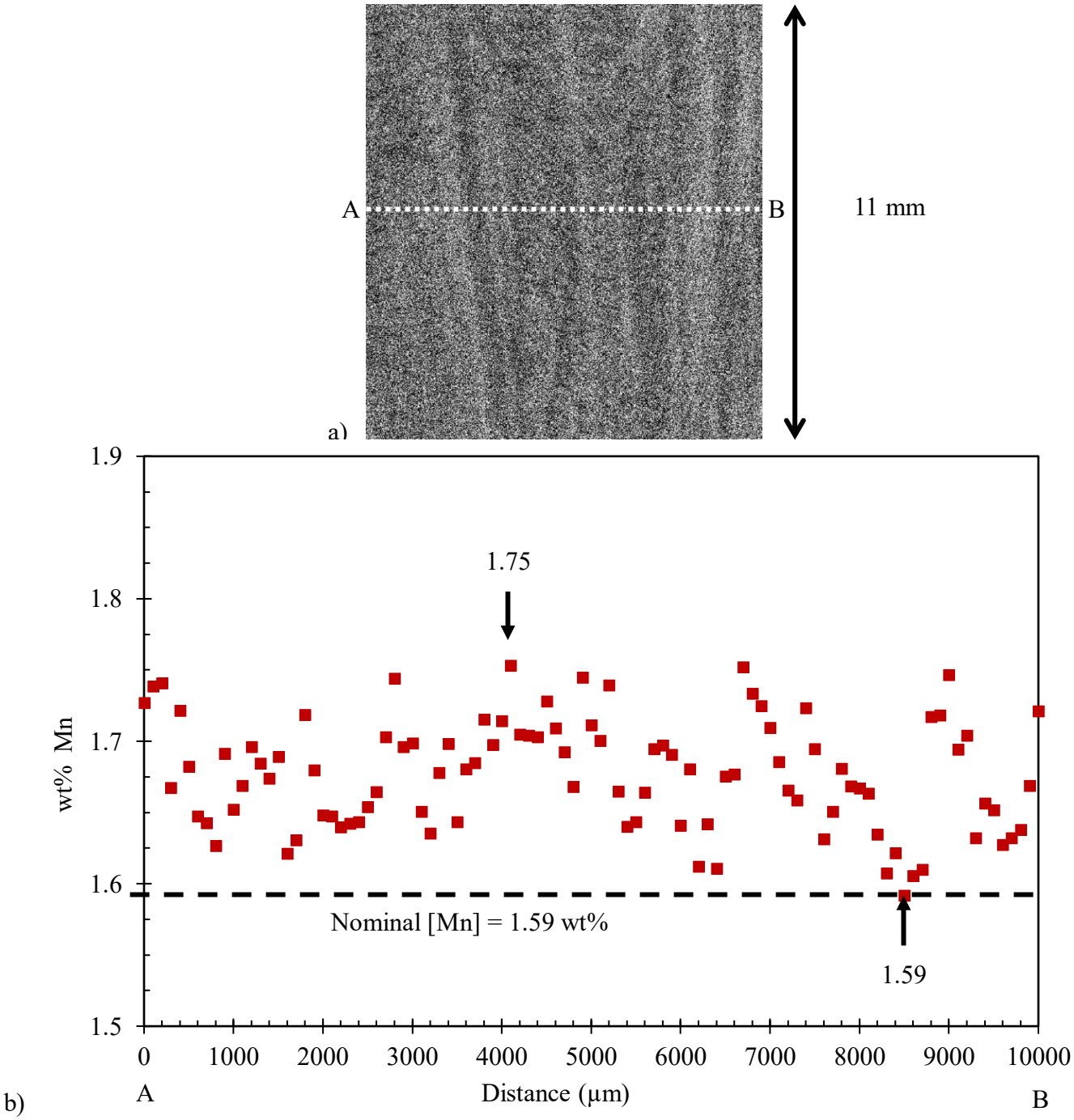

Fig. 4.6: a) As-cast EMPA enhanced inverted map and b) line scan plot for Mn from QT of S1.

Figure 4.7 shows a magnified view of the line scan AB (in the range 0-3000 µm) for the QT sample. Vertical dotted lines at each peak are again added and the distance between the peak locations are labeled. The interpeak distance varies depending on the local variation in the wt% Mn. For the QT sample, the average PDAS value is 633 µm with a SD of 225 µm.

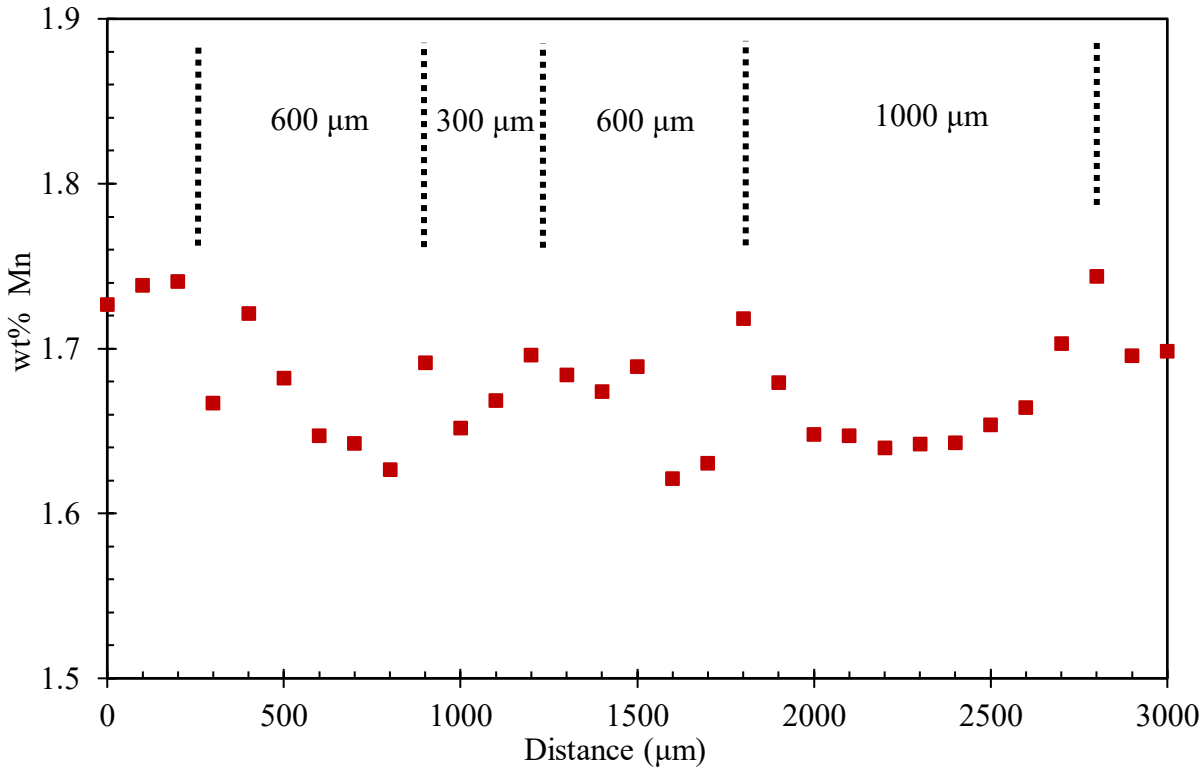

Fig. 4.7: Mn line scan corresponding to dashed line AB in Figure 4.6-a, magnified in the 0-3000 µm range.

The concentration distribution of Mn in the bottom sample is shown in Figure 4.8-a. A fine dendritic distribution is observed, although the dendrites are difficult to resolve as compared with the top and QT samples of S1. The close proximity of peaks and troughs in the corresponding wt% Mn vs distance plot (Figure 4.8-b) further illustrates the fineness in Mn distribution. The maximum and minimum measured wt% Mn in this sample are 1.74 and 1.48, respectively (Figure 4.8-b). Figure 4.8-c shows the same line scan plot shown in Figure 4.8-b, magnified in the 2000-5000 µm range. Local peaks corresponding to high wt% Mn are again illustrated by dotted lines. Ten peaks were identified within a distance of 2700 µm and the average PDAS was estimated as 305 µm with a SD of 64 µm for the bottom sample of S1.

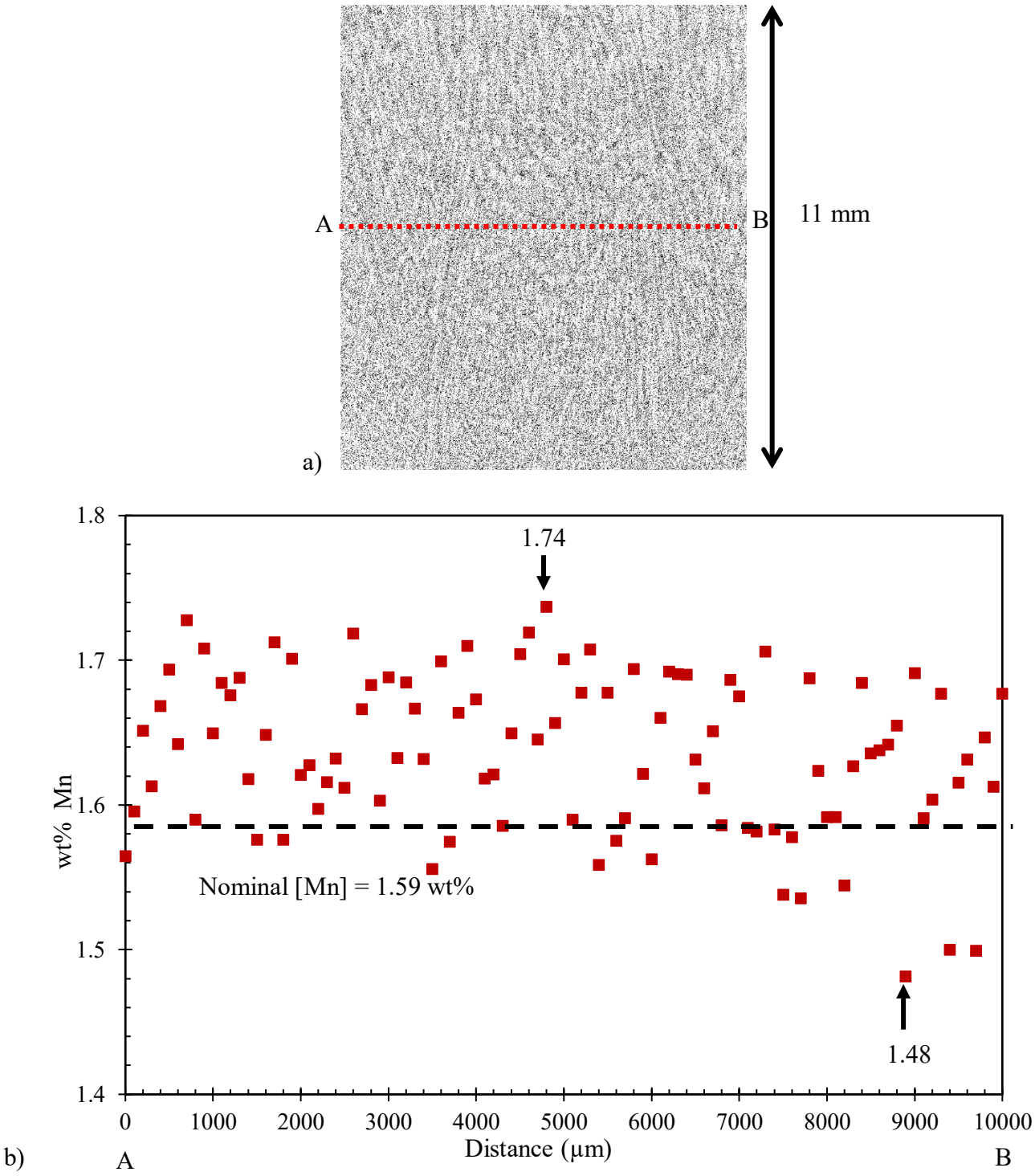

Fig. 4.8: a) As-cast EMPA enhanced inverted Mn map and b) line scan plot from bottom sample of slab S1.

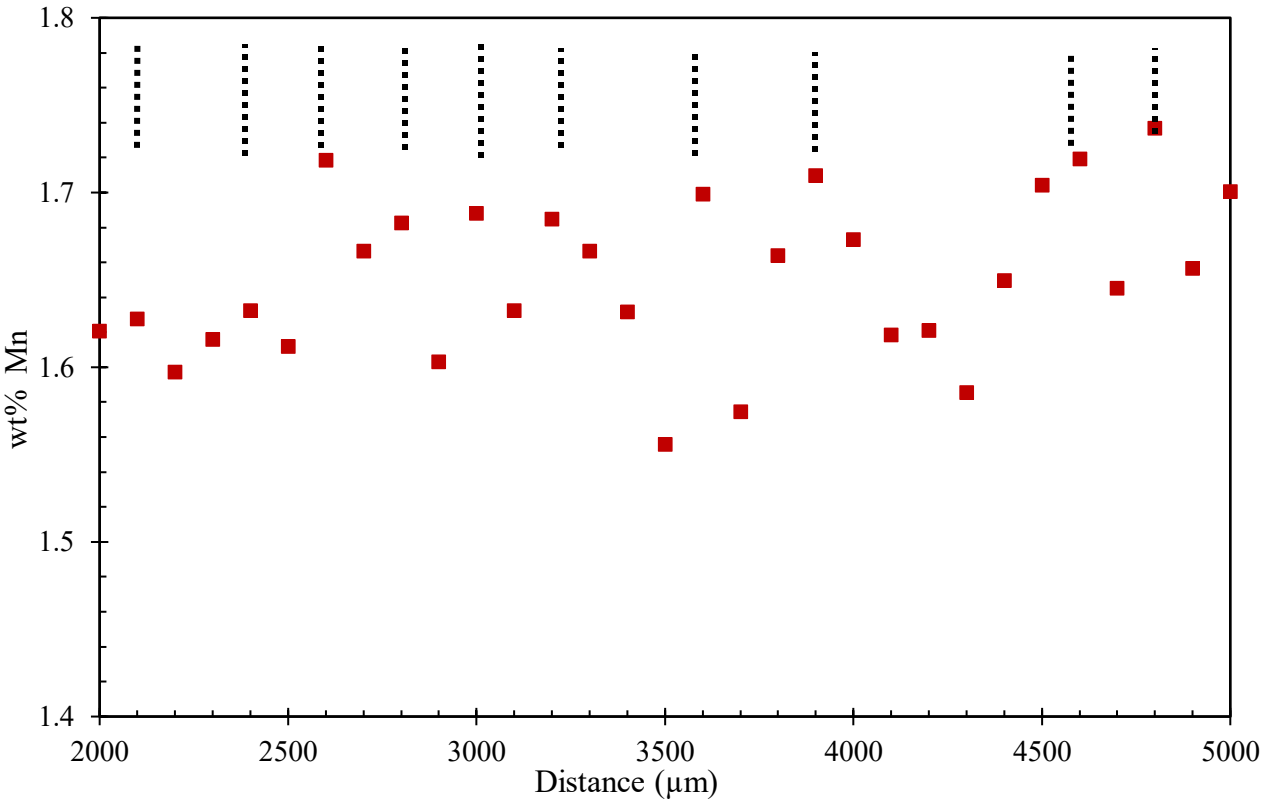

Fig. 4.8: c) Mn line scan corresponding to line AB in Figure 4.8-a, magnified in the 2000-5000 µm range.

Summary for 4.1.1:

- A visual difference in Mn distribution is observed between the top and bottom samples of S1, with the bottom sample having a finer distribution.
- The PDAS in the bottom sample (300 µm) is finest, followed by the top sample (575 µm) and the QT sample (625 µm).
- Centerline segregation is not present at the geometric center of the slab, but is shifted 30 mm towards the top surface of the slab.

4.1.2 As cast EMPA data for Mn from CL and QT samples of slab S2

Figure 4.9-a shows the Mn EMPA enhanced inverted map from the CL sample of S2. The CL sample has an equiaxed distribution of Mn similar to the CL sample of S1. The wt% Mn vs distance distribution corresponding to line scan AB is shown in Figure 4.9-b. The maximum and minimum measured wt% Mn for CL sample are 1.59 (from another line scan) and 1.18.

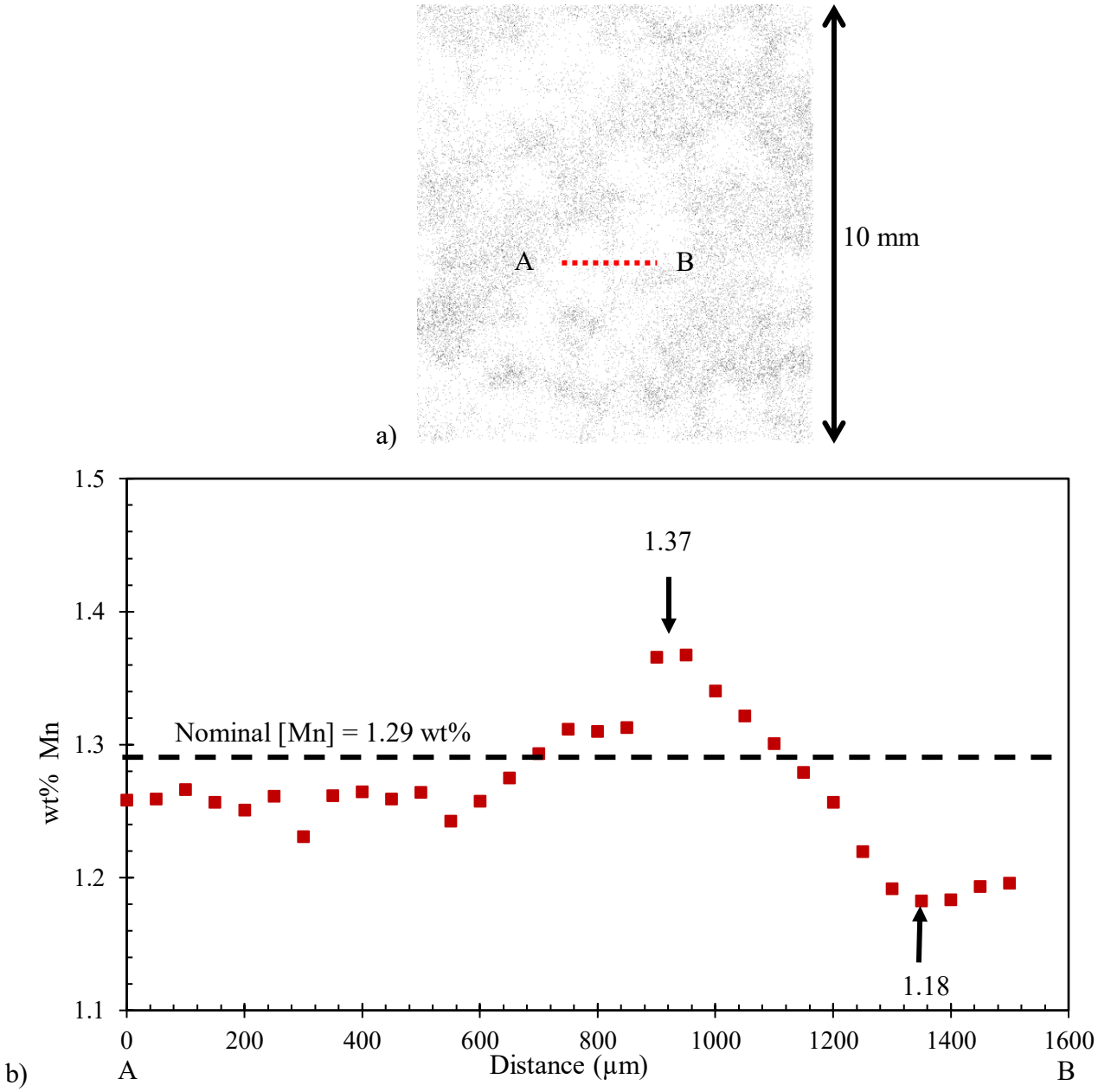

Fig. 4.9: a) As-cast EMPA enhanced inverted Mn map and b) line scan plot from CL sample of S2.

The Mn EMPA enhanced inverted map from the QT sample of S2 is shown in Figure 4.10-a. The QT sample has a dendritic distribution of Mn similar to the QT sample of S1. The PDAS calculation is again illustrated with the help of vertical dotted lines in the wt% Mn vs distance plot shown in Figure 4.10-b. The average PDAS for the QT sample is 600 µm with a SD of 71 µm. The maximum and minimum measured wt% Mn for QT sample are 1.41 and 1.26.

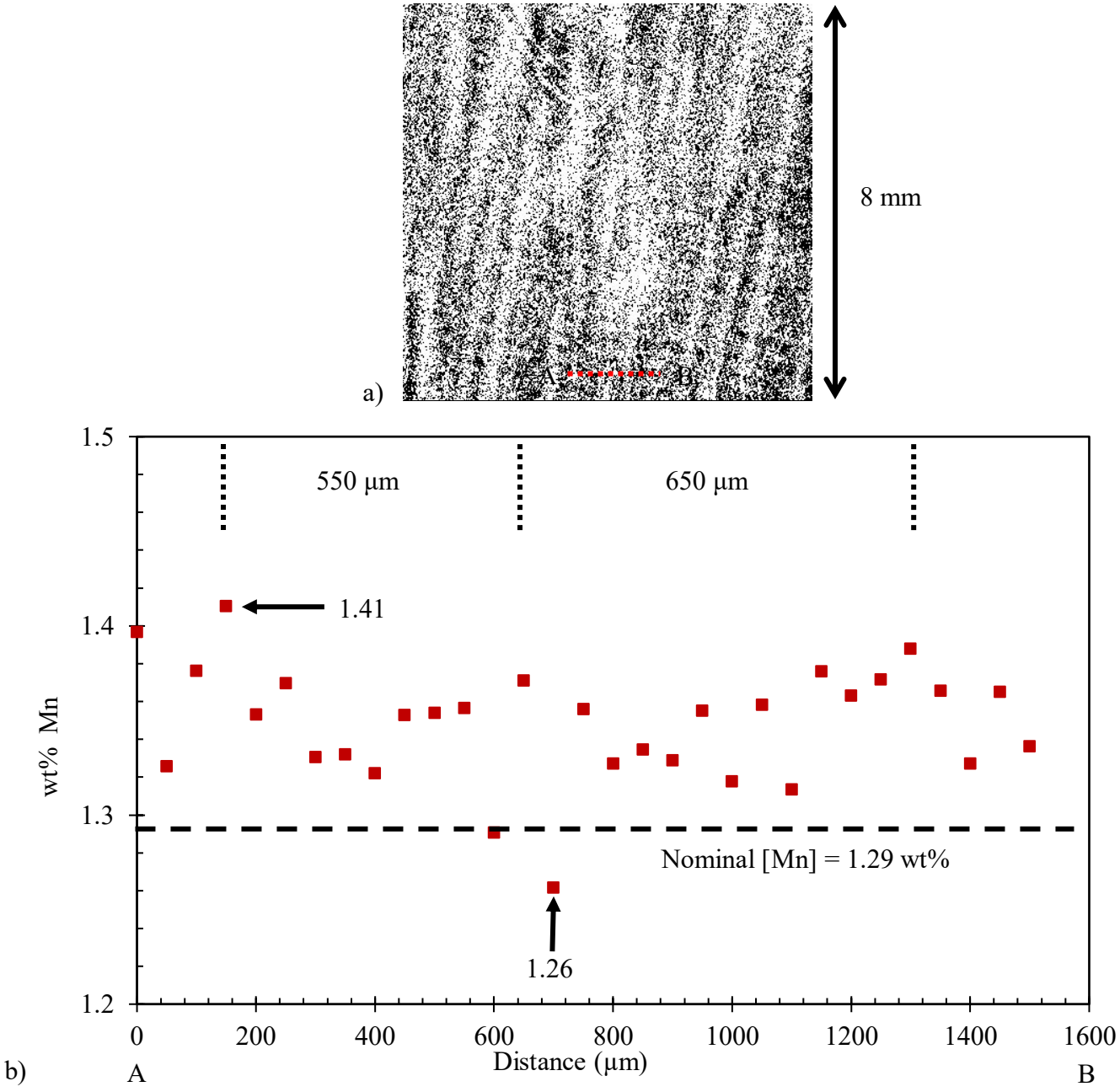

Fig. 4.10: a) As-cast EMPA enhanced inverted Mn map and b) line scan plot from QT sample of S2.

Summary for 4.1.2:

- The spatial concentration distribution of Mn in the CL and QT samples of S2 is the same as that for S1.
- Similar to S1, the location of centerline is shifted towards the top surface in S2.

4.1.3 Distribution of Mn through the thickness of as-cast microalloyed steel slabs

Figure 4.11-a shows the distribution of Mn in the sample taken near the top surface of slab S1. The scale bar included in the figure indicates the spatial extent of the segregation. This will have implications in terms of the time and temperature of homogenization required to reduce the segregation. Primary dendrite arm spacing was used as a measure of spatial distribution, since secondary dendrites are not as apparent as the primary dendrites. Figure 4.11-b shows the enhanced inverted map for Mn in the sample taken near the bottom surface of slab S1. A finer distribution of Mn was observed in the bottom surface sample as compared to the top surface sample. This implies that the bottom surface of slab S1 cooled faster than the top surface of the slab; a faster cooling rate produces in a finer distribution [310, 311]. The distribution in bottom surface is also similar to that in the chilled zone of castings. The faster cooling of bottom surface of slabs can occur due to a larger surface contact area and unequal water spray cooling efficiency in the mold. This difference in cooling also resulted in a shift of the centerline region towards the top half of the slab for both S1 and S2.

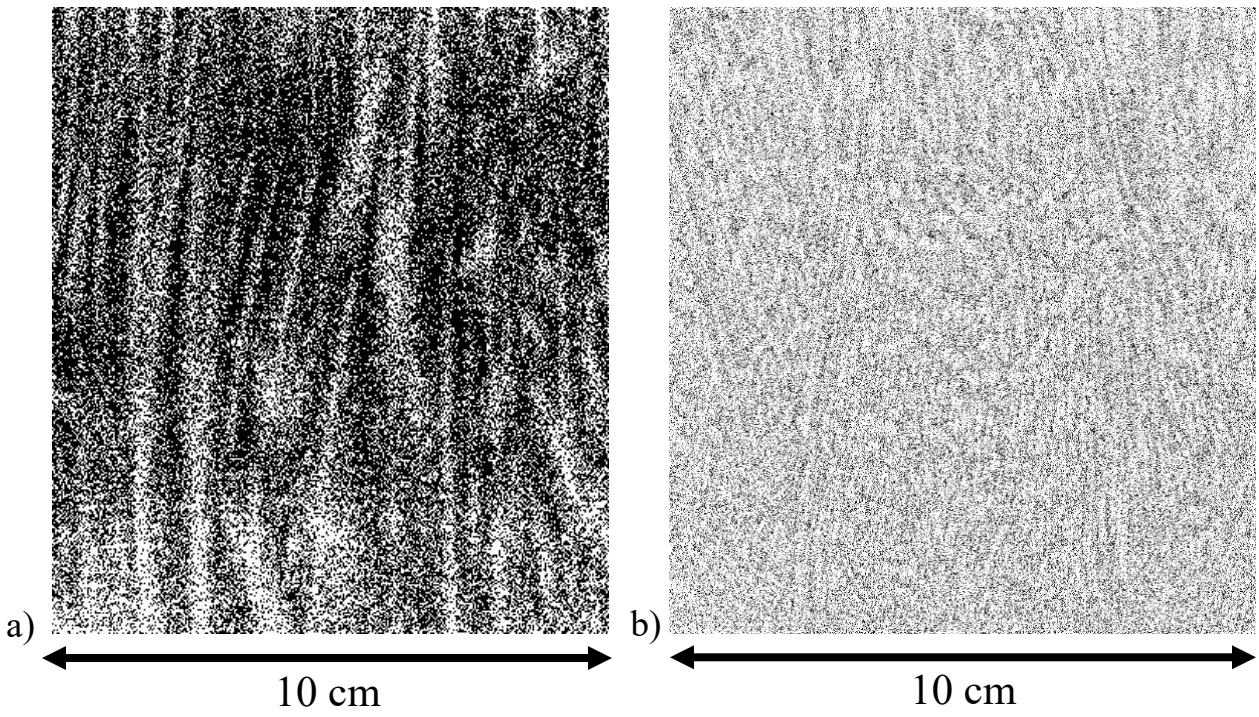

Fig. 4.11: As-cast EMPA enhanced inverted Mn map for sample taken a) near the top surface b) near the bottom surface of slab S1.

Figure 4.12-a and b show the Mn distribution in the centerline (CL) and quarter thickness (QT) locations of the slab S1, respectively. The CL sample has a patch like distribution of Mn, where high concentrations of Mn appear as clumps. There are randomly oriented discontinuous regions with a coarse dendritic distribution. This is due to the implementation of soft reduction during casting of the slab. Mechanical forces during the application of soft reduction result in redistribution of the last solidifying solute rich liquid. Samples from the CL locations were used to quantify macrosegregation and the effects of homogenization on macrosegregation. For the QT sample, the distribution of Mn is similar to that in the sample taken from near the top surface of the slab (Figure 4.11-a), however, the primary dendrite arm spacing is relatively larger for the QT sample. This is due to slower cooling experienced by the interior of the slab as compared to the slab surfaces. Samples from the QT locations were used to quantify microsegregation and the effects of homogenization on microsegregation.

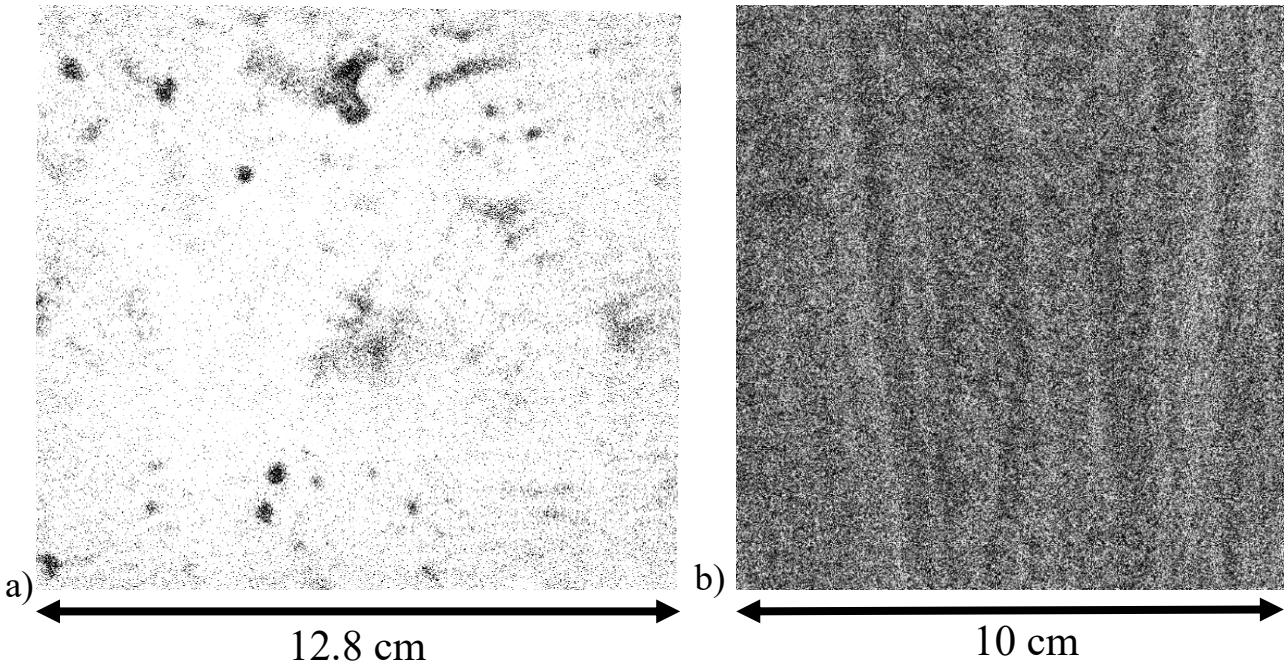

Fig. 4.12: As-cast EMPA enhanced inverted Mn maps at a) CL and b) QT location of slab S1.

The centerline segregation regions in both studied slabs are different than those observed in conventional as-cast steel slabs. This is another consequence of implementation of soft reduction during continuous casting. Centerline segregation for different as-cast microalloyed steel slabs is shown in Figure 4.13. The first 2 images (Figure 4.13-a and b) are from S1 and S2, with the application of soft reduction during casting, and the third image (Figure 4.13-c) is from a previous

study [312], where the slab was cast without the application of soft reduction. A continuous centerline segregation band is visible in Figure 4.13-c, whereas no continuous centerline is present in slabs S1 and S2, which is favourable in terms of the final quality of the cast slabs [312- 314].

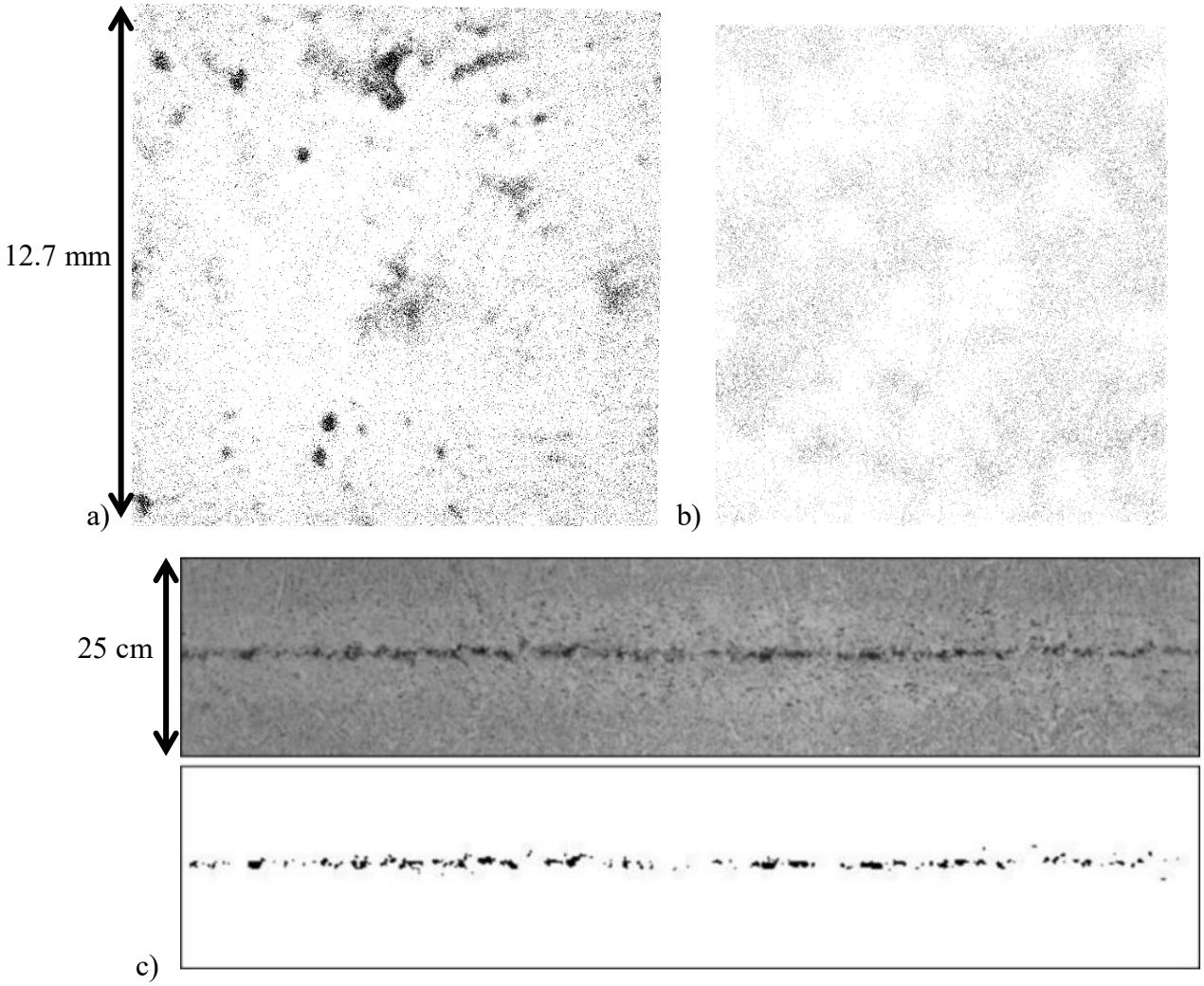

Fig. 4.13: As-cast EMPA inverted maps showing centerline distribution for a) S1 b) S2 and c) a conventional cast slab from a previous study [312].

4.2 Distribution of Cr in as-cast microalloyed steel slabs

This section presents the as-cast Cr EMPA maps and point scans obtained from different locations across the thickness of as-cast slabs. As mentioned in Section 3.4.3, since each point scan provides with the wt% value of 5 different elements, the locations of the line scans on the Cr maps were the same for the Mn maps for a particular sample.

4.2.1 As-cast EMPA data for Cr from CL and QT samples of slab S1

The enhanced inverted Cr map from the CL sample of S1 is shown in Figure 4.14-a. The Cr map does not reveal any defined segregation pattern due to a lack of concentration gradient for Cr. This is further confirmed by the point scan measurements. The maximum and minimum measured wt % Cr in the CL sample of S1 are 0.068 wt% and 0.050 wt%, respectively. The variation in measured wt% Cr within the CL sample is only 0.018 wt%, which corresponds well with the contrast of the map.

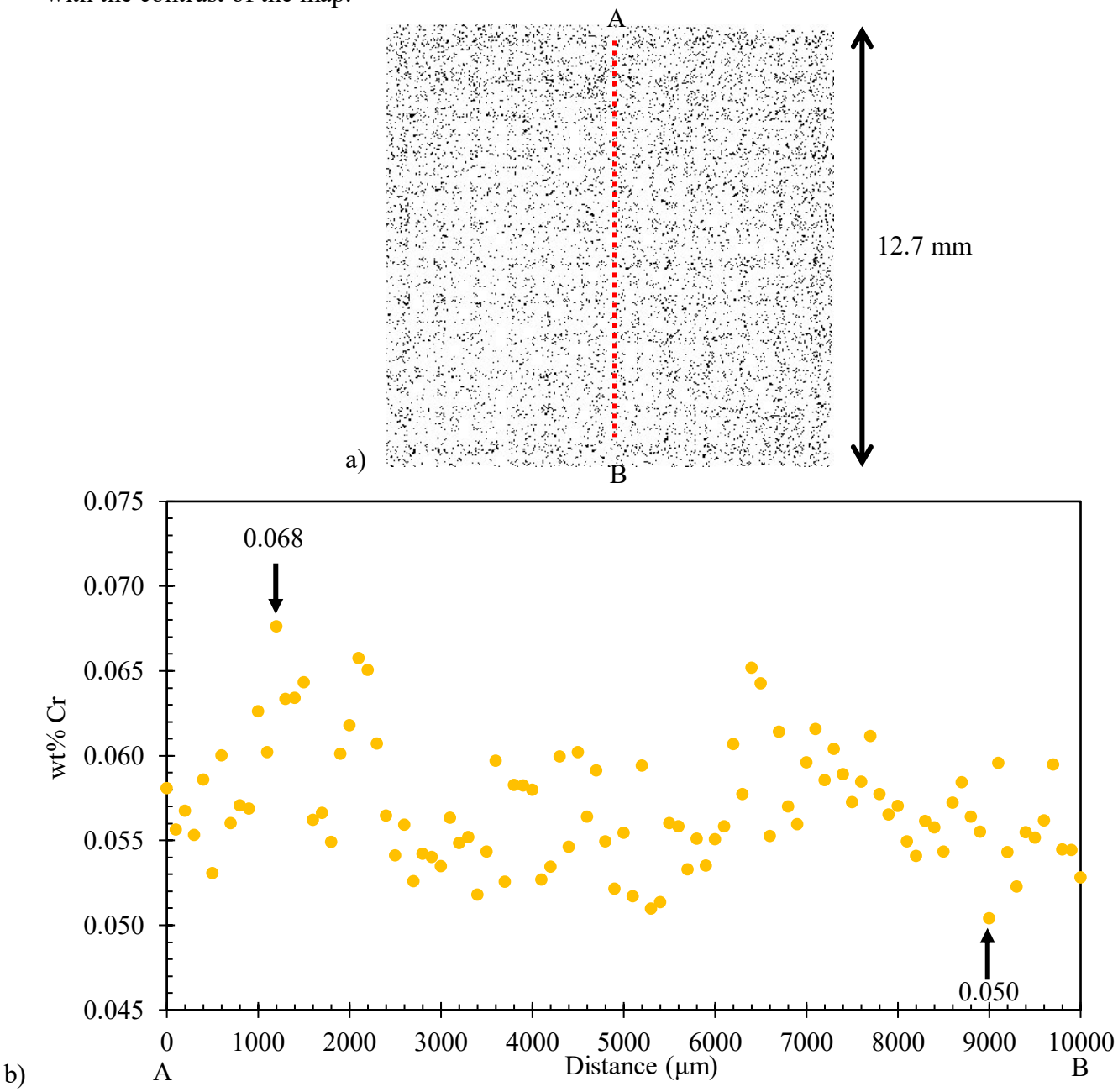

Fig. 4.14: a) As-cast EMPA enhanced inverted map and b) line scan plot for Cr from CL of S1.

The EMPA map for Cr in the QT sample of S1 has a similar distribution as that for the CL sample of S1. The enhanced inverted map for Cr from QT sample along with the line scan plot are shown in Figure 4.15. The maximum and minimum measured wt % Cr are 0.067 wt% and 0.053 wt%, with the same variation in measured wt% Cr of 0.014 wt% as that in the CL sample.

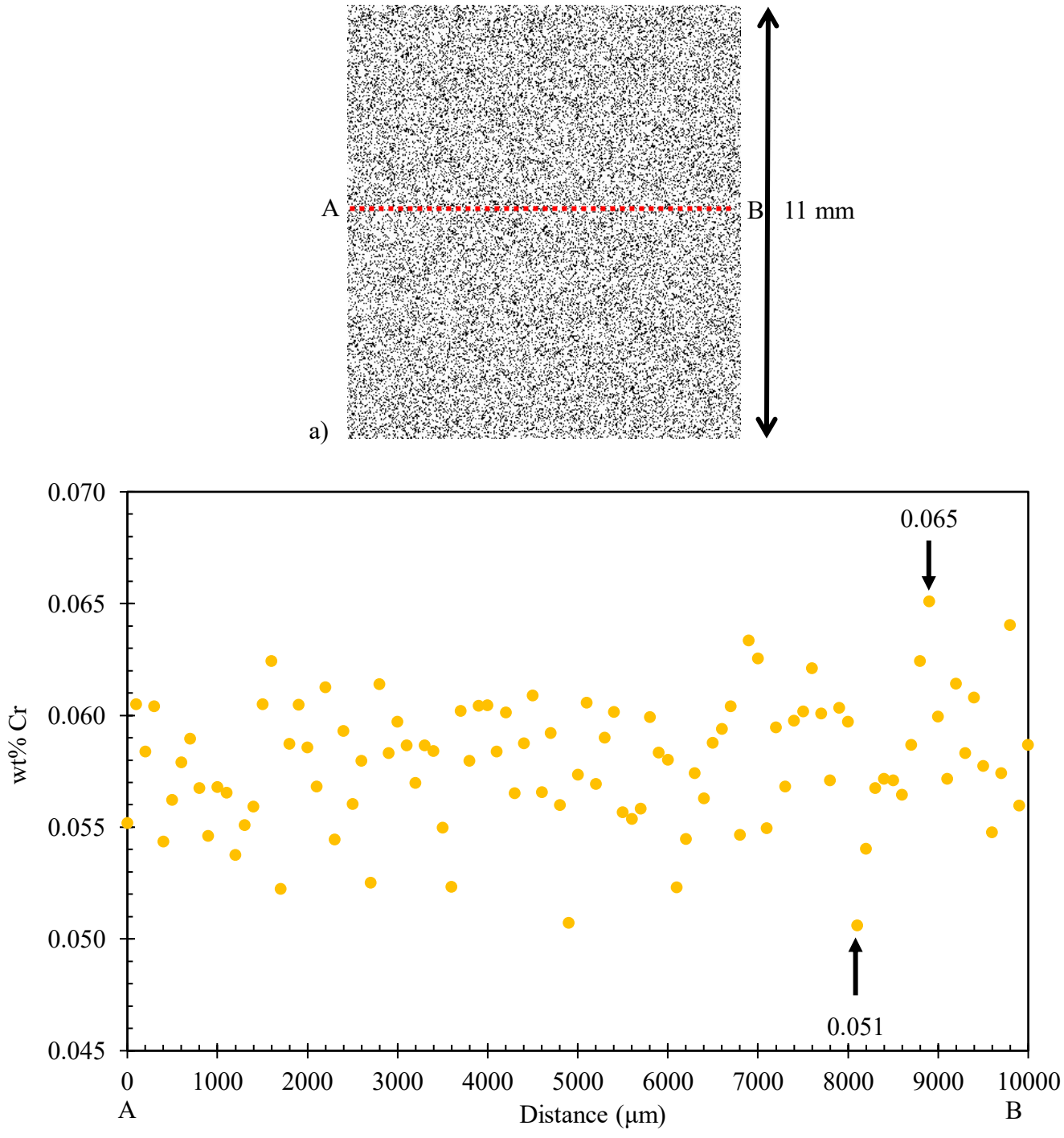

Fig. 4.15: a) As-cast EMPA enhanced inverted map and b) line scan plot for Cr from QT of S1.

4.2.2 As-cast EMPA data for Cr from CL and QT samples of slab S2

The enhanced inverted Cr map from the CL sample of slab S2 is shown in Figure 4.16-a. The maximum and minimum measured wt % Cr in the CL sample of S2 are 0.243 wt% (from another line scan) and 0.207 wt%, respectively. The variation in measured wt% Cr within the CL sample is only 0.036 wt%.

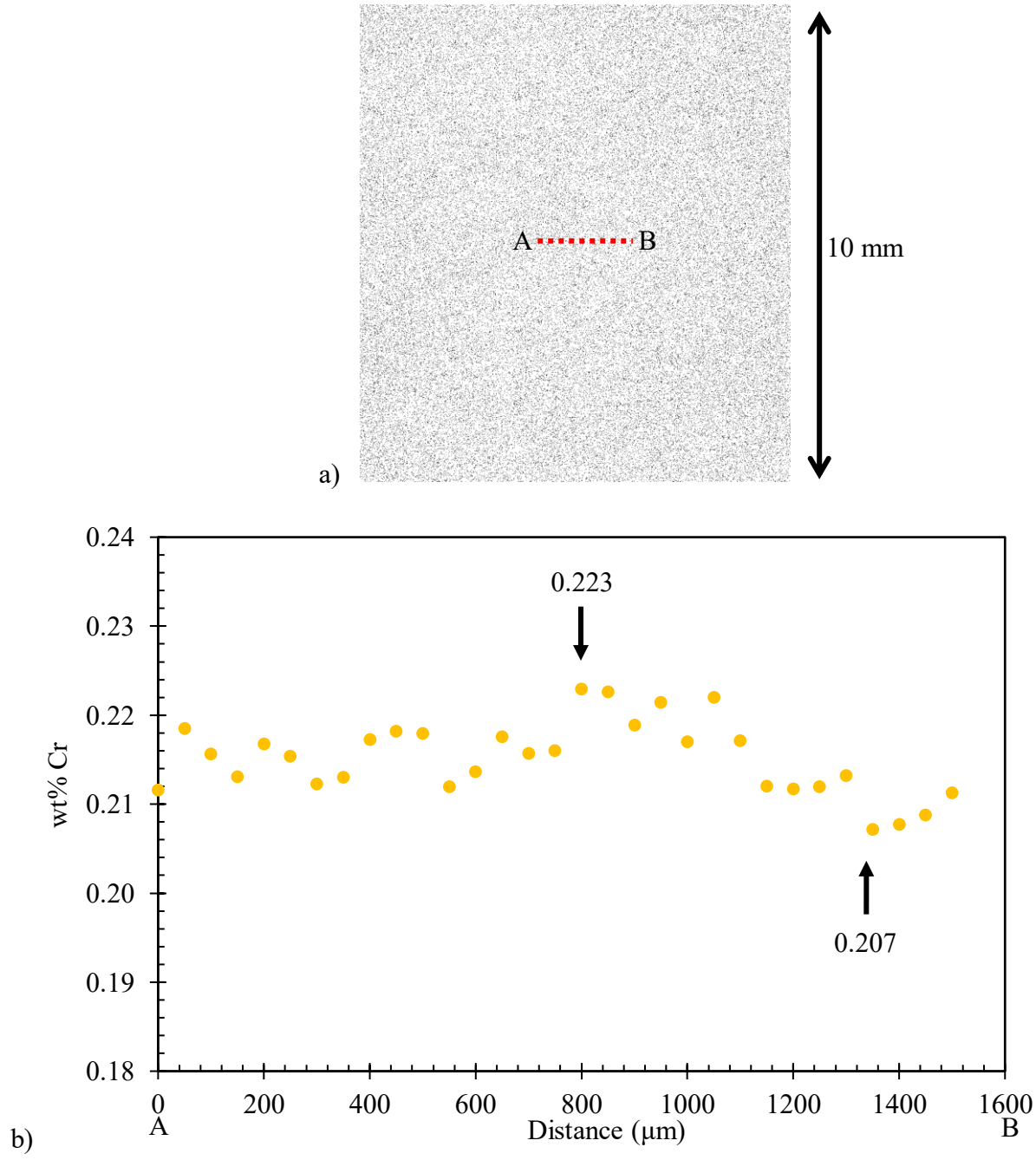

Fig. 4.16: a) As-cast EMPA enhanced inverted map and b) line scan plot for Cr from CL of S2.

The EMPA map for Cr in the QT sample of S2 has a similar distribution as that for the CL sample of S2. The enhanced inverted map for Cr from the QT sample along with the line scan plot are shown in Figure 4.17. The maximum and minimum measured wt% Cr are 0.226 wt% and 0.213 wt%, with a variation in measured wt% Cr of 0.013 wt%. The variation in measured wt% Cr in the QT sample of S2 is lower than that in the CL sample of S2.

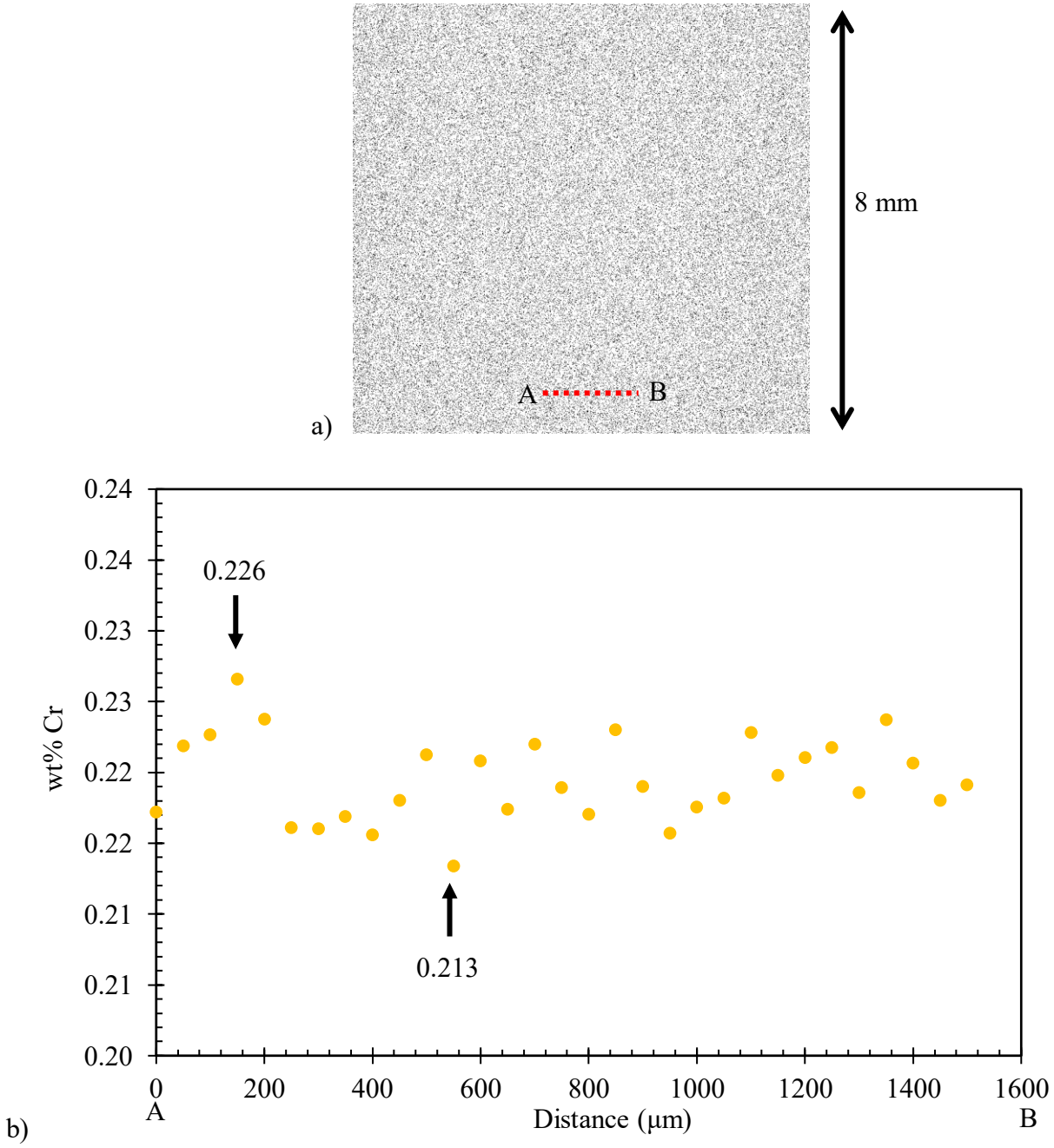

Fig. 4.17: a) As-cast EMPA enhanced inverted map and b) line scan plot for Cr from QT of S2.

4.2.3 Distribution of Cr in as-cast microalloyed steel slabs

The lack of concentration gradient in the Cr maps is due to a higher partition coefficient of Cr. It has the highest partition coefficient (0.93) among Mn, Cr, Nb and P. A higher k results in a larger wt% of the element in the first solid that forms and leads to a lower degree of segregation. Figure 4.18 shows the concentration profiles for Mn and Cr versus fraction solid in S1 predicted through the modified GS model. The concentration gradient for Cr as solidification proceeds is low; therefore, the Cr maps look homogenous and lack any features.

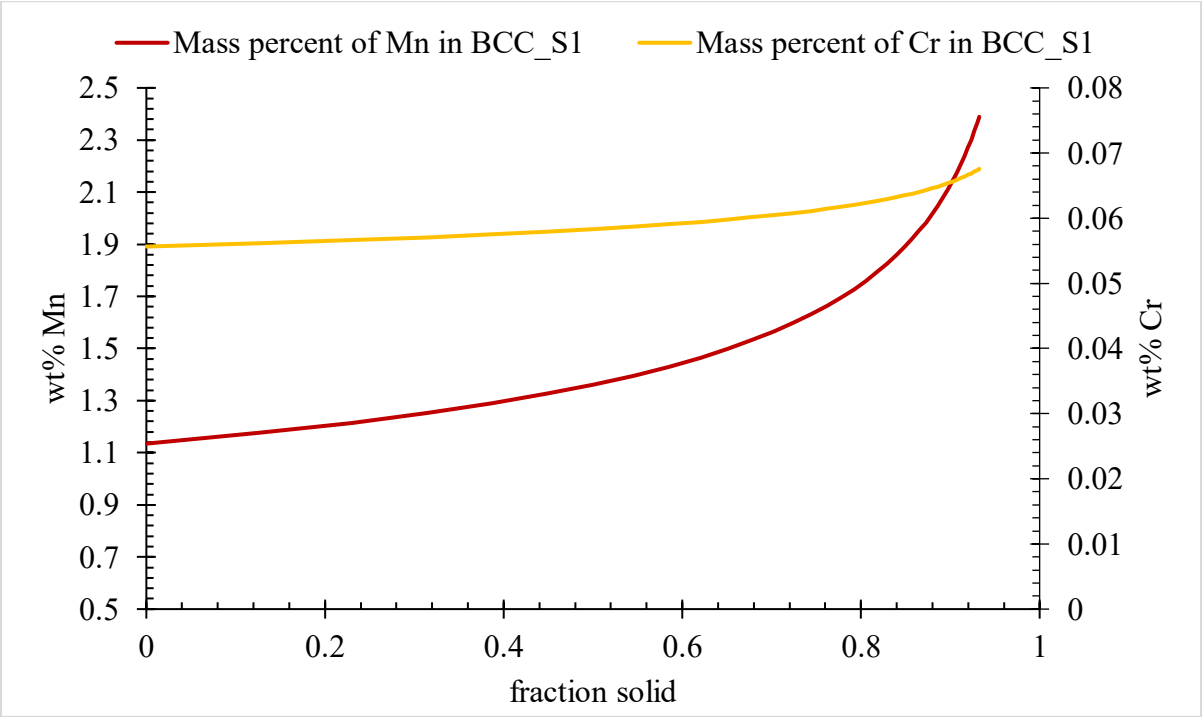

Fig. 4.18: Concentration profile of Mn and Cr for S1 calculated using the modified GS model.

4.3 Distribution of Nb in as-cast microalloyed steel slabs

This section contains the as-cast Nb EMPA maps and point scans obtained from the CL and QT locations of as-cast slabs S1 and S2. The observed distributions are discussed and are also compared with that of Mn in terms of the relative partition coefficients of Mn and Nb.

4.3.1 As-cast EMPA data for Nb from CL and QT samples of slab S1

The Nb distribution in the CL sample of S1 is shown in Figure 4.19. The original grayscale Nb map was completely dark in appearance with regions having a few very bright points. The

segregation pattern of Nb becomes apparent in the enhanced grayscale and enhanced inverted Nb maps (Figure 4.11-a and 4.11-b).

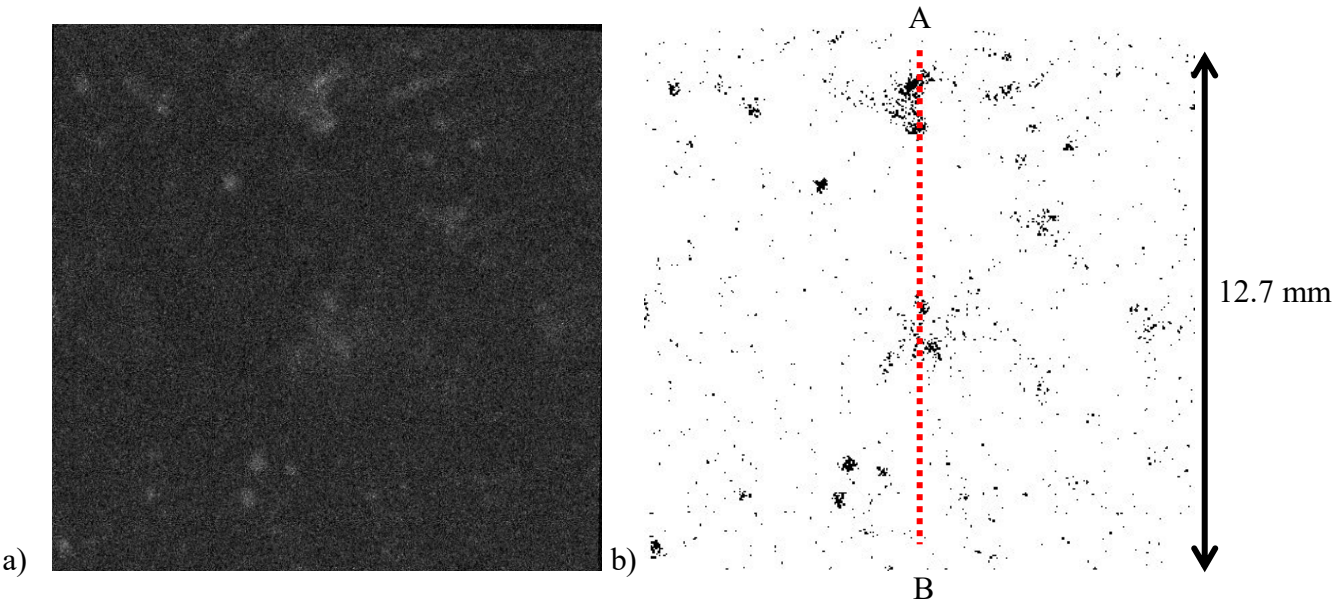

Fig. 4.19: As-cast a) enhanced grayscale and b) enhanced inverted Nb map from CL of S1.

The type of contrast in the Nb EMPA map suggests that some pixels (10 µm x 10 µm area) on the map (10000 µm x 10000 µm area) correspond to a very high concentration of Nb, which results in a large spatial concentration gradient and hence the observed contrast of the maps. This is further supported by the point scan measurements, shown in Figure 4.20-b, where some points have a high Nb concentration (1.06, 0.68 and, 0.32 wt%) while the majority of points have a low Nb concentration (less than 0.05 wt%). It is postulated that the high wt% Nb values are associated with NbC precipitates. As the interaction volume of EMPA point scans are larger than possible NbC precipitate volume; therefore, the high measured wt% Nb (1.06, 0.68 and, 0.32 wt%) in the EMPA point scans are not as high as the wt% Nb (88.57 wt%) in NbC precipitates. The low wt% Nb values (less than 0.05 wt%) are well below the nominal composition of Nb (0.075 wt%), suggesting that the solubility or partition coefficient of Nb in microalloyed steel is quite low. The variation in measured wt% Nb within the CL sample is 1.03 wt% (1.06 wt% - 0.03 wt%), which is the highest among Mn, Cr, Nb and P.

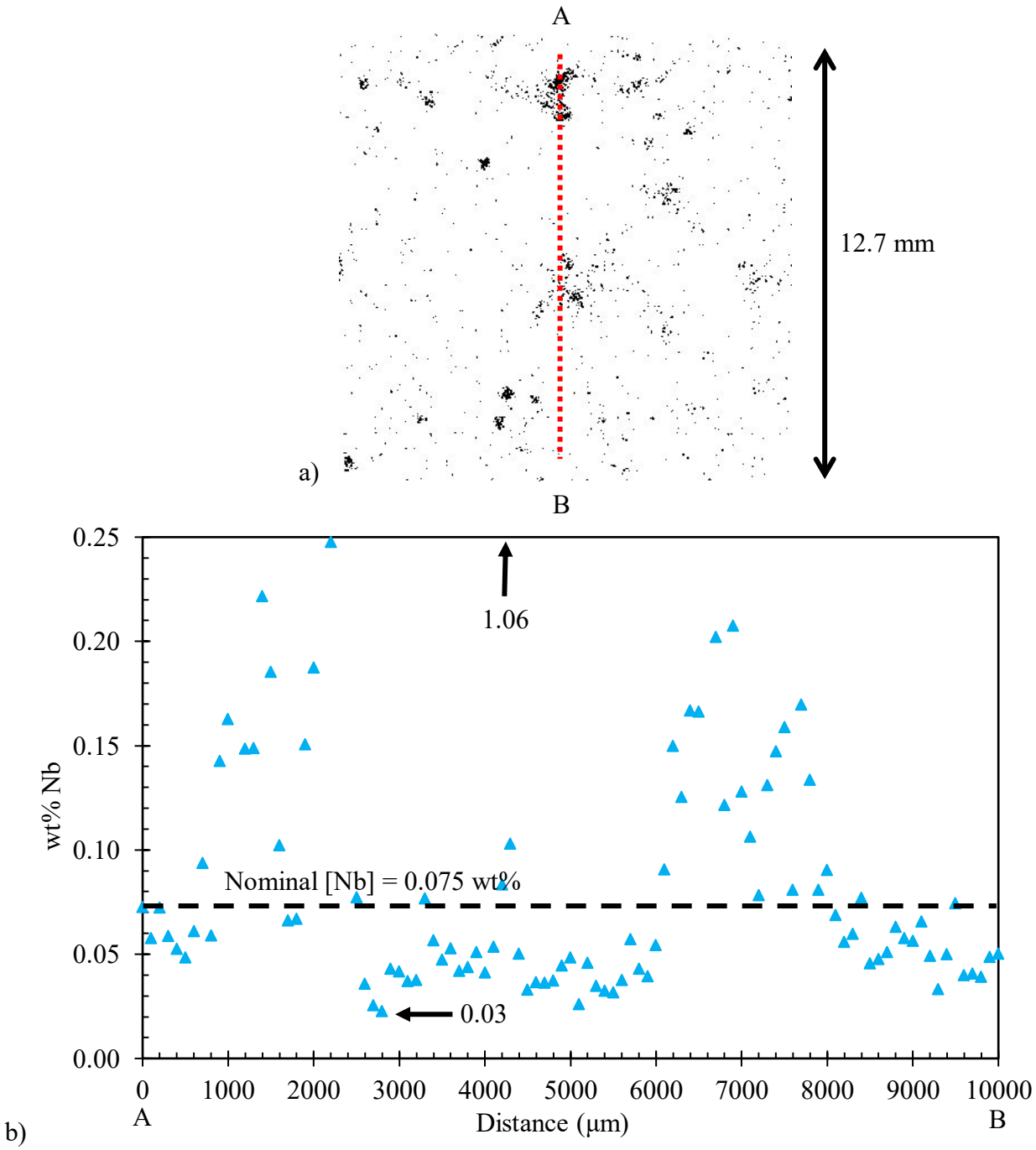

Fig. 4.20: a) As-cast EMPA enhanced grayscale map and b) line scan plot for Nb from CL of S1.

The enhanced inverted Nb distribution map from the QT sample of S1 is shown in Figure 4.21-a. Similar to the CL Nb map, the grayscale Nb map in QT sample was completely dark in appearance. The enhanced inverted Nb map revealed a dendritic distribution; however, the contrast is not as apparent as the enhanced maps in CL sample. Most of the measured point scan wt% Nb values are below the nominal concentration of Nb (0.075 wt%), with a few points showing higher

Nb concentration (0.19 and 0.18 wt%). The maximum and minimum measured wt % Nb values are 0.19 and 0.04, respectively, for the QT sample. The variation in measured wt% Nb is 0.15 within dendrites in the QT sample, which is considerably lower than the variation in the CL sample. This reconfirms the lower interdendritic contrast of the enhanced Nb map. The distributions of Nb in the CL and QT samples of S2 are similar to those in S1.

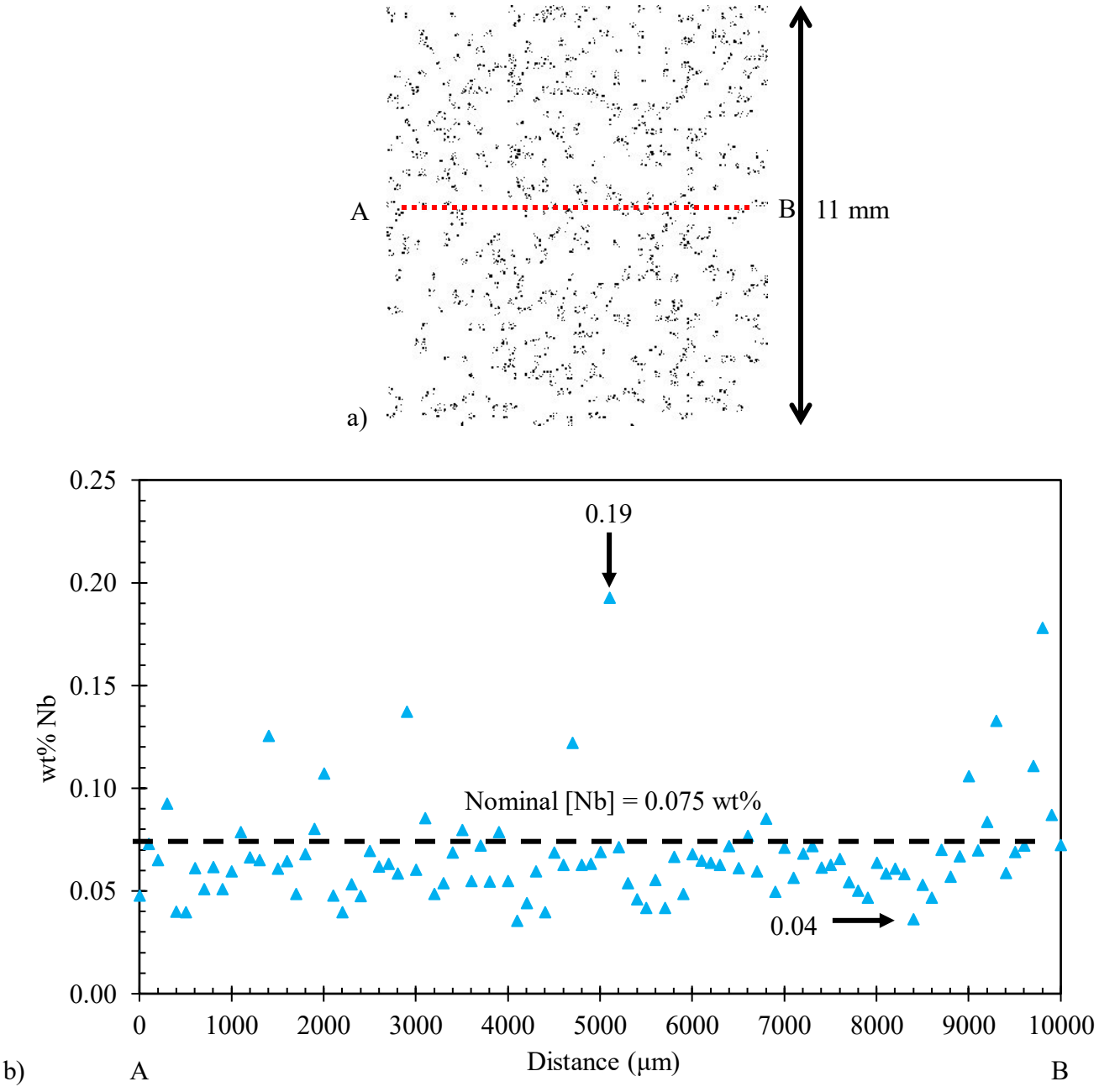

Fig. 4.21: a) As-cast EMPA enhanced inverted map and b) line scan plot for Nb from QT of S1.

4.3.2 Distribution of Nb in as-cast microalloyed steel slabs

The segregation pattern for Nb directly followed that of Mn. Figure 4.22 shows a comparison of as-cast enhanced inverted Mn and Nb EMPA maps from CL sample of slab S1. The location of segregated regions for both Mn and Nb are the same. However, a greater fraction of white space appears in the Nb inverted maps.

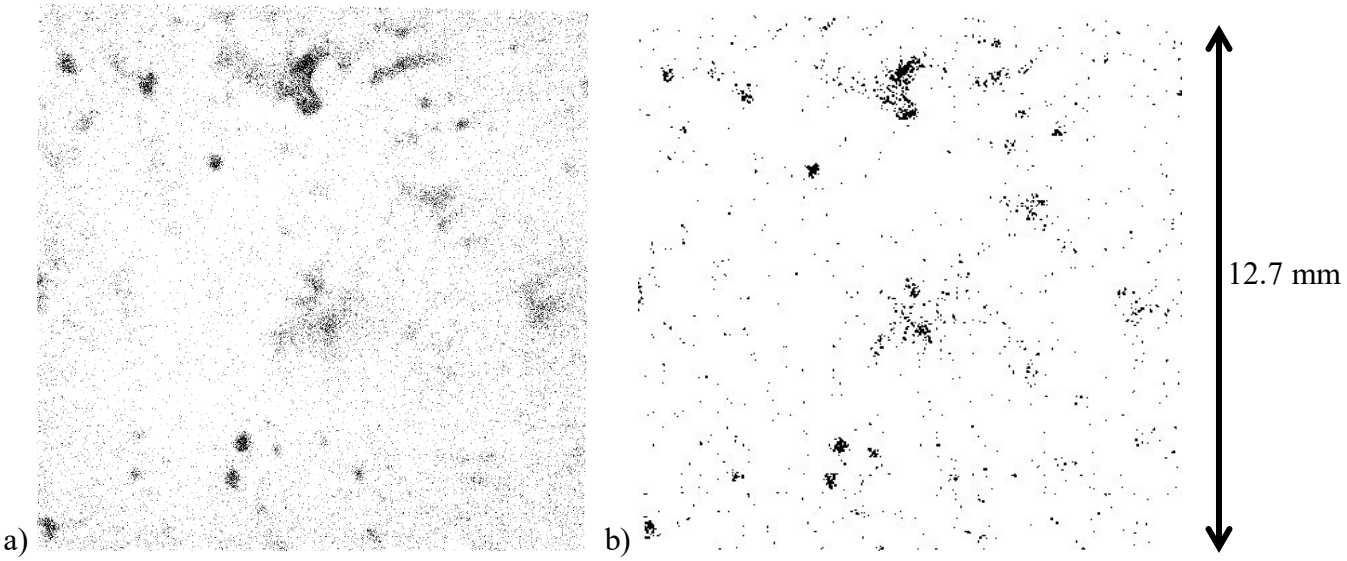

Fig. 4.22: As-cast EMPA enhanced inverted map for a) Mn and b) Nb from CL sample of slab S1.

The greater fraction of white space is due to a lower partition coefficient for Nb (0.21) than that for Mn (0.71). A lower k results in a smaller wt% of the element in the first solid that forms and so it takes longer for its segregation build up. Figure 4.23 shows the concentration of Mn and Nb versus fraction solid in S1 predicted through the modified GS model. The concentration of Mn reaches its nominal composition (1.59) at an earlier stage of solidification (f_s = 0.71), while Nb reaches its nominal composition (0.075) at a much later stage of solidification (f_s = 0.87). This implies that a larger area fraction of the Nb map will have a lower Nb content than the nominal composition of Nb. The precipitate forming nature of Nb can also be explained to some extent through the concentration profile of Nb. Since the majority of Nb is being rejected to the liquid, the Nb concentration in the liquid at the later stages (f_s > 0.70) of solidification becomes large enough to exceed the solubility limit and eventually result in precipitation.

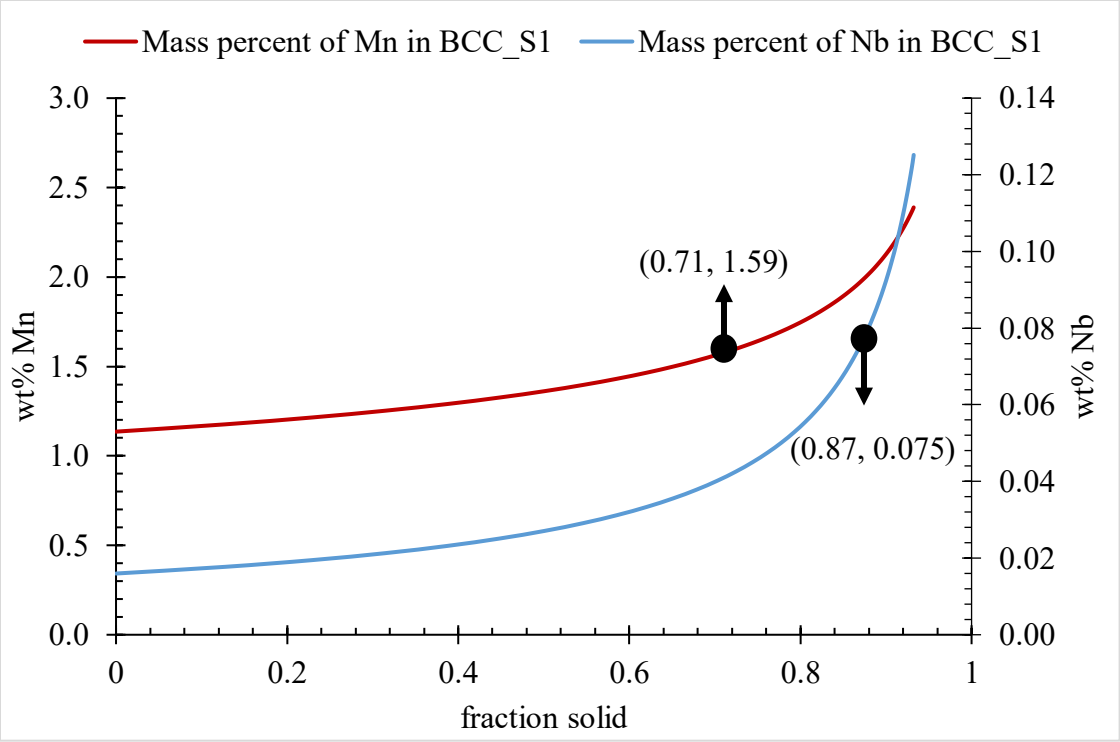

Fig. 4.23: Concentration profile of Mn and Nb for S1 calculated using the modified GS model.

4.4 Distribution of P in as-cast microalloyed steel slabs

This section presents the as-cast P EMPA maps and point scans obtained from the CL and QT locations of as-cast slab S2. Due to limited equipment time, P was not mapped for the as cast samples of S1; however, point scans were performed on both CL and QT samples of S1 to quantify the micro and macro S.R. values for P. The measured S.R. values for P are included in Section 4.5. The observed P distributions are discussed in terms of the relative partition coefficients of Mn, Cr, Nb and P in the steels. Figure 4.24-a shows the P EMPA enhanced inverted map from the CL sample of S2. For P, similar to Cr, there is no apparent segregation pattern visible in the map. The maximum and minimum measured wt% P for the CL sample are 0.033 and 0.000, respectively, as shown in Figure 4.24-b. The variation in measured wt% P for the CL sample is 0.033 wt%.

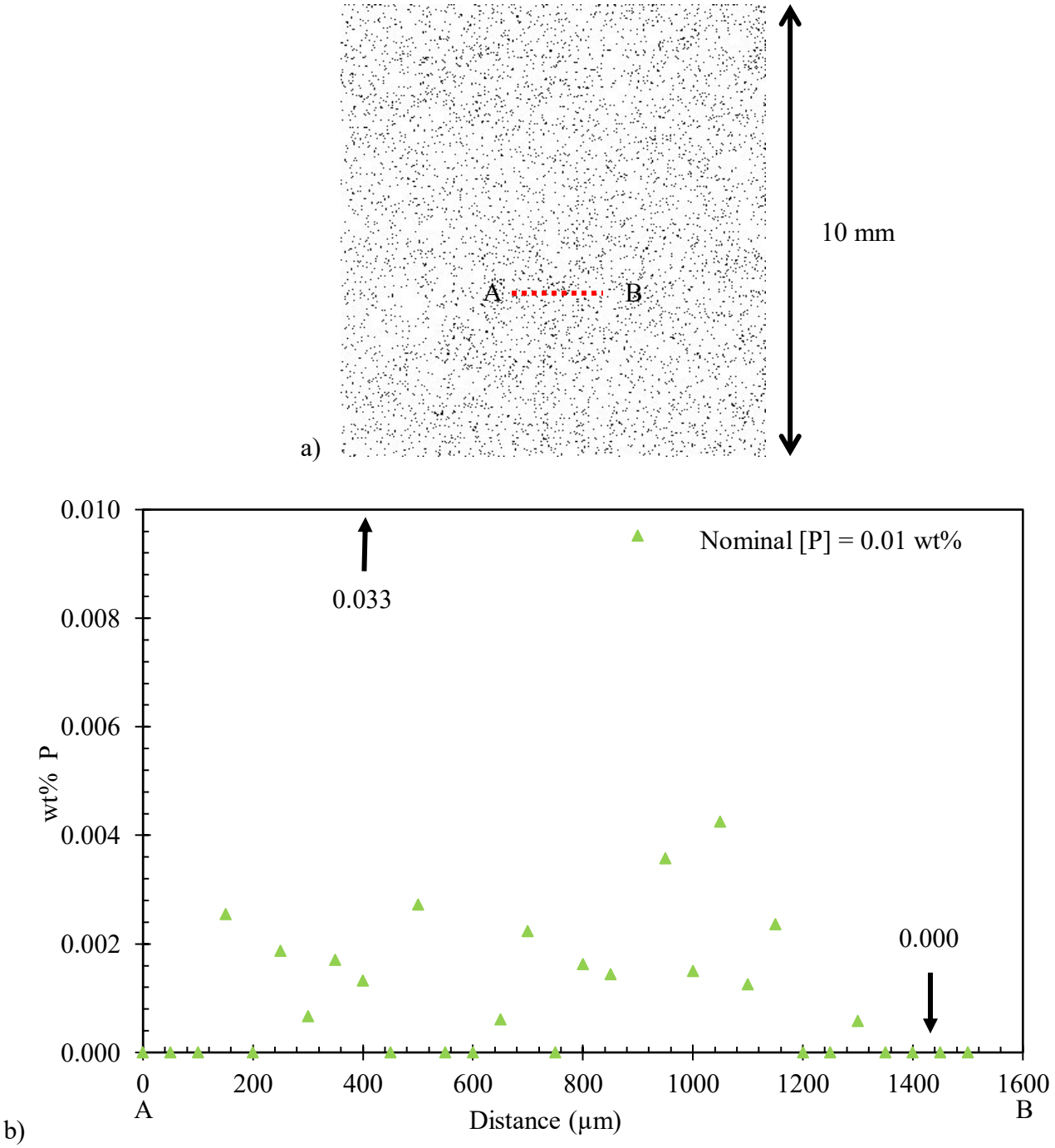

Fig. 4.24: a) As-cast EMPA enhanced inverted map and b) line scan plot for P from CL sample of S2.

The P EMPA enhanced inverted map from the QT sample of S2 is shown in Figure 4.25-a. No apparent segregation pattern is visible for P in the QT sample. The measured P in the interdendritic regions is below the nominal composition of P (0.01 wt%). The maximum and

minimum measured wt% P for QT sample are 0.009 (from another line scan) and 0.000, respectively. The variation in the measured value within QT sample is 0.009 wt% in the QT sample, which is considerably lower than that in the CL sample.

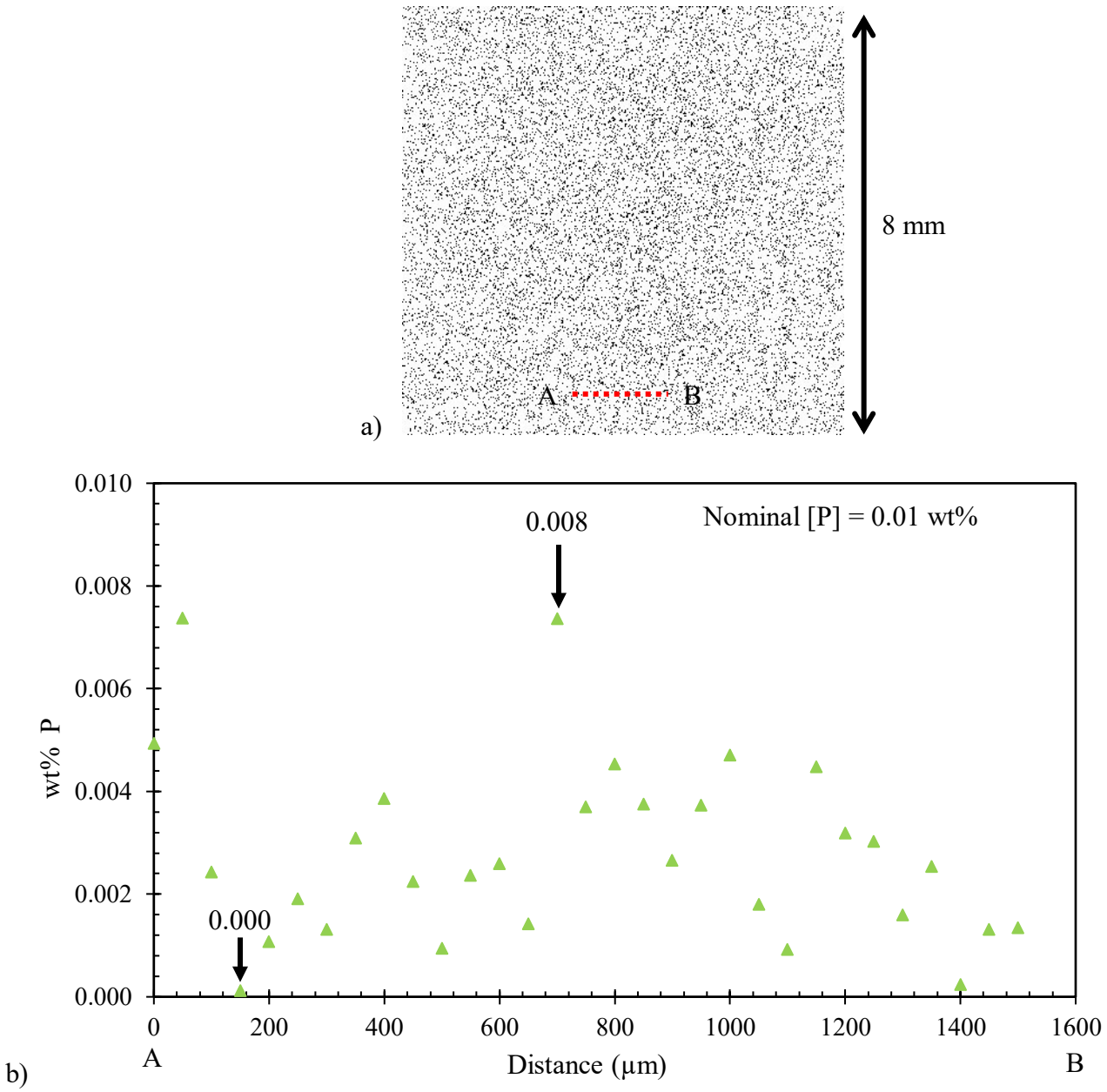

Fig. 4.25: a) As-cast EMPA enhanced inverted map and b) line scan plot for P from QT sample of S2.

P, similar to Nb, has a low k value (0.29); therefore, the expected concentration distribution of P should be the same as that of Nb. However, since P has a significantly higher diffusivity than

Nb, the concentration gradient of P is much lower than that for Nb because of P diffusion within the forming solid. The higher diffusivity of P is accounted for in the modified GS calculations by selecting P to be a fast diffuser. Another factor behind the low concentration gradient for P is its extremely low nominal concentration (0.01 wt%). A combination of high diffusivity and a low nominal content results in a small concentration gradient for P. Figure 4.26 shows the concentration of Mn and P versus fraction solid in S1 predicted through the modified GS model.

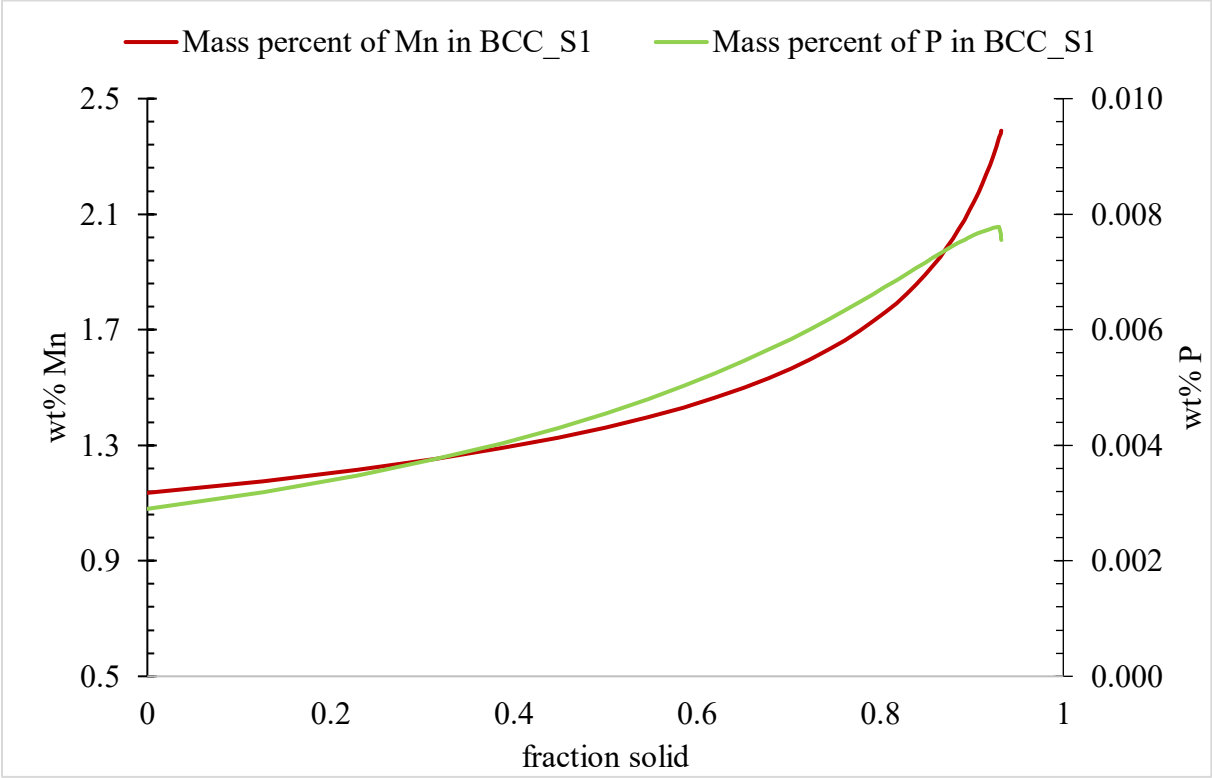

Fig. 4.26: Concentration profile of Mn and P for S1 calculated using the modified GS model.

4.5 Micro and macrosegregation ratios for Mn, Cr, Nb and P from S1 and S2

The degree of segregation for Mn, Cr, Nb and P is quantified in the regions of interest using point scans during EMPA. The measured wt% values are converted into segregation ratio for comparison of the elements and with steels of different composition. The microsegregation ratio is calculated as the ratio of maximum measured wt% value to the nominal composition in the QT sample and the macrosegregation ratio is calculated as the ratio of maximum measured wt% value to nominal composition in the CL sample for each alloying element. The calculated micro and macrosegregation ratios from both slabs are shown in Table 4.1 and 4.2, respectively.

Table 4.1: As-cast microsegregation (interdendritic) ratios for Mn, Cr, Nb and P in as-cast slabs S1 and S2.

Slab	Mn	Nb	P	Cr
S1	1.10	2.57	0.66	1.08
S2	1.09	1.69	0.90	1.04

Table 4.2: As-cast macrosegregation (centerline) ratios for Mn, Cr, Nb and P in as-cast slabs S1 and S2.

Slab	Mn	Nb	P	Cr
S1	1.45	14.13	3.90	1.13
S2	1.23	3.26	3.71	1.10

The results for as-cast micro and macrosegregation ratio measurements in slab S1 and S2 can be summarized as follows:

- The measured micro S.R. values for Mn (1.09) are the same for both the slabs.
- The measured micro and macro S.R. values for Cr are slightly higher in S1 compared with S2.
- The S.R. values for Mn are consistently higher than those for Cr in all samples.
- The micro S.R. for P is less than 1 in both slabs. Nb has the highest and P has the lowest measured S.R. values, except for the CL sample in S2, where P has a higher S.R. value than that for Nb.
- The macro S.R. values for Nb and P (>3) are significantly higher than those for Mn and Cr (<1.5).
- The measured macro S.R. values for Mn and Nb in S1 (1.45 and 14.13, respectively) are significantly higher than those in S2 (1.23 and 3.26, respectively).

The following sub sections discuss the measured individual Mn, Cr, Nb and P concentration for both as-cast slabs S1 and S2.

4.5.1 Mn segregation

Mn has an intermediate value for equilibrium partition coefficient (0.71) between BCC ferrite and liquid iron. Consequently, the extent of microsegregation ratio for Mn (1.10) is higher than that for Cr (1.03), but lower than that for Nb (1.69). Composition values as low as 1.41 wt% Mn in S1 and 1.18 wt% Mn in S2 were measured, which are below the nominal compositions of

Mn (1.59 wt% in S1 and 1.29 wt% in S2) in the respective slabs. The low measured values can be explained using the predicted concentration profile of Mn in the solid using the modified GS calculation. Figure 4.27 shows the evolution of Mn in both S1 and S2.

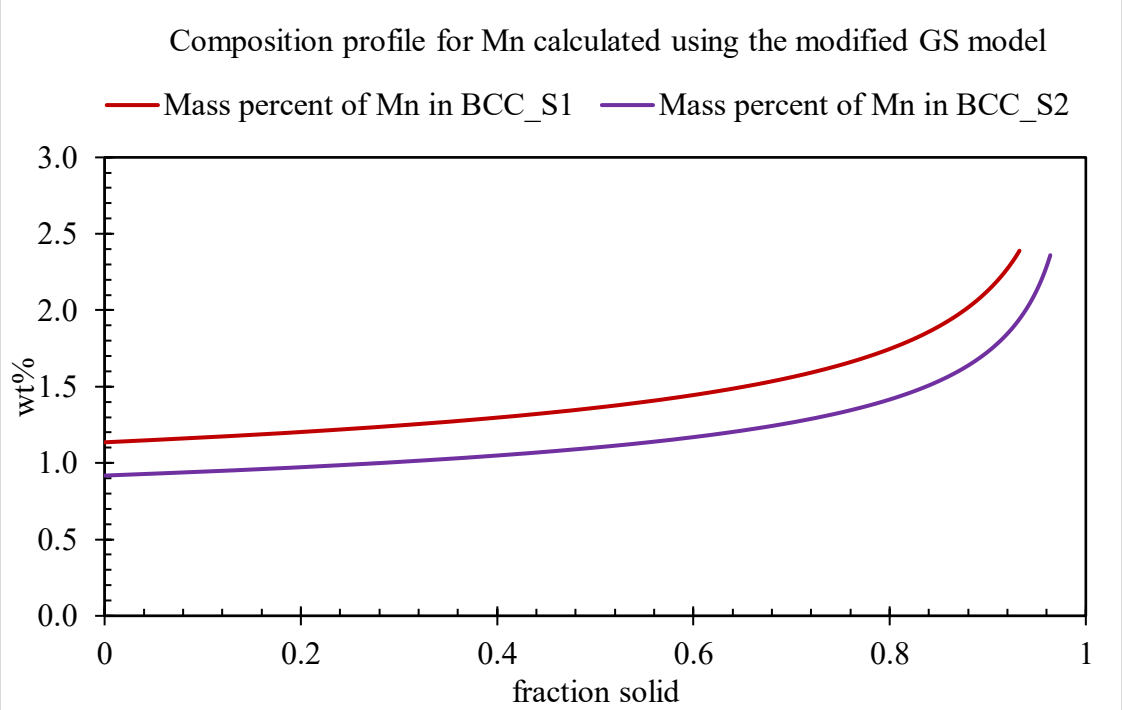

Fig. 4.27: Concentration profiles of Mn for S1 and S2 calculated using the modified GS model.

The predicted concentration profile for Mn in the solid using the modified GS calculation starts at 1.14 wt% Mn for S1 and 0.92 wt% Mn for S2. As such, the low measured wt% Mn values are justified. The measured values are not as low as the predicted Mn concentration due to diffusion of Mn that takes place within solid phase during casting; however, the predictions do not consider any diffusion in the solid phase once it forms. Therefore, the lowest measured values of Mn are higher than the predicted concentration of Mn in the first solid that forms. Figure 4.28 illustrates diffusion of Mn calculated for a binary Fe-Mn system. A step profile of Mn with initial concentration of 1.14 wt% and a final concentration of 2.30 wt% was defined in a 200 µm wide BCC region. The temperature was set to 1500°C and the simulation was run. It is evident from the simulation that wt% Mn increases from 1.14 to 1.4 in just 180 s at 1500°C. The predicted micro S.R. values for Mn (1.19 for both S1 and S2) are higher than the EMPA measurements (1.10 for S1 and 1.09 for S2), again due to the underlying assumption of no diffusion in the solid phase during GS calculations.

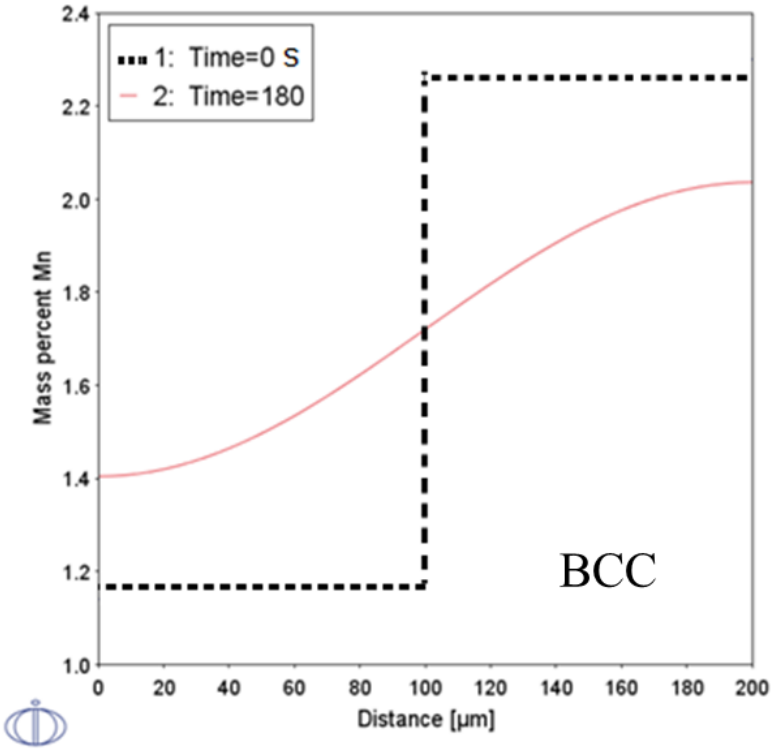

Fig. 4.28: Diffusion of Mn in BCC Fe phase at 1500°C.

Table 4.3 shows a comparison of micro and macro S.R. values for Mn with a previous study [243] of segregation in a continuous cast steel.

Table 4.3: As-cast micro and macrosegregation ratios for 3 different as-cast slabs.

Slab	Nominal Mn (wt%)	Microsegregation ratio for Mn	Macrosegregation ratio for Mn
S1	1.59	1.10	1.45
S2	1.29	1.10	1.23
Slab X[243]	1.50	1.37	1.87

The measured micro S.R. values for Mn are lower for S1 and S2 compared with the steel in the previous study. This is likely due to the lower C content for S1 and S2 (0.04 wt%) compared with slab X (0.17 wt%). It has been shown previously that an increase in the nominal C

concentration in a steel results in an increased degree of segregation for Mn [243, 317]. The measured macro S.R. is lowest for S2, which also has the lowest nominal Mn content. The macro S.R. values in S1 and S2 are considerably lower than for slab X due to the application of soft reduction.

4.5.2 Cr segregation

Cr has a high value of equilibrium partition coefficient (0.93) between BCC ferrite and liquid iron, which is the highest value among Mn, Cr, Nb and P. This suggests that the extent of segregation for Cr should be low and that the S.R. of Cr should be close to 1. The measured micro S.R. values for Cr for S1 (1.08) and S2 (1.04) correspond well with the postulation. ThermoCalc predicts a micro S.R. of 1.06 for both S1 and S2, which is close (within 5%) to the measured values. The measured macro S.R. values for Cr are 1.13 for S1 and 1.10 for S2. Similar values have been observed in previous chromium segregation studies [243, 248] as well.

4.5.3 Nb segregation

Nb has a low value of equilibrium partition coefficient (0.21) between BCC ferrite and liquid iron. Consequently, the predicted concentration profile of Nb (Figure 5.6) suggests that the amount of Nb in the solid stays below the nominal composition of Nb up to $f_s = 0.87$. Therefore, the predicted micro S.R. values for Nb at 0.85 f_s are below 1. The predicted micro S.R. values for Nb are 0.91 and 0.89 for S1 and S2, respectively, while the measured maximum micro S.R. values for Nb are 2.57 and 1.69 in S1 and S2, respectively. The measured values are considerably higher than the predicted values as Nb tends to form precipitates during solidification of the steel. The quantitative point scans do not ensure the measurement of Nb in solution in ferrite. Therefore, the measured segregation ratios using one maximum point for Nb does not necessarily lead to an understanding of the segregation behavior of Nb. The predicted concentration profile of Nb also suggests that the expected degree of segregation in the CL samples should be high, which corresponds well with the measured macro S.R. values (14.13 for S1 and 3.26 for S2) of Nb. Previous studies [318-320] on Nb segregation have also reported exceedingly high values of S.R. for Nb (3.71, 10.95 and 271.76) in steel compared to elements like Mn and Cr.

4.5.4 P segregation

Similar to Nb, the equilibrium partition coefficient of P (0.29) between BCC ferrite and liquid iron is low, which means that the solubility of P in delta iron is quite low and that majority of P will segregate at the centerline. However, the diffusivity of P is significantly higher than Nb,

which results in a low interdendritic concentration of P (<0.01 wt%) for most of the area fraction of the P EMPA maps. Since the diffusivity of P is accounted for in the modified GS model, the predicted micro S.R. values for P in S1 (0.72) and S2 (0.70) are close to the measured micro S.R. values (0.66 in S1 and 0.90 in S2) for P. The predicted micro S.R. values for P are below 1 for the same reason as for Nb. A few points with relatively high measured concentrations of P (> 0.03 wt%) in the CL samples also fit well with the presumption. A similar trend regarding the variation in segregation of P has been observed in previous studies [80, 108], where the degree of macrosegregation (CL region) of P was significantly higher than the degree of microsegregation (interdendritic region) of P.

4.6 Effects of soft reduction on segregation

Mechanical soft reduction was implemented during continuous casting of the steel slabs S1 and S2. The severity of macrosegregation is reduced as the mechanical forces from soft reduction causes redistribution of the remaining solute enriched liquid at the centerline. Table 4.4 shows a comparison of S.R. values of 3 slabs. The first 2 values are from S1 and S2, with the application of soft reduction during casting, and the third measurement (slab Y) is from a previous study [247], where the slab was cast without the application of soft reduction. The measured micro S.R. values for all 3 slabs are close (within 5%). The measured macro S.R. for slab Y (1.68) is higher than the values in slabs S1 (1.45) and S2 (1.23). The measurements suggest that soft reduction has a significant influence on the metallurgical center or the solidification structure near the centerline of continuous cast microalloyed steel slabs; however, soft reduction does not significantly influence microsegregation.

Table 4.4: As-cast micro and macrosegregation ratios for 3 different as-cast slabs.

Slab	Soft reduction?	Nominal C (wt%)	Nominal Mn (wt%)	Microsegregation ratio (QT location) for Mn	Macrosegregation ratio (CL location) for Mn
S1	Yes	0.04	1.59	1.10	1.45
S2	Yes	0.04	1.29	1.10	1.23
Slab Y[247]	No	0.05	1.58	1.14	1.68

4.7 ThermoCalc based segregation simulation results

This section presents the segregation calculation results from GS simulations for both S1 and S2. Two different approaches were used for the predictions; simple GS and modified GS. In the modified GS model, C, P and S were considered as fast diffusers, i.e., infinite diffusivity of C, P and S in the solid phase(s).

4.7.1 GS solidification of microalloyed steels

As mentioned in Section 2.7.1, temperature versus solid fraction plots were obtained using the simple GS and modified GS models for both steel S1 and S2. Figure 4.29 shows the temperature versus fraction solid plot for S1.

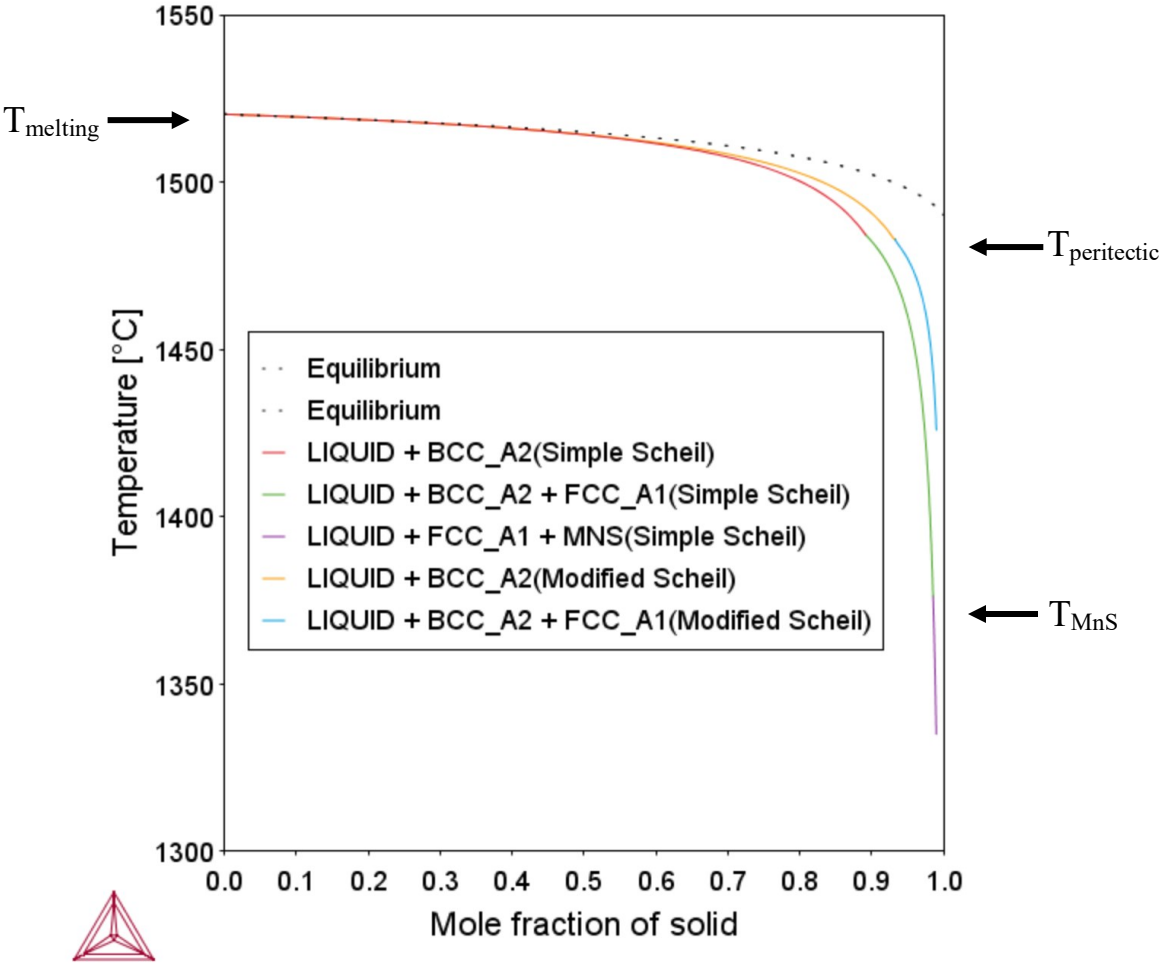

Fig. 4.29: Equilibrium and GS calculation plots for slab S1.

The black dotted line in the figure denotes equilibrium solidification, while the colored dotted lines denote the phase formation as per GS calculations. Different phases are represented

by different colors as per the legend inside the plot. The melting point and peritectic temperature for S1 calculated using the simple GS model are 1520°C and 1484°C, respectively, and the formation of MnS is predicted at 1376°C (98.5% solidification). The melting point and peritectic temperature calculated using the modified GS model are 1520°C and 1483°C, respectively, and unlike the simple GS model, the modified GS model does not predict the formation of any other phase such as MnS even at the end of solidification.

The melting point and peritectic temperature for S2 using the simple GS model are 1522°C and 1476°C, respectively, as shown in Figure 4.30. Similar to the simple GS calculation for S1, the formation of MnS is predicted for S2, but at 1397°C (98.0% solidification). The melting point and peritectic temperature calculated using the modified GS model are 1522°C and 1470°C, respectively. Similar to the modified GS calculation for S1, the modified GS calculations for S2 do not show the formation of any other phase such as MnS even at end of solidification.

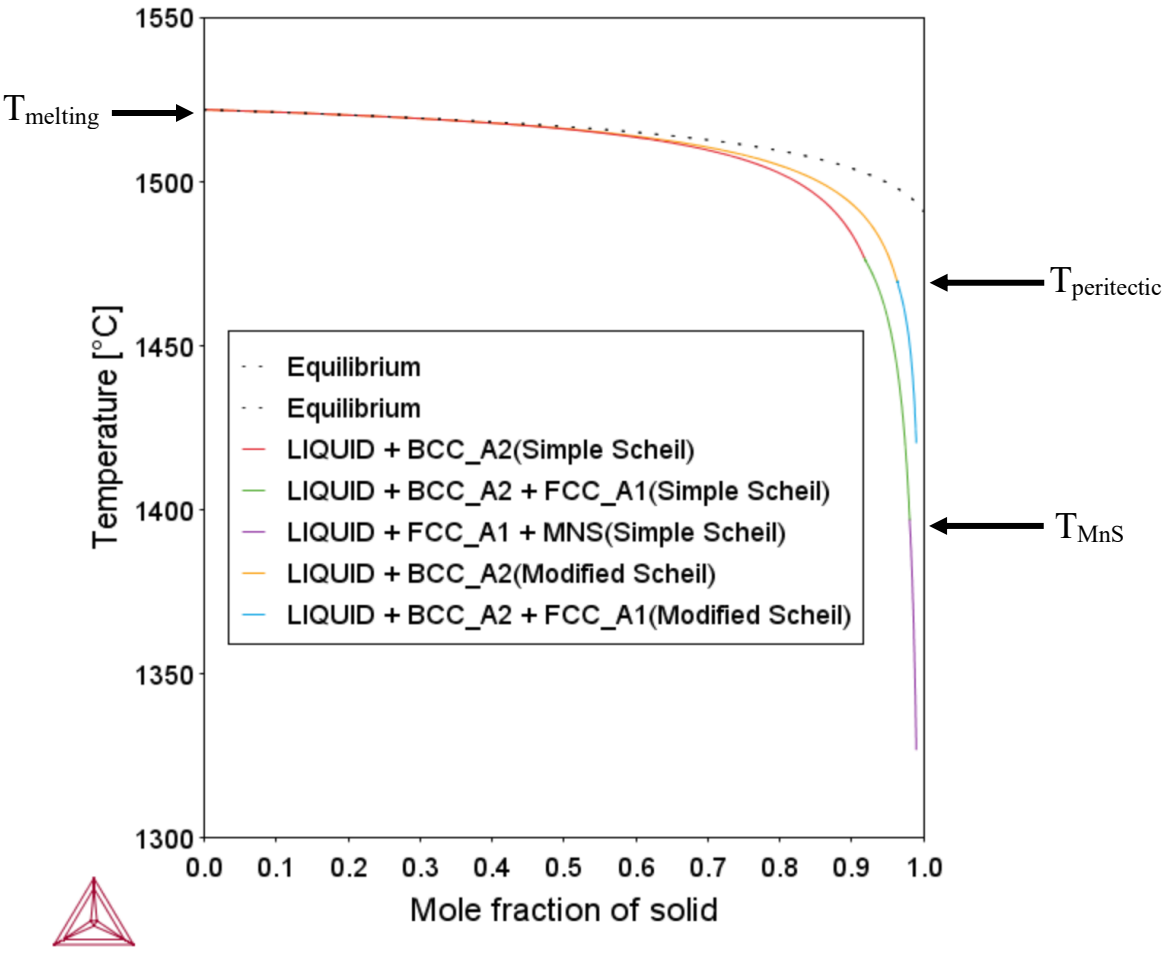

Fig. 4.30: Equilibrium and GS calculation plots for slab S2.

The difference in the predicted melting temperatures for S1 and S2 is negligible (2°C). The predicted peritectic temperature is slightly higher for S1. The difference in the predicted peritectic temperatures through both models is negligible for S1; however, a small difference (6°C) in the predicted peritectic temperature through both models is observed for S2. Since the phase transformation temperatures of steels are highly dependent on the C content, which is the same for both S1 and S2, the predicted temperatures being similar is justified. The predicted peritectic temperature is lower from the modified GS model for both steels. The solidification temperature range ($T_{melting} - T_{99.9\% solidification}$) is also smaller for the modified GS calculations for both steels. This is because of consideration of C as a fast diffuser for the modified GS calculations. In the modified GS calculations, S was also considered to be a fast diffuser. Consequently, the amount of S rejected in the remaining liquid as solidification proceeded was less compared with the simple GS calculations. Since the amount of S in the remaining liquid was lower for the modified GS calculations, MnS formation was not predicted.

4.7.2 Solute concentration evolution during solidification of microalloyed steels

As mentioned in Section 2.7.1, the composition profiles of solutes in all phases as a function of fraction solid were also obtained using the simple and modified GS solidification models. The profiles for Mn predicted through both the models for S1 are shown in Figure 4.31.

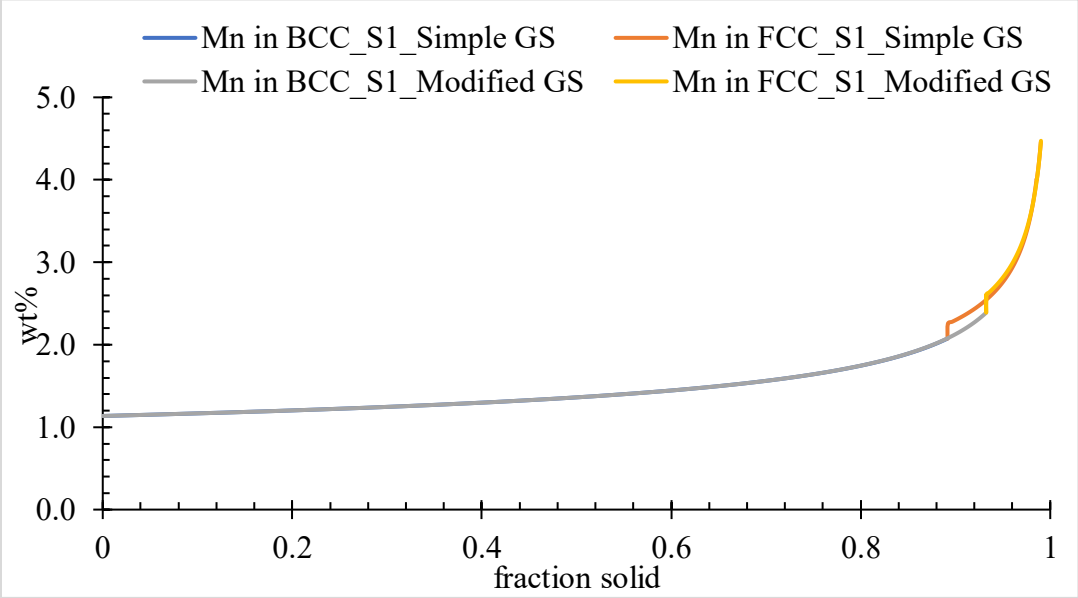

Fig. 4.31: Concentration profiles for Mn in solid phases of S1.

According to the predicted Mn profile, the first solid formed contains 1.14 wt% Mn and the concentration of Mn in the solid increases with increasing solid fraction. There is no visible difference in the predicted concentration profiles of Mn in the bcc phase up to 90% solidification through both the simple and modified GS models. For this work, the focus is only on the solute profiles in solids predicted through the GS models up to 85% solidification, i.e., fraction solid (f_s) = 0.85, as GS calculations are known to deviate at higher solid fraction [309]. The predicted concentration profiles for Mn are also similar using both models for S2. Like Mn, the predicted concentration profiles for Cr and Nb are similar using both models as well.

Figure 4.32 shows the concentration profile for P for S1 predicted using both simple and modified GS models. The predicted profiles start to deviate after f_s = 0.6, with a lower predicted concentration for the modified GS calculation. This is due to the consideration of P as a fast diffuser, since P diffuses considerably faster in steel as compared to Mn, Cr and Nb.

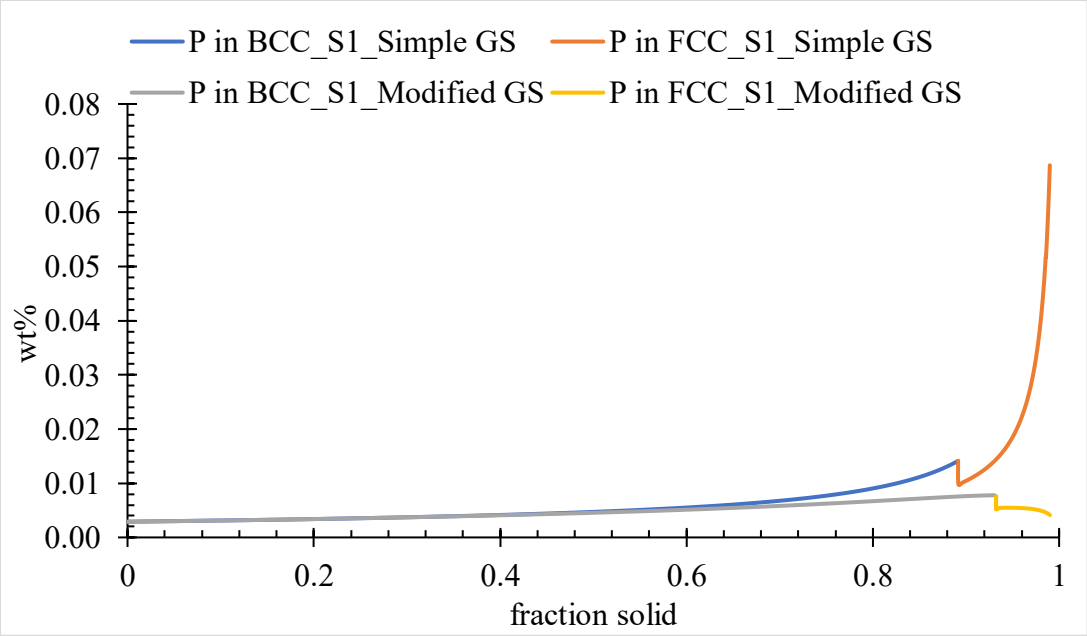

Fig. 4.32: Concentration profiles for P in solid phases of S1.

Since there is no considerable difference between the simple and modified GS calculation for Mn, Cr and Nb and the modified GS calculations predict a profile closer to the EMPA measurements of P, the modified GS values are considered for comparison in the sections that follow.

Figure 4.33 shows the equilibrium partition coefficient (k) variation for Mn in both S1 and S2 calculated through the modified GS model. The equilibrium k values were calculated as the ratio of concentration of Mn in BCC solid to that in liquid. The equilibrium partition coefficient for Mn (k_{Mn}) decreases for both S1 and S2 as solidification proceeds, with k_{Mn} being slightly smaller for S2. Since k is not constant, the k value at fraction solid of 0.5 is used for comparison purposes.

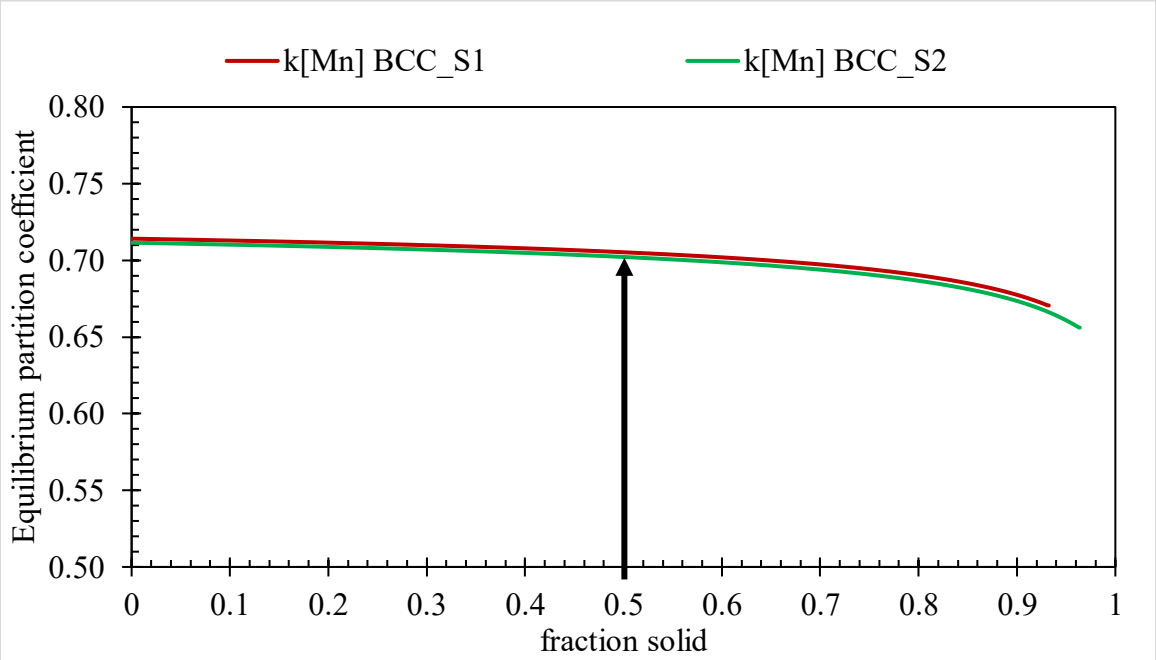

Fig. 4.33: Variation of equilibrium partition coefficient of Mn for S1 and S2 calculated using the modified GS model.

Similar to Mn, the equilibrium partition coefficients were calculated for Cr, Nb and P. The calculated values are listed in Table 4.5.

Table 4.5: Equilibrium partition coefficient for Mn, Cr, Nb and P for S1 and S2 calculated using the modified GS model.

	Mn	Cr	Nb	P
S1	0.71	0.93	0.21	0.29
S2	0.70	0.93	0.21	0.28

4.7.3 Comparison of as-cast EMPA measurements with GS calculations

This section contains the comparison of predicted microsegregation ratio values for Mn, Cr, Nb and P using the modified GS calculations with the EMPA segregation measurements. Tables 4.6 contains the predicted microsegregation ratio values for Mn, Cr, Nb and P using the modified GS model for both slab S1 and S2.

Table 4.6: Predicted microsegregation ratios for Mn, Cr, Nb and P in S1 and S2 using the modified GS model.

	Mn	Cr	Nb	P
S1	1.19	1.06	0.91	0.72
S2	1.19	1.06	0.89	0.70

The predicted micro S.R. values are lowest for P followed by Nb, Cr and Mn. The predicted microsegregation ratios for Mn (1.19) and Cr (1.06) are the same for both the simple and modified GS calculations for both S1 and S2. The predicted micro S.R. for Nb in S1 (0.91) is slightly higher than that in S2 (0.89). For P, similar to Nb, the micro S.R. in S1 (0.72) is slightly higher than that in S2 (0.70). Since the C content of both S1 and S2 are the same, and the segregation ratio is calculated relative to the composition of individual elements in the alloy, both S1 and S2 have similar predicted microsegregation ratio values.

The measured and predicted micro S.R. values for Mn, Cr, Nb and P using the modified GS approach for both S1 and S2 are shown in Table 4.7. The predicted micro S.R. values for Mn and Cr differ by less than 10% from the measurements, with the predicted values being higher than the measurements. This suggests that finite diffusion of Mn and Cr should be taken into account. The measured microsegregation ratio of P in S1 (0.66) is significantly lower than in S2 (0.90) and in the sample homogenized for 3 h at 1000^{o}C (1.10). This suggests that the highest P concentration point in the as-cast sample of S1 was missed during point scan measurement, which is another limitation of using a single point quantitative measure. Considering a similar extent of micro S.R. of P in S1 as in S2, it can be said that the modified GS model predicts a lower S.R. for P than the measurements. This indicates that finite diffusion of P should also be considered instead of infinite diffusion of P. The measured values of Nb are significantly higher than the predicted values because of Nb precipitates encountered during point scan measurements. Since the point scan

measurements do not correlate with the solid solution content of Nb, a direct comparison between the segregation models and Nb measurements can not be made.

Table 4.7: Measured and predicted micro S.R. values for Mn, Cr, Nb and P in steels S1 and S2.

	Mn	Cr	Nb	P
S1 (measured)	1.10	1.08	2.57	0.66
S1 (predicted)	1.19	1.06	0.91	0.72
S2 (measured)	1.09	1.04	1.69	0.90
S2 (predicted)	1.19	1.06	0.89	0.70

5. Unidirectional solidification of microalloyed steel

The EMPA results from directionally solidified Bridgman samples are presented and discussed in this chapter. Segregation evaluation has been done using the partition coefficient calculations. The effect of change in cooling rate on the partition coefficient (k) and, hence, the segregation of Mn, Cr, Nb and P in microalloyed steel is evaluated. The measured k values are compared with the segregation calculation results from GS simulations. Trends and values observed in the EMPA results are also compared with the available literature in the field of directional solidification of steels.

5.1 Distribution of Mn in directionally solidified microalloyed steel

The Mn EMPA maps from different sections of Bridgman sample 1 are shown in Figure 5.1.

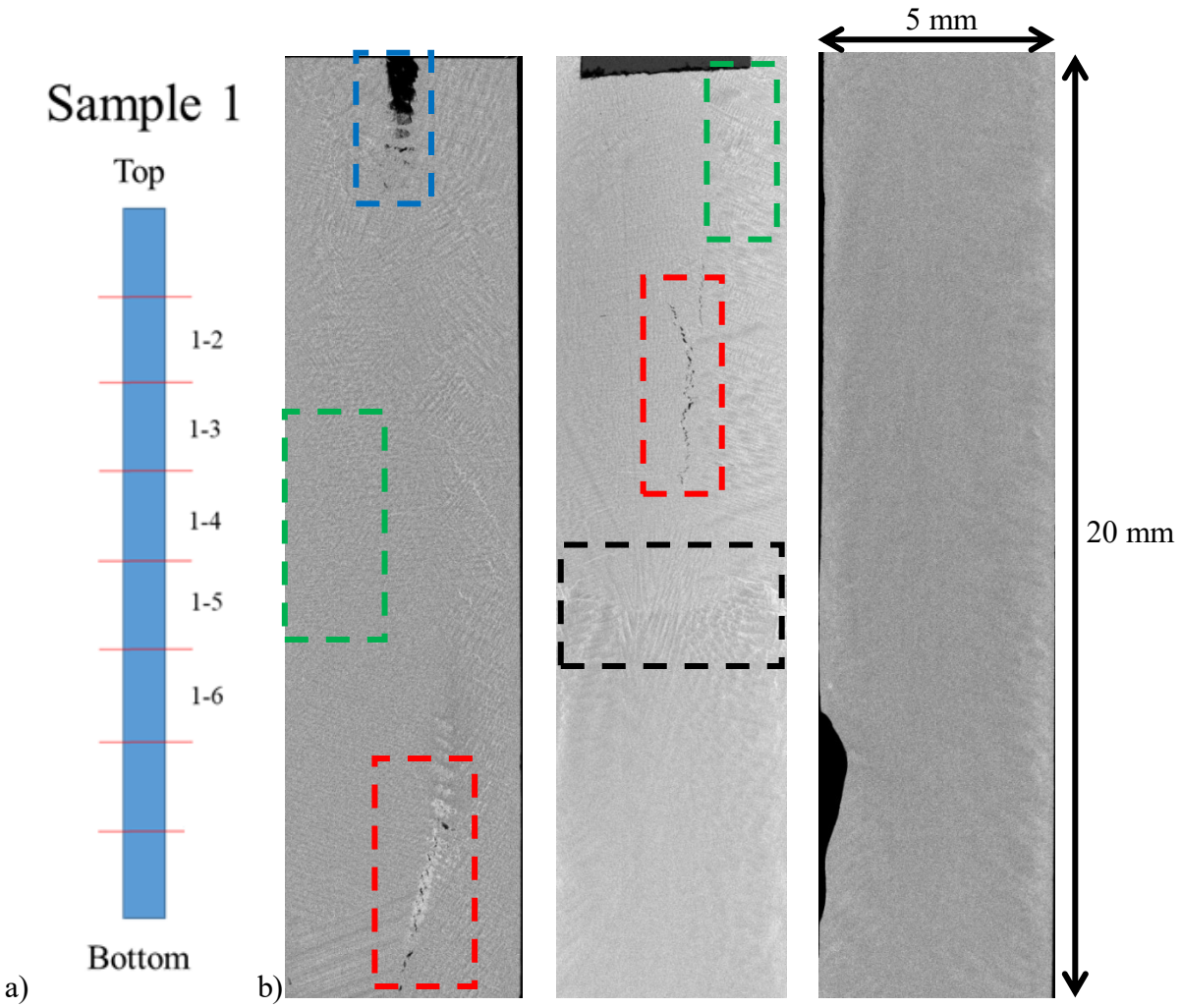

Fig. 5.1: a) Bridgman sample sectioning and b) EMPA Mn maps for samples 1-2, 1-4 and 1-6.

Figure 5.1-a illustrates sample sectioning and nomenclature used for the Bridgman samples. There are some solidification defects, such as cracks (shown in Figure 5.1 by red dotted rectangles) and porosities (shown in Figure 5.1 by blue dotted rectangles) in the samples. The solid liquid interface is visible in sample 1-4 (shown in Figure 5.1 by black dotted rectangle). The Mn distribution above the interface is dendritic, while the distribution below the interface does not represent any well defined solidification structure. A significant amount of dendritic growth is also observed from side wall of the samples as shown in Figure 5.1 by the green dotted rectangles. The black rectangular region at the top of the EMPA maps in samples 1-4 is from the copper tape applied to ensure electronic conductivity and avoid any charging of samples during EMPA.

Figure 5.2 shows a comparison of the Mn distribution in Bridgman samples 1-4 and 2-4 solidified at cooling rates of 0.4°C/s and 0.2°C/s, respectively. Samples 1-4 and 2-4 have a similar distribution of Mn which suggests that the qualitative distribution of Mn does not change during directional solidification in the 0.2-0.4°C/s cooling rate range. A similar trend was also observed for Cr, Nb and P EMPA maps.

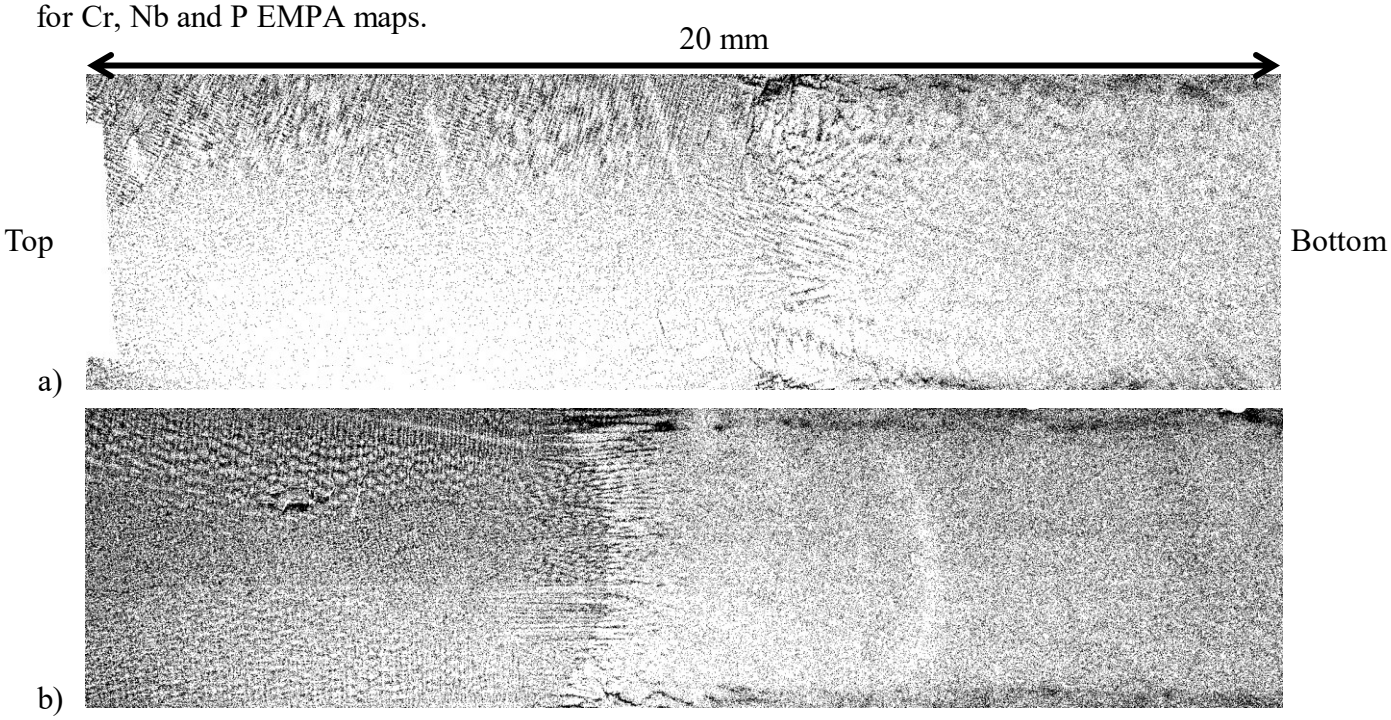

Fig. 5.2: Enhanced inverted Mn map for Bridgman samples a) 1-4 and b) 2-4.

5.2 Distribution of Cr, Nb and P in directionally solidified microalloyed steel

Figure 5.3 shows a comparison of the Mn, Cr, Nb and P distributions in Bridgman sample 2-4. Similar to the as-cast samples, the solidification structure is most apparent for the Mn map. The Cr map shows the lowest concentration gradient because of the relatively high partition coefficient for Cr. The Nb and P maps have similar distributions as Mn; however, the distributions are not as apparent as Mn because of the lower partition coefficients and lower nominal compositions for Nb and P compared with Mn in the studied steel. Similar to the as-cast samples, the observed distributions of Mn, Cr, Nb and P in the Bridgman samples correlate well in terms of their relative k values (Table 4.5).

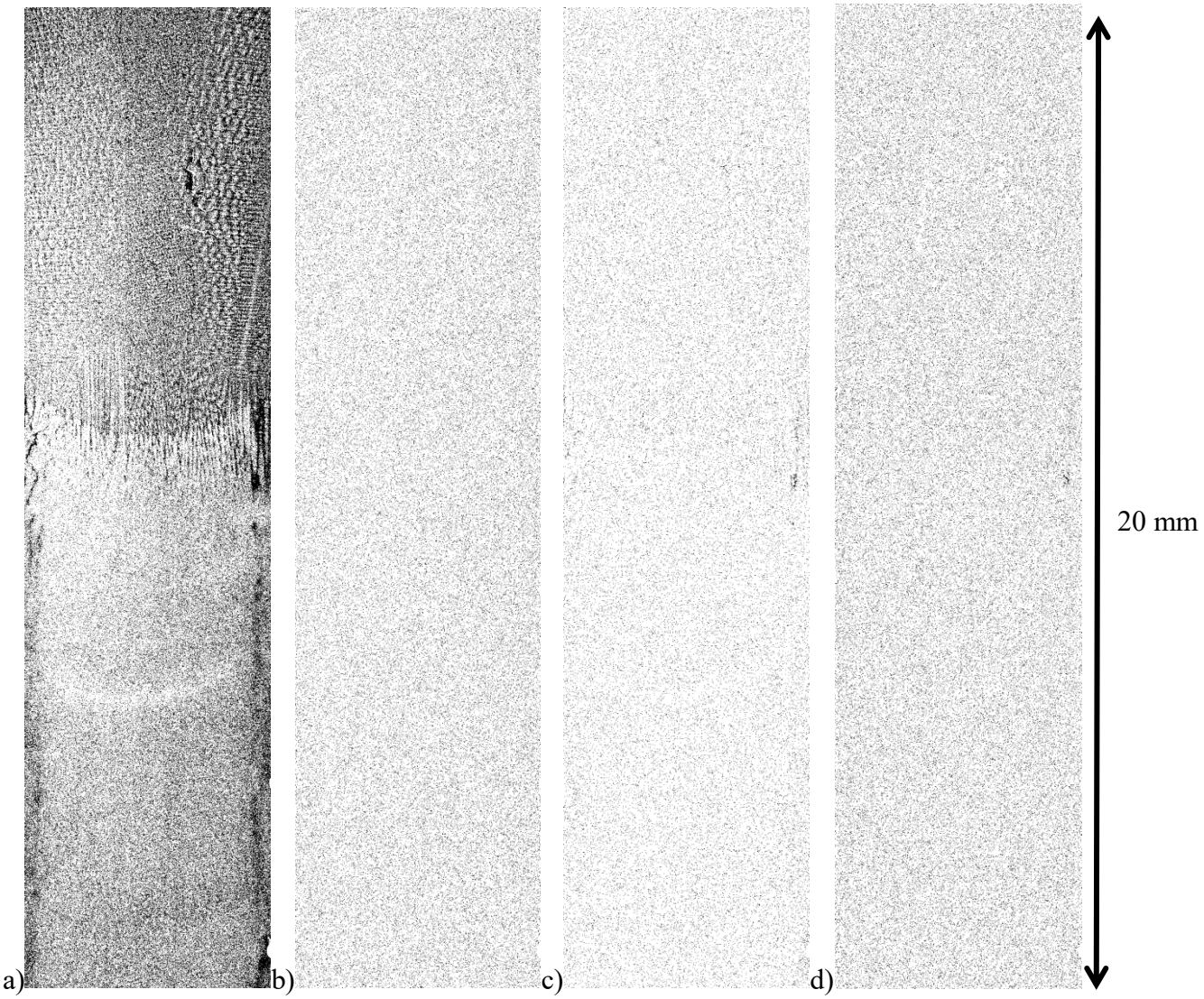

Fig. 5.3: Enhanced inverted EMPA maps for a) Mn, b) Cr, c) Nb and d) P for Bridgman sample 2-4.

5.3 Effect of cooling rate on partition coefficient in microalloyed steel

The composition values from area enclosing the solid-liquid interface was used to obtain the required data for partition coefficient calculations after these maps were converted into concentration maps using the method explained in Section 3.4.5. Table 5.1 shows the calculated k values for Mn, Cr and P distributions in Bridgman samples.

Table 5.1: Calculated partition coefficients for Mn, Cr and P.

Sample	Cooling rate (°C/s)	k_{Mn}	k_{Cr}	k_P
1	0.4	0.913	0.927	0.249
2	0.2	0.910	0.886	0.169

The calculated k is highest for Cr followed by Mn and P. The partition coefficient for all elements is lowest for sample 3. For Mn and Cr, the values are slightly lower in sample 2. The difference in k between sample 1 and 2 is largest for P (0.249-0.169 = 0.080). For each element, the partition coefficients decreases with a decrease in cooling rate from 0.4°C/s to 0.2°C/s. The partition coefficients for Mn (0.913 and 0.910) and Cr (0.927 and 0.886) were significantly higher than the values for P (0.169 and 0.249), which matches well with the previously reported [73, 309, 320, 323] values of experimentally obtained partition coefficients in Fe-based alloys. As mentioned in Section 2.3, slower cooling results in a larger dendrite arm spacing and, hence, a higher degree of microsegregation. This correlates well with the decrease in the observed k values. The partition coefficient of Nb could not be calculated because of the nature of Nb distribution in the obtained EMPA maps. The following explains the limitation of k calculation for Nb.

Figure 5.4 shows the EMPA Nb map and a magnified version of a part of it. It is visible from the map of Nb, that a few pixels are significantly brighter than the rest of the pixels on the Nb map. The few pixels/locations (10 µm x 10 µm) which have a significantly higher concentration of Nb are likely precipitates of Nb. Consequently, the relative X-ray counts corresponding to the low wt% Nb regions are extremely low. Since the grayscale values corresponding to the EMPA maps vary between 0-255, the X-ray counts are scaled accordingly. This leads to a loss of the actual variation of composition of Nb and results in a false k value for Nb.

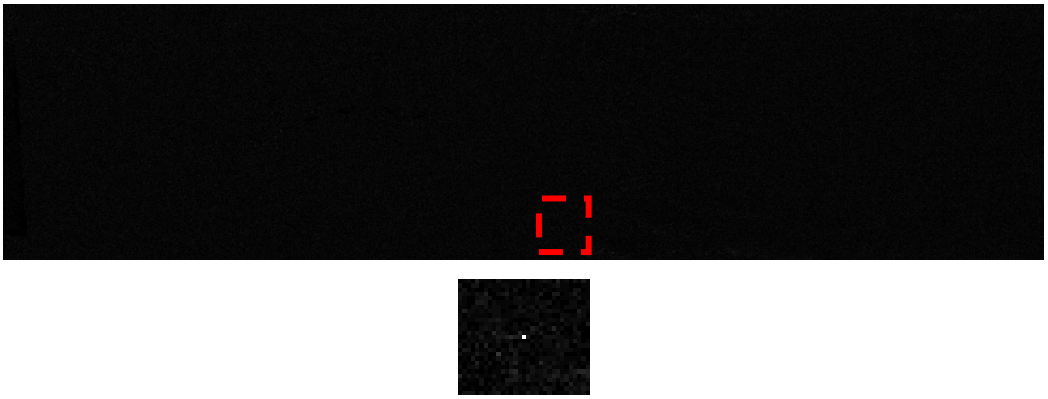

Fig. 5.4: EMPA original grayscale Nb map for Bridgman sample 1-4 and a magnified view of the region enclosed by the red dotted rectangle.

Table 5.2 shows a hypothetical example to illustrate the aforementioned. When the Nb maps are converted into concentration contours using the image conversion method mentioned in Section 3.4.5, the resulting wt% distribution is also as per the scaled grayscale values and not the original X-ray count. Therefore, the resulting k for Nb is for the scaled data (0, 0, 0, 255, 1, 1, 1) and not for the original relative distribution data (0.1, 0.2, 0.3, 255, 0.8, 0.9, 1.0), which eventually results in a false k for Nb. Therefore, the k values for Nb are not reported.

Table 5.2: Illustration of EMPA mapping process for Nb.

Location	X-ray counts	Relative X-ray counts	Scaled grayscale values
1	10	0.1	0
2	20	0.2	0
3	30	0.3	0
4	25500	255	255
5	80	0.8	1
6	90	0.9	1
7	100	1.0	1

6. Homogenization of microalloyed steel

This chapter presents the results from homogenization of CL and QT samples of S1 at 1000ºC, 1100ºC and 1200ºC for 3, 6 and 12 h. The measured changes in segregation ratio values for Mn, Cr, Nb and P are also compared with DICTRA based homogenization simulations and with previous work on steel homogenization.

6.1 Qualitative assessment of homogenized samples

Figure 6.1 and 6.2 show a comparison between Mn EMPA maps of as-cast and homogenized samples from the CL and QT locations of S1. The only visible difference between the EMPA maps is the oxidation ring along the boundary of the EMPA maps of the homogenized samples. Oxidation of steel occurs during heating to elevated temperatures (>700ºC). The relative amount of oxidation in samples homogenized for 12 h is more than that in samples homogenized for 6 h, as evident from Figure 6.1-b and Figure 6.2-b. A similar oxidation trend has been observed in previous oxidation studies [315, 316] of steel. The distribution of Cr, Nb and P also showed similar trends to Mn for as-cast and homogenized samples.

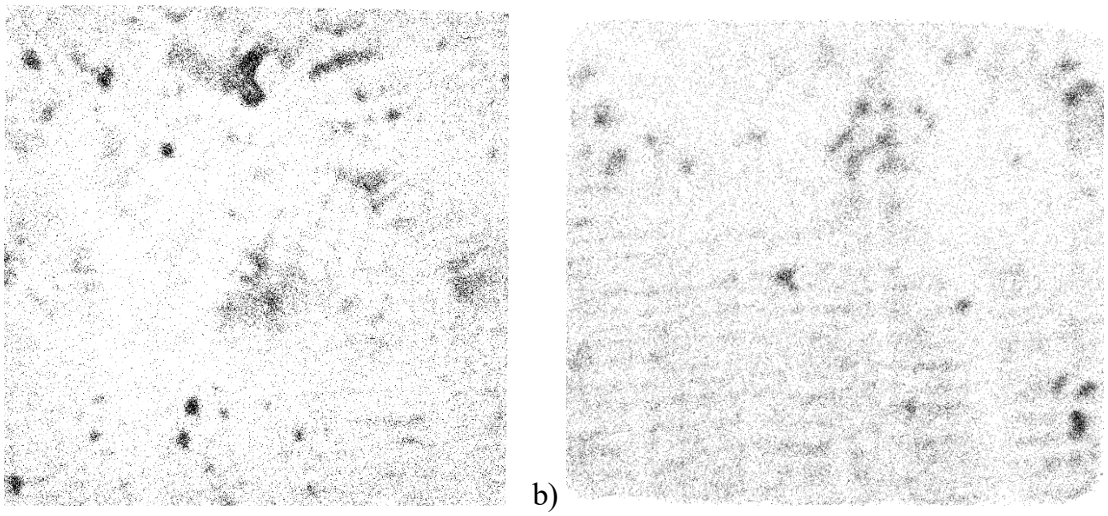

Fig. 6.1: Enhanced inverted Mn map from CL location of S1 a) as-cast; b) homogenized at 1200ºC for 6 h.

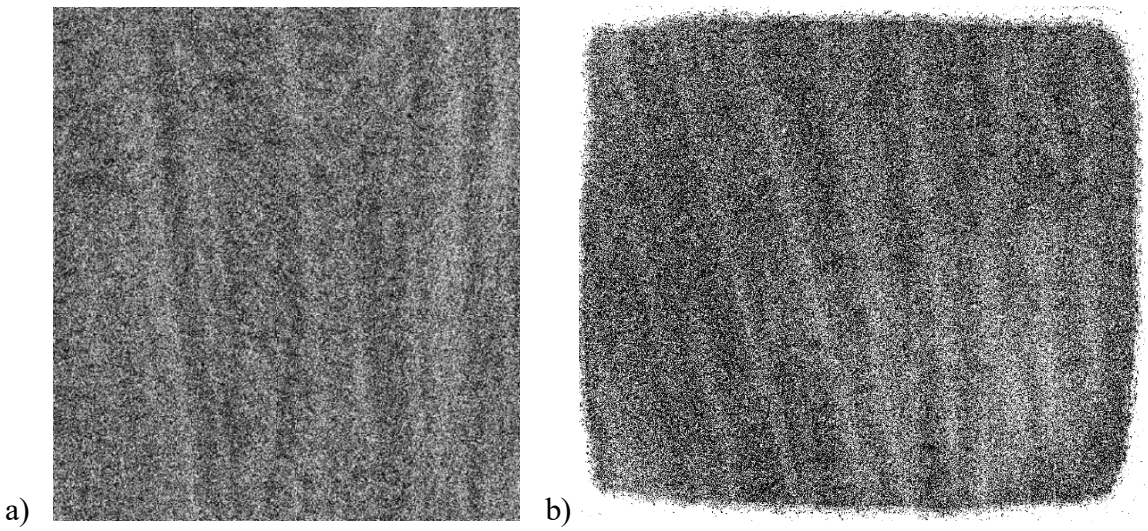

Fig. 6.2: Enhanced inverted Mn map from QT location of S1 a) as-cast and b) homogenized at 1200ºC for 12 h.

6.2 Quantitative assessment of homogenized samples

The distribution of Mn in CL samples of S1 homogenized under two extreme cases (1000ºC for 3 h and 1200ºC for 6 h) is shown in Figure 6.3. The maximum measured wt% value of Mn after homogenization at 1000ºC for 3 h and 1200ºC for 6 h are 2.32 and 1.94, respectively. The increased number of data points in Figure 6.3-b is because of a closer point scan spacing used during this measurement. Similar to Mn, the maximum measured wt% values for each element were noted and converted into segregation ratios using Equation 2.2.

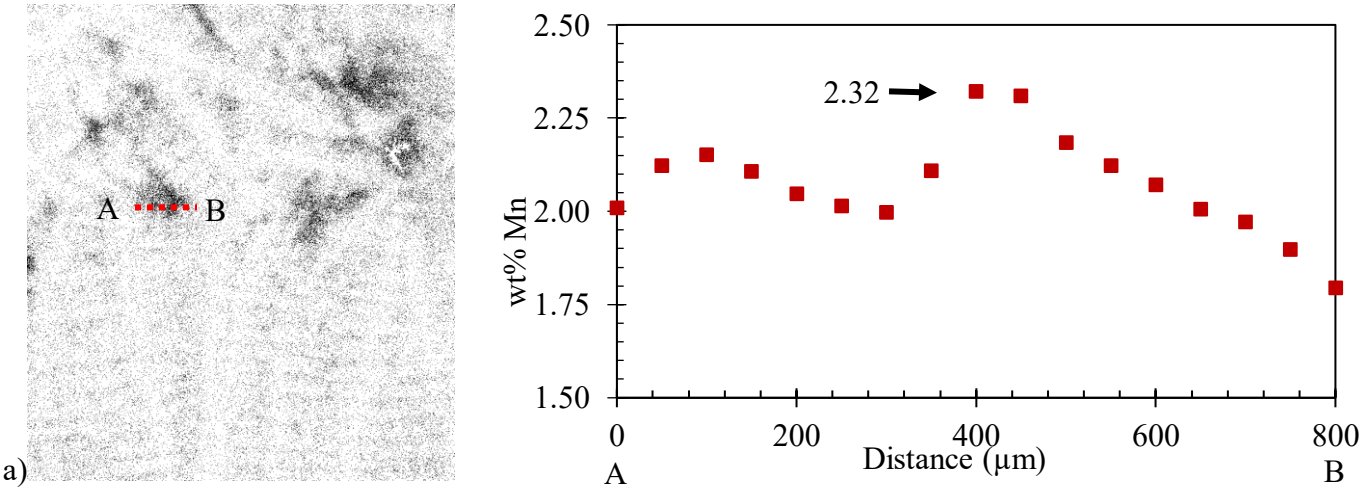

Fig. 6.3: a) Enhanced inverted Mn map and wt% distribution from CL location of S1 homogenized at 1000ºC for 3 h.

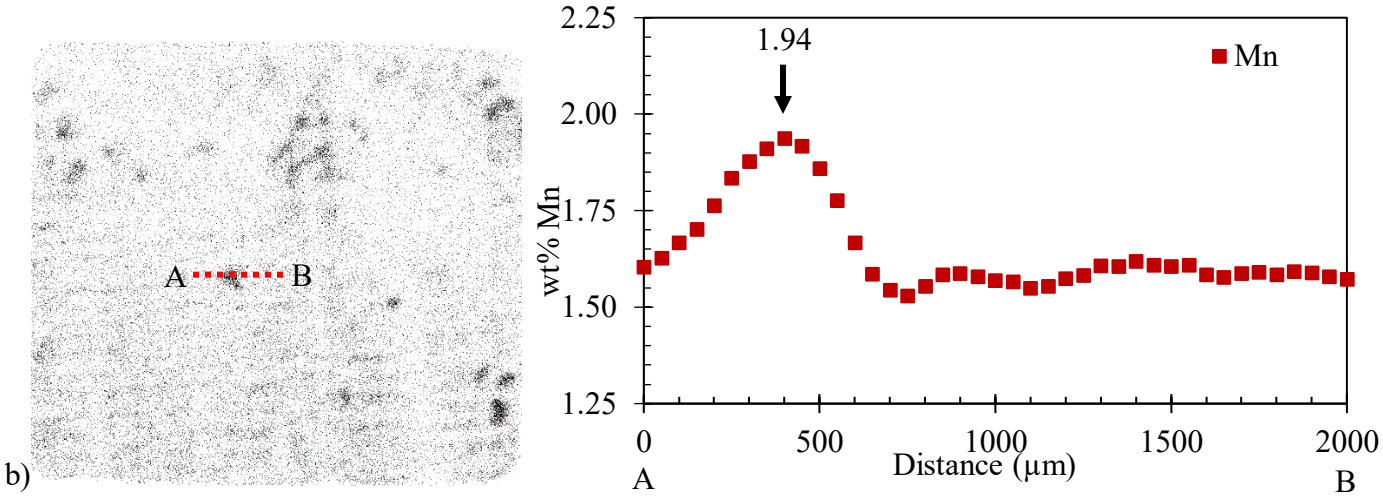

Fig. 6.3: b) Enhanced inverted Mn map and wt% distribution from CL location of S1 homogenized at 1200ºC for 6 h.

6.2.1 Homogenization results from QT samples of S1

The variation of microsegregation ratio as function of homogenization time at 1000ºC, 1100ºC and 1200ºC for Mn, Cr, Nb and P is shown in Figure 6.4. The decrease in micro S.R. for Mn and Cr, even after homogenization for 12 h, is not significant (< 0.05) because of their low diffusivities and their low initial as-cast segregation ratio (< 1.10). Previous studies on homogenization of Mn and Cr [189, 321, 322] with similar initial segregation ratios and large dendrite arm spacing (> 200 µm) have also reported insignificant (< 5%) decreases in segregation of Mn and Cr at 1200ºC. The S.R. for Nb in homogenized QT samples does not follow any particular trend, due to competing dissolution and coarsening of Nb precipitates taking place in the temperature range of 1000-1200ºC. The decrease in micro S.R. for P is also less than 0.02, except for a point with a higher measured micro S.R. (1.08) in the sample homogenized at 1100ºC for 3 h. The high diffusivity of P combined with the low P content within the dendrites are considered to be the reasons behind the low measured microsegregation ratio values of P.

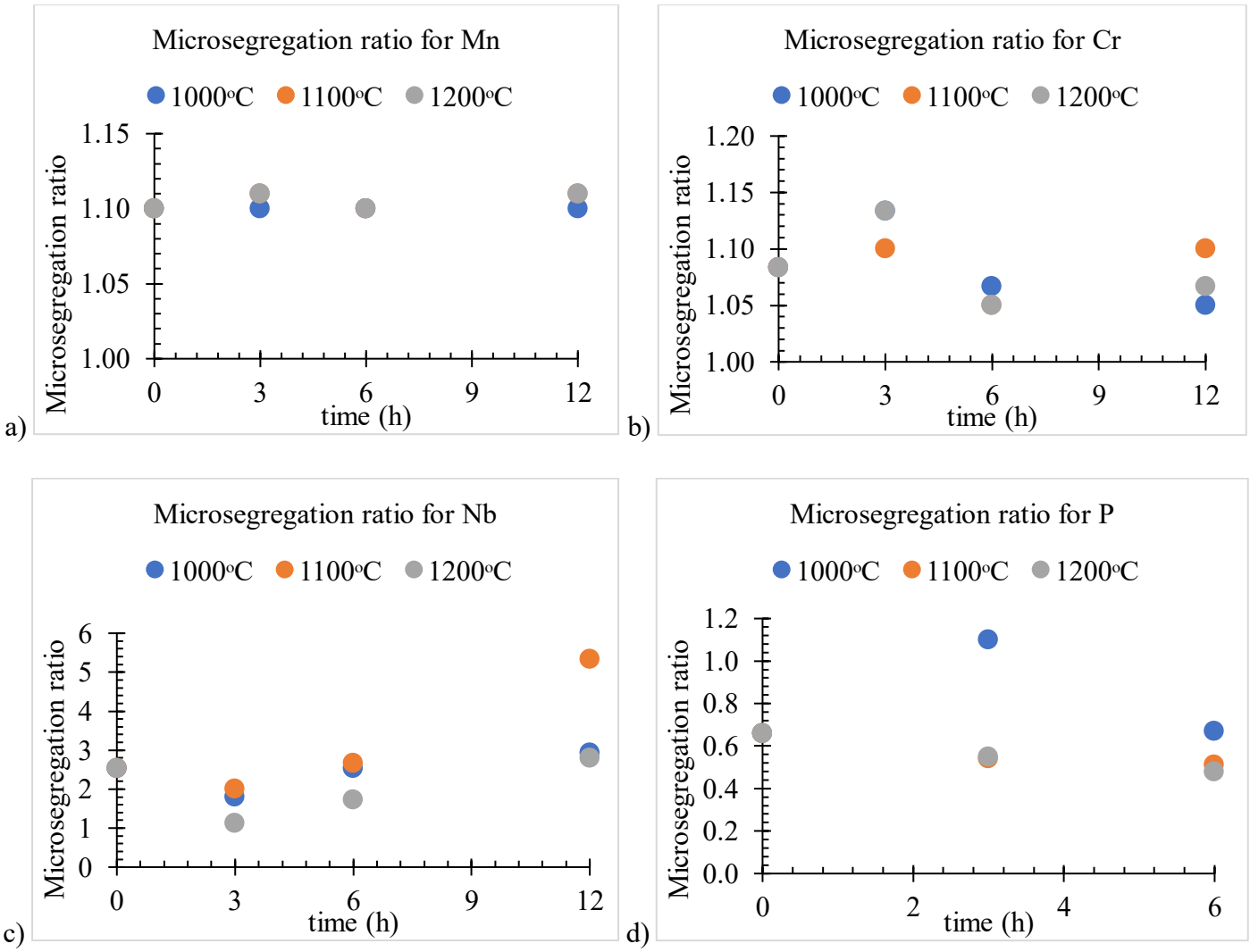

Fig. 6.4: Microsegregation ratios for a) Mn, b) Cr, c) Nb and d) P in homogenized samples.

6.2.2 Homogenization results from CL samples of S1

Figure 6.5 shows the variation of macrosegregation ratio as a function of homogenization time at 1000ºC, 1100ºC and 1200ºC for Mn, Cr, Nb and P. The macro S.R. for Mn decreases from 1.45 to 1.21 after 6 h at 1200ºC. A point with a S.R. higher than the as-cast measurement is observed in the sample homogenized at 1000ºC for 6 h. Cr and Nb macro S.R. values generally decrease with increasing time. The Cr macro S.R. decreases from 1.12 to 1.03 and the Nb macro S.R. decreases from 14.13 to 2.47 after 6 h at 1200ºC. Similar to Mn, points with S.R. higher than the as-cast measurement in the sample homogenized at 1100ºC were observed for P. The minimum macro S.R. for P (2.06) is also observed for the sample homogenized at 1200ºC for 6 h.

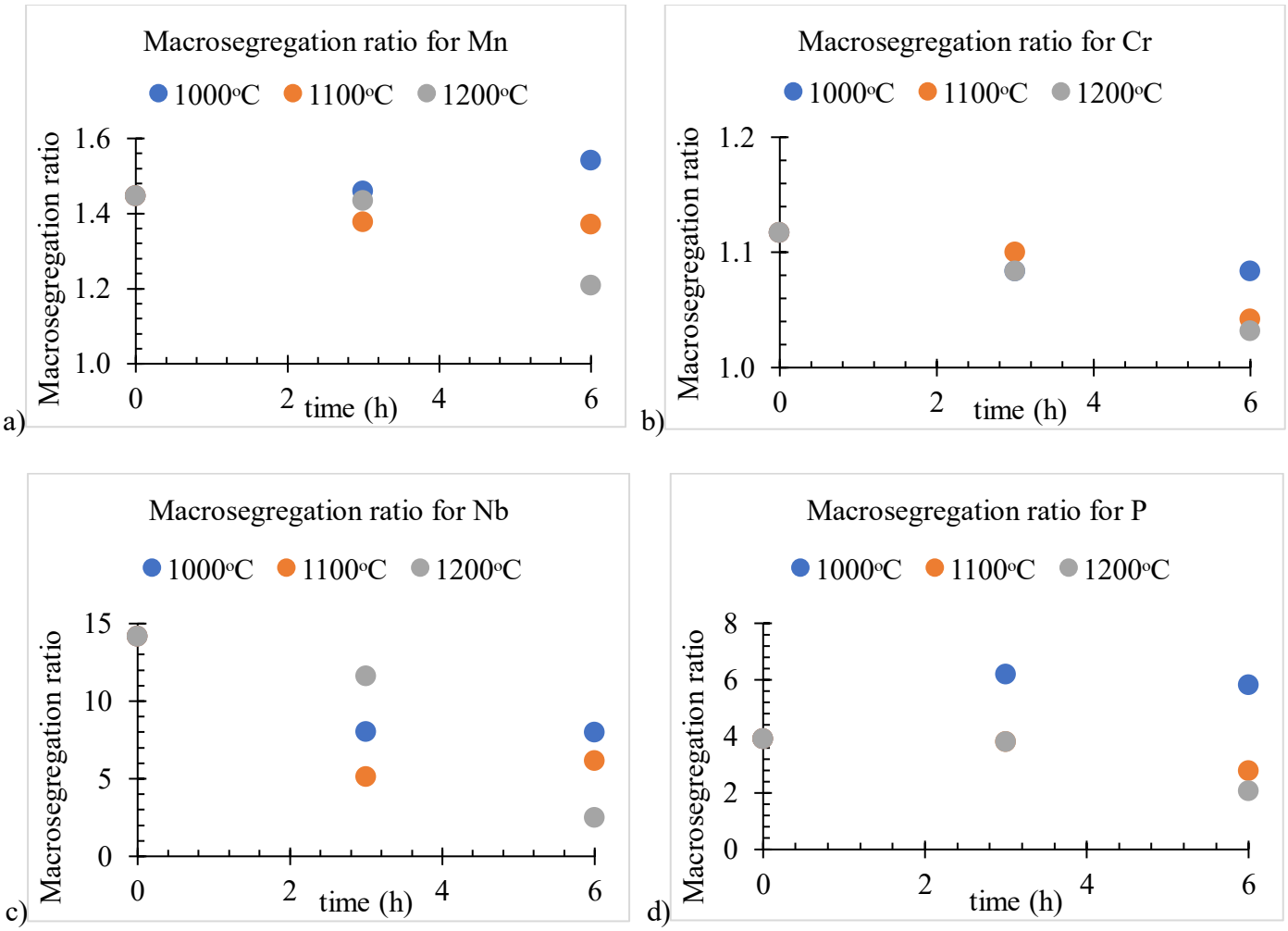

Fig. 6.5: Macrosegregation ratios for a) Mn, b) Cr, c) Nb and d) P in homogenized samples.

A large decrease in the macrosegregation ratio (>0.10) with increasing time and temperature is observed for Mn, Cr, Nb and P. The degree of decrease in macrosegregation ratio (>0.10) is greater because of the larger initial concentration gradient in the as-cast centerline samples compared with the quarter thickness samples. The macrosegregation ratio of Mn decreases by 20%, which is considerably higher than the decrease in microsegregation ratio of Mn (< 5%) for a hold time of 6 h at 1200°C. The macrosegregation ratio for Cr decreases from 1.12 to 1.03 after homogenization at 1200°C for 6 h, which is similar to a previous work [230], where the S.R. for Cr decreased from 1.16 to 1.09 after homogenization at 1200°C for 10 h. All elements except Nb follow the same trend, with the lowest macrosegregation ratio in the sample homogenized at 1200°C for 6 h. Macrosegregation ratio values for Nb again do not show any particular trend. The extent of decrease in macro S.R. is highest for P (~50%), because of the high diffusivity of P.

6.3 DICTRA based homogenization calculation results

The results from DICTRA based diffusion simulations are presented in this section. The diffusion behavior for both micro and macrosegregation of Mn, Cr, Nb and P at 1000ºC, 1100ºC and 1200ºC were simulated. The diffusivities of Mn, Cr, Nb and P were also obtained directly, as a function of temperature, using the equilibrium calculator and MOBFE3 database of ThermoCalc. Figure 6.6 shows the macrosegregation diffusion of Mn at 1200ºC for up to 12h. The calculated diffusion coefficient (D) for Mn in austenite (FCC) at 1200ºC is 8.00×10^{-15} m^2/s. The peak S.R. of Mn decreases from 1.45 to 1.41 after 12 h.

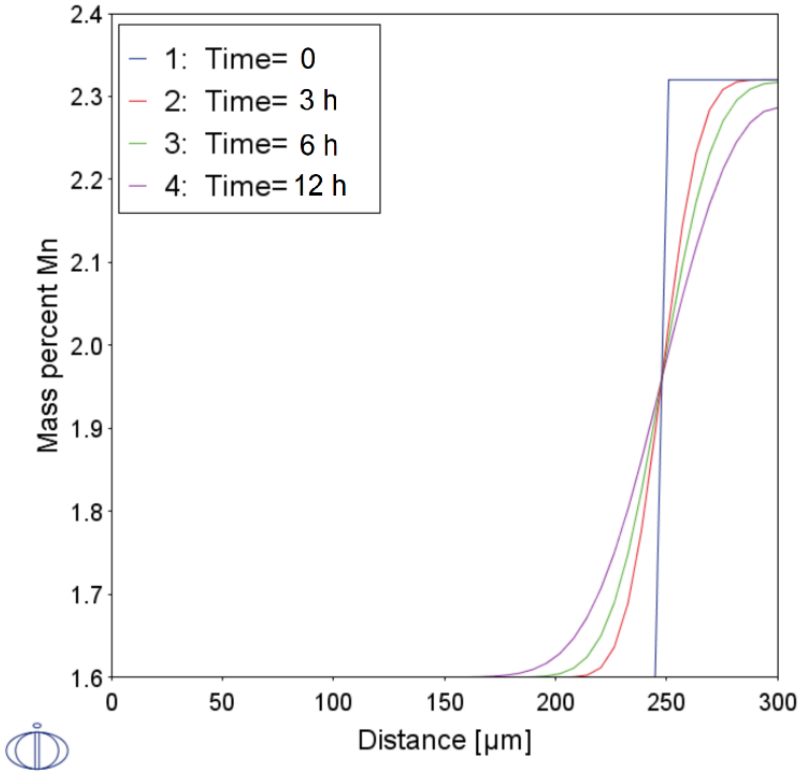

Fig. 6.6: Macrosegregation diffusion simulation plot for the binary Fe-Mn system at 1200ºC.

Similar to the macrosegregation diffusion of Mn at 1200ºC, micro and macrosegregation diffusion were simulated for Cr, Nb and P. The obtained diffusion coefficients and the change in peak segregation ratios at two extreme cases (1000ºC for 3 h and 1200ºC for 12 h) are listed in Table 6.1. P has the highest diffusion coefficient value followed by Nb, Cr and Mn. Accordingly, the decrease in peak S.R. is largest for P and lowest for Mn. As expected, the diffusion coefficients are lower at 1000ºC than at 1200ºC for all elements. Simulations with reduced chemistry (Section 3.5-b) produced similar values as the binary Fe-X simulations.

Table 6.1: Diffusion coefficients and S.R. values of elements predicted through DICTRA.

	S.R. at t = 0	S.R. after 3 h at 1000°C	S.R. after 12 h at 1200°C	D_{1000} (m^2/s)	D_{1200} (m^2/s)
Mn	1.10	1.10	1.09	3.01×10^{-16}	8.00×10^{-15}
	1.45	1.45	1.41		
Cr	1.10	1.10	1.08	3.24×10^{-16}	1.27×10^{-14}
	1.20	1.20	1.17		
Nb	2.00	2.00	1.69	9.67×10^{-16}	2.95×10^{-14}
	5.00	5.00	3.80		
P	2.00	1.80	1.17	7.36×10^{-14}	8.78×10^{-13}
	5.00	4.22	1.73		

Table 6.2 shows a comparison between ThermoCalc and experimentally obtained diffusivities [76] of Mn, Cr, Nb and P in austenite at 1000°C and 1200°C. The diffusivities for Mn and Nb are quite close to experimentally obtained diffusivities. However, the diffusivities for Cr at 1200°C and for P at 1000°C are higher in the ThermoCalc calculation. Both ThermoCalc and experimentally obtained diffusivities are highest for P, as it is an interstitial solute in iron, followed by Nb, Mn and Cr, which are substitutional solutes in iron.

Table 6.2: Diffusivity of elements in austenite at 1000°C and 1200°C.

Element	D_{1000} (m^2/s)		D_{1200} (m^2/s)	
	ThermoCalc	Experiment [76]	ThermoCalc	Experiment [76]
Mn	3.01×10^{-16}	3.22×10^{-16}	8.00×10^{-15}	7.89×10^{-15}
Cr	3.24×10^{-16}	1.24×10^{-16}	1.27×10^{-14}	2.06×10^{-15}
Nb	9.67×10^{-16}	9.65×10^{-16}	2.95×10^{-14}	2.94×10^{-14}
P	7.36×10^{-14}	3.14×10^{-14}	8.78×10^{-13}	3.28×10^{-13}

For Mn at 1200ºC, DICTRA predicted an insignificant (~1%) decrease in peak segregation for microsegregation diffusion and a 3% decrease in peak segregation for macrosegregation diffusion. The predictions are considerably less than the changes for the EMPA measurements (3% decrease in QT sample and 20% decrease in CL sample) in the homogenized samples. The predicted and measured decreases in microsegregation for Cr are low (< 2%). The decreases in peak macro S.R. values for Cr are higher for the EMPA measurements (~8%) than those for DICTRA predictions. A similar trend has been observed in previous studies [186] for Cr segregation reduction. For P, both the measured and predicted decrease in peak S.R. are significantly higher than the corresponding changes in Mn, Cr and Nb, because of the higher diffusivity of P. Since the starting S.R. for Nb and P were assumed based on their low partition coefficient, a direct comparison between measurements and simulations of segregation homogenization for Nb and P is not presented. The observed differences in the predicted and measured decrease in degree of segregation is due to the variable local concentration gradient within each sample. The variation in local concentration gradient arises due to random (variable dendrite arm spacing (DAS)) dendritic growth during solidification and the degree of homogenization is higher for smaller DAS compared with larger DAS [221, 322]. Since the DICTRA based diffusion model used in this work is for a constant DAS, it is not an absolute spatial representation of the homogenized samples. The higher degree of decrease in macrosegregation for both experiment and simulations is due to a greater initial concentration gradient of individual elements in the CL samples compared with the QT samples. A closer approximation of decrease in degree of segregation can be obtained by including multiple peak profiles as the initial state of segregation.

7. Conclusions and future work

In this study, the micro and macrosegregation behavior of Mn, Cr, Nb and P in microalloyed steels was investigated. Two industrial grade as-cast slabs with different nominal composition were characterized using EMPA. Another set of microalloyed steel samples was directionally solidified using a Bridgman furnace to study the effects of cooling rate on the partition coefficients of Mn, Cr, Nb and P. Furthermore, isothermal heat treatments were carried out at 1000°C, 1100°C and 1200°C for hold times of up to 12 h to study the diffusion behaviour of Mn, Cr, Nb and P in microalloyed steel. Finally, ThermoCalc based segregation and diffusion calculations were performed to formulate methods that can be used to predict the segregation and diffusion of alloying elements in microalloyed steels.

7.1 Segregation during continuous casting of microalloyed steels

- EMPA proved to be a particularly useful method to map and to quantify the concentration distribution of various elements in relatively large areas (~100 mm^2). The solute content of Mn was highest for all samples and, hence, the Mn EMPA maps provided the best contrast to study the segregation pattern.
- Both as-cast slabs S1 and S2 exhibited unequal amount of cooling from top and bottom surfaces. The segregation pattern suggested that the bottom of the slabs cooled faster as compared to the top part. For the investigated compositions, among Mn, Cr and P, Mn displayed the highest magnitude of microsegregation followed by Cr and P. However, for macrosegregation, P had the highest degree followed by Mn and Cr. The measured macro segregation ratio for Mn was higher for S1, which had a higher nominal Mn content.
- Nb segregation was difficult to study because of the presence of Nb precipitates which form during continuous casting of microalloyed steels. High measured Nb concentrations at a few locations on the EMPA maps and the contrast in EMPA grayscale Nb maps conformed well to the low partition coefficient of Nb in microalloyed steels.
- The measured interdendritic concentration of P was relatively low, but macrosegregation ratios for P were higher, which also agreed well with the low partition coefficient value of P in microalloyed steels.
- Mn EMPA maps illustrating centerline segregation of 3 different as-cast microalloyed steel slabs were also compared. Soft reduction leads to a decrease in the severity of centerline

segregation. Soft reduction also results in a discontinuous centerline segregation band. Soft reduction had insignificant effect on microsegregation.

- The "Scheil Solidification Simulation" module of ThermoCalc software was used for segregation ratio predictions for Mn, Cr, Nb and P. Two models were considered, the simple GS model and a modified GS model where the back diffusion of interstitial elements like C, P and S was considered. The concentrations of the elements in the solid phase at 0.85 fraction solid were chosen for comparison with the measured microsegregation values. The predicted microsegregation ratio values for Mn and Cr were higher as compared to the measurements. However, for P, the measured values were considerably higher than the predictions. This suggested that finite diffusion of Mn, Cr and P needs to be taken into account in the solidification simulations.
- The quantification of segregation using segregation ratio, i.e., based on just one point is not suitable, particularly for elements like Nb and P, which have a low partition coefficient value.

7.2 Effect of cooling rate on partition coefficient

- Unidirectional solidification at cooling rates of 0.4°C/s and 0.2°C/s were used to study the variation of partition coefficients for Mn, Cr, Nb and P. The qualitative distribution of individual elements was same in both samples. The composition of elements from the area covering the solid-liquid interface was used to calculate partition coefficients. A decrease in partition coefficient with a decrease in cooling rate from 0.4°C/s to 0.2°C/s was observed for Mn, Cr and P. Nb precipitates limited the k calculation for Nb.

7.3 Diffusion during homogenization of microalloyed steels

- The decrease in microsegregation ratio for Mn and Cr were small (< 5%). The microsegregation ratio for Nb showed an increase after homogenizing at 1200°C, likely due to Nb precipitate coarsening. Microsegregation ratio values for P were quite low (<1.00) for all quarter thickness samples. Both Nb and P microsegregation did not show a definite trend with respect to increasing homogenization time or temperature.

- For centerline samples, the decrease in macrosegregation was relatively high for all the elements of interest. A decrease of 20% in peak measured macrosegregation value for Mn was observed. The P peak value decreased from 3.9 to 2.1 at 1200^{o}C in 6 h.
- From DICTRA simulations, the microsegregation diffusion plots for Mn, Cr and Nb showed small changes (< 5%) in peak segregation as the diffusivities of substitutional solutes in austenite are quite low even at 1200^{o}C. P had the highest calculated diffusivity followed by Nb, Cr and Mn. Macrosegregation diffusion simulations displayed the same trend as microsegregation diffusion simulations.
- A significant decrease in measured macrosegregation for all elements was observed, which was not the case for macrosegregation diffusion simulation. The predicted decrease in peak macrosegregation value for Mn was small (~3%), but a greater decrease in Mn macrosegregation (~20%) was observed experimentally. P diffusion simulations corresponded well with the measured values. The decrease in Nb macrosegregation simulations were also lower than measurements. The measured values of Nb segregation in homogenized CL samples were quite high again due to Nb precipitates.

7.4 Proposed future work

This section outlines further scope of this research and identifies the areas that can be improved upon.

- Another as-cast slab with a higher nominal Mn content should be analysed to further support the assertion of increased segregation ratio with increasing weight percent of Mn. This will also help further support the observed trends for Cr, Nb and P. To study Nb segregation, a threshold value differentiating Nb segregation and Nb precipitates should be set. An average of a few higher measured wt% points could also be used instead of using just one maximum measured wt% value for segregation ratio determination.
- In this work, other possible factors which could affect segregation behavior of elements like changing grain size and changing dendrite arm spacing were not considered in detail. The effects of changing grain structure and dendrite arm spacing on segregation can be further explored.

- Another set of unidirectional solidification trials at increased cooling rates should be performed and analyzed to establish the relation between partition coefficient and cooling rate during solidification over a wider range.
- Quantification of segregation based on segregation ratio is limited as it is based on one data point. Quantification of segregation in cast slabs should also be done based on the partition coefficient calculations.
- The above mentioned calculation was performed for Mn in 2 samples, as-cast and homogenized QT sample. The partition coefficient, k, for Mn increased from 0.932 in as-cast condition to 0.968 in the sample homogenized at 1200°C for 12 h, which follows well in terms of segregation reduction after homogenization. This further supports the use of k instead of an one point segregation ratio as a measure to quantify segregation.
- GS calculations with modified k values, as suggested in some previous works [278-285], should be conducted for the studied low C steels. This would identify the further possibilities of improvement in the GS model implemented in this work.
- A DICTRA model with multi-peak initial segregation profiles and non isothermal heat treatment should be defined to better replicate the homogenization experiments.
- DICTRA based solidification modeling with varying cooling rates should also be undertaken to model the effects of varying cooling rate on partition coefficients of solutes in microalloyed steels.

8. References

1. Zhao, J. W., Jiang, Z. Y., & Wei, D. B. (2013). Analysis of elemental segregation in a microalloyed cast steel. In *Advanced Materials Research* (Vol. 652, pp. 2465-2468). Trans Tech Publications Ltd.
2. Hansen, S. S., Vander Sande, J. B., & Cohen, M. (1980). Niobium carbonitride precipitation and austenite recrystallization in hot-rolled microalloyed steels. *Metallurgical Transactions A*, *11*(3), 387-402.
3. Duckworth, W. E., Phillips, R., & Chapman, J. A. (1965). Pearlite reduced structural steels. *Iron Steel Inst J*, *203*(11), 1108-1114.
4. Irvine, K. J., Pickering, F. B., & Gladman, T. (1967). Grain-refined C-Mn steels. *Iron Steel Inst J*, *205*(2), 161-182.
5. Villalobos, J. C., Del-Pozo, A., Campillo, B., Mayen, J., & Serna, S. (2018). Microalloyed steels through history until 2018: review of chemical composition, processing and hydrogen service. *Metals*, *8*(5), 351.
6. DeArdo, A. J., Hua, M. J., Cho, K. G., & Garcia, C. I. (2009). On strength of microalloyed steels: an interpretive review. *Materials Science and Technology*, *25*(9), 1074-1082.
7. Vervynckt, S., Verbeken, K., Lopez, B., & Jonas, J. J. (2012). Modern HSLA steels and role of non-recrystallisation temperature. *International Materials Reviews*, *57*(4), 187-207.
8. McMahon Jr, C. J. (1980). Solute segregation and intergranular fracture in steels: a status report. *Materials Science and Engineering*, *42*, 215-226.
9. Khalid, F. A., Farooque, M., Ul Haq, A., & Khan, A. Q. (1999). Role of ferrite/pearlite banded structure and segregation on mechanical properties of microalloyed hot rolled steel. *Materials science and technology*, *15*(10), 1209-1215.
10. Wang, J., Hodgson, P. D., Bikmukhametov, I., Miller, M. K., & Timokhina, I. (2018). Effects of hot-deformation on grain boundary precipitation and segregation in Ti-Mo microalloyed steels. *Materials & Design*, *141*, 48-56.
11. Zheng, S., Davis, C., & Strangwood, M. (2014). Elemental segregation and subsequent precipitation during solidification of continuous cast Nb–V–Ti high-strength low-alloy steels. *Materials characterization*, *95*, 94-104.
12. Jablonski, P. D., & Hawk, J. A. (2017). Homogenizing advanced alloys: thermodynamic and kinetic simulations followed by experimental results. *Journal of Materials Engineering and Performance*, *26*(1), 4-13.
13. Xie, Z. J., Fang, Y. P., Han, G., Guo, H., Misra, R. D. K., & Shang, C. J. (2014). Structure–property relationship in a 960 MPa grade ultrahigh strength low carbon niobium–vanadium microalloyed steel: The significance of high frequency induction tempering. *Materials Science and Engineering: A*, *618*, 112-117.
14. Hu, J., Du, L. X., Xie, H., Gao, X. H., & Misra, R. D. K. (2014). Microstructure and mechanical properties of TMCP heavy plate microalloyed steel. *Materials Science and Engineering: A*, *607*, 122-131.
15. Wang, B., & Lian, J. (2014). Effect of microstructure on low-temperature toughness of a low carbon Nb–V–Ti microalloyed pipeline steel. *Materials Science and Engineering: A*, *592*, 50-56.
16. Kumar, A. S., Kumar, B. R., Datta, G. L., & Ranganath, V. R. (2010). Effect of microstructure and grain size on the fracture toughness of a micro-alloyed steel. *Materials Science and Engineering: A*, *527*(4-5), 954-960.

17. Xie, H., Du, L. X., Hu, J., & Misra, R. D. K. (2014). Microstructure and mechanical properties of a novel 1000 MPa grade TMCP low carbon microalloyed steel with combination of high strength and excellent toughness. *Materials Science and Engineering: A*, *612*, 123-130.
18. Baker, T. N. (2016). Microalloyed steels. *Ironmaking & Steelmaking*, *43*(4), 264-307.
19. Fu, J., Wang, Z. B., & Kang, Y. L. (2002, December). Research and development of HSLC steels produced by EAF-CSP technology. In *Proceedings of the International Symposium on Thin Slab Casting and Rolling, Guangzhou, China* (pp. 3-5).
20. Xu, G., Gan, X., Ma, G., Luo, F., & Zou, H. (2010). The development of Ti-alloyed high strength microalloy steel. *Materials & Design*, *31*(6), 2891-2896.
21. Kamoutsi, H., Gioti, E., Haidemenopoulos, G. N., Cai, Z., & Ding, H. (2015). Kinetics of solute partitioning during intercritical annealing of a medium-Mn steel. *Metallurgical and Materials Transactions A*, *46*(11), 4841-4846.
22. Sugimoto, K. I., Tanino, H., & Kobayashi, J. (2015). Impact Toughness of Medium-Mn Transformation-Induced Plasticity-Aided Steels. *steel research international*, *86*(10), 1151-1160.
23. Lee, S., Lee, K., & De Cooman, B. C. (2015). Observation of the TWIP+ TRIP plasticity-enhancement mechanism in Al-added 6 wt pct medium Mn steel. *Metallurgical and Materials Transactions A*, *46*(6), 2356-2363.
24. Xiao, F., Liao, B., Ren, D., Shan, Y., & Yang, K. (2005). Acicular ferritic microstructure of a low-carbon Mn–Mo–Nb microalloyed pipeline steel. *Materials Characterization*, *54*(4-5), 305-314.
25. Evans, P. J., Crawford, L. K., & Jones, A. (1997). High strength C-Mn steels for automotive applications. *Ironmaking and steelmaking*, *24*(5), 361-367.
26. Lu, Q., Xu, W., & van der Zwaag, S. (2014). Designing new corrosion resistant ferritic heat resistant steel based on optimal solid solution strengthening and minimisation of undesirable microstructural components. *Computational materials science*, *84*, 198-205.
27. Kusakin, P., Belyakov, A., Molodov, D. A., & Kaibyshev, R. (2017). On the effect of chemical composition on yield strength of TWIP steels. *Materials Science and Engineering: A*, *687*, 82-84.
28. Vervynckt, S., Verbeken, K., Thibaux, P., Liebeherr, M., & Houbaert, Y. (2009). Austenite recrystallization–precipitation interaction in niobium microalloyed steels. *ISIJ international*, *49*(6), 911-920.
29. Klinkenberg, C., Hulka, K., & Bleck, W. (2004). Niobium carbide precipitation in microalloyed steel. *steel research international*, *75*(11), 744-752.
30. Abad, R., AI, F., Lopez, B., & JM, R. I. (2001). Interaction between recrystallization and precipitation during multipass rolling in a low carbon niobium microalloyed steel. *ISIJ international*, *41*(11), 1373-1382.
31. Lan, L. Y., Qiu, C. L., Zhao, D. W., Gao, X. H., & Du, L. X. (2011). Dynamic and static recrystallization behavior of low carbon high niobium microalloyed steel. *Journal of Iron and Steel Research, International*, *18*(1), 55-60.
32. Gómez, M., Rancel, L., & Medina, S. F. (2009). Assessment of austenite static recrystallization and grain size evolution during multipass hot rolling of a niobium-microalloyed steel. *Metals and Materials International*, *15*(4), 689-699.
33. Gómez, M., Medina, S. F., & Valles, P. (2005). Determination of driving and pinning forces for static recrystallization during hot rolling of a niobium microalloyed steel. *ISIJ international*, *45*(11), 1711-1720.

34. Klinkenberg, C. (2007). Niobium in microalloyed structural and engineering steels. In *Materials science forum* (Vol. 539, pp. 4261-4266). Trans Tech Publications Ltd.
35. Kostryzhev, A. G., Al Shahrani, A., Zhu, C., Ringer, S. P., & Pereloma, E. V. (2013). Effect of deformation temperature on niobium clustering, precipitation and austenite recrystallisation in a Nb–Ti microalloyed steel. *Materials Science and Engineering: A*, *581*, 16-25.
36. Bracke, L., & Xu, W. (2015). Effect of the Cr content and coiling temperature on the properties of hot rolled high strength lower bainitic steel. *ISIJ International*, *55*(10), 2206-2211.
37. Lee, H. J., & Lee, H. W. (2015). Effect of Cr content on microstructure and mechanical properties of low carbon steel welds. *International Journal of Electrochemical Science*, *10*(10), 8028-8040.
38. Zhou, M., Xu, G., Tian, J., Hu, H., & Yuan, Q. (2017). Bainitic transformation and properties of low carbon carbide-free bainitic steels with Cr addition. *Metals*, *7*(7), 263.
39. Gorokhova, N. A., Sarrak, V. I., & Suvorova, S. O. (1986). Solubility of titanium and niobium carbides in high-chromium ferrite. *Metal Science and Heat Treatment*, *28*(4), 276-279.
40. Tsai, S. P., Su, T. C., Yang, J. R., Chen, C. Y., Wang, Y. T., & Huang, C. Y. (2017). Effect of Cr and Al additions on the development of interphase-precipitated carbides strengthened dual-phase Ti-bearing steels. *Materials & Design*, *119*, 319-325.
41. Koyama, S., Ishii, T., & Narita, K. (1971). Effects of Mn, Si, Cr, and Ni on the solution and precipitation of niobium carbide in iron austenite. Kobe Steel Ltd., Japan.
42. Ray, A. (2017). Niobium microalloying in rail steels. *Materials Science and Technology*, *33*(14), 1584-1600.
43. YAMAMOTO, S., SAKIYAMA, T., & OUCHI, C. (1987). Effect of alloying elements on recrystallization kinetics after hot deformation in austenitic stainless steels. *Transactions of the Iron and Steel Institute of Japan*, *27*(6), 446-452.
44. de Abreu Martins, C., Poliak, E., Godefroid, L. B., & Fonstein, N. (2014). Determining the conditions for dynamic recrystallization in hot deformation of C–Mn–V steels and the effects of Cr and Mo additions. *ISIJ international*, *54*(1), 227-234.
45. Kundu, A., Davis, C. L., & Strangwood, M. (2010). Grain structure development during reheating and deformation of niobium-microalloyed steels. *Materials and Manufacturing Processes*, *25*(1-3), 125-132.
46. Shi, L., Yan, Z. S., Liu, Y. C., Yang, X., Zhang, C., & Li, H. J. (2014). Effect of acicular ferrite on banded structures in low-carbon microalloyed steel. *International Journal of Minerals, Metallurgy, and Materials*, *21*(12), 1167-1174.
47. Sasidhar, K. N., Dhande, T., Javed, N., Ghosh, A., Mukherjee, M., Sharma, V., ... & Bakshi, S. D. (2017). Effect of transformation texture on the impact toughness of hot-rolled Ti+ Nb microalloyed steel. *Materials & Design*, *128*, 86-97.
48. Abramova, M. M., Enikeev, N. A., Valiev, R. Z., Etienne, A., Radiguet, B., Ivanisenko, Y., & Sauvage, X. (2014). Grain boundary segregation induced strengthening of an ultrafine-grained austenitic stainless steel. *Materials letters*, *136*, 349-352.
49. Lee, H., Jo, M. C., Sohn, S. S., Zargaran, A., Ryu, J. H., Kim, N. J., & Lee, S. (2018). Novel medium-Mn (austenite+ martensite) duplex hot-rolled steel achieving 1.6 GPa strength with 20% ductility by Mn-segregation-induced TRIP mechanism. *Acta Materialia*, *147*, 247-260.

50. Shen, T. D., Schwarz, R. B., Feng, S., Swadener, J. G., Huang, J. Y., Tang, M., ... & Zhao, Y. (2007). Effect of solute segregation on the strength of nanocrystalline alloys: Inverse Hall–Petch relation. *Acta materialia*, *55*(15), 5007-5013.
51. Hu, C., Wu, K., Trotsan, A., Li, Y., Isayev, O., Hress, O., & Rodionova, I. (2016). Effect of microadditives on center segregation and mechanical properties of high-strength low-alloy steels. *Metallurgist*, *60*(7-8), 888-895.
52. Yamaguchi, M., & Kameda, J. (2014). Multiscale thermodynamic analysis on fracture toughness loss induced by solute segregation in steel. *Philosophical Magazine*, *94*(19), 2131-2149.
53. Naudin, C., Pineau, A., & Frund, J. M. (2002, January). Numerical Modeling of Fracture Toughness in RPV Steel Containing Segregated Zones. In *ASME Pressure Vessels and Piping Conference* (Vol. 46547, pp. 69-75).
54. Na, H., Lee, S., & Kang, C. (2018). Effect of micro-segregation on impact toughness of 2.25 Cr-1Mo steel after post weld heat treatment. *Metals*, *8*(6), 373.
55. Atrens, A., Wang, J. Q., Stiller, K., & Andrén, H. O. (2006). Atom probe field ion microscope measurements of carbon segregation at an α: α grain boundary and service failures by intergranular stress corrosion cracking. *Corrosion science*, *48*(1), 79-92.
56. Kai, W. A. N. G., Xu, T. D., Chong, S. H. A. O., & Chun, Y. A. N. G. (2011). Nonequilibrium grain boundary segregation of sulfur and its effect on intergranular corrosion for 304 stainless steel. *Journal of Iron and Steel Research, International*, *18*(6), 61-66.
57. Park, J. H., Kim, J. K., Lee, B. H., Kim, S. S., & Kim, K. Y. (2013). Three-dimensional atom probe analysis of intergranular segregation and precipitation behavior in Ti–Nb-stabilized low-Cr ferritic stainless steel. *Scripta Materialia*, *68*(5), 237-240.
58. NH, H., & JK, L. (2011). Grain Boundary Segregation of Phosphorus and Columnar Grain Growth during Decarburization in Plain Carbon Steels. *Materials transactions*, *52*(2), 219-223.
59. Nikolaeva, A. V., Nikolaev, Y. A., & Kevorkyan, Y. R. (2001). Grain-boundary segregation of phosphorus in low-alloy steel. *Atomic energy*, *91*(1), 534-542.
60. Kim, J. I., Pak, J. H., Park, K. S., Jang, J. H., Suh, D. W., & Bhadeshia, H. K. D. H. (2014). Segregation of phosphorus to ferrite grain boundaries during transformation in an Fe–P alloy. *International Journal of Materials Research*, *105*(12), 1166-1172.
61. Song, S. H., Zhao, Y., & Si, H. (2015). Non-equilibrium phosphorus grain boundary segregation and its effect on embrittlement in a niobium-stabilized interstitial-free steel. *Materials Letters*, *140*, 20-22.
62. Song, S. H., Wu, J., Weng, L. Q., & Xi, T. H. (2009). Phosphorus grain boundary segregation under an intermediate applied tensile stress in a Cr–Mo low alloy steel. *Materials Science and Engineering: A*, *520*(1-2), 97-100.
63. Song, S. H., Zhuang, H., Wu, J., Weng, L. Q., Yuan, Z. X., & Xi, T. H. (2008). Dependence of ductile-to-brittle transition temperature on phosphorus grain boundary segregation for a 2.25 Cr1Mo steel. *Materials Science and Engineering: A*, *486*(1-2), 433-438.
64. Sabeghi, M., Shukla, R., Allen, J. K., & Mistree, F. (2016, August). Solution Space Exploration of the Process Design for Continuous Casting of Steel. In *International Design Engineering Technical Conferences and Computers and Information in Engineering Conference* (Vol. 50114, p. V02BT03A005). American Society of Mechanical Engineers.

65. Gránásy, L., Tóth, G. I., Warren, J. A., Podmaniczky, F., Tegze, G., Rátkai, L., & Pusztai, T. (2019). Phase-field modeling of crystal nucleation in undercooled liquids–A review. *Progress in Materials Science*, *106*, 100569.
66. Steinbach, S., & Ratke, L. (2007). Effects of controlled convections on dendritic microstructure and segregation during microgravity-solidification. In *Proc. of the 18th ESA Symposium on European Rocket and Balloon Programmes and Related Research, Visby, Sweden, ESA SP-647* (pp. 373-378).
67. Yang, X. G., Xu, Q. T., Wu, C. L., & Chen, Y. S. (2017, December). Experimental study of the continuous casting slab solidification microstructure by the dendrite etching method. In *IOP Conference Series: Materials Science and Engineering* (Vol. 283, No. 1, p. 012017). IOP Publishing.
68. Louhenkilpi, S. (2014). Continuous casting of steel. In *Treatise on process metallurgy* (pp. 373-434). Elsevier.
69. Huang, Y., Long, M., Liu, P., Chen, D., Chen, H., Gui, L., & Yu, S. (2017). Effects of partition coefficients, diffusion coefficients, and solidification paths on microsegregation in Fe-based multinary alloy. *Metallurgical and Materials Transactions B*, *48*(5), 2504-2515.
70. Won, Y. M., & Thomas, B. G. (2001). Simple model of microsegregation during solidification of steels. *Metallurgical and materials transactions A*, *32*(7), 1755-1767.
71. Li, J., Wu, M., Ludwig, A., & Kharicha, A. (2014). Simulation of macrosegregation in a 2.45-ton steel ingot using a three-phase mixed columnar-equiaxed model. *International Journal of Heat and Mass Transfer*, *72*, 668-679.
72. Aboutalebi, M. R., Hasan, M., & Guthrie, R. I. L. (1995). Coupled turbulent flow, heat, and solute transport in continuous casting processes. *Metallurgical and materials transactions b*, *26*(4), 731-744.
73. Battle, T. P., & Pehlke, R. D. (1989). Equilibrium partition coefficients in iron-based alloys. *Metallurgical and Materials Transactions B*, *20*(2), 149-160.
74. Gui, L., Long, M., Chen, D., Zhao, J., Wang, Q., & Duan, H. (2020). Thermodynamic study on the solute partition coefficients on L/δ and L/δ+ γ phase interfaces for 1215 high-sulfur steel solidification by orthogonal design. *Journal of Materials Research and Technology*, *9*(1), 89-103.
75. Fujda, M. (2005). Centerline segregation of continuously cast slabs influence on microstructure and fracture morphology. *Journal of Metals, Materials and Minerals*, *15*(2), 45-51.
76. Zhang, D. (2015). *Characterisation and modelling of segregation in continuously cast steel slab* (Doctoral dissertation, University of Birmingham).
77. Guo, J., & Wen, G. (2019). Influence of Alloy Elements on Cracking in the Steel Ingot during Its Solidification. *Metals*, *9*(8), 836.
78. Tsuchida, Y., Nakada, M., Sugawara, I., Miyahara, S., Murakami, K., & Tokushige, S. (1984). Behavior of semi-macroscopic segregation in continuously cast slabs and technique for reducing the segregation. *Transactions of the Iron and Steel Institute of Japan*, *24*(11), 899-906.
79. Ghosh, A. (2001). Segregation in cast products. *Sadhana*, *26*(1-2), 5-24.
80. Choudhary, S. K., Ganguly, S., Sengupta, A., & Sharma, V. (2017). Solidification morphology and segregation in continuously cast steel slab. *Journal of Materials Processing Technology*, *243*, 312-321.

81. Buschow, K. J., Cahn, R. W., Flemings, M. C., Ilschner, B., Kramer, E. J., & Mahajan, S. (2001). Encyclopedia of materials. *Science and technology*, *1*(11).
82. Pickering, E. J. (2013). Macrosegregation in steel ingots: the applicability of modelling and characterisation techniques. *ISIJ international*, *53*(6), 935-949.
83. Singh, A. K., & Basu, B. (1995). Mathematical modeling of macrosegregation of iron carbon binary alloy: Role of double diffusive convection. *Metallurgical and Materials Transactions B*, *26*(5), 1069-1081.
84. Jiang, D., Wang, W., Luo, S., Ji, C., & Zhu, M. (2017). Mechanism of macrosegregation formation in continuous casting slab: A numerical simulation study. *Metallurgical and Materials Transactions B*, *48*(6), 3120-3131.
85. Schneider, M. C., & Beckermann, C. (1995). Formation of macrosegregation by multicomponent thermosolutal convection during the solidification of steel. *Metallurgical and Materials Transactions A*, *26*(9), 2373-2388.
86. Ueyama, S., Niizuma, M., & Yonezawa, K. (2013). Development of high quality heavy plates on steelmaking process at Kimitsu Works. *Nippon Steel Techn. Report*, (104), 102-108.
87. Haida, O., Kitaoka, H., Habu, Y., Kakihara, S., Bada, H., & Shiraishi, S. (1984). Macro-and semi-macroscopic features of the centerline segregation in CC slabs and their effect on product quality. *Transactions of the Iron and Steel Institute of Japan*, *24*(11), 891-898.
88. Mendoza, R., Alanis, M., Perez, R., Alvarez, O., Gonzalez, C., & Juarez-Islas, J. A. (2002). On the processing of Fe–C–Mn–Nb steels to produce plates for pipelines with sour gas resistance. *Materials Science and Engineering: A*, *337*(1-2), 115-120.
89. Lin, B. Y., Chen, E. T., & Lei, T. S. (1998). The effect of segregation on the austemper transformation and toughness of ductile irons. *Journal of materials engineering and performance*, *7*(3), 407-419.
90. Kyada, T., Shant, J. R., Goyal, R. K., & Kathayat, T. S. (2014). Understanding the Delamination and Its Effect on Charpy Impact Energy in Thick Wall Linepipe Steel. *J. Mater. Metall. Eng*, *4*(1), 31-39.
91. Bhattacharya, D., Roy, T. K., & Mahashabde, V. V. (2016). A study to establish correlation between intercolumnar cracks in slabs and off-center defects in hot-rolled products. *Journal of Failure Analysis and Prevention*, *16*(1), 95-103.
92. Loucif, A., Fredj, E. B., Harris, N., Shahriari, D., Jahazi, M., & Lapierre-Boire, L. P. (2018). Evolution of A-type macrosegregation in large size steel ingot after multistep forging and heat treatment. *Metallurgical and Materials Transactions B*, *49*(3), 1046-1055.
93. Tao, J., Hu, S., Yan, F., Zhang, Y., & Langley, M. (2016). A study of the mechanism of delamination fracture in bainitic magnetic yoke steel. *Materials & Design*, *108*, 429-439.
94. Guo, F., Liu, W., Wang, X., Misra, R. D. K., & Shang, C. (2019). Controlling Variability in Mechanical Properties of Plates by Reducing Centerline Segregation to Meet Strain-Based Design of Pipeline Steel. *Metals*, *9*(7), 749.
95. Guo, F., Wang, X., Liu, W., Shang, C., Misra, R. D. K., Wang, H., ... & Peng, C. (2018). The Influence of Centerline Segregation on the Mechanical Performance and Microstructure of X70 Pipeline Steel. *steel research international*, *89*(12), 1800407.
96. Guo, F., Wang, X., Wang, J., Misra, R. D. K., & Shang, C. (2020). The Significance of Central Segregation of Continuously Cast Billet on Banded Microstructure and Mechanical Properties of Section Steel. *Metals*, *10*(1), 76.
97. Miyazaki, M., Isobe, K., & Murao, T. (2013). Formation mechanism and modeling of centerline segregation. *Nippon steel technical report*, *104*.

98. Sang, B., Kang, X., & Li, D. (2010). A novel technique for reducing macrosegregation in heavy steel ingots. *Journal of Materials Processing Technology*, *210*(4), 703-711.
99. Zhang, C., Loucif, A., Jahazi, M., Tremblay, R., & Lapierre, L. P. (2018). On the effect of filling rate on positive macrosegregation patterns in large size cast steel ingots. *Applied Sciences*, *8*(10), 1878.
100. An, H., Bao, Y. P., Wang, M., & Zhao, L. H. (2017). Reducing macro segregation of high carbon steel in continuous casting bloom by final electromagnetic stirring and mechanical soft reduction integrated process. *Metallurgical Research & Technology*, *114*(4), 405.
101. Grundy, A. N., Münch, S., Feldhaus, S., & Bratberg, J. (2019, May). Continuous Casting of High Carbon Steel: How Does Hard Cooling Influence Solidification, Micro-and Macro Segregation?. In *IOP Conference Series: Materials Science and Engineering* (Vol. 529, No. 1, p. 012069). IOP Publishing.
102. Nayak, S. S., Misra, R. D. K., Hartmann, J., Siciliano, F., & Gray, J. M. (2008). Microstructure and properties of low manganese and niobium containing HIC pipeline steel. *Materials Science and Engineering: A*, *494*(1-2), 456-463.
103. Nakai, Y., Kurahashi, H., Emi, T., & Haida, O. (1979). Development of steels resistant to hydrogen induced cracking in wet hydrogen sulfide environment. *Transactions of the Iron and Steel Institute of Japan*, *19*(7), 401-410.
104. Olivares, I., Alanis, M., Mendoza, R., Campillo, B., & Juarez-Islas, J. A. (2008). Development of microalloyed steel for pipeline applications. *Ironmaking & Steelmaking*, *35*(6), 452-457.
105. Lesoult, G. (2005). Macrosegregation in steel strands and ingots: Characterisation, formation and consequences. *Materials Science and Engineering: A*, *413*, 19-29.
106. Ji, Y., Lan, P., Geng, H., He, Q., Shang, C., & Zhang, J. (2018). Behavior of spot segregation in continuously cast blooms and the resulting segregated band in oil pipe steels. *steel research international*, *89*(3), 1700331.
107. Wang, X. (2018). *Microsegregation and high temperature properties of high manganese steels* (Doctoral dissertation, Technische Universität Clausthal).
108. Choudhary, S. K., & Ganguly, S. (2007). Morphology and segregation in continuously cast high carbon steel billets. *ISIJ international*, *47*(12), 1759-1766.
109. Lan, P., Tang, H., & Zhang, J. (2016). Hot ductility of high alloy Fe–Mn–C austenite TWIP steel. *Materials Science and Engineering: A*, *660*, 127-138.
110. Sasaki, D., Koyama, M., & Noguchi, H. (2015). Factors affecting hydrogen-assisted cracking in a commercial tempered martensitic steel: Mn segregation, MnS, and the stress state around abnormal cracks. *Materials Science and Engineering: A*, *640*, 72-81.
111. Chakrabarti, D., Davis, C. L., & Strangwood, M. (2009). Effect of deformation and Nb segregation on grain size bimodality in HSLA steel. *Materials science and Technology*, *25*(8), 939-946.
112. Wang, M., Ma, D., Liu, Z., Zhou, J., Chi, H., & Dai, J. (2014). Effect of Nb on segregation, primary carbides and toughness of H13 steel. *Acta Metall Sin*, *50*(3), 285-293.
113. Chen, T., Hua, M., Garcia, C. I., & DeArdo, A. J. (2005). Role of Niobium on the Segregation Behavior of Phosphorus and Manganese in High Strength IF Sheet Steels for Automotive Use. *Materials Science and Technology – Association for Iron and Steel Technology* -, *2*, 2.
114. Lapin, J., & Gabalcová, Z. (2011). Solidification behaviour of TiAl-based alloys studied by directional solidification technique. *Intermetallics*, Volume *19, Issue* 6, 797-804.

115. Yang, L., Li, S., Guo, J., Fan, K., Li, Y., Zhong, H., & Fu, H. (2018). Pattern selection of twinned growth in aluminum alloys during Bridgman solidification. *Journal of Alloys and Compounds*, *741*, 131-140.
116. Jaradeh, M., & Carlberg, T. (2007). Analysis of solidification in Bridgman furnace as simulation of DC casting of aluminium alloy slabs. *Materials science and technology*, Volume *23, Issue* 4, 475-482.
117. Cui, C., Lai, Y., Liu, W., Wang, P., Liu, Y., Wang, C., & Su, H. (2019). Tensile and fatigue properties of the Bridgman directionally solidified Fe-Al-Ta eutectic. *Materials Science and Engineering: A*, *765*, 138257.
118. Chakraborty, S., Gadkari, S., Steinmetz, P., Monroe, C. A., & Genau, A. L. (2019). Evolution of Microstructure in Directionally Solidified Cast Iron Treated with Cerium and Magnesium. *Metallurgical and Materials Transactions A*, *50*(6), 2922-2932.
119. Liu, L., Huang, T., Qu, M., Liu, G., Zhang, J., & Fu, H. (2010). High thermal gradient directional solidification and its application in the processing of nickel-based superalloys. *Journal of Materials Processing Technology*, *210*(1), 159-165.
120. Han, Y. S., Choi, J. O., Choi, C. O., & McCartney, D. G. (2004). Intermetallic phase formation in directionally solidified Al− Si− Fe alloy. *Metals and Materials International*, *10*(1), 27-32.
121. Mooney, R. P., McFadden, S., Gabalcová, Z., & Lapin, J. (2014). An experimental–numerical method for estimating heat transfer in a Bridgman furnace. *Applied Thermal Engineering*, *67*(1-2), 61-71.
122. Ghedjati, K., Fleury, E., Hamani, M. S., Benchiheub, M., Bouacha, K., & Bolle, B. (2015). Elaboration of AlSi10Mg casting alloys using directional solidification processing. *International Journal of Minerals, Metallurgy, and Materials*, *22*(5), 509-515.
123. Shaojun Liu, Guangyu Yang, Wanqi Jie. Microstructure, Microsegregation, and Mechanical Properties of Directional Solidified Mg-3.0Nd-1.5Gd Alloy. *Acta Metallurgica Sinica(English Letters)*, 27(6): 1134-1143.
124. Cui, C., Wang, C., Wang, P., Liu, W., Lai, Y., Deng, L., & Su, H. (2020). Microstructure and fracture toughness of the Bridgman directionally solidified Fe-Al-Ta eutectic at different solidification rates. *Journal of Materials Science & Technology*, *42*, 63-74.
125. Liu H., Xie J., Zhong H., Zhai Q., Fu J. (2019) Dependency of Microstructure and Inclusions on the Different Growth Rate for Directionally Solidified Non-quenched and Tempered Steel. In: Jiang T. et al. (eds) 10th International Symposium on High-Temperature Metallurgical Processing. The Minerals, Metals & Materials Series. Springer, Cham 10th International Symposium on High-Temperature Metallurgical Processing pp 279-287.
126. Niknafs, S., & Dippenaar, R. (2014). Experimentally-aided simulation of directional solidification of steel. *ISIJ international*, *54*(3), 526-532.
127. Ma, J. C., Yang, Y. S., Tong, W. H., Fang, Y., Yu, Y., & Hu, Z. Q. (2007). Microstructural evolution in AISI 304 stainless steel during directional solidification and subsequent solid-state transformation. *Materials Science and Engineering: A*, *444*(1-2), 64-68.
128. Liu, J., Su, X., Liu, H., Han, Z., He, Y., & Qiu, S. (2017). Solidification interface transformation and solute redistribution of FeCrAl stainless steel. *Metallurgical Research & Technology*, *114*(4), 409.
129. Hou, Y., Zhang, Z. Q., Xuan, W. D., Wang, J., Yu, J. B., & Ren, Z. M. (2018). Grain refinement during directionally solidifying GCr18Mo steel at low pulling speeds under an axial static magnetic field. *Acta Metallurgica Sinica (English Letters)*, *31*(7), 681-691.

130. Agarwal, G., Amirthalingam, M., Moon, S. C., Dippenaar, R. J., Richardson, I. M., & Hermans, M. J. M. (2018). Experimental evidence of liquid feeding during solidification of a steel. *Scripta Materialia*, *146*, 105-109.
131. Park, K., Gu, J., Lee, J., Seo, S., Jeong, H., Shin, J., & Sim, K. (2013). Solidification and Segregation Behaviors during Directional Solidification of High Chromium Martensitic Steels. *Journal of the Korean Institute of Metals and Materials*, *51*(3), 211-220.
132. Böttger, B., Apel, M., Eiken, J., Schaffnit, P., & Steinbach, I. (2008). Phase-Field Simulation of Solidification and Solid-State Transformations in Multicomponent Steels. *steel research international*, *79*(8), 608-616.
133. Dhindaw, B. K., Antonsson, T., Fredriksson, H., & Tinoco, J. (2004). Characterization of the peritectic reaction in medium-alloy steel through microsegregation and heat-of-transformation studies. *Metallurgical and Materials Transactions A*, *35*(9), 2869-2879.
134. Ferrandini, P. L., Rios, C. T., Dutra, A. T., Jaime, M. A., Mei, P. R., & Caram, R. (2006). Solute segregation and microstructure of directionally solidified austenitic stainless steel. *Materials Science and Engineering: A*, *435*, 139-144.
135. Shen, Y., Liu, J., Yang, S., Yan, B., He, Y., Liu, H., & Xu, H. (2019). Dendrite growth behavior in directionally solidified Fe–C–Mn–Al alloys. *Journal of Crystal Growth*, Volume *511*, 118-126.
136. Górecki, K., Bala, P., Cios, G., Koziel, T., Stępień, M., & Wieczerzak, K. (2016). The influence of cooling rate during crystallization on the effective partitioning coefficient in high-entropy alloys from Al-Ti-Co-Ni-Fe system. *Metallurgical and Materials Transactions A*, *47*(7), 3257-3262.
137. Shi, X., Duan, S. C., Yang, W. S., Guo, H. J., & Guo, J. (2018). Effect of cooling rate on microsegregation during solidification of superalloy INCONEL 718 under slow-cooled conditions. *Metallurgical and Materials Transactions B*, *49*(4), 1883-1897.
138. Hao, Y., Li, J., Li, X., Liu, W., Cao, G., Li, C., & Liu, Z. (2020). Influences of cooling rates on solidification and segregation characteristics of Fe-Cr-Ni-Mo-N super austenitic stainless steel. *Journal of Materials Processing Technology*, *275*, 116326.
139. Gui, L., Long, M., Huang, Y., Chen, D., Chen, H., Duan, H., & Yu, S. (2018). Effects of inclusion precipitation, partition coefficient, and phase transition on microsegregation for high-sulfur steel solidification. *Metallurgical and Materials Transactions B*, *49*(6), 3280-3292.
140. Nouri, A., Saghafian, H., & Kheirandish, S. (2010). Effects of silicon content and intercritical annealing on manganese partitioning in dual phase steels. *Journal of Iron and Steel Research, International*, *17*(5), 44-50.
141. Gui, L., Long, M., Wu, S., Dong, Z., Chen, D., Huang, Y., ... & Vitos, L. (2019). Quantitative effects of phase transition on solute partition coefficient, inclusion precipitation, and microsegregation for high-sulfur steel solidification. *Journal of Materials Science & Technology*, *35*(10), 2383-2395.
142. MC Flemings, M. C., Poirier, D. R., & RV, R. B. (1970). Microsegregation in iron-base alloys. In *Journal of Iron and Steel Institute (London)* vol 208 (pp. 371-381).
143. Lacaze, J., Benigni, P., & Howe, A. (2003). Some issues concerning experiments and models for alloy microsegregation. *Advanced Engineering Materials*, *5*(1-2), 37-46.
144. Xie, F. Y., Kraft, T., Zuo, Y., Moon, C. H., & Chang, Y. A. (1999). Microstructure and microsegregation in Al-rich Al–Cu–Mg alloys. *Acta Materialia*, *47*(2), 489-500.

145. Xie, F., Yan, X., Ding, L., Zhang, F., Chen, S., Chu, M. G., & Chang, Y. A. (2003). A study of microstructure and microsegregation of aluminum 7050 alloy. *Materials Science and Engineering: A*, *355*(1-2), 144-153.
146. Lacaze, J., & Lesoult, G. R. (1993). Experimental investigation of the development of microsegregation during solidification of an Al□ Cu□ Mg□ Si aluminium alloy. *Materials Science and Engineering: A*, *173*(1-2), 119-122.
147. Lacaze, J., & Lesoult, G. (1995). Modelling the development of microsegregation during solidification of an Al-Cu-Mg-Si alloy. *ISIJ international*, *35*(6), 658-664.
148. Beech, J., & Jones, H. (1997). Solidification Processing 1997. In *4 th Decennial International Conference on Solidification Processing* (p. 1997).
149. Fuchs, G. E. (2001). Solution heat treatment response of a third generation single crystal Ni-base superalloy. *Materials Science and Engineering: A*, *300*(1-2), 52-60.
150. Tin, S., & Pollock, T. M. (2003). Phase instabilities and carbon additions in single-crystal nickel-base superalloys. *Materials Science and Engineering: A*, *348*(1-2), 111-121.
151. Gungor, M. N. (1989). A statistically significant experimental technique for investigating microsegregation in cast alloys. *Metallurgical Transactions A*, *20*(11), 2529-2533.
152. Yang, W., Chang, K. M., Chen, W., Mannan, S., & DeBarbadillo, J. (2000). Monte carlo sampling for microsegregation measurements in cast structures. *Metallurgical and Materials Transactions A*, *31*(10), 2569-2574.
153. W. Yang, W. Chen, K.M. Chang, S. Manna, and J. DeBarbadillo: in Superalloys 2000, T.M. Pollock, R.D. Kissinger, R.R. Bowman, K.A. Green, M. McLean, S. Olson, and J.J. Schirra, eds., TMS, Seven Springs, PA, 2000, pp. 75-84.
154. Ganesan, M., Dye, D., & Lee, P. D. (2005). A technique for characterizing microsegregation in multicomponent alloys and its application to single-crystal superalloy castings. *Metallurgical and Materials Transactions A*, *36*(8), 2191-2204.
155. Smith, R. (2018). Microsegregation measurement: methods and applications. *Metallurgical and Materials Transactions B*, *49*(6), 3258-3279.
156. Cappel, J., Flender, R., Höffken, R., Kemper, G., & Wünnenberg, K. (2005). Centre segregation, soft reduction and oxide cleanness for large diameter line pipe with highest demands on HIC. *steel research international*, *76*(8), 588-594.
157. Bleck, W., Wang, W., & Bülte, R. (2006). Influence of soft reduction on internal quality of high carbon steel billets. *steel research international*, *77*(7), 485-491.
158. Thome, R., & Harste, K. (2004). Study on the Design of the Soft Reduction Unit of High-Speed Billet Casters. *steel research international*, *75*(10), 693-700.
159. Thome, R., & Harste, K. (2006). Principles of billet soft-reduction and consequences for continuous casting. *ISIJ international*, *46*(12), 1839-1844.
160. Humes, D. M., Korzi, M. J., Kozak, B. A., & Laughlin, J. T. (2008). Dynamic soft reduction of continuously cast slabs. *Iron & steel technology*, *5*(7), 29-36.
161. Byrne, C., & Tercelli, C. (2002). Mechanical soft reduction in billet casting. *Steel Times International*, *26*(9), 33.
162. Morsut, L. (2003). Technological packages for the effective control of slab casting. *Metallurgical Plant and Technology International*, *26*(2), 44-46.
163. Mörwald, K., Thalhammer, M., Federspiel, C., & Gould, L. (2002). Benefits of SMART® segment technology and ASTC strand taper control in continuous casting. *Steel Times International*, *27*(1), 17.

164. Sivesson, P., Raihle, C. M., & Konttinen, J. (1993). Thermal soft reduction in continuously cast slabs. *Materials Science and Engineering: A*, *173*(1-2), 299-304.
165. Sivesson, P., Örtlund, T., & Widell, B. (1996). Improvement of inner quality in continuously cast billets through thermal soft reduction and use of multivariate analysis of saved process variables. *Ironmaking & steelmaking*, *23*(6), 504-511.
166. Sivesson, P., Hallen, G., & Widell, B. (1998). Improvement of inner quality of continuously cast billets using electromagnetic stirring and thermal soft reduction. *Ironmaking & steelmaking*, *25*(3), 239.
167. Raihle, C. M., Sivesson, P., Tukiainen, M., & Fredriksson, H. (1994). Improving inner quality in continuously cast billets: comparison between mould electromagnetic stirring and thermal soft reduction. *Ironmaking & steelmaking*, *21*(6), 487-495.
168. Li, J., Wang, B., Ma, Y., & Cui, J. (2006). Effect of complex electromagnetic stirring on inner quality of high carbon steel bloom. *Materials Science and Engineering: A*, *425*(1-2), 201-204.
169. Ludlow, V., Normanton, A., Anderson, A., Thiele, M., Ciriza, J., Laraudogoitia, J., & Van Der Knoop, W. (2005). Strategy to minimise central segregation in high carbon steel grades during billet casting. *Ironmaking & steelmaking*, *32*(1), 68-74.
170. Luo, S., Zhu, M., & Ji, C. (2014). Theoretical model for determining optimum soft reduction zone of continuous casting steel. *Ironmaking & Steelmaking*, *41*(3), 233-240.
171. Ji, C., Zhu, M. Y., Cheng, N. L., Guo, Z. H., & Leng, X. G. (2008). Development and Application of Dynamic Soft Reduction Control Model for Slab Caster [J]. *Iron & Steel*, *9*.
172. Litju, K. M. R. P. K., Termi, S. S., & Modelom, N. (2015). Control of soft reduction of continuous slab casting with a thermal model. *Materiali in tehnologije*, *49*(5), 725-729.
173. Kong, Y. W., Feng, K., Han, Z. W., & Cao, J. F. (2011). The Industrial Application of Dynamic Soft-Reduction Technology on the No.1 Slab Continuous Caster in No.2 Steelmaking Plant of Xinyu Steel. Applied Mechanics and Materials, 120, 510–515.
174. Ji, C., Luo, S., & Zhu, M. (2014). Analysis and application of soft reduction amount for bloom continuous casting process. *ISIJ international*, *54*(3), 504-510.
175. Lin, Q., & Zhu, M. (2007). Theoretical model and analysis of soft reduction gradient for continuous casting slab. *Acta Metallurgica Sinica-Chinese Edition-*, *43*(8), 847-850.
176. Wu, M., Domitner, J., & Ludwig, A. (2012). Using a two-phase columnar solidification model to study the principle of mechanical soft reduction in slab casting. *Metallurgical and Materials Transactions A*, *43*(3), 945-964.
177. Luo, S., Zhu, M., & Louhenkilpi, S. (2012). Numerical simulation of solidification structure of high carbon steel in continuous casting using cellular automaton method. *ISIJ international*, *52*(5), 823-830.
178. Luo, S., Zhu, M. Y., Ji, C., & Chen, Y. (2010). Characteristics of solute segregation in continuous casting bloom with dynamic soft reduction and determination of soft reduction zone. *Ironmaking & Steelmaking*, *37*(2), 140-146.
179. Luo, S., Zhu, M. Y., Ji, C., Yang, Y. B., & Yang, J. L. (2010). Deformation behavior of continuous casting blooms during soft reduction process. *Journal of University of Science and Technology Beijing*, *32*(7), 890-894.
180. Lynch, P. C., & Grimm, T. J. (2019). Reducing Microsegregation in Next-Generation High-Strength Low-Alloy Cast Steels. *International Journal of Metalcasting*, *13*(4), 783-792.
181. Malinovskaya, T. I., Kurasov, A. H., Glaskova, G. V., & Spektor, Y. I. (1975). Effect of homogenization of dendritic segregation of chromium and manganese in steel ShKh15. *Metal Science and Heat Treatment*, *17*(7), 609-610.

182. Khan, F. A. (2018). The effect of soaking on segregation and primary-carbide dissolution in ingot-cast bearing steel. *Metals*, *8*(10), 800.
183. Fossaert, C., Rees, G., Maurickx, T., & Bhadeshia, H. K. D. H. (1995). The effect of niobium on the hardenability of microalloyed austenite. *Metallurgical and Materials Transactions A*, *26*(1), 21-30.
184. Kim, K. H., Park, S. D., & Bae, C. M. (2014). New approach to the soaking condition of 100Cr6 high-carbon chromium bearing steel. *Metals and Materials International*, *20*(2), 207-213.
185. Reger, M., Vero, B., Felde, I., & Kardos, I. (2010). The effect of heat treatment on the stability of centerline segregation. *J. Mech. Eng*, *56*(2), 143-149.
186. Lippard, H. E., Campbell, C. E., Dravid, V. P., Olson, G. B., Björklind, T., Borggren, U., & Kellgren, P. (1998). Microsegregation behavior during solidification and homogenization of AerMet100 steel. *Metallurgical and Materials Transactions B*, *29*(1), 205-210.
187. Villanueva-Perez, O. E., Mejía, I., García-García, V., & Bedolla-Jacuinde, A. (2018). Metallographic, Structural and Mechanical Characterization of a Low Density Fe-Mn-Al-C Steel Microalloyed with Ti/B in As-Cast and Homogenized Conditions. *MRS Advances*, *3*(64), 3971-3978.
188. Naghizadeh, M., & Mirzadeh, H. (2016). Microstructural evolutions during annealing of plastically deformed AISI 304 austenitic stainless steel: martensite reversion, grain refinement, recrystallization, and grain growth. *Metallurgical and Materials Transactions A*, *47*(8), 4210-4216.
189. Abuluwefa, H. T. (2013). Optimizing the process of steel slab reheating in pusher type reheat furnace prior to hot working. In *Applied Mechanics and Materials* (Vol. 325, pp. 364-370). Trans Tech Publications Ltd.
190. Lee, H., Park, K. S., Lee, J. H., Heo, Y. U., Suh, D. W., & Bhadeshia, H. K. D. H. (2014). Dissolution behaviour of NbC during slab reheating. *ISIJ international*, *54*(7), 1677-1681.
191. Hong, S. G., Jun, H. J., Kang, K. B., & Park, C. G. (2003). Evolution of precipitates in the Nb–Ti–V microalloyed HSLA steels during reheating. *Scripta materialia*, *48*(8), 1201-1206.
192. Davis, C. L., & Strangwood, M. (2002). Preliminary study of the inhomogeneous precipitate distributions in Nb-microalloyed plate steels. *Journal of materials science*, *37*(6), 1083-1090.
193. Jung, J. G., Park, J. S., Ha, Y. S., Lee, Y. K., Bae, J. H., & Kim, K. (2008). Dissolution Behavior of Complex Carbonitrides in a Microalloyed Steel. *Journal of the Korean Society for Heat Treatment*, *21*(6), 287-292.
194. Nöhrer, M., Zamberger, S., & Leitner, H. (2013). Strain-induced precipitation behavior of a Nb–Ti–V steel in the austenite phase field. *steel research international*, *84*(9), 827-836.
195. Yuan, S. Q., & Liang, G. L. (2009). Dissolving behaviour of second phase particles in Nb–Ti microalloyed steel. *Materials Letters*, *63*(27), 2324-2326.
196. Palmiere E J, Garcia C I, DeArdo A J; "Compositional and microstructural changes which attend reheating and grain coarsening in steels containing niobium"; Metallurgical and Materials Transactions A, v 25A, n 2, (1994), pp. 277-286.
197. Han, S. H., Chang, D., & Kim, C. Y. (2010). A numerical analysis of slab heating characteristics in a walking beam type reheating furnace. *International Journal of Heat and Mass Transfer*, *53*(19-20), 3855-3861.
198. Pereda, B., Uranga, P., López, B., Rodriguez-Ibabe, J. M., Stalheim, D., Barbosa, R., & Rebellato, M. A. (2016). Through-Thickness Homogenization in Thin Slab Direct Rolling of

Nb Microalloyed Steels. In *HSLA Steels 2015, Microalloying 2015 & Offshore Engineering Steels 2015* (pp. 309-315). Springer, Cham.
199. Xia, Q., Wang, X., & Tang, L. (2016). Operation optimization of slab reheating process based on differential evolution. *ISIJ International*, *56*(11), 2006-2015.
200. Chen, W. H., Lin, M. R., & Leu, T. S. (2010). Optimal heating and energy management for slabs in a reheating furnace. *Journal of Marine Science and Technology*, *18*(1), 24-31.
201. Han, S. H., Baek, S. W., & Kim, M. Y. (2009). Transient radiative heating characteristics of slabs in a walking beam type reheating furnace. *International Journal of Heat and Mass Transfer*, *52*(3-4), 1005-1011.
202. Tang, G., Saavedra, A., Okosun, T., Wu, B., Zhou, C. Q., Bai, D., ... & Bodnar, R. (2016, July). Modeling of steel slab reheating process in a walking beam reheating furnace. In *Heat Transfer Summer Conference* (Vol. 50336, p. V002T15A005). American Society of Mechanical Engineers.
203. Lee, D. E., & Kim, M. Y. (2013). Optimum residence time for steel productivity and energy saving in a hot rolled reheating furnace. *Journal of Mechanical Science and Technology*, *27*(9), 2869-2877.
204. John G. Lenard, 1 - Introduction, Editor(s): John G. Lenard, Primer on Flat Rolling (Second Edition), Elsevier, 2014, Pages 1-15.
205. Gong, M., Li, H., Wang, B., Wang, Z., & Misra, R. D. K. (2019). Interaction of Strain Refined Precipitates and Recrystallized Grains in Nb-Ti Microalloyed Steel during Continuous Casting, Hot-Core Heavy Reduction Rolling, and Reheating Process. *Journal of Materials Engineering and Performance*, *28*(6), 3539-3550.
206. Maalekian, M., Radis, R., Militzer, M., Moreau, A., & Poole, W. (2012). In situ measurement and modelling of austenite grain growth in a Ti/Nb microalloyed steel. *Acta materialia*, *60*(3), 1015-1026.
207. Wang, F., Strangwood, M., & Davis, C. (2019). Grain growth during reheating of HSLA steels with a narrow segregation separation. *Materials Science and Technology*, *35*(16), 1963-1976.
208. Napitupulu, R. A. (2017, September). Influence of heating rate and temperature on austenite grain size during reheating steel. In *IOP Conference Series: Materials Science and Engineering* (Vol. 237, No. 1, p. 012038). IOP Publishing.
209. Shirdel, M., Mirzadeh, H., & Parsa, M. H. (2014). Microstructural evolution during normal/abnormal grain growth in austenitic stainless steel. *Metallurgical and Materials Transactions A*, *45*(11), 5185-5193.
210. Shirdel, M., Mirzadeh, H., & Parsa, M. H. (2014). Abnormal grain growth in AISI 304L stainless steel. *Materials characterization*, *97*, 11-17.
211. Zhang, S. S., Li, M. Q., Liu, Y. G., Luo, J., & Liu, T. Q. (2011). The growth behavior of austenite grain in the heating process of 300M steel. *Materials Science and Engineering: A*, *528*(15), 4967-4972.
212. Alibeyki, M., Mirzadeh, H., & Najafi, M. (2018). The effects of primary thermo-mechanical processing routes and intercritical annealing on the mechanical properties of st37 low carbon steel. *Kovove Mater*, *56*, 297-303.
213. Azizi, G., Mirzadeh, H., & Habibi Parsa, M. (2016). Unraveling the Effect of Homogenization Treatment on Decomposition of Austenite and Mechanical Properties of Low-Alloyed TRIP Steel. *steel research international*, *87*(7), 820-823.
214. Chakrabarti, D., Strangwood, M., & Davis, C. (2009). Effect of bimodal grain size distribution on scatter in toughness. *Metallurgical and Materials Transactions A*, *40*(4), 780-795.

215. Wu, S. J., & Davis, C. L. (2004). Effect of duplex ferrite grain size distribution on local fracture stresses of Nb-microalloyed steels. *Materials Science and Engineering: A*, *387*, 456-460.
216. Davut, K., & Zaefferer, S. (2012). The Effect of Size and Shape of Austenite Grains on the Mechanical Properties of a Low-Alloyed TRIP Steel. *steel research international*, *83*(6), 584-589.
217. Cui, J., Liu, Y. Z., Pan, H., & Gao, L. F. (2008). Reheating austenitizing temperature of spring steel 60Si2MnA for railway. *Journal of Iron and Steel Research International*, *15*(6), 62-67.
218. Ai, J. H., Zhao, T. C., Gao, H. J., Hu, Y. H., & Xie, X. S. (2005). Effect of controlled rolling and cooling on the microstructure and mechanical properties of 60Si2MnA spring steel rod. *Journal of Materials Processing Technology*, *160*(3), 390-395.
219. Jacobi, H. F. (2003). Investigation of Centreline Segregation and Centreline Porosity in CC-Slabs. *steel research international*, *74*(11-12), 667-678.
220. He, S., Li, C., Ren, J., & Han, Y. (2018). Investigation on Alloying Element Distribution in Cr8Mo2SiV Cold-Work Die Steel Ingot during Homogenization. *steel research international*, *89*(10), 1800148.
221. Han, Y., Li, C., Ren, J., Qiu, C., Zhang, Y., & Wang, J. (2019). Dendrite segregation changes in high temperature homogenization process of As-cast H13 steel. *ISIJ International*, ISIJINT-2019.
222. Ray, A. (2005). Electron-probe microanalysis: some revelations in the investigation of defects in steel products. In *Materials Science Forum* (Vol. 492, pp. 627-634). Trans Tech Publications Ltd.
223. Collins, L. E., Wei, P., Nafisi, S., Wang, P., & Wiskel, J. B. (2016, September). Effects of Segregation on the Mechanical Performance of X70 Line Pipe. In *International Pipeline Conference* (Vol. 50275, p. V003T05A028). American Society of Mechanical Engineers.
224. He, S., Li, C., Guo, R., Xuan, W., Wang, J., & Ren, Z. (2019). Evolution of microsegregation in directionally solidified Al–Cu alloys under steady magnetic field. *Journal of Alloys and Compounds*, *800*, 41-49.
225. Liu, H., Liu, J., Wu, B., Shen, Y., He, Y., Ding, H., & Su, X. (2017). Effect of Mn and Al contents on hot ductility of high alloy Fe-xMn-C-yAl austenite TWIP steels. *Materials Science and Engineering: A*, *708*, 360-374.
226. Ren, X., Fu, H., Xing, J., Yang, Y., & Tang, S. (2017). Effect of boron concentration on microstructures and properties of Fe–B–C alloy steel. *Journal of Materials Research*, *32*(16), 3078-3088.
227. Basso, A., Toda-Caraballo, I., San-Martín, D., & Caballero, F. G. (2020). Influence of cast part size on macro-and microsegregation patterns in a high carbon high silicon steel. *Journal of Materials Research and Technology*.
228. HajyAkbary, F., Sietsma, J., Petrov, R. H., Miyamoto, G., Furuhara, T., & Santofimia, M. J. (2017). A quantitative investigation of the effect of Mn segregation on microstructural properties of quenching and partitioning steels. *Scripta Materialia*, *137*, 27-30.
229. Xu, X. J., Song, L., Jin, X. O., Han, D. D., Wang, X., & Lin, J. P. (2016). Microstructure and microsegregation of directionally solidified Ti–45Al–8Nb alloy with different solidification rates. *Rare Metals*, *35*(1), 70-76.
230. Jia'an, W., Jiahe, W., & Zhongxiao, S. (2017). Microstructures and microsegregation of directionally solidified Mg-1.5 Gd magnesium alloy with different growth rates. *Rare Metal Materials and Engineering*, *46*(1), 12-16.

231. Shen, Y., Yang, S., Liu, J., Liu, H., Zhang, R., Xu, H., & He, Y. (2019). Study on Micro Segregation of High Alloy Fe–Mn–C–Al Steel. *steel research international*, *90*(5), 1800546.
232. Zhao, D., Zhang, Y., & Essene, E. J. (2015). Electron probe microanalysis and microscopy: Principles and applications in characterization of mineral inclusions in chromite from diamond deposit. *Ore Geology Reviews*, *65*, 733-748.
233. Frahm E. (2017) Scanning Electron Microscopy (SEM). Gilbert, A. S., Goldberg, P., Holliday, V. T., Mandel, R. D., & Sternberg, R. S. (Eds.). (2017). *Encyclopedia of geoarchaeology*. Springer Netherlands.
234. https://epmalab.uoregon.edu/epmatext.htm
235. JEOL 8200 ELECTRON MICROPROBE (EPMA), THE UNIVERSITY OF TEXAS AT AUSTIN, http://www.jsg.utexas.edu/microbeam/epma/
236. Geochemical Instrumentation and Analysis, **Electron probe micro-analyzer (EPMA),** John Goodge, University of Minnesota-Duluth; https://serc.carleton.edu/research_education/geochemsheets/techniques/EPMA.html
237. Reed, S. J. B. (2005). *Electron microprobe analysis and scanning electron microscopy in geology*. Cambridge university press.
238. Thompson, K. (2018). Advances in SDD-based EDS and Comparisons to WDS for Light Element Sensitivity. *Microscopy and Microanalysis*, *24*(S1), 754-755.
239. Allaz, J. M., Popa, R. G., Reusser, E., & Martin, L. (2019). Electron Microprobe Analysis of Minor and Trace Elements in Beam Sensitive Materials: How Far Can We Go?. *Microscopy and Microanalysis*, *25*(S2), 2312-2313.
240. Zeng, Y. N., Li, J. G., & Wang, Y. J. (2019). Thermodynamic and Kinetic Analysis of Inhomogeneous Distribution of Solute on Precipitations in as Cast Nb–V–Ti Microalloyed Steel. In *TMS 2019 148th Annual Meeting & Exhibition Supplemental Proceedings* (pp. 1237-1247). Springer, Cham.
241. Wang, W., Zhu, C., Zeng, J., Lu, C., Lyu, P., Qian, H., & Xu, H. (2020). MnS Precipitation Behavior of High-Sulfur Microalloyed Steel Under Sub-rapid Solidification Process. *Metallurgical and Materials Transactions B*, *51*(1), 45-53.
242. Yang, S., Gao, Y., Xue, X., & Li, B. (2018). Influence of titanium on transformation behaviour during continuous cooling of boron microalloyed steels. *Ironmaking & Steelmaking*, *45*(10), 959-968.
243. Ilie, S., Preßlinger, H., Reisinger, P., Mayr, M., & Etzelsdorfer, K. (2007). Results of research into the segregation behaviour of manganese, silicon and chromium in continuous casting. *steel research international*, *78*(4), 327-332.
244. Yamashita, T., Torizuka, S., & Nagai, K. (2003). Effect of manganese segregation on fine-grained ferrite structure in low-carbon steel slabs. *ISIJ international*, *43*(11), 1833-1841.
245. Senk, D., Erdem, E., & Stratemeier, S. (2009). Statistical analysis of EPMA results for numerical modelling of micro-segregation in steel. *International Journal of Cast Metals Research*, *22*(1-4), 94-98.
246. Yan, C., Ju, X., Meng, Y., & Shi, X. (2019). Quantification of manganese dendritic segregation in 380CL steel billet by electron probe microanalysis. *SN Applied Sciences*, *1*(6), 623.
247. Wang, P. (2017). Characterization of Centreline Segregation of Continuously Cast Microalloyed Pipeline Steel.

248. Preßlinger, H., Ilie, S., Reisinger, P., Schiefermüller, A., Pissenberger, A., Parteder, E., & Bernhard, C. (2006). Methods for assessment of slab centre segregation as a tool to control slab continuous casting with soft reduction. *ISIJ international*, *46*(12), 1845-1851.
249. Flemings, M.C. (2001) Solute Segregation, Encyclopedia of Materials: Science and Technology, Elsevier, 8753-8755.
250. https://www.cameca.com/products/epma/technique
251. https://www.thermocalc.com/
252. Scheil, E. (1942). Bemerkungen zur schichtkristallbildung. *Zeitschrift für Metallkunde*, *34*(3), 70-72.
253. Xiong, M., Kuznetsov, A. Comparison between Lever and Scheil Rules for Modeling of Microporosity Formation during Solidification. *Flow, Turbulence and Combustion* **67,** 305–323 (2001).
254. Kumar, T. P. (2014). Casting Simulation Methods.
255. Flemings, M.C. (1974) Solidification processing Mcgraw-Hill College New York.
256. Ghosh, S. (2015). *Effects of solid-solid boundary anisotropy on directional solidification microstructures* (Doctoral dissertation).
257. Schmid-Fetzer, R. (2014). Phase diagrams: the beginning of wisdom. *Journal of Phase Equilibria and Diffusion*, *35*(6), 735-760.
258. Zhang, C., Jahazi, M., & Isabel Gallego, P. (2020). On the impact of microsegregation model on the thermophysical and solidification behaviors of a large size steel ingot. *Metals*, *10*(1), 74.
259. Wu, M., Li, J., Ludwig, A., & Kharicha, A. (2013). Modeling diffusion-governed solidification of ternary alloys–Part 1: Coupling solidification kinetics with thermodynamics. *Computational materials science*, *79*, 830-840.
260. Wikimedia Commons contributors, "File:Scheil graphics.gif," *Wikimedia Commons, the free media repository,* https://commons.wikimedia.org/w/index.php?title=File:Scheil_graphics.gif&oldid=69615131 (accessed May 26, 2020).
261. Du, Y., Chang, Y. A., Liu, S., Huang, B., Xie, F. Y., Yang, Y., & Chen, S. L. (2005). Thermodynamic description of the Al–Fe–Mg–Mn–Si system and investigation of microstructure and microsegregation during directional solidification of an Al–Fe–Mg–Mn–Si alloy. *Zeitschrift für Metallkunde*, *96*(12), 1351-1362.
262. Klančnik, G., Medved, J., Nagode, A., Novak, G., & Petrovič, D. S. (2014). Influence of Mn on the solidification of Fe–Si–Al alloy for non-oriented electrical steel. *Journal of Thermal Analysis and Calorimetry*, *116*(1), 295-302.
263. Yan, X., Chen, S., Xie, F., & Chang, Y. A. (2002). Computational and experimental investigation of microsegregation in an Al-rich Al–Cu–Mg–Si quaternary alloy. *Acta materialia*, *50*(9), 2199-2207.
264. Bower, T. F., Brody, H. D., & Flemings, M. C. (1966). Measurements of solute redistribution in dendritic solidification. *Transaction of the Metallurgical Society of AIME*, *236*, 624-633.
265. Clyne, T. W., & Kurz, W. (1981). Solute redistribution during solidification with rapid solid state diffusion. *Metallurgical Transactions A*, *12*(6), 965-971.
266. Ohnaka, I. (1986). Mathematical analysis of solute redistribution during solidification with diffusion in solid phase. *Transactions of the Iron and Steel Institute of Japan*, *26*(12), 1045-1051.

267. Voller, V. R., & Beckermann, C. (1999). A unified model of microsegregation and coarsening. *Metallurgical and Materials Transactions A*, *30*(8), 2183-2189.
268. Ueshima, Y., Mizoguchi, S., Matsumiya, T., & Kajioka, H. (1986). Analysis of solute distribution in dendrites of carbon steel with δ/γ transformation during solidification. *Metallurgical Transactions B*, *17*(4), 845-859.
269. Nastac, L., & Stefanescu, D. M. (1993). An analytical model for solute redistribution during solidification of planar, columnar, or equiaxed morphology. *Metallurgical Transactions A*, *24*(9), 2107-2118.
270. Lee, H. M., Bae, J. S., Soh, J. R., Kim, S. K., & Lee, Y. D. (1998). Diffusional solidification behavior in 304 stainless steel. *Materials transactions, JIM*, *39*(6), 633-639.
271. You, D., Bernhard, C., Wieser, G., & Michelic, S. (2016). Microsegregation model with local equilibrium partition coefficients during solidification of steels. *steel research international*, *87*(7), 840-849.
272. Sun, H., & Zhang, J. (2014). Macrosegregation improvement by swirling flow nozzle for bloom continuous castings. *Metallurgical and materials transactions B*, *45*(3), 936-946.
273. Liu, Z., Wei, J., & Cai, K. (2002). A coupled mathematical model of microsegregation and inclusion precipitation during solidification of silicon steel. *ISIJ international*, *42*(9), 958-963.
274. Kagawa, A., Hirata, M., & Sakamoto, Y. (1990). Solute partitioning on solidification of nickel-base ternary alloys. *Journal of materials science*, *25*(12), 5063-5069.
275. Sung, P. K., & Poirier, D. R. (1999). Liquid-solid partition ratios in nickel-base alloys. *Metallurgical and Materials Transactions A*, *30*(8), 2173-2181.
276. Gui, L., Duan, H., Huang, Y., & Liu, T. (2018). Effect of MnS precipitation on solute equilibrium partition coefficients in high sulfur steel during solidification. *Journal of Materials Research*, *33*(20), 3490-3500.
277. Chen, H., Long, M., Cao, J., Chen, D., Liu, T., & Dong, Z. (2017). Phase transition of peritectic steel Q345 and its effect on the equilibrium partition coefficients of solutes. *Metals*, *7*(8), 288.
278. Niessen, F., Tiedje, N. S., & Hald, J. (2017). Kinetics modeling of delta-ferrite formation and retainment during casting of supermartensitic stainless steel. *Materials & Design*, *118*, 138-145.
279. Lindwall, G., & Frisk, K. (2012). Assessment and evaluation of mobilities for diffusion in the bcc Cr-Mo-Fe system. *Journal of phase equilibria and diffusion*, *33*(5), 375-389.
280. Kozeschnik, E. (2000). A Scheil-Gulliver model with back-diffusion applied to the microsegregation of chromium in Fe-Cr-C alloys. *Metallurgical and Materials Transactions A*, *31*(6), 1682-1684.
281. E. Kozeschnik, W. Rindler, and B. Buchmayr (2007). Scheil–Gulliver simulation with partial redistribution of fast diffusers and simultaneous solid–solid phase transformations. International Journal of Materials Research: Vol. 98, No. 9, pp. 826-831.
282. Koshikawa, T., Gandin, C. A., Bellet, M., Yamamura, H., & Bobadilla, M. (2014). Computation of phase transformation paths in steels by a combination of the partial-and para-equilibrium thermodynamic approximations. *ISIJ international*, *54*(6), 1274-1282.
283. Ferreira, A. F., & Ferreira, L. D. O. (2009). Microsegregation in Fe-C-P ternary alloys using a phase-field model. *Journal of the Brazilian Society of Mechanical Sciences and Engineering*, *31*(3), 173-180.

284. Krauss, G. (2003). Solidification, segregation, and banding in carbon and alloy steels. *Metallurgical and Materials Transactions B*, *34*(6), 781-792.
285. Lee, S. J., Matlock, D. K., & Van Tyne, C. J. (2011). Carbon diffusivity in multi-component austenite. *Scripta Materialia*, *64*(9), 805-808.
286. Andersson, J. O., Helander, T., Höglund, L., Shi, P., & Sundman, B. (2002). Thermo-Calc & DICTRA, computational tools for materials science. *Calphad*, *26*(2), 273-312.
287. MatCalc, 2014, "MatCalc," "matcalc.tuwien.ac.at (Last accessed 14 Jan 2015).
288. Lage, M. G. (2015). Evaluating segregation in HSLA steels using computational thermodynamics. *Journal of Materials Research and Technology*, *4*(4), 353-358.
289. Schaffnit, P., Stallybrass, C., Konrad, J., Stein, F., & Weinberg, M. (2015). A Scheil–Gulliver model dedicated to the solidification of steel. *Calphad*, *48*, 184-188.
290. Klančnik, U., Košec, B., Mrvar, P., & Medved, J. (2018). Non-equilibrium solidification and microsegregation in centrifugally cast high speed steel for rolls. *Journal of Mining and Metallurgy, Section B: Metallurgy*, *54*(1), 59-66.
291. Eiken, J., Subasic, E., & Lacaze, J. (2020). 3D phase-field computations of microsegregation in nodular cast iron compared to experimental data and CalPhad-based Scheil-prediction. *Materialia*, *9*, 100538.
292. Chen, Q., & Sundman, B. (2002). Computation of partial equilibrium solidification with complete interstitial and negligible substitutional solute back diffusion. *Materials transactions*, *43*(3), 551-559.
293. Walker, P., Kerrigan, A., Green, M., Cardinal, N., Connell, J., & Rivera-Díaz-del-Castillo, P. (2015). Modelling of micro-segregation in a 1C-1.5 Cr type bearing steel. In *Bearing Steel Technologies: 10th Volume, Advances in Steel Technologies for Rolling Bearings*. ASTM International.
294. Lee, S. J., & Clarke, K. D. (2015). A quantitative investigation of cementite dissolution kinetics for continuous heating of hypereutectoid steel. *Metallurgical and Materials Transactions A*, *46*(9), 3917-3923.
295. Liu, S., Xiong, Z., Guo, H., Shang, C., & Misra, R. D. K. (2017). The significance of multi-step partitioning: Processing-structure-property relationship in governing high strength-high ductility combination in medium-manganese steels. *Acta materialia*, *124*, 159-172.
296. Kamoutsi, H., Gioti, E., Haidemenopoulos, G. N., Cai, Z., & Ding, H. (2015). Kinetics of solute partitioning during intercritical annealing of a medium-Mn steel. *Metallurgical and Materials Transactions A*, *46*(11), 4841-4846.
297. De Moor, E., Kang, S., Speer, J. G., & Matlock, D. K. (2014, August). Manganese diffusion in third generation advanced high strength steels. In *Proceedings of the International Conference on Mining, Materials and Metallurgical Engineering, Prague, Czech Republic* (pp. 11-12).
298. Xia, C. H., Lu, X. G., & Li, Y. (2019). Two-dimensional simulations and experiments of homogenization and Kirkendall effect in single-phase diffusion triples. *Journal of Alloys and Compounds*, *790*, 871-883.
299. Priya, P., Johnson, D. R., & Krane, M. J. (2016). Numerical study of microstructural evolution during homogenization of Al-Si-Mg-Fe-Mn alloys. *Metallurgical and Materials Transactions A*, *47*(9), 4625-4639.
300. Larsson, H., & Höglund, L. (2009). Multiphase diffusion simulations in 1D using the DICTRA homogenization model. *Calphad*, *33*(3), 495-501.

301. Song, P., Liu, W., Zhang, C., Liu, L., & Yang, Z. (2016). Reversed austenite growth behavior of a 13% Cr-5% Ni stainless steel during intercritical annealing. *ISIJ International*, *56*(1), 148-153.
302. Atkinson, C., & Akbay, T. (1996). The effect of the concentration-dependent diffusivity of carbon in austenite on a model of reaustenitisation from ferrite/cementite mixtures in FeC steels. *Acta materialia*, *44*(7), 2861-2868.
303. Ochsner, A., Gegner, J., & Mishuris, G. (2004). Effect of diffusivity as a function of the method of computation of carbon concentration profiles in steel. *Metal science and heat treatment*, *46*(3-4), 148-151.
304. Yamamoto, T., Takashima, T., & Nishida, K. (1980). Interdiffusion in the ζ-Solid Solution of a Ni–Al System. *Transactions of the Japan Institute of Metals*, *21*(9), 601-608.
305. L.S. Darken, Diffusion of carbon in austenite with a discontinuity in composition. Transactions of the American Institute of Mining and Metallurgical Engineers, 1949. 180: p. 430-438.
306. Onsager, L. (1931). Reciprocal relations in irreversible processes. I. *Physical review*, *37*(4), 405.
307. Borgenstam, A., Höglund, L., Ågren, J., & Engström, A. (2000). DICTRA, a tool for simulation of diffusional transformations in alloys. *Journal of phase equilibria*, *21*(3), 269.
308. Zhang, L. J., Liu, D. D., Zhang, W. B., Wang, S. Q., Tang, Y., Ta, N., ... & Du, Y. (2014). A new diffusivity database for multi-component Al alloys: focusing on ternary systems and its effect on microstructure evolution during solidification. In *Materials Science Forum* (Vol. 794, pp. 611-616). Trans Tech Publications Ltd.
309. Ghosh, A. (2009). Mathematical model for prediction of composition of inclusions formed during solidification of liquid steel. *ISIJ international*, *49*(12), 1819-1827.
310. Imagumbai, M. (1994). Relationship between primary-and secondary-dendrite arm spacing of C-Mn steel uni-directionally solidified in steady state. *ISIJ International*, *34*(12), 986-991.
311. Kobayashi, Y., & Nagai, K. (2014). A Study on the Relationship between Primary Dendrite Arm Spacing of Low Carbon Steel and Solidification Cooling Rate up to 103 K/s. *Journal of the Japanese Society for Experimental Mechanics*, *14*(Special_Issue), s216-s220.
312. Su, L., Li, H., Lu, C., Li, J., Simpson, I., Barbaro, F., ... & Fan, L. (2014). Automatic measurement of Centreline segregation in continuously cast line pipe steel slabs. In *Energy Materials 2014* (pp. 575-581). Springer, Cham.
313. Su, L., Li, H., Lu, C., Li, J., Fletcher, L., Simpson, I., ... & Qu, X. (2016). Transverse and z-direction CVN impact tests of X65 line pipe steels of two centerline segregation ratings. *Metallurgical and Materials Transactions A*, *47*(8), 3919-3932.
314. Réger, M., Verő, B., & Józsa, R. (2014). Control of centerline segregation in slab casting. *Acta Polytech. Hung*, *11*, 119-137.
315. Chen, R. Y., & Yeun, W. Y. D. (2003). Review of the high-temperature oxidation of iron and carbon steels in air or oxygen. *Oxidation of metals*, *59*(5-6), 433-468.
316. Hao, M., Sun, B., & Wang, H. (2020). High-Temperature Oxidation Behavior of Fe–1Cr–0.2 Si Steel. *Materials*, *13*(3), 509.
317. Turkeli, A. (1993). The Effect of Carbon Content on the Segregation of Manganese in Steel. *The Minerals, Metals & Materials Society(TMS)(USA),*, 81-87.
318. Sharma, M., Richter, S., Prahl, U., & Bleck, W. (2017). Characterization of Nb-Microsegregation and Eutectic Carbide in As-Cast Nb-Microalloyed Al-Free Case Hardening Steel. *steel research international*, *88*(10), 1700092.

319. Davis, C. L., & Strangwood, M. (2009). Segregation behaviour in Nb microalloyed steels. *Materials Science and Technology*, *25*(9), 1126-1133.
320. Roy, S., Patra, S., Neogy, S., Laik, A., Choudhary, S. K., & Chakrabarti, D. (2012). Prediction of inhomogeneous distribution of microalloy precipitates in continuous-cast high-strength, low-alloy steel slab. *Metallurgical and Materials Transactions A*, *43*(6), 1845-1860.
321. Javaheri, V., Nyyssönen, T., Grande, B., & Porter, D. (2018). Computational design of a novel medium-carbon, low-alloy steel microalloyed with niobium. *Journal of Materials Engineering and Performance*, *27*(6), 2978-2992.
322. Lynch, P. C. (2011). the Development of Ultrahigh Strength Low Alloy Cast Steels with Increased Toughness.
323. Cicutti, C., & Boeri, R. (2006). Analysis of solute distribution during the solidification of low alloyed steels. *steel research international*, *77*(3), 194-201.
324. Potts, P. J., & Cresser, M. (1987). A handbook of silicate rock analysis: Blackie, Glasgow, 1987 (ISBN 0-216-91794-8). xi+ 622 pp. Price£ 128.00.
325. Hafner, B. (2007). Scanning electron microscopy primer. *Characterization Facility, University of Minnesota-Twin Cities*, 1-29.
326. Goldstein, J. I., Newbury, D. E., Michael, J. R., Ritchie, N. W., Scott, J. H. J., & Joy, D. C. (2017). *Scanning electron microscopy and X-ray microanalysis*. Springer.

Appendix A

A-1 Interaction volume

Figure A.1 illustrates the interaction of a high energy electron beam with a sample. The size of interaction volume directly affects the EMPA setup. According to Goldstein [326], the interaction volume can be calculated using the X-ray range. For a 5 μm beam generated from a 20 kV source, the interaction volume can be calculated as shown below.

$R(nm) = \frac{27.6\ A\ E_0^{1.67}}{Z^{0.89}\rho}$ = 1578.47 nm = 1.6 μm.

Therefore, the effective beam diameter (d_{eff}) = Beam diameter + 2 x R = 5 + 2 x 1.6 = 8.2 μm

The interaction volume (assuming a hemispherical shape) = $\frac{\pi\ d_{eff}^3}{12}$ = 144.35 μm^3

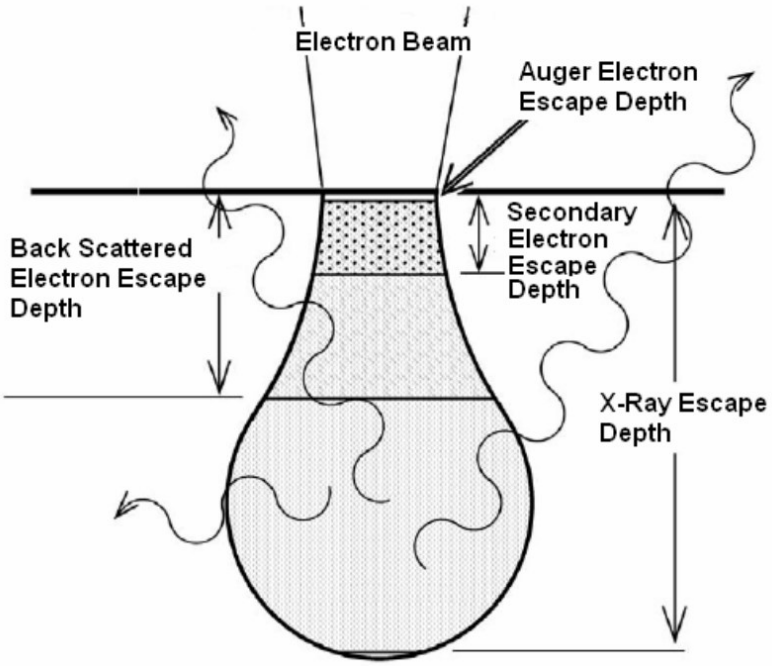

Fig. A.1: Schematic of electron beam interaction with sample [325].

A-2 Quantitative point scanning

Table A.1 contains the details of quantitative point scans performed in this work. The crystals and standards used are also included in the table.

Table A.1: EMPA equipment parameters used for point scanning.

Element/Line	Crystal	OnPeak Time	OffPeak Time	Standard	Analytical Error (rel%)	Detection Limit (99%)
Nb La	LPET	30	30	Niobium, Nb - ESPI	4.49871	0.00893
Mn Ka	LPET	30	30	Alabandite MnS	0.222523	0.00414
Cr Ka	PET	30	30	Cr_2O_3 chromium oxide Alfa	1.08032	0.004231
P Ka	LTAP	30	30	Apatite, Durango	55.8539	0.004159

Appendix B

B-1 EMPA grayscale map to concentration contour

An example of the conversion of a grayscale EMPA map to a concentration contour is shown in this section. Figure B.1-a and b shows the obtained grayscale map and point scan data corresponding to the line scan location shown in Figure B.1-a.

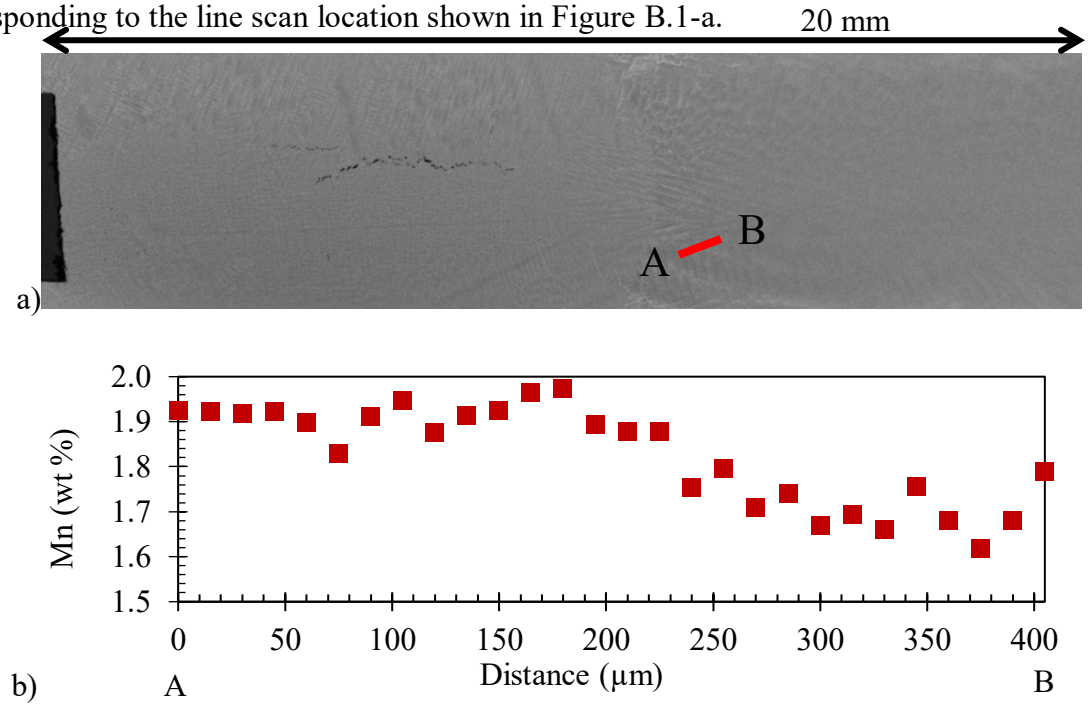

Fig. B.1: a) EMPA Mn map for a section from Bridgman sample 1 and b) Mn line scan plot corresponding to the line scan AB.

Table B.1: EMPA quantitative data for Mn corresponding to line AB.

Distance from A (µm)	wt% Mn
0	1.92
15	1.92
……	……
195	1.89
…….	……
405	1.79

The EMPA Mn map was first converted into a grayscale value (0-255) map. A screenshot of the converted map with grayscale values is shown in Figure B.2. A higher grayscale value corresponds to a brighter spot on the map and vice-versa. The value in cell A1 in the screenshot is the grayscale value of the top left corner pixel of the original grayscale Mn map.

	A	B	C	D	E	F	G
1	118	142	145	160	136	145	139
2	137	149	127	133	141	150	150
3	138	153	143	166	152	140	140
4	130	139	153	136	152	139	125
5	146	159	144	154	147	148	156
6	163	159	131	155	133	150	145
7	135	162	135	146	135	140	127

Fig. B.2: Mn map pixels converted into grayscale values.

The grayscale value of the pixels corresponding to the measured point scan locations were noted. The relation between grayscale value of pixels and wt% Mn using point scan locations was established. The whole grayscale map was then converted into concentration value points using the established relation between grayscale value of the pixels and wt% Mn. The concentration points were then converted into a concentration contour, as shown in Figure B.3.

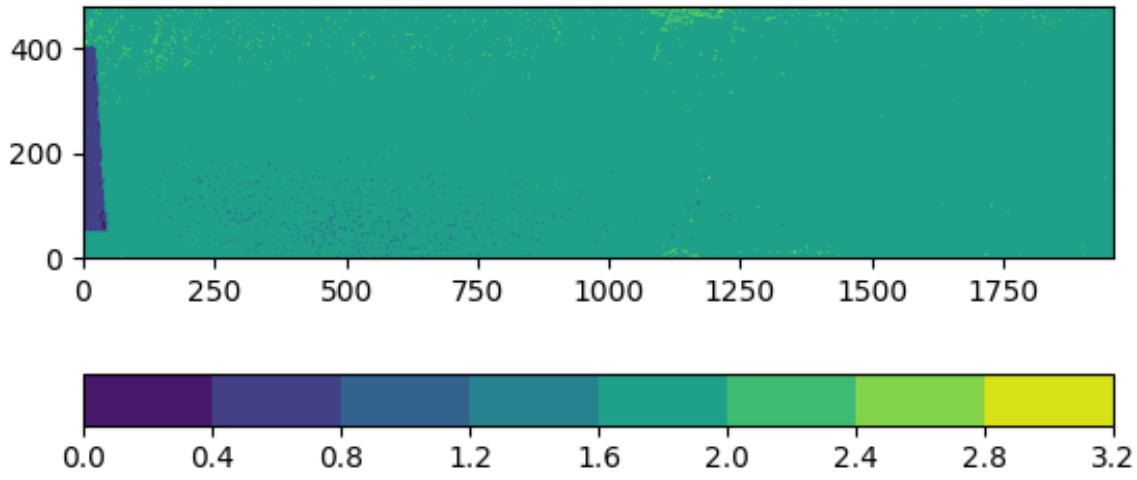

Fig. B.3: Predicted Mn concentration contour of Bridgman sample 1.

Appendix C

C-1 Partition coefficient calculation

An example of partition coefficient calculation process for Mn in Bridgman sample 1 is shown in this section. After the conversion of grayscale map into concentration contour. The points in the region covering the solid-liquid interface as shown in Figure C.1, were used as an input for partition coefficient calculation.

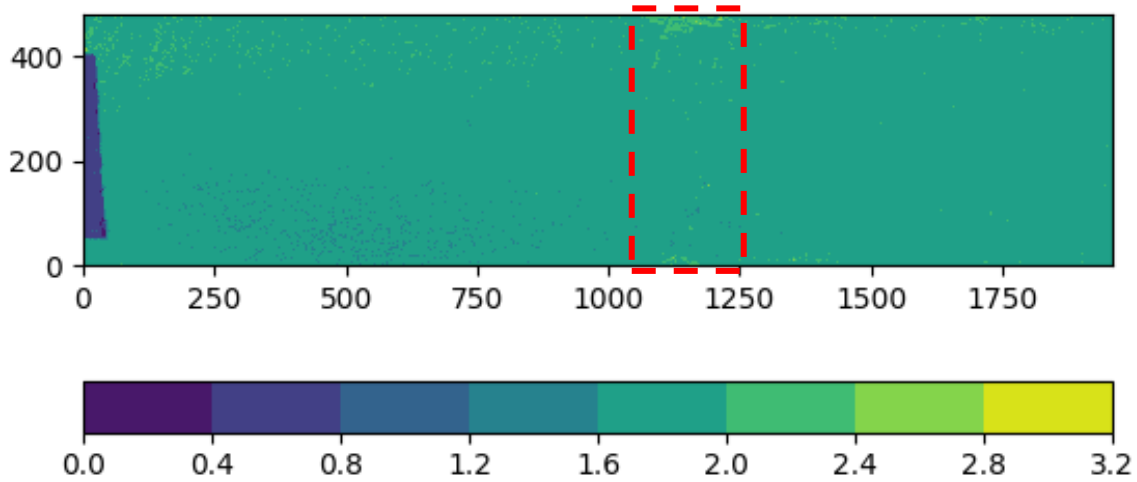

Fig. C.1: Region for input data for partition coefficient calculation for Mn in Bridgman sample 1.

The steps for calculation of partition coefficient for Mn using the data obtained from Figure C.1 are as follows.

Step 1: The obtained composition data for the element was sorted in ascending order.

Step 2: Ordered integer values were assigned to each data point and the total number of data points was noted. The modified data after these two steps is shown in Figure C.2. At this point, the data values are of the form shown in Table C.1.

Fig. C.2: Ordered Mn data for Bridgman sample 1.

Table C.1: Ordered data with assigned integer numbers.

Data point	X	Y
1	0	0.95
2	1	1.16
……	……	……
24001	24000	1.63
…….	……	……
48001	48000	2.61

Step 3: The assigned ordered integers, i.e., the X axis values, were then converted into normalized fraction values by dividing them by the total number of data points (48000). The resulting data values are shown in Table C.2. The normalized fraction values were considered as fraction solid (f_s) values for the corresponding composition.

Table C.2: Ordered data with assigned integer numbers converted into fraction solid.

	Normalized X	Fraction solid	Y
1	0/48000	0	0.95
2	1/48000	0.00005	1.16
……		……	……
24001	24000/48000	0.5	1.63
…….		……	……
48001	48000/48000	1	2.61

Step 4: Composition versus fraction solid was plotted using the processed data. The plot obtained is shown in Figure C.3.

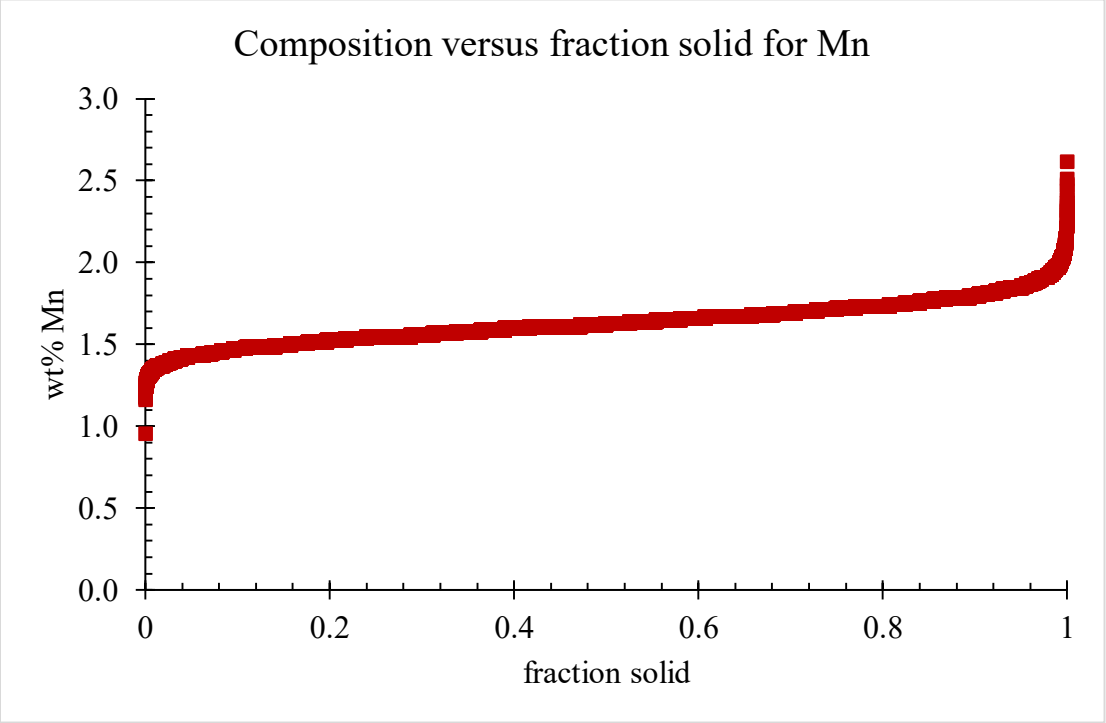

Fig. C.3: Ordered Mn data versus fraction solid.

Step 5: The best fit function of the type $C_o (1-f_s)^{(k-1)}$ (commonly known as the GS equation) was determined by varying the values of C_o and k. The k value from the best fit plot was the required partition coefficient. An illustration is shown in Figure C.4.

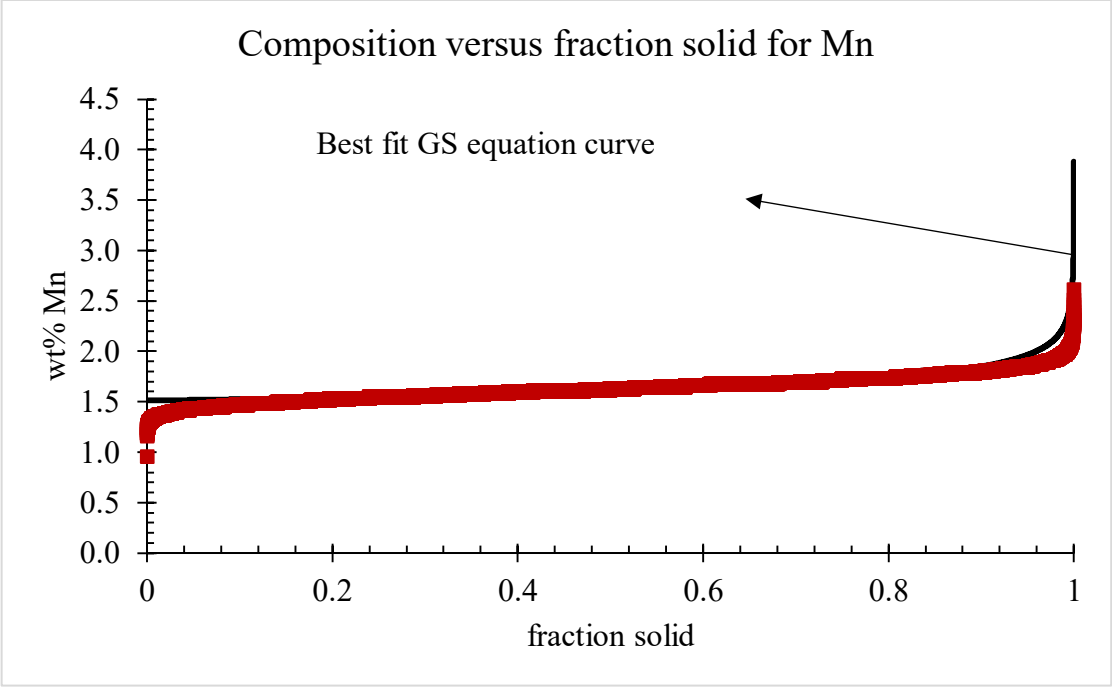

Fig. C.4: Ordered Mn data and GS equation plots with varying Co and k.

Appendix D

D-1 Surface layer diffusion model

This section shows a detailed solution for a surface layer diffusion model. Figure D.1 shows a schematic of diffusion in a fixed volume domain. The initial and final solute profile at t = 0 and t = t are given by the dotted and solid lines, respectively. The overall solute content of the domain is fixed.

Fig. D.1: Schematic of a surface layer diffusion model.

As the total amount of solute is fixed,

$$\int_0^\infty C(x)dx = Constant = \text{N} \qquad \text{D.1}$$

The change in concentration as function of time and distance is given by the Fick's Second Law (Equation 2.9) as explained in Section 2.7. A general solution of the Fick's Second Law is of the form:

$$C\ (x,t) = \ \frac{\alpha}{\sqrt{t}}\exp(\frac{-x^2}{4Dt}) \qquad \text{D.2}$$

where D is the diffusion coefficient of the solute, x is distance and t is time.

Substituting Equation D.2 in D.1:

$$\int_0^\infty \frac{\alpha}{\sqrt{t}}\exp(\frac{-x^2}{4Dt})\,dx = \text{N}$$

$$=> \int_0^{\infty} 2\alpha \sqrt{D} \exp(\frac{-x^2}{4Dt})\, d\frac{x}{2\sqrt{Dt}} = \mathrm{N}$$

Defining

$$\eta = \frac{x}{2\sqrt{Dt}}$$

$$=> 2\alpha \sqrt{D} \int_0^{\infty} \exp(-\eta^2)\, d\eta = \mathrm{N}$$

From the definition of error function:

$$\mathrm{erf}(x) = \frac{2}{\sqrt{\pi}} \int_0^{x} \exp(-\eta^2)\, d\eta$$

$$\mathrm{erf}(\infty) = 1$$

$$=> \int_0^{\infty} \exp(-\eta^2)\, d\eta = \frac{\sqrt{\pi}}{2}$$

$$=> \alpha = \frac{N}{\sqrt{\pi D}}$$

Therefore, for the surface layer diffusion model:

$$C\ (x,t) = \frac{N}{\sqrt{\pi Dt}} \exp(\frac{-x^2}{4Dt}) \qquad \text{D.3}$$

A different case with an initial condition as shown in Figure D.2 can also be reduced to example D.1 simply by considering N to be the solute content within the dotted rectangular region (N').

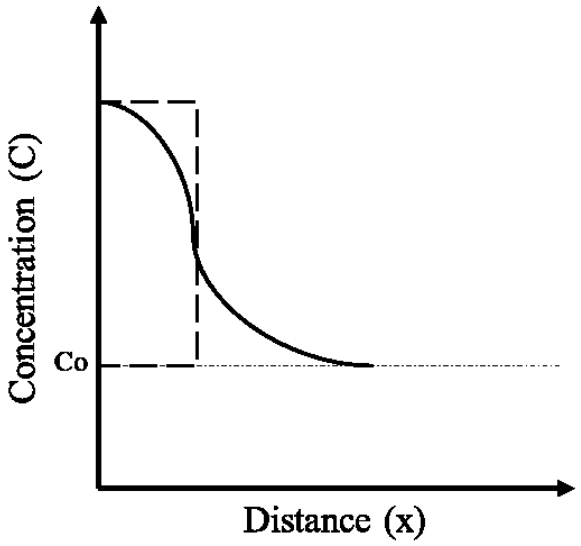

Fig. D.2: Schematic of a modified surface layer diffusion model.

For this case, the solution becomes of the form:

$$C\ (x,t) = \ C_o + \frac{N'}{\sqrt{\pi Dt}} \exp\left(\frac{-x^2}{4Dt}\right) \qquad \text{D.4}$$

Appendix E

E-1 Through thickness EMPA Mn maps for S1

The as-cast Mn EMPA enhanced inverted maps from samples across the thickness of S1 are shown in Figure E.1.

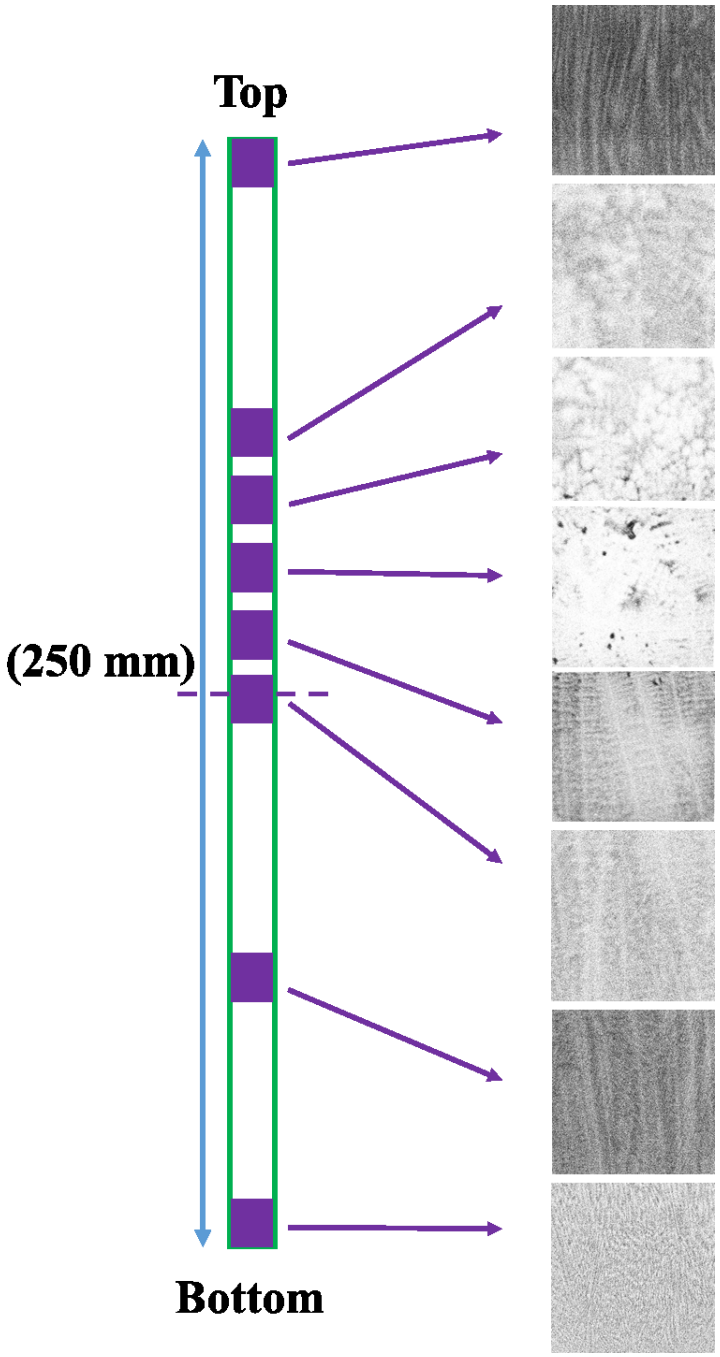

Fig. E.1: As-cast EMPA enhanced inverted Mn maps from S1.